Integration of Virtual and On-line Machining Process Control and Monitoring using CNC Drive Measurements

by

Deniz Aslan

B.Sc., Sabanci University, 2011

M.Sc., Sabanci University, 2014

A THESIS SUBMITTED IN PARTIAL FULFILLMENT OF

THE REQUIREMENTS FOR THE DEGREE OF

Doctor of Philosophy

in

THE FACULTY OF GRADUATE AND POSTDOCTORAL STUDIES

(Mechanical Engineering)

THE UNIVERSITY OF BRITISH COLUMBIA

(Vancouver)

March 2019

The following individuals certify that they have read, and recommend to the Faculty of Graduate and Postdoctoral Studies for acceptance, the dissertation entitled:

Integration of Virtual and On-line Machining Process Control and Monitoring using CNC Drive Measurements

submitted by Deniz Aslan in partial fulfillment of the requirements for

the degree of Doctor of Philosophy

in Mechanical Engineering

Examining Committee:

Dr. Yusuf Altintas, Mechanical Engineering

Supervisor

Dr. Ryozo Nagamune, Mechanical Engineering

Supervisory Committee Member

Dr. Boris Stoeber, Mechanical Engineering

University Examiner

Dr. Juri Jatskevich, Electrical and Computer Engineering

University Examiner

Abstract

The recent trend in manufacturing is to develop intelligent and self-adjusting machining systems to improve productivity without overloading the machine tool. This thesis presents a novel digital machining system: the use of virtual machining simulation to feed predicted process data to on-line monitoring and control system to improve its robustness. The process states (i.e. cutting forces, vibration, torque) are also extracted from CNC drive measurements to auto-tune the virtual model and control the process on-line.

An on-line communication link between the CNC and external computer is developed where the virtual process model and on-line algorithms run in parallel with information exchange. Prior to the cutting operation, the machining process is simulated using a virtual machining system to calculate cutter-workpiece engagement and process states along tool-path. During the cutting operation, process forces are identified from feed drive motor current command measurements by compensating the corresponding friction, inertia of each drive and disturbance of structural dynamics through Kalman filters. The kinematics of the machine tool is solved to transform the individual compensated motor torque to the cutting forces acted on the tool without having to use external force sensors. The speed and load dependent structural dynamics of the spindle assembly are updated in a Kalman filter model by monitoring the vibrations at the spindle.

Simulated machining states are accessed by the on-line machining process monitoring and control system as a virtual feedforward information to avoid false tool failure detection and transient force overshoots during adaptive control. The chatter vibrations are detected from the Fourier Spectrum of the spindle motor current measurements by compensating the structural

dynamics of the drive train. The proposed algorithms are integrated to an on-line process monitoring and control system, and demonstrated on a five-axis CNC machining center.

The thesis presents the first comprehensive virtual process model assisted machining process monitoring and control system in the literature to form the foundations of a comprehensive digital twin for machining systems. The prediction of process states from mainly CNC inherent data makes the system more industry friendly. The system has been designed to be reconfigurable to add new monitoring and control algorithms.

Lay Summary

In order to realize a digital machining twin within Industry 4.0 principles, the next generation CNC machine tools need to be self-adjusting, by using any inherently available sensory data and virtual process simulation feedback that assist the machine during cutting operations. The reliability of current machining process monitoring, and control systems have been suffering mainly because of having difficulties in installing practical and reliable sensors on the machine, and not being able to distinguish the actual machining process states from the effects of geometric changes along the tool path.

This thesis develops an integrated system where the virtual machining process model and the on-line monitoring algorithms run in parallel with information exchange to increase the robustness of the on-line applications. The process states are identified from CNC inherent data which eliminates the need to mount costly and impractical sensors on the machine.

Preface

This Ph.D. dissertation proposes a method to identify machining process states (i.e. cutting forces, torque, power, vibrations) from CNC inherent data and a novel integrated virtual and on-line machining process monitoring and control system. All the work presented was conducted by the Ph.D. candidate in the Manufacturing Automation Laboratories (MAL) at the University of British Columbia, under the supervision of Professor Yusuf Altintas. The research chapters of this dissertation are either already published or currently under preparation for submission. The contributions of the Ph.D. candidate for each chapter are explained as follows:

- A concise version of Chapter 3 which is about prediction of cutting forces from feed drive current measurements has been published in [1], "Aslan, D., and Altintas, Y., 2018, Prediction of cutting forces in five-axis milling using feed drive current measurements, IEEE/ASME Transactions on Mechatronics, 23(2), pp. 833-844". The manuscript was written by myself and edited by my supervisor. I was responsible for all of the system identification, concept formulation and implementation of the force prediction from the drive current measurements method. In addition, the validation experiments were completely planned, carried out, and analyzed by myself. This chapter also formed a basis for two other journal publications with Dr. Jixiang Yang who is a Post-Doctoral Fellow in MAL; [2] - "Yang, J., Aslan, D., and Altintas, Y., 2018, Identification of workpiece location on rotary tables to minimize tracking errors in five-axis machining, International Journal of Machine Tools and Manufacture, 125, pp. 89-98." and [3] - "Yang, J., Aslan, D., and Altintas, Y., 2018, A feed rate scheduling algorithm to constrain tool tip position and tool orientation errors of five-axis CNC machining under cutting load disturbances, CIRP Journal of Manufacturing Science and Technology -

https://doi.org/10.1016/j.cirpj.2018.08.005". I provided the process state prediction model to estimate the tracking errors due to cutting disturbances along the toolpath; Dr. Yang developed the workpiece location optimization and feed rate scheduling algorithms. Manuscripts were written by Dr. Yang and myself and edited by our supervisor.

- There will be another journal paper that proposes a milling process monitoring algorithm by considering speed and load dependency of spindle and tool dynamics through sensor fusion which is described in Chapter 4. This work is from my 3-month CANRIMT internship at ETH Zürich, Institute of Machine Tools and Manufacturing (IWF), under supervision of Prof. Konrad Wegener. Martin Postel, a Ph.D. Candidate at the same Institute, and I did all the identification and cutting experiments together. Specially designed fixtures for system identification experiments are designed and patented by IWF, ETH Zürich and their industrial partners.
- Contents of Chapter 5 which are about detecting chatter vibrations from CNC drive measurements has been published in [4], "Aslan, D., and Altintas, Y., 2018, Online chatter detection in milling using drive motor current commands extracted from CNC, International Journal of Machine Tools and Manufacture, 132, pp. 64-80". The manuscript was written by myself and edited by my supervisor. I have developed the conceptual ideas, implemented the algorithm on the machine and conducted the verification experiments.
- Chapter 6, which describes the virtual process model integrated on-line system architecture, has been published in [5], "Altintas, Y., and Aslan, D., 2017, Integration of virtual and on-line machining process control and monitoring, CIRP Annals – Manufacturing Technology 66(1), pp. 349-352". The draft manuscript was written by myself and extensively revised by my supervisor. Algorithms developed previously by my

supervisor were used with virtual process model feedback by identifying the process states from CNC drive measurements. I was responsible for the implementation of the on-line system on the machine and conducted extensive experiments for validation.

Table of Contents

List of Tables

List of Figures

List of Symbols

$\mathbf{A}, \mathbf{A}_{\mathbf{exp}}$	Normalized equivalent and expanded system matrices of feed drives
$\mathbf{A}_{\mathrm{S}}, \mathbf{A}_{\mathbf{exps}}$	Normalized equivalent and expanded system matrices of spindle drive
$\mathbf{A}_{\mathbf{disp}}, \mathbf{A}_{\mathbf{exp\_disp}}$	Normalized equivalent and expanded system matrices of vibration sensors
$\mathbf{A}_{\mathbf{ds}}$	Discrete observer state matrix of spindle drive
a_2	Linear offset between tilt-axis and table coordinate frames
$a_{acc_i} (i = 1, ..., 5)$	Accelerations at the vibration sensors (accelerometer) on spindle body
a	Axial depth of cut
$\mathbf{B}$	Normalized equivalent input matrix of feed drives
$\mathbf{B}_{\mathrm{S}}$	Normalized equivalent input matrix of spindle drive
$\mathbf{B}_{\mathbf{disp}}$	Normalized equivalent input matrix of vibration sensors
B_e	Equivalent viscous friction of spindle drive
b	Width of cut
$\mathbf{C}, \mathbf{C}_{\mathbf{exp}}$	Normalized equivalent and expanded output matrices of feed drives
$\mathbf{C}_{\mathrm{S}}, \mathbf{C}_{\mathbf{exps}}$	Normalized equivalent and expanded output matrices of spindle drive
$\mathbf{C}_{\mathbf{disp}}, \mathbf{C}_{\mathbf{exp\_disp}}$	Normalized equivalent and expanded output matrices of vibration sensors
$\mathbf{C}_{\mathbf{ds}}$	Discrete observer output matrix of spindle drive
c	Feed rate (chip load per tooth)
$\mathbf{D}$	Input transmission matrix of feed drives

$\mathbf{D}_{\mathrm{S}}$	Input transmission matrix of spindle drive
$d_{moment-i}(i = x, y, z)$	Moment arm length between the tool tip and table center
d_{disp}	Actual tool tip displacement (vibration) at the displacement sensor location
$\hat{d}_{disp}$	Estimated tool tip displacement (vibration) at the displacement sensor location through weighted average data fusion
$d_{acc_i}(i = 1, \ldots, 5)$	Actual displacements (vibration) at the vibration sensors (accelerometer) on spindle body
$\hat{d}_{acc_i}(i = 1, \ldots, 5)$	Estimated tool tip displacements (vibration) from individual vibration sensors (accelerometer) without data fusion
d_4	Linear offset between tilt-axis and rotary-axis coordinate frames
E_j, F_j, G_j	Recursively calculated polynomials uniquely defined in GPC algorithm
$F_{a,}\hat{F}_a$	Actual and estimated cutting force acting on drive
$\hat{F}_t$	Estimated tangential cutting force at the tool tip
F_t, F_r	Cutting forces in tangential and radial directions
F_h	Impulse force by hammer
F_p	Peak force per spindle period
F_r	Reference force level for adaptive control
F_1	Actual force at the tool tip in displacement sensor direction
$\hat{F}_1$	Estimated force at the tool tip in displacement sensor direction through weighted average data fusion

$\hat{F}_{acc_i}\ (i = 1,...,5)$	Estimated forces at the tool tip in displacement sensor direction from individual vibration (accelerometer) sensors without data fusion
f_c	Commanded feed rate of adaptive controller
f_a	Actual feed rate of machine
$\mathbf{F_{WP}}$	Cutting forces and torques vector acted on the tool in workpiece frame
$F_{t-x}, F_{t-y}, F_{t-z}$	Cutting forces in x-y-z directions in tool coordinate frame
$F_{wp-x}, F_{wp-y}, F_{wp-z}$	Cutting forces in x-y-z directions in workpiece coordinate frame
$\hat{F}_{X_a}, \hat{F}_{Y_a}, \hat{F}_{Z_a}$	Estimated cutting forces in x-y-z directions in drive coordinate frame
$F_{\mathrm{resultant}}$	Resultant force in X-Y plane (tool coordinate frame)
$F_{magnet-Z}$	Force applied at the tool tip by the magnet in Z direction (tool coordinate frame)
G_{Ω}	Transfer function of the PI velocity controller of spindle drive
G_I	Transfer function of the PI current controller of spindle drive
G_m	Transfer function of the closed current loop of spindle drive
$G_{o\Omega}$	Transfer function of the open velocity loop of spindle drive
$G_{c\Omega}$	Transfer function of the closed velocity loop of spindle drive
G_{sp}	Transfer function of spindle drive
$G_{d\tau}$	Transfer function between the disturbance torque and nominal (commanded) current of spindle drive

$G_{d\Omega}$	Transfer function between disturbance torque and actual velocity of spindle drive
$G_{L\tau}$	Transfer function of Luenberger state observer designed for nominal (commanded) current of spindle drive
$G_{c\tau}$	Transfer function of compensated disturbance system of spindle drive
G_{cb}	Transfer function of comb filter
G_c	Combined feed drive and cutting process transfer function for adaptive control
$\{G_I\}$	Control vector for GPC
h_p	Pitch length of ball screw
I_{nom}	Nominal (commanded) current
I_{act}	Actual current of feed drive
I_{actS}	Actual current of spindle drive
J_d	Drive inertia
J_e	Equivalent inertia of feed drive
J_{eS}	Equivalent inertia of spindle drive
J_m	Motor mass inertia
$\mathbf{J}$	Jacobian matrix
$\mathbf{K}$	Kalman Filter gain vector of feed drives
$\mathbf{K_{disp}}$	Kalman Filter gain vector of vibration sensors

K_b	Back emf constant of spindle drive
K_t	Motor torque constant of feed drives
K_{tS}	Motor torque constant of spindle drive
K_{tc}, K_{rc}	Cutting force coefficients in tangential and radial directions
K_{te}, K_{re}	Edge force coefficients in tangential and radial directions
$\mathbf{L}$	System noise vector
$\mathbf{L_{ds}}$	Luenberger observer gain vector of spindle drive
N	Number of teeth (flutes) on cutter tool
N_s	Stator turn ratio of spindle induction motor
N_r	Rotor turn ratio of spindle induction motor
$N_{1,} N_2$	Minimum and maximum prediction horizons of GPC
n_s	Stator electrical speed of spindle induction motor
n_r	Rotor mechanical speed of spindle induction motor
$\mathbf{P}$	Estimation error covariance matrix of feed drives
$\mathbf{P}_\mathrm{S}$	Estimation error covariance matrix of spindle drive
O_i, O_j, O_k	i-j-k orientations of tool in workpiece coordinate frame
$P_{x,} P_y, P_z$	x-y-z positions of tool in workpiece coordinate frame
$\mathbf{Q}$	System noise covariance matrix of feed drives
$\mathbf{Q}_\mathrm{S}$	System noise covariance matrix of spindle drive
Q_{comb}	Quality factor of comb filter

$\mathbf{q}$	Linear and angular position command vector in machine coordinate frame
$\mathbf{R}$	Measurements noise covariance matrix of feed drives
R_S	Stator resistance of spindle induction motor
R_r	Rotor resistance of spindle induction motor
$\mathbf{R_{spindle}}$	Measurements noise covariance matrix of spindle drive
r_{tool}	Radius of the cutter tool
r_g	Transmission ratio of ball screw
S	Slip of spindle induction motor
t_s	Sampling time
V_{qs}, V_{ds}, V_{0s}	Stator voltage values in q, d and 0 frames of spindle induction motor
$V_{qr}^{'}, V_{dr}^{'}, V_{0r}^{'}$	Normalized rotor voltage values in q, d and 0 frames of spindle induction motor
v	Measurement noise term
v_f	Relative velocity between two interacting surfaces
v_s	Stribeck velocity
w	Process noise term
w_{AC}	AC periodic disturbance noise
w_{DC}	DC process noise
$weight_m (m = 1, ..., 5)$	Assigned weights to vibration sensors (accelerometers) installed on spindle body

X_m	Motor magnetizing reactance of spindle induction motor
X_r	Rotor leakage reactance of spindle induction motor
X_S	Stator leakage reactance of spindle induction motor
z	Average deflection of the material bristles between two interacting surfaces
z_s	Infinitesimally small step of z in the sticking region
$\alpha \, \& \, \beta$	Residues of transfer function in s domain
a_{comb}, β_{comb}	Bandwidth coefficients of comb filter
a_1, a_2	Predetermined threshold factors for tool breakage alarm
$\boldsymbol{\delta}_{\mathbf{T}}$	Infinitesimally small displacement vector at the tool in workpiece frame
$\boldsymbol{\delta}_{\mathbf{q}}$	Infinitesimally small displacement vector of drives in drive frame
$\varepsilon_1, \varepsilon_2$	Residues of time series filters applied on average torque per tooth in the tool breakage detection algorithm
ζ	Damping ratio
ζ_{AR}	Uncorrelated random noise sequence of ARIMAX form in GPC
η	Efficiency
θ	Angular position of motor shaft
θ_{DC}, θ_{AC}	DC (static) and AC (harmonic) noise ratio terms
λ	Weighting factor on the GPC input increment
Φ_d	Drive disturbance Frequency Response Function

Φ_{KL}	Kalman Filter FRF
σ_0	Stiffness of the elastic bristles between two interacting surfaces
σ_1	Damping coefficient of the elastic bristles between two interacting surfaces
σ_2	Viscous friction coefficient
σ_{TB}	Percentage threshold value for tool breakage alarm
$\tau_a, \hat{\tau}_a$	Actual and estimated cutting torque acting on drive
$\hat{\tau}_d$	Estimated disturbance torque acting on drive
τ_{a_DC}, τ_{a_AC}	DC (static) and AC (harmonic) components of the actual cutting torque acting on drive
$\boldsymbol{\tau}_{\mathbf{Drives}}$	Drive forces and torques vector in drive frame
$\hat{\tau}_{A_a}, \hat{\tau}_{C_A}$	Estimated cutting torque for A and C rotary drives in drive coordinate frame
τ_m, τ_c	Measured motor and cutting torque of feed drives
τ_{mS}, τ_{cS}	Measured motor and cutting torque of spindle drive
τ_{sa}	Average cutting torque per tooth period
τ_f	Friction torque of feed drives
τ_{fS}	Friction torque of spindle drive
τ_{coul}, τ_{stat}	Coulomb and static friction torque of feed drive
$\tau_{coulomb-S}$	Coulomb friction torque of spindle drive

Φ_{sys_d}	FRF between tool tip displacement and vibration sensors (accelerometer)
Φ_{sys_F}	FRF between force at the tool tip and vibration sensors (accelerometer)
ϕ	Instantaneous angle of cutter tool immersion in workpiece
$\hat{\phi}_1, \hat{\phi}_2$	First-order adaptive time series filters to remove varying DC trend and runout on the signal
ψ	Flux linkage per second of spindle induction motor
Ω_m	Angular velocity of the motor shaft of feed drives
Ω_S	Angular velocity of spindle shaft
Ω_{nom}	Nominal (commanded) velocity
Ω_{act}	Actual velocity
Ω_{S-rs}	Spindle speed in revolutions per second
ω_a	Angular velocity of the arbitrary reference frame of spindle induction motor
ω_b	Angular velocity of the base electrical frame of spindle induction motor
ω_{bw}	Normalized bandwidth of comb filter
ω_c	Chatter frequency
ω_r	Angular velocity of the rotor frame of spindle induction motor
ω_n	Natural frequency
ω_t	Tooth passing frequency

ω_r	Frequency resolution
ω_p	Frequency with the highest magnitude in the comb filtered signal
$\omega_{sampling}$	Sampling frequency

List of Abbreviations

ARIMA	Autoregressive integrated moving average
ARIMAX	ARIMA model with additional time series input variables
CWE	Normalized equivalent and expanded system matrices for feed drives
CNC	Computer numerical control
DNC	Direct numerical control
FRF	Normalized equivalent and expanded system matrices for spindle drive
GPC	Adaptive generalized predictive control
NC	Numerical control
PLC	Programmable logic controller

Acknowledgements

I would like to start by thanking Prof. Yusuf Altintas for his support and guidance throughout my Ph.D. years. I appreciate his patience, excellent vision for engineering and research which helped me greatly to toughen up and improve myself every single day.

Prof. Erhan Budak, my MSc supervisor, who supported me throughout all these years unconditionally, has my utmost respect and gratitude, he is and always will be more than a supervisor to me.

I would also like to extend my gratitude towards all my colleagues and friends in Manufacturing Automation Laboratory (MAL), especially Onur Mert Ozturk, Alptunc Comak, Coskun Islam, Oguzhan Tuysuz, Ahmet Yildiz and Tayfun Ozdemir. I am grateful for all the technical and emotional support.

I thank Prof. Konrad Wegener, Martin Postel and the Institute of Machine Tools and Manufacturing (IWF), ETH Zürich; for the opportunities I was provided during my stay.

I thank the industrial supporter of this research; Hyundai WIA Machine Tools, and NSERC-CANRIMT for the support during my PhD and internships. I thank Industrial Technology Research Institute of Taiwan (ITRI) for providing the Quaser UX-600 5-axis machining center.

I cannot express how thankful I am to my family for their support, love and encouragement throughout my life. My dear mother and father, Gülser and Güven and my lovely sister Helin Su, I love you all. Finally, Genevieve, she is and was always right next to me when I had difficulties in my research and life and provided unquestioned support. I will do my best to reflect all the love and support back.

Chapter 1: Introduction

In recent years, there has been an increasing interest in achieving unattended and self-adjusting machining systems. Researchers in the field mainly focus on the machining process monitoring and control where the primary applications can be listed as: tool wear and breakage monitoring, chatter detection and avoidance, adaptive control of the process forces and dimensional errors, thermal compensation of machines, collision avoidance, and machine tool health monitoring. A variety of sensors have been used such as force, vision, acoustic emission, vibration, power, strain gages, thermocouples and laser devices depending on the application.

Though externally installed sensors provide useful information from the cutting region with high bandwidth, the reliability of such systems highly depends on the availability of industry friendly sensors and robustness of methods to avoid false alarms and incorrect actions. Installing external sensors within the work envelope increases the cost, as well as the risk of frequent failures due to harsh machining environment which disrupts the production. Not being able to distinguish the actual machining process states from the effects of geometric changes along the tool path leads to false alarms and poor performance of the process control algorithms, therefore the majority of such systems have not been used in industry. Given the limitations of the above-mentioned systems, the use of CNC inherent data to predict process states and integration of virtual process model into the on-line algorithms is proposed to achieve an intelligent and robust unattended machining system in this thesis, as shown in Figure 1.1. The system extracts the cutting forces at the tool tip from the feed and spindle drive motor current commands and uses virtual model feedback to eliminate or reduce the false alarms while adaptively controlling the machining process.

First, an on-line communication link between CNC and external PC is developed in C++ via Ethernet connection. External PC can collect data from the CNC with up to 10 kHz sampling frequency and it can vary the spindle and feed overrides at 10 Hz interval which is sufficient for the targeted on-line applications.

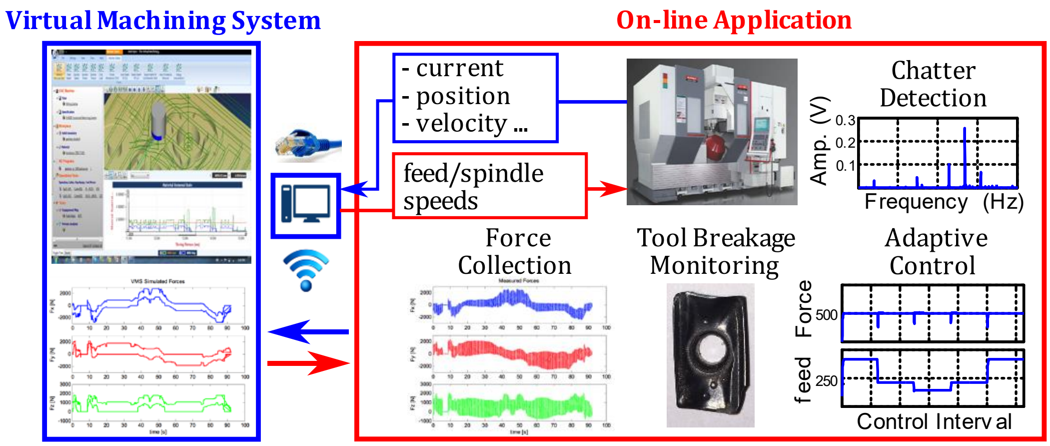

Figure 1.1: Parallel execution of virtual and on-line system with information exchange on external PC [5]

By being able to read data from the CNC drives and write feed and spindle overrides back to CNC on-line, it is possible to monitor and control the machining process without installing external sensors on the machine tool. However, the prediction of cutting forces at the tool tip from servo drive measurements and running the on-line monitoring and control functions integrated with the virtual machining system introduce research challenges.

It has been shown in the past that cutting force measurements leads to the most reliable process monitoring and control performance in machining operations. Typically, the cutting forces are measured via external sensors installed close to the cutting region which are prone to failures and increase the overall cost. Hence, it is desirable to solely use available information in the CNC system to monitor and control the machining processes. This thesis presents a method to predict the cutting forces at the tool tip from the feed drive motor current commands of CNC systems.

Remaining process states (i.e. torque, power, vibrations) are identified from either feed or spindle drive measurements to assist the monitoring and control functions.

It is also important to note that the structural dynamics of the spindle, tool holder and tool system may change as a function of speed, load and thermal expansion as reported in the literature. Therefore, the intelligent machining systems should not rely on system models identified at idle state of the spindle or machine tool entirely but update themselves according to in-process variations. To investigate these in-process variations, vibration sensors are installed on the non-rotating parts of the spindle structure, far from the cutting region. The variations of the structural dynamics of the spindle and tool are monitored on-line, and corresponding observer transfer functions are updated accordingly to predict tool tip vibration and process forces accurately.

With the process states identified on-line, it is desired to ensure that the machining process is chatter free and stable. Chatter is typically detected by a microphone, accelerometer or acoustic emission sensor close to the cutting region and analyzing the frequency content of the corresponding measurements. Microphones tend to pick ambient noise from adjacent machines, and the sound signals may be amplified at certain frequencies as tool goes into cavities which trigger false alarms. Accelerometers and acoustic emission sensors are delicate and require additional analog to digital converters adding cost and complexity to the CNC systems. This thesis presents a method to detect chatter by using the spindle motor current commands readily available in CNCs. The dynamics of closed spindle velocity controller is identified automatically using available CNC functions. The effects of structural dynamics and servo elements on the measurements are compensated by state observers and the resulting signal is analyzed to isolate the chatter frequency. The spindle speed is regulated to avoid chatter on-line.

Once the process is chatter free, tool breakage monitoring and adaptive control of the process forces are run with the virtual model feedback. The proposed system brings critical information from the virtual machining system, and prevents false breakage alarms, transient overloads of the tool and collisions during adaptive control. The uncertainties in the virtual process model, such as cutting force coefficients, are calibrated from the on-line measurements at the beginning of the machining process and monitored continuously afterwards.

Henceforth, the thesis is structured as follows: Chapter 2 discusses past research reported in the literature specifically in regard to process state prediction from drive current measurements, on-line tool breakage and chatter vibration monitoring, adaptive control of machining operations and varying spindle dynamics in milling operations. In Chapter 3, a comprehensive method to predict the cutting forces at the tool tip from CNC drive current measurements is presented. The method includes system identification of a feed drive, calculation of the force Jacobian and compensation of the structural dynamics between the tool tip and servo location. Chapter 4 investigates the speed and load dependency of the spindle and tool dynamics from vibration sensors installed on the spindle structure with the purpose of updating the observer transfer functions depending on the varying process conditions to predict tool tip vibration and process forces. Chapter 5 describes an on-line chatter detection method using drive motor current commands where the spindle drive transfer function is identified automatically through sine sweeps. The structural dynamic modes of the spindle are compensated via a proposed observer. Chapter 6 presents the integrated intelligent machining system where the virtual process model and on-line monitoring and control functions run in parallel with information exchange. Benefits of the system are demonstrated on a sample part. Thesis is concluded in Chapter 7 and future research directions are suggested.

Chapter 2: Literature Review

2.1 Overview

The main objective of this thesis is to develop an intelligent, robust machining monitoring and control system that predicts the process states from CNC drive measurements and self-adjusts itself to varying process conditions. This chapter reviews the previous research related to process state predictions from drive measurements (Section 2.2) and from vibration sensors mounted on the spindle structure by considering in-process varying system dynamics (Section 2.3), on-line machining monitoring and control algorithms: chatter detection (Section 2.4) and tool breakage monitoring and adaptive control of machining operations (Section 2.5). Each section is concluded with a short summary that points out the gaps in the relevant literature where the fundamental contributions of this thesis are founded.

2.2 Prediction of Process States from CNC inherent measurements

Typically, intelligent machining systems are expected to monitor tool breakage, detect and suppress chatter and adaptively control maximum cutting loads to increase the material removal rates without violating the machine and cutting tool limits. It is desired to achieve these tasks by collecting critical information from the cutting region without increasing the overall cost of the production. It has been agreed in literature that the cutting forces provide the most valuable insight about the cutting process which are generally used in tool condition monitoring, adaptive control and cutting performance diagnosis [6].

There have been several force measurement techniques reported in literature, which can be classified as direct or indirect approaches. In the direct approach, the cutting forces are measured via external sensors installed within the cutting region, which can be combined with position tracking from CNC. Klocke et al. [7] and Totis et al. [8] used stationary and rotating dynamometers installed on the table and spindle-tool interface, respectively, to measure the cutting forces and map them along the tool path. Although dynamometers provide high bandwidth and reliable force measurements, they are not resistant to cutting fluid, chips etc. and restrict the accessibility of the work envelope. In addition, they increase the overall cost, inertia and reduce the static and dynamic stiffness of the machine tool. To overcome these limitations, Mohring et al. [9] developed a system where three force sensors were embedded in the fixture system and Xie et al. [10] designed a smart tool holder with four displacement sensors installed. However, these systems are still costly, and their use is limited to a laboratory environment due to their delicate nature. Fusion of force and Acoustic Emission (AE) signals have also been commonly used especially for tool health monitoring in turning operations [11], [12], [13]. AE sensors are powerful in terms of detecting high frequency content generated by plastic deformation in the cutting region, yet, they are not applicable for milling operations since signals are extremely sensitive to interrupted nature of the cut and noise [14].

In the indirect force measuring category, there are also two approaches: sensors (force or displacement) can be built into the machine tool or forces can be extracted from the feed and spindle drive measurements without installing any external sensor. For the first approach, Tlusty [15] and Jeppsson [16] placed strain gauges on the outer ring of the spindle bearings and the housing, respectively, and measured the cutting forces indirectly. Later, Stein and Tu [17] modeled the spindle bearings to predict the forces caused by the thermally induced preloads using strain gauges and thermocouples where temperature dependency, sensor failures and complexity of the thermal modeling are major issues. Sarhan et al. [18] and Kang et al. [19] used displacement sensors such as capacitance and optical fiber but these sensors are limited to monitor the tool deflection due to their coarse resolutions and are prone to drive vibrations.

Park and Altintas [20] utilized a spindle integrated ring shaped force sensor installed between the spindle housing and the spindle flange at the bolt holes where piezoelectric sensors can measure the forces in three directions. They expanded the bandwidth of the sensing system by compensating the disturbance effects of structural dynamics of the spindle. Similarly, Bryne and O'Donnell [21] installed two piezoelectric force sensors between the spindle shaft and the housing in order to measure the process forces as well as monitor the spindle health. For the displacement sensors, Albrecht et al. [22] installed capacitance displacement sensors in the spindle housing and the measurements were interpreted as forces through calibration factors and dynamic compensation. Smith et al. [23] used strain gauges embedded in a spindle and measured the torque during milling operations. They benefit from the wide bandwidth due to high torsional stiffness. In these systems, the force is transmitted to the sensor location through the cutting tool and holder, whose structural deflection and moment arm lengths affect the force transmission ratios. As a result, the force sensors need to be calibrated for each tool and holder couple. Furthermore, the instrumentation of the spindle increases the installation and the operating cost considering that the spindles require frequent maintenance in industry.

On the other hand, retrofit measurement solutions can be avoided since the latest modern control systems allow access to internal signals in the numerical controller [24] such as drive positions, velocity, motor torque, power and so forth. Matsushima et al. [25] and Constantinides and Bennett [26] attempted this first by predicting the cutting torque and forces from spindle motor and power. The issue with these studies were that the spindle motors only provide the tangential component of the cutting forces and the temperature dependence of the induction motor current measurements are significant as reported by Mannan and Broms [27]. Later, Altintas [28] was able to show that cutting forces can also be predicted from feed drive current measurements provided that the friction in the drives are considered, and tooth passing frequency is within the bandwidth of the servo. Shinno et al. [29] developed a disturbance observer and implemented it within the position controller of a linear-motor driven aerostatic table system and predicted the cutting forces by only considering the rigid body transfer function of the drive system. The high bandwidth of linear feed drives is beneficial, and these systems have no considerable losses due to friction [6]. However, these studies do not consider the structural dynamics of the machine tool. Since the vast majority of the machine tool industry uses ball screw drive systems to handle the high cutting disturbance in machining operations, it can be concluded that, at the moment, force sensing from feed drive measurements has very narrow frequency bandwidths, limited to 2.5 and 3 axis operations with straight cuts, and do not consider the non-linear behavior of friction on translational and rotary drives of the machine tool, especially at transients where motion direction changes.

Based on this literature survey it can be seen that there exists a gap in literature. At present, techniques have not been developed where the cutting forces are predicted from the CNC inherent signals for 5-axis milling operations by considering the complex nature of the friction on drives, compensating the distortions on the measurements due to structural dynamics of the machine tool and mapping the estimated cutting torque on each drive to the tool coordinate frame using the force Jacobian of the multi-axis machine tool.

2.3 Process State Predictions by Considering Speed and Load Dependent Spindle Dynamics

It has been observed in the literature that the structural dynamics of the spindle system change as a function of speed, load and thermal expansions [30], [31]. Since the measurement of tool tip Frequency Response Function (FRF) or tool tip to external sensor location FRFs are usually performed at zero speed (idle state) under no load, it leads to inaccurate prediction of stability lobes and state observer designs for process monitoring and control purposes. Therefore, in-process identification of speed and load dependent FRF of the spindle structure and updating corresponding stability lobes and state observers is essential.

The spindle systems that operate at high speeds ($>$ 10000 rev/min) are commonly used in industry for high speed machining operations where the dynamics of the system change significantly [32]. This change is usually attributed to centrifugal forces and gyroscopic moments acting on bearings and the shaft. In addition, thermal expansion of the shaft changes the bearing preload where the load applied at the tool tip during cutting also affects the dynamics between the shaft and the bearing [33]. Cao et al. [34] and Rantatalo et al. [35] both developed detailed finite element models of the spindle structure and investigated the effects of gyroscopic moments and centrifugal forces on the spindle dynamics. The main drawback of these kind of modeling studies is that the accurate modeling of the entire spindle system requires the exact geometries of components, bearing preloads and contact parameters of the assembly locations which are also varying in-process continuously.

Most commonly used approach for investigating the varying spindle dynamics is to identify the FRFs experimentally through shaker systems or impact tests during rotation. Cheng et al. [36] and Mascardelli et al. [37] performed impact tests on a standard, rotating artifact with a focus on regular ($>$ 20 mm diameter) and micro milling ($<$ 5 mm diameter), respectively. Postel et al. [31] identified the speed dependent spindle dynamics isolated from the tool holder-tool assembly, and used a receptance coupling approach afterwards to add tool holder and tool substructures to the identified spindle dynamics in order to obtain the tool tip FRFs. Effect of lateral forces, thermal variations and speed were investigated, and the updated stability charts were verified with experiments. Besides impact tests, Matsubara et al. [38] used a non-contact excitation method with magnetic actuators and displacement sensors for evaluating the dynamic stiffness of a rotating spindle. Nonlinearities in the dynamic spindle stiffness were captured and its effect on cutting stability were investigated.

In addition to these studies which are focusing on system identification under different conditions, an inverse stability method was also used to identify the FRF at the tool tip from cutting experiments [39]. Suzuki et al. [40] and Eynian [41] measured the chatter frequency in-process and solved the inverse stability to identify the tool tip FRF. Later, Ozsahin et al. [30] considered the shifting spindle modes and used the inverse stability technique as well. However, these studies assume that the mode shapes of the structure remain the same and they require chatter frequency measurements from unstable cutting experiments in a short range of spindle speeds. Researchers also applied receptance coupling (RC) analysis to rotating structures [36], [42] where Grossi et al. [43] used RC and predicted the speed varying dynamics of different setups but with the same tool holder.

For the process monitoring and control part, although researches used sensory spindle systems before, there are no reported studies in the literature that consider the in-process variations of the spindle-holder-tool structure for predicting process states at the tool tip from externally installed sensors. Recently, Denkena et al. [44], [45] installed strain gauges between the guide rails and shoes of the spindle structure and performed tool deflection control. Force calibration and measurements were performed by linear regression analysis using the strain signals and the reference force signals applied at the tool tip, which makes the sensing system limited to only DC component of the process states (i.e. force and vibration at the tool tip). The spindle structure was also equipped with piezoelectric force sensors [46] and capacitance displacement sensors [22], where the dynamic effects of the structural modes in the sensor measurements were properly compensated using state observers. However; system identification was performed in idle state at zero speed with no preload applied at the tool tip in all these studies.

Based on this literature survey it can be concluded that the in-process variation of the spindle-holder-tool assembly is not only crucial for stability predictions of machining operations, but also for on-line monitoring and control functions. There is still room for improvement in the literature in terms of updating the state observers of monitoring functions according to in-process varying structural dynamics. At present, studies focusing on process state (i.e. vibration, force) predictions from external sensors installed on the spindle structure do not consider these varying system dynamics under operational conditions.

2.4 On-line Chatter Detection in Milling Operations

Unless avoided, the self-excited vibrations (chatter) cause poor surface finish, reduces the tool and spindle life, hence limit the productivity in machining operations. As a result, automatic chatter detection and avoidance has been an important goal to achieve intelligent, productive machine tools without operator intervention.

Early classical chatter theories presented by Tobias [47], and Tlusty [48] explain the fundamental mechanism of self-excited chatter vibrations for time invariant orthogonal cutting. Later, dynamics of milling and its stability have been modeled both in frequency [49], [50], [51] and discrete time domains [52]. It has been shown that the vibrations and forces are periodic at tooth passing frequencies when the process is stable, exhibiting a forced vibration phenomenon [53]. When a milling process chatters, the process exhibits both forced vibration at the harmonics of spindle/tooth passing frequencies as well as at the vicinity of the chattering natural frequency plus/minus the integer multiples of frequencies away from the chatter frequency. The challenge is to separate the forced vibrations from chatter signals, and use robust and practical sensors to detect chatter and avoid it by changing the speed or cutting conditions automatically during machining. Furthermore, the chatter frequency may continuously change as the cutting conditions change or the machine exhibits position dependent structural dynamics.

There have been several on-line chatter detection methods reported in literature, which can be classified as direct or indirect approaches as in Section 2.2. In the direct approach, researchers tried to achieve on-line detection of chatter vibrations by using external sensors installed either within the workspace or integrated with the machine tool. The most commonly used method is to collect sound measurements from the cutting region via microphone and use the spectrum of the measured signals to detect the chatter vibrations as implemented by Altintas and Chan [54], Sekhon [55], and Schmitz et al. [56]. These methods have been suffering from poor robustness since it is challenging to eliminate the ambient noise in the microphone measurements which can contain the sound from neighbouring machine tools and the sound signals show unpredictable behavior at certain frequencies as the tool goes in and out of cut, and through cavities along the toolpath. Researchers also used accelerometers [57], [58], AE sensors or dynamometers [59], spindle integrated force or displacement sensors [46] and sensory workpiece clamping systems [60]. These sensors need additional analog to digital converters adding cost and complexity to the CNC systems. In addition, instrumented spindle or workpiece clamping systems reduce the dynamic stiffness of the spindle, or the setup requires calibration for each tool, holder couple or workpiece geometry to compensate the effects coming from the structural dynamics in the measured signals.

In the indirect approach, chatter vibrations are detected by estimating the process states (i.e. force, torque, vibration) from spindle and feed drive motor or encoder measurements. Soliman and Ismail [61] first attempted to detect chatter vibrations from spindle current measurements by applying a statistical indicator which was found to be insensitive to speed, feed rate and geometry of the cut. However, the authors noted that further work is needed to investigate the sensitivity of the much-reduced current signals at higher frequencies due to decaying behavior of the drive disturbance transfer function. More recent studies from Kakinuma et al. [62] and Yoneoka et al. [63] applied disturbance observers on spindle current measurements in order to remove the effects of the structural and servo dynamics and isolate the chatter frequency. Shimoda et al. [64] expanded the disturbance observer approach to feed drives by also using high resolution linear encoder measurements. However, these studies ([62], [63], [64]) use low pass filter (LPF) based disturbance observers and case dependent band pass filters (BPF) to focus on a specific frequency range in order to detect the chatter frequency. Usage of BPF eliminates the need to compensate the effects of structural dynamics or servo elements along the signal transmission path from tool tip to the drive motor or the encoder location. However, it is not possible to pre-determine the bandpass frequency in a way that the output signal is free of dynamic distortions without losing the chatter vibration related frequency content for each tool/holder couple. Hence, the present methods need a manual intervention to adjust the parameters based on cutting conditions and structural frequencies of the machine tool and workpiece.

Based on this literature survey, many techniques exist to detect chatter vibrations by installing external sensors or using drive current and encoder measurements with case dependent, manually tuned observers. However; there is still a gap in the literature in terms of considering the true dynamics of the drive and compensating the corresponding effects in the measurements to cover a wider frequency range without any need to install external sensors on the machine, case-dependent frequency range selection and experience-based observer tuning.

2.5 Process Monitoring and Control of Machining Operations

There is a rich history of research and publication on the development and implementation of intelligent manufacturing systems since the early 1980s. In addition to detecting and suppressing chatter vibrations, intelligent machining systems are expected to monitor tool breakage and adaptively control maximum cutting loads to increase the material removal rates without violating process constraints.

Several researchers have worked on tool condition monitoring for milling operations since on-line tool breakage detection is crucial to prevent catastrophic failures in production. First, Matsushima et al. [25] applied a 28^{th} order Auto-Regressive (AR) filter to detect tool breakage using the spindle motor current measurements. Lan et al. [65] used a similar approach by using a 15^{th} order AR filter where the high order filters cannot effectively distinguish tool breakages during the transient cutter-workpiece engagement variations such as entry-exit to cut, holes, feed rate variations and they require large computation time windows. In order to overcome these, Altintas [28], [66] proposed a 1^{st} order AR filter to detect tool breakage with two residual indexes indicating the difference between the measured and predicted forces based on the AR filter and give large magnitudes when the tool is damaged. Altintas [53] also stated that the 1^{st} order AR filter is sufficient since the cutting forces are functions of spindle and tooth passing frequencies with their harmonics. He argued that synchronization of cutting force measurements with these frequencies provide sufficient information to detect the tool breakage.

It is also important to increase the productivity of machining processes through adaptive control (AC) of milling forces or tool tip deflection by adapting feed rate to changes in cutting conditions such as depth and width of cuts along the toolpath. Several researchers have used AC under different constraints to maximize the productivity by maintaining cutting forces at a desired level. Tlusty and Elbestawi [67] analyzed the transients in an AC servomechanism for milling operations by using a state-space approach and focused on the time delay between drive velocity and cutting force change. Lauderbaugh [68] investigated process dynamics and included the corresponding effects in his controller design where Liu et al. [69] compared the performances of different controller types to show that early AC systems with fixed gains result in slow response or instability depending on process conditions along the toolpath. Finally, Altintas [53] presented an AC framework based on either pole-placement or a generalized predictive control (GPC) law, which is utilized to adjust feed rates of the XY table of the milling machine to keep the peak resultant force at a desired level. In addition, his approach can keep the static tool deflection within tolerances since the force in the normal to the finished surface can be constrained. Later, Park [46] used the same algorithm with the spindle integrated force sensor combined with the disturbance Kalman Filter to compensate dynamical distortions in the sensor measurements.

There are also more recent studies in the literature under the category of intelligent machining systems which use the above listed algorithms by utilizing an externally installed sensory system or the CNC inherent data, some with position tracking from CNC [70], [71]. Klocke et al. [7] presented a position-oriented process monitoring strategy in freeform milling where stationary and rotating dynamometer measurements were synchronized with the encoder measurements from drives in order to monitor the process states by considering the cutter-workpiece engagement variations along the toolpath. Nouri et al. [72] also used a stationary dynamometer to monitor tool wear through a global parameter they defined based on the cutting coefficients. The wear coefficient's behavior was tracked by using a mechanistic force model approach and looking at the total distance traveled by the tool, rather than considering complex cutter-workpiece engagement conditions. Mohring et al. [73] used an integrated sensory spindle and a fixture system to monitor the process forces through sensor fusion. Koike et al. [74] followed a different path by utilizing a sensorless approach to detect the tool fracture in milling by integrating multi-axial servo information through case dependent observers with a rigid body drive model. Verl et al. [75] also used the signals available within the CNC to monitor the wear of feed drives by comparing the states with the initial measurements from when the machine is new. Van Houten and Kimura [76] developed a maintenance system to relate the predicted machining behavior and signals measured from multiple sensors to avoid machine tool part failures. Shinno and Hashuzime [29] and Hayashi et al. [77] proposed an on-line process monitoring and adaptive control system for ultra-precision machining by using a sensorless approach and a temperature sensor mounted on the tool's rake face to keep the temperature at a desired level along the toolpath, respectively.

The Listed studies in this chapter which utilize tool breakage, wear monitoring and adaptive control of machining operations have not been used in industry due to false alarms, poor robustness of algorithms, and the lack of practical cutting force sensors. Therefore, it can be concluded from the literature survey that there is still a need for a system which performs the process monitoring and control functions by using only the CNC inherent data, with an integrated virtual model feedback not just for position tracking, but also for tracking the process states and providing critical feedback to the on-line algorithms to improve robustness. In addition, the virtual model can be calibrated from on-line measurements for improved accuracy.

Chapter 3: Prediction of Cutting Forces in Milling using Feed Drive Current Measurements

3.1 Overview

It is desired to use CNC inherent data for process monitoring and control of machining operations. However, at present no works are able to use CNC inherent data to control and monitor machining operations in a reliable way, where the machine tool structure, servo dynamics and kinematics are considered while simultaneously compensating the corresponding distortions in the measured signals in order to predict the cutting forces at the tool tip along the tool path for multi-axis milling operations. Conversely, literature consists of techniques either utilizing external sensors installed within the work envelope or using CNC inherent data without compensating the distortions on measured signals appropriately.

In this chapter, a new framework is presented to identify cutting forces in five-axis milling operations using the feed drive motor current control commands obtained directly from the CNC of the machine tool. The friction and inertial loads, which are used for the rigid body motion of the machine, are first separated from the current commands, and the remaining current is considered to be spent on cutting. The dynamic force is distorted by the structural dynamics of the feed drive chain between the cutting point on the table and the drive motor. These structural dynamic effects are compensated by Kalman filters, which expand the bandwidth of the current sensing from the CNC data significantly. The estimated cutting torque at each feed axis is transmitted to the tool coordinate frame using the inverse kinematic model of the five-axis machine tool. The estimated forces can be used in monitoring the cutting forces along the five-axis tool path, which in turn can be used for both online calibration of virtual machining model as well as for tool condition monitoring and adaptive control of maximum forces with virtual machining system assistance.

3.2 Identification of Feed Drive Dynamics

In order to predict the cutting forces at the tool tip from drive motor current measurements, feed drive dynamics have to be identified for each axis of the machine tool. A five-axis machine tool with three ball screw driven translational (X-Y-Z) and two rotational (A-C) drives with worm gear transmission mechanism is used for the illustration of the proposed methodology (see Figure 3.1).

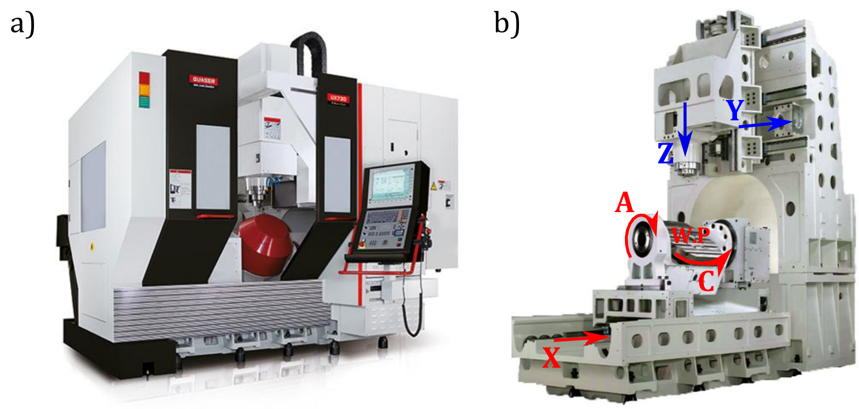

Figure 3.1: a) Quaser UX600 5-axis machining center with Heidenhain CNC, **b)** Translational and rotary axes configuration of the machine tool

Regardless of the kinematic configuration of the machine tool, each feed drive motor must overcome both static and dynamic loads. Static loads include friction in the feed drive's kinematic chain (i.e. ball screw, thrust bearing, and guideways), whereas dynamic loads are contributed by the acceleration and cutting forces delivered to the feed drive motor as torque disturbances. The total torque delivered by the motor (τ_m) is spent to overcome all loads as [53];

$$\tau_m = K_t I_{nom} = J_e \frac{d\Omega_m}{dt} + \tau_f + \tau_c \tag{3.1}$$

where τ_f and τ_c are the friction and cutting torque, respectively; J_e is the equivalent inertia reflected on the motor, and Ω_m is the angular velocity of the motor shaft. The motor torque is proportional to the nominal current I_{nom} drawn by the motor, where K_t is the motor torque constant. Since the goal is to obtain the cutting torque portion (τ_c) from the nominal current (I_{nom}) measurements, the first step in system identification is to identify friction characteristics and the equivalent inertia for each drive as described in the following section.

3.2.1 Equivalent Inertia and Friction Identification

The friction and equivalent inertia of all drives can be identified from the velocity and current values supplied by the CNC while moving the drives at different velocities. In general, open architecture CNC systems allows on-line identification of drive dynamics. A square wave signal with variable pulse width, which has a rich frequency content, is supplied to the drive as the control signal by the CNC and the equivalent inertia is identified from the measured response [78]. However; the 5-axis machining center used in this study has a commercial Heidenhain iTNC530 CNC which has a semi-open structure since it allows access from an external PC but only by using its proprietary communication libraries in Visual Studio C++. For system identification purposes, Heidenhain's TNCopt® software is used which is a PC program for commissioning, optimizing and diagnostic of digital control loops. The dialog between TNCopt® installed on an external PC and CNC takes place via Ethernet connection.

Table mass, motor shaft (J_m) and drive screw (J_d) are used to form an equivalent moment (J_e) of inertia reflected on the motor and the motor torque constants are identified using built-in identification functions of TNCopt® which are given in Table 3.1.

Table 3.1: Inertia and motor torque constant values of axis feed drives

	X	Y	Z	A	C
J_m[kg.m^2]	0.0077	0.0077	0.0077	0.0015	0.001
J_d[kg.m^2]	0.00596	0.00624	0.00440	0.009	0.00455
J_e[kg.m^2]	0.01366	0.01394	0.01210	0.00240	0.00555
K_t[Nm/A]	1.964	1.964	1.964	2.106	1.522

The Lund-Grenoble (LuGre) friction model is used to capture the Coulomb friction, Stribeck effect, hysteresis and pre-sliding displacement which introduces non-linear friction behavior. Unlike the classical Coulomb friction model, LuGre friction does not treat the non-linear friction regions as discontinuous changes at especially motion direction changes. Instead, it considers the average deflection of the material bristles between two surfaces (z), see Figure 3.2, which are in contact and captures the friction dynamics in the sticking region as well.

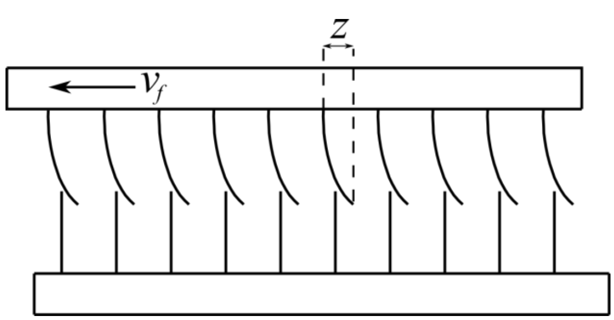

Figure 3.2: Illustration of material bristle deflection for LuGre model

The LuGre friction torque generated from the bending of the bristles between two surfaces is expressed as [79];

$$\tau_f = \sigma_0 z + \sigma_1 \frac{dz}{dt} + \sigma_2 v_f \tag{3.2}$$

where σ_0 and σ_1 are the stiffness and damping coefficient of the elastic bristles within the friction interface between two interacting surfaces, respectively and are approximated as outlined in [80]. σ_2 is the viscous friction coefficient and identified from the slope of the velocity-friction curve at the sliding region as described in [1], v_f is the relative velocity and z is the average deflection of the bristles (see Figure 3.2) with its derivative defines as;

$$\frac{dz}{dt} = v_f - \frac{|v_f|}{g(v_f)} \sigma_0 z \tag{3.3}$$

The Stribeck effect is captured by $g(v_f)$ which depends on speed, material properties, lubrication and surface roughness, and defined as;

$$g(v_f) = \tau_{coul} + (\tau_{stat} - \tau_{coul}) e^{-(v_f/v_s)^2} \tag{3.4}$$

where v_s is the Stribeck velocity, and τ_{coul} and τ_{stat} are coulomb and static friction values, respectively and identified from the velocity and current values supplied by the CNC while moving the drives at different velocities [80]. For σ_0, a very small step of z in the sticking region, referred as z_s, is introduced to the drive and the stiffness constant is approximated as;

$$\sigma_0 = \tau_{coul} \frac{\mathrm{sgn}(dz/dt)}{z_s} \tag{3.5}$$

In addition, in the sticking region, where there is no apparent motion, the friction in Eq. (3.2) can be approximated as ($z \approx \theta$);

$$\tau_f \approx \sigma_0 \theta + \sigma_1 \dot{\theta} + \sigma_2 \dot{\theta} \tag{3.6}$$

where θ is the angular displacement of the motor shaft. Therefore, the dynamics of the interaction between materials are modeled as in [80];

$$J\ddot{\theta} + (\sigma_1 + \sigma_2)\dot{\theta} + \sigma_0\theta = u(t) \tag{3.7}$$

where Eq. (3.7) represents a damped second-order system, assuming a sufficiently damped motion which is the case for the feed drives considered in machine tools, σ_1 can be calculated as [80];

$$\sigma_1 = 2\sqrt{J\sigma_0} - \sigma_2 \tag{3.8}$$

The friction parameters σ_0, σ_1, σ_2 and $g(v_f)$ are approximated from measurements, but the average displacement of the bristles (z) is not measurable, hence it is solved numerically by solving Eq. (3.3) and using the Forward Euler Approximation as follows [78];

$$\begin{aligned}
&v_f[0] = 0, \quad z[0] = 0, \quad \frac{dz[0]}{dt} = 0 \\
&\frac{dz}{dt} = v_f[k] - \frac{|v_f[k]|}{g(v_f[k])}\sigma_0 z[k-1] \\
&z[k] = z[k-1] + \frac{dz[k]}{dt} t_s
\end{aligned} \tag{3.9}$$

where t_s is the sampling time and k is the discrete time step. Once the friction parameters are identified for each drive, the corresponding average displacements of the bristles are calculated as given in Eq. (3.9) and the friction value is calculated with Eq. (3.2). The tuned friction parameters which give the identified LuGre curve shown in Figure 3.3, are given in Table 3.2 for both translational and rotary axes per each direction.

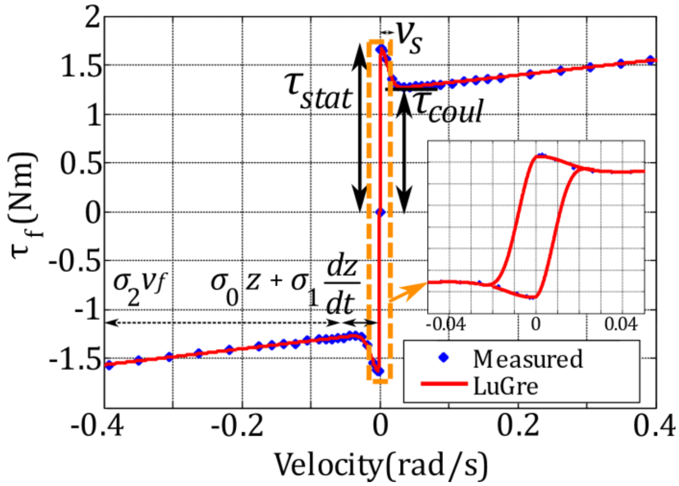

Figure 3.3: Experimental and LuGre friction curves for C-axis with model parameters

Table 3.2: LuGre friction parameters for axis feed drives

	X (+, -)	Y (+, -)	Z (+, -)	A (+, -)	C (+, -)
σ_0[Nm/rad]	525, 525	575, 575	475, 475	28e3, 28e3	20e3, 20e3
σ_1[Nm.s/rad]	15, 15	12.5, 12.5	10, 10	25, 15	20, 25
σ_2[Nm.s/rad]	0.175, 0.15	0.15, 0.11	0.065, 0.082	4.25, 1.3	0.82, 0.82
τ_{stat}[Nm]	1.34, 1.32	1.62, 1.68	2.3, 2.3	2.7, 2.9	1.9, 1.82
τ_{coul}[Nm]	1.73, 1.84	1.78, 1.86	2.15, 2.1	1.57, 1.05	1.24, 1.24
v_s[rad/s]	0.061, 0.087	0.087, 0.065	0.571, 0.222	0.012, 0.013	0.016, 0.017

Corresponding LuGre friction curves for each axis are given in Figure 3.4 with the experimentally measured values.

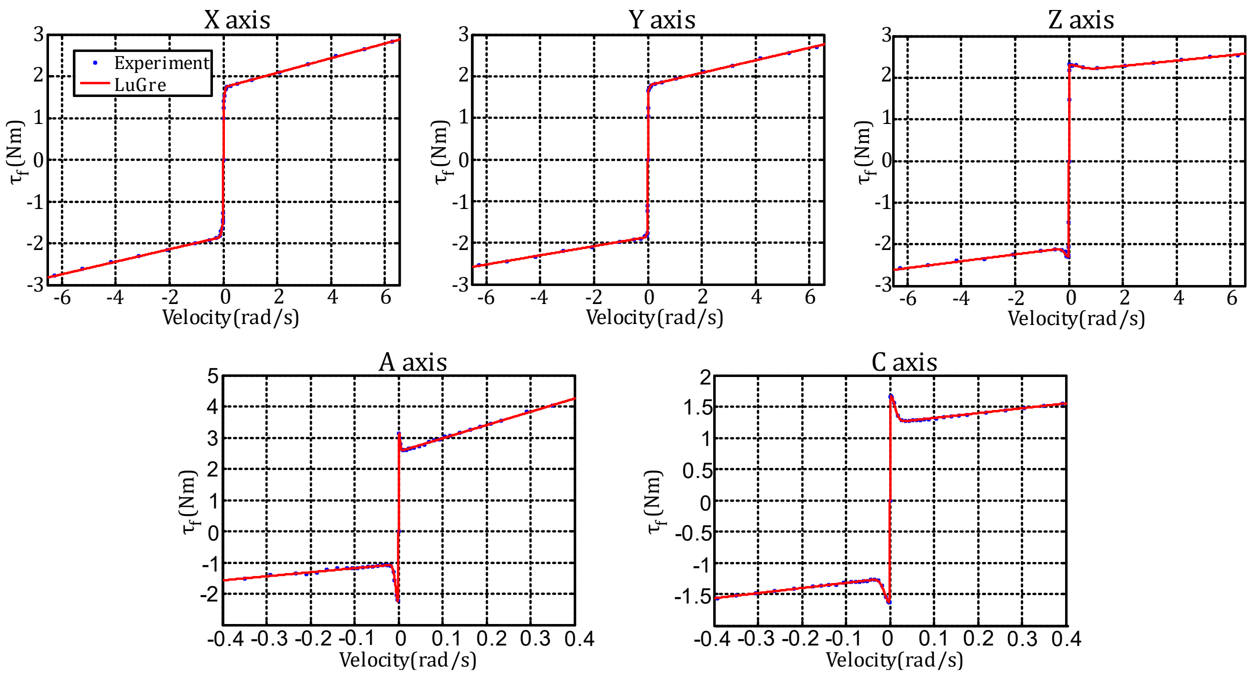

Figure 3.4: Experimental and LuGre friction curves for axes

3.2.2 Transmission of Cutting Forces to Feed Drive Motor

Given that the equivalent inertia and friction characteristics are known for a drive, cutting torque component can be extracted from the measured motor torque by rewriting Eq. (3.1) as follows;

$$\tau_c = \tau_m - \tau_f - J_e \frac{d\Omega}{dt} = K_t I_{nom} - \tau_f - J_e \frac{d\Omega}{dt} \tag{3.10}$$

where the source of the cutting torque (τ_c) is the cutting force (F_a) at the tool tip in the corresponding direction which is transmitted to the feed drive as a disturbance. First, using rigid body assumption for the feed drive, the relation between the cutting force (F_a) and the cutting torque (τ_c) delivered to the feed drive motor can be derived by the principle of conservation of work and energy as;

$$\tau_{at} = \frac{r_g}{\eta} F_a \;\leftarrow\; r_g = \frac{h_p}{2\pi} \tag{3.11}$$

where r_g is the transmission ratio of ball screw with a pitch length of h_p, and η is the efficiency. For rotary drives, cutting force at the tool tip (F_a) is transmitted to the servo as follows;

$$\tau_{ar} = \frac{r_g d_{moment-i}}{\eta} F_a \tag{3.12}$$

where $d_{moment-i}(i = x, y, z)$ is the moment arm length between the tool tip and table center. The efficiency values (η) of the translational drives are obtained from the manufacturer catalogue, and they are identified experimentally for the rotational drives (A and C).

Since the range of efficiency is quite wide (40-90%) for worm gears due to dependency on the preload amplitude, static load tests are performed to identify the specific efficiency values of the rotary drives. Both A and C axes are loaded from 31.75 kg (70 lbs) to 45.36 kg (100 lbs) with 4.53 kg (10 lbs) increments applied at a specific location and the corresponding motor torque is obtained from the CNC (see Figure 3.5).

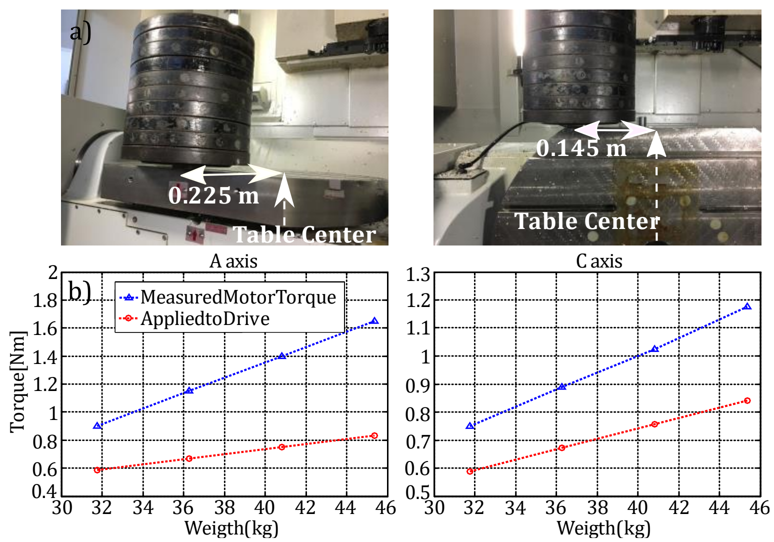

Figure 3.5: Static load experiments to identify efficiency for A and C axes

Efficiency is calculated as the ratio between the applied torque to the drive and the corresponding measured motor torque for four different loading conditions and the average values are given in Table 3.3.

Table 3.3: Pitch and efficiency values of axis feed drives

	X	Y	Z	A	C
h_p[mm/rev] or [rad/rev]	12	12	12	0.05235	0.06981
η[%]	92	92	92	62	81

It should be noted that the equations provided so far in this chapter are only valid within the bandwidth of the disturbance transfer function between the cutting force and the drive motor current measurements. For higher frequencies, the corresponding disturbance transfer function should be identified and the effect of structural and servo dynamics on drive motor current measurements must be compensated as described in the following two sections, respectively.

3.2.3 Identification of Feed Drive Disturbance Frequency Response Function (FRF)

The cutting forces are transmitted to the feed drive motors as disturbance torque through the drive's structural chain and servo amplifier as shown in Figure 3.6.

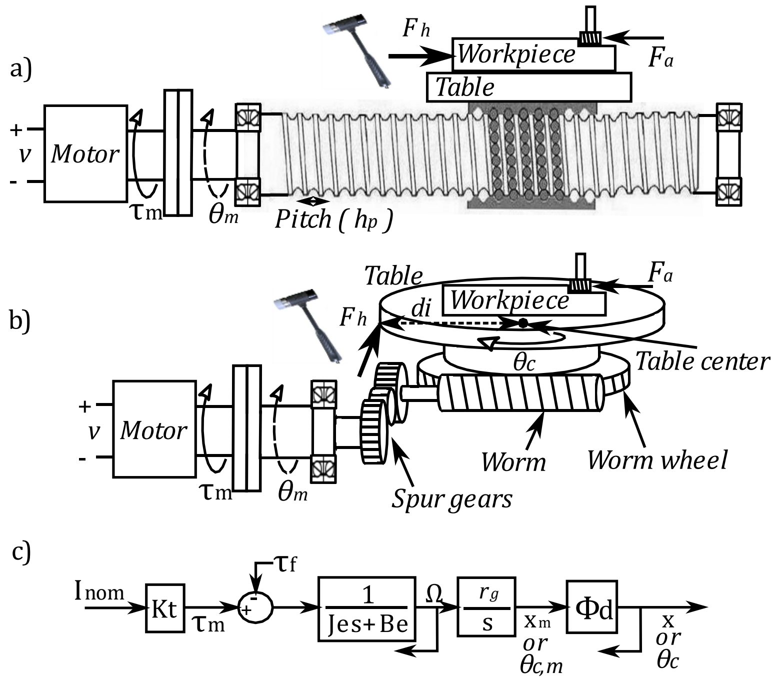

Figure 3.6: (a) Translational and (b) Rotary feed drive mechanism, (c) Disturbance transfer function (Φ_d)

In milling, the cutting forces are periodic at tooth passing frequency which is equal to spindle speed times number of teeth on the cutter. In order to capture the milling forces, the bandwidth of the disturbance transfer function between the cutting force and the drive motor current must be at least higher than the tooth passing frequencies used during machining operations. Although the current amplifier of the CNC has >700 Hz bandwidth, unless compensated, the structural dynamics of the drive with natural frequencies around 20-70 Hz reduces the bandwidth of the force prediction from motor current to around 10-15 Hz or 300-450 rev/min spindle speed when a two-fluted cutter is used.

Disturbance FRFs (Φ_d) are measured by applying impulse force excitation at the table (see Figure 3.6 a & b), while measuring the current and angular position of motor shaft from the Heidenhain CNC via Ethernet connection. The impulse force ($F_h(\omega)$) is converted as an equivalent applied (input) torque by using Eq. (3.11) and (3.12), and the response torque from the motor is

$\tau_c(\omega)$. The experimentally measured FRFs are identified by a modal curve fitting technique (using CutPro® Modal Analysis [81]), which leads to the following transfer function;

$$\Phi_d(s) = \frac{\tau_c(s)}{\tau_a(s)} = \sum_k \frac{\alpha_k + \beta_k s}{s^2 + 2\zeta_k \omega_{nk} s + \omega_{nk}^2} \tag{3.13}$$

where α_k & β_k, ζ_k, ω_{nk} are the residues, damping, and natural frequency of mode k, respectively. The identified transfer function parameters of all five drives are listed in Table 3.4 where the experimental and curve fitted drive disturbance FRFs can be seen in Figure 3.7.

Table 3.4: Modal parameters for drive disturbance FRFs

Axis	Mode	ω_{nk} (Hz)	ζ_k (%)	α_k	β_k
X	1	36.1	4.7	3042	38.1
	2	40.2	2.14	9413	47.1
	3	42	3.5	-292	86.8
	4	62.5	5	24575	152.5
	5	145	5	34073	-18.7
	6	179	4.23	195281	-99
Y	1	16.3	4.96	518	1.3
	2	31	2.9	2719	7.1
	3	36	3.3	6183	7.8
	4	47	2.8	2673	-10.2
	5	52	5	15591	9.98
	6	63.5	6	8849	21.1
	7	71	2.2	11459	3.9

	8	77.5	3	57547	96.1
	9	85	2.2	16125	17.4
	10	102	1.2	5831	-10
	11	130	9.8	22339	115.6
	12	180	3.9	-108153	-158.2
Z	1	39	7	-1913	43.1
	2	43	3.81	3980	-3.3
	3	63.74	4.97	29270	55.8
	4	86	0.4	852	-1.5
	5	89	6.2	109192	185.1
	6	92.5	3	-38413	10.1
	7	150.5	1.8	30800	34.9
	8	183.3	0.31	11631	4.7
A	1	19.9	0.69	-8053	-26.2
	2	50	0.47	-123072	263.9
	3	63.86	0.22	105425	-132
	4	81.31	0.16	14992	-115
	5	167.8	0.122	140159	-44.6
	6	176.34	0.13	-116470	74.6
C	1	45.3	0.14	-11820	-244
	2	52.6	0.086	70505	453.6
	3	66.3	0.035	30915	16.6

	4	75.2	0.022	9365	6.44
	5	98.9	0.052	-1126	-65.5

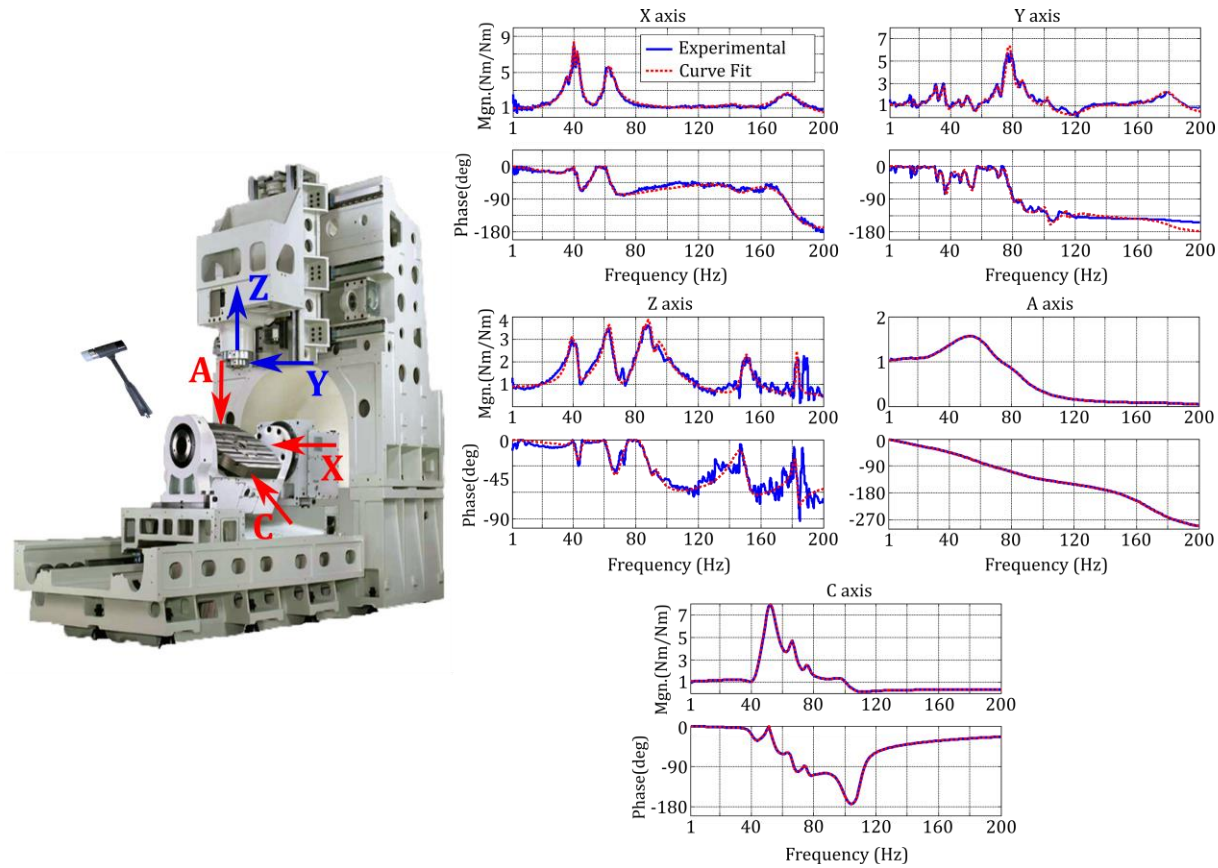

Figure 3.7: Experimental and curve fitted drive disturbance FRFs

The curve fitted transfer function in Eq. (3.13) can be mapped to polynomial form as;

$$\Phi_d(s) = \frac{\tau_c(s)}{\tau_a(s)} = \frac{b_0 s^n + b_1 s^{n-1} + b_2 s^{n-2} + b_3 s^{n-3} + \dots}{s^m + a_1 s^{m-1} + a_2 s^{m-2} + \dots} \tag{3.14}$$

Parameters of the transfer function polynomials (b_i, a_i) for each axis can be obtained from Table 3.4. The disturbance transfer functions given in Eq. (3.13) and (3.14) are mapped to the state-space form but by applying similarity transformation matrix on the states due to poorly conditioned state matrices [20];

$$\begin{aligned} \dot{\mathbf{x}}(t) &= \mathbf{Ax}(t) + \mathbf{Bu}(t) \\ y(t) = \tau_c(t) &= \mathbf{Cx}(t) + \mathbf{Du}(t) \end{aligned} \tag{3.15}$$

where $\mathbf{x}(t)$ and $y(t)$ are state and output vectors, respectively. The state space model in continuous time domain consists of the normalized state $\mathbf{A}$, the input $\mathbf{B}$, the output $\mathbf{C}$, and the input transmission $\mathbf{D}$ matrices, which are given in Appendix A for each drive. The state-space model is used for dynamic compensation of drive current measurements to estimate the cutting torque caused by the forces on the feed drive motor at higher spindle speeds.

3.3 Dynamic Compensation of Feed Drive Current Measurements

The objective of dynamic compensation of drive current measurements is to reduce the influence of the structural dynamic modes (see Figure 3.7) that distort the measurements containing frequencies above the servo bandwidth (10-15 Hz). Prior to performing the dynamic compensation, friction, and inertial torque portions are removed from the motor torque.

The inversion of the transfer function may lead to amplification of low amplitude noise and instabilities when the system has a nonminimum phase dynamics, hence it is not suited to use an inverse filtering of commanded motor torque obtained from the CNC. Instead, a disturbance Kalman Filter has been proposed to attenuate the noise and compensate the influence of structural modes on the cutting torque commands sampled at 0.1 millisecond (ms) intervals.

3.3.1 State Space Representation with the Disturbance Model Expansion

The actual cutting force acting on the cutting tool (F_a) is distorted by the structural dynamics of the feed drive system governed by the disturbance transfer function given in Eq. (3.13). The aim of the Kalman Filter is to reconstruct the actual cutting torque (τ_a) contributed by the machining process force (F_a) to the motor torque command (τ_c) by removing the effect of disturbance dynamics in Eq. (3.13). The actual cutting torque reflected to the drive (τ_a) can be separated to dc (static) and ac (harmonic) components as;

$$\tau_a = \tau_{a\_DC} + \tau_{a\_AC} \tag{3.16}$$

The derivative of the dc process noise (w_{DC}) is constant;

$$\dot{\tau}_{a\_DC} = w_{DC} \tag{3.17}$$

The harmonic part of the cutting torque can be represented as a cosine function at the tooth passing frequency (ω_t), which can be expressed in the Laplace domain with a periodic disturbance noise (w_{AC}) as;

$$\frac{\tau_{a\_AC}(s)}{w_{AC}(s)} = \frac{s}{s^2 + \omega_t^2} \tag{3.18}$$

with the corresponding state-space representation;

$$\begin{aligned} \dot{\mathbf{x}}_{\mathbf{F}} &= \underbrace{\begin{bmatrix} 0 & -\omega_t^2 \\ 1 & 0 \end{bmatrix}}_{\mathbf{A_F}} \underbrace{\begin{bmatrix} \tau_{a\_AC} \\ \dot{\tau}_{a\_AC} \end{bmatrix}}_{\mathbf{x_F}} + \underbrace{\begin{bmatrix} 1 \\ 0 \end{bmatrix}}_{\mathbf{B_F}} w_{AC} \\ \tau_{a\_AC} &= \underbrace{\begin{bmatrix} 1 & 0 \end{bmatrix}}_{\mathbf{C_F}} \underbrace{\begin{bmatrix} \tau_{a\_AC} \\ \dot{\tau}_{a\_AC} \end{bmatrix}}_{\mathbf{x_F}} \end{aligned} \tag{3.19}$$

The normalized expanded state space equation can be written by substituting Eq. (3.16) and (3.19) into (3.15) as follows [20];

$$
\begin{aligned}
\dot{\mathbf{x}}_{\mathbf{exp}}(t) &= \underbrace{\begin{bmatrix} \mathbf{A} & \mathbf{B} & \mathbf{BC_F} \\ 0 & 0 & 0 \\ 0 & 0 & \mathbf{A_F} \end{bmatrix}}_{\mathbf{A_{exp}}} \underbrace{\begin{Bmatrix} \{\mathbf{x}\} \\ \tau_{a\_DC} \\ \{\mathbf{x_F}\} \end{Bmatrix}}_{\mathbf{x_{exp}}} + \underbrace{\begin{bmatrix} 0 \\ \theta_{DC} \\ \theta_{AC} \end{bmatrix}}_{\mathbf{L}} w(t) \\
\tau_c(t) &= \underbrace{\begin{bmatrix} \mathbf{C} & 0 & 0 \end{bmatrix}}_{\mathbf{C_{exp}}} \underbrace{\begin{Bmatrix} \{\mathbf{x}\} \\ \tau_{a\_DC} \\ \{\mathbf{x_F}\} \end{Bmatrix}}_{\mathbf{x_{exp}}} + v(t)
\end{aligned}
\tag{3.20}
$$

where $\mathbf{A_{exp}}$ and $\mathbf{C_{exp}}$ are the state and output matrices of the expanded state space model. Process and measurement noise terms are $w(t)$ and $v(t)$, respectively. $\mathbf{L}$ is the noise coupling matrix, where θ_{DC} and θ_{AC} are the noise ratio terms ($\theta_{DC} = w_{DC}/w(t)$, $\theta_{AC} = w_{AC}/w(t)$).

Since the sampling frequency (10 kHz) is quite high relative to the maximum tooth passing frequency achievable with the measured drive disturbance FRFs (0.2 kHz), the input torque can be treated as piecewise constant and the derivative of the applied torque depends only on the process noise (w);

$$
\dot{\tau}_a = w \tag{3.21}
$$

Therefore, the piecewise constant applied torque can be modeled as another state of the system as a single term;

$$
\mathbf{x_{exp}} = \begin{Bmatrix} \{\mathbf{x}\} \\ \tau_a \end{Bmatrix} \tag{3.22}
$$

The expanded state-space form in Eq. (3.20) is reduced to;

$$
\begin{aligned}
\dot{\mathbf{x}}_{\mathbf{exp}}(t) &= \underbrace{\begin{bmatrix} \mathbf{A} & \mathbf{B} \\ 0 & 0 \end{bmatrix}}_{\mathbf{A}_{\mathbf{exp}}} \underbrace{\begin{Bmatrix} \{\mathbf{x}\} \\ \tau_a \end{Bmatrix}}_{\mathbf{x}_{\mathbf{exp}}} + \underbrace{\begin{bmatrix} 0 \\ 1 \end{bmatrix}}_{\mathbf{L}} w(t) \\
\tau_c &= \underbrace{\begin{bmatrix} \mathbf{C} & 0 \end{bmatrix}}_{\mathbf{C}_{\mathbf{exp}}} \underbrace{\begin{Bmatrix} \{\mathbf{x}\} \\ \tau_a \end{Bmatrix}}_{\mathbf{x}_{\mathbf{exp}}} + v(t)
\end{aligned} \tag{3.23}
$$

The actual cutting torque (τ_a) is now a state of the system and the cutting portion of the measured torque (τ_c) depends on the disturbance dynamics ($\mathbf{A}_{\mathbf{exp}}$, $\mathbf{C}_{\mathbf{exp}}$), and the process ($w(t)$) and measurements ($v(t)$) noises.

3.3.2 Disturbance Kalman Filter Design

The actual torque (τ_a) is estimated as $\hat{\tau}_a$ using the disturbance Kalman Filter of an individual drive as;

$$
\begin{aligned}
\dot{\hat{\mathbf{x}}}_{\mathbf{exp}} &= \mathbf{A}_{\mathbf{exp}}\hat{\mathbf{x}}_{\mathbf{exp}} + \mathbf{K}(y_{\mathrm{exp}} - \hat{y}_{\mathrm{exp}}) \\
&= \mathbf{A}_{\mathbf{exp}}\hat{\mathbf{x}}_{\mathbf{exp}} + \mathbf{K}(y_{\mathrm{exp}} - \mathbf{C}_{\mathbf{exp}}\hat{\mathbf{x}}_{\mathbf{exp}}) \\
&= (\mathbf{A}_{\mathbf{exp}} - \mathbf{K}\mathbf{C}_{\mathbf{exp}})\hat{\mathbf{x}}_{\mathbf{exp}} + \mathbf{K}y_{\mathrm{exp}} \\
\hat{\tau}_a &= \mathbf{C}_{\mathbf{0}}\hat{\mathbf{x}}_{\mathbf{exp}} \leftarrow \mathbf{C}_{\mathbf{0}} = \begin{bmatrix} \mathbf{0}_{1xn} & 1 \end{bmatrix}
\end{aligned} \tag{3.24}
$$

where $\mathbf{K}$ is continuous Kalman Filter gain and $\hat{\mathbf{x}}_{\mathbf{exp}}$ is the estimated state vector. The transfer function of the Kalman Filter can be derived from the state space representation given in Eq. (3.24) ;

$$
\hat{\tau}_a = \left\{ \frac{\mathbf{C}_{\mathbf{0}} adj\left[s\mathbf{I} - (\mathbf{A}_{\mathbf{exp}} - \mathbf{K}\mathbf{C}_{\mathbf{exp}}) \right]}{\det[s\mathbf{I} - (\mathbf{A}_{\mathbf{exp}} - \mathbf{K}\mathbf{C}_{\mathbf{exp}})]} \mathbf{K} \right\} \tau_c \tag{3.25}
$$

The discrete equivalent of the estimated state vector $\hat{\mathbf{x}}_{\mathbf{exp}}$ can be expressed as;

$$
\begin{aligned}
\hat{\mathbf{x}}_{\mathbf{exp}}(k+1) &= \exp\left\{(\mathbf{A}_{\mathbf{exp}} - \mathbf{K}\mathbf{C}_{\mathbf{exp}})t_d\right\}\hat{\mathbf{x}}_{\mathbf{exp}}(k) \\
&\quad + \left[\int_0^{t_d} \exp\left\{(\mathbf{A}_{\mathbf{exp}} - \mathbf{K}\mathbf{C}_{\mathbf{exp}})t_\tau\right\}\mathbf{K}dt_\tau\right]y(k) \\
\hat{\tau}_a(k+1) &= \mathbf{C_0}\hat{\mathbf{x}}_{\mathbf{exp}}
\end{aligned}
\tag{3.26}
$$

where the discrete sampling time (t_d) is 0.1 ms. The Kalman Filter Gain ($\mathbf{K}$) is identified by minimizing the state estimation error ($\tilde{\mathbf{x}}_{\mathbf{exp}}$) between the actual ($\mathbf{x}_{\mathbf{exp}}$) and estimated states ($\hat{\mathbf{x}}_{\mathbf{exp}}$);

$$
\tilde{\mathbf{x}}_{\mathbf{exp}} = \hat{\mathbf{x}}_{\mathbf{exp}} - \mathbf{x}_{\mathbf{exp}} \tag{3.27}
$$

The differential equation for the state estimation error covariance matrix ($\mathbf{P}$) is;

$$
\begin{aligned}
\dot{\mathbf{P}}(t\,|\,t) &= \mathbf{A}_{\mathbf{exp}}(t)\mathbf{P}(t\,|\,t) + \mathbf{P}(t\,|\,t)\mathbf{A}_{\mathbf{exp}}^{\mathbf{T}}(t) + \mathbf{L}(t)\mathbf{Q}(t)\mathbf{L}^{\mathbf{T}}(t) \\
&\quad - \mathbf{P}(t\,|\,t)\mathbf{C}_{\mathbf{exp}}^{\mathbf{T}}(t)\mathbf{R}^{\mathbf{-1}}\mathbf{C}_{\mathbf{exp}}(t)\mathbf{P}(t\,|\,t)
\end{aligned}
\tag{3.28}
$$

which is solved by using the Riccati Equation [82] and has to approach to zero for a stable observer. The measurement covariance matrix ($\mathbf{R}$) is determined from the root mean square (RMS) of the air cutting torque fluctuations, whereas system covariance matrix ($\mathbf{Q}$) is tuned to accommodate the compensations. The Kalman Filter gain is evaluated as follows;

$$
\mathbf{K}(t) = \mathbf{P}(t\,|\,t)\mathbf{C}_{\mathbf{exp}}^{\mathbf{T}}(t)\mathbf{R}^{\mathbf{-1}}(t) \tag{3.29}
$$

where the measurement ($\mathbf{R}$), system noise ($\mathbf{Q}$) covariance and the noise coupling matrix ($\mathbf{L}$) for each drive shown in Figure 3.7 are;

$$
\begin{aligned}
\mathbf{R}_x &= [0.0776], \quad \mathbf{Q}_{\mathbf{x}} = [200], \quad \mathbf{L}_{\mathbf{x}} = [0_{1x12} \quad 1]^T \\
\mathbf{R}_{\mathbf{y}} &= [0.1159], \quad \mathbf{Q}_{\mathbf{y}} = [700], \quad \mathbf{L}_{\mathbf{y}} = [0_{1x24} \quad 1]^T \\
\mathbf{R}_{\mathbf{z}} &= [0.6665], \quad \mathbf{Q}_{\mathbf{z}} = [2000], \quad \mathbf{L}_{\mathbf{z}} = [0_{1x16} \quad 1]^T \\
\mathbf{R}_{\mathbf{A}} &= [1.0235], \quad \mathbf{Q}_{\mathbf{A}} = [800], \quad \mathbf{L}_{\mathbf{A}} = [0_{1x12} \quad 1]^T \\
\mathbf{R}_{\mathbf{c}} &= [1.4903], \quad \mathbf{Q}_{\mathbf{C}} = [10000], \quad \mathbf{L}_{\mathbf{C}} = [0_{1x10} \quad 1]^T
\end{aligned}
\tag{3.30}
$$

The measured FRF of the uncompensated system ($\Phi_d(s) = \tau_c(s)/\tau_a(s)$), the FRF of the Kalman Filter ($\Phi_{KL}(s) = \hat{\tau}_a(s)/\tau_c(s)$), and the FRF of the compensated system ($\Phi_d(s) \times \Phi_{KL}(s) = \hat{\tau}_a(s)/\tau_a(s)$) are illustrated for three translational (x, y, z) and two rotary drives (A, C) in Figure 3.8.

In addition to the Kalman filtering, compensated force signals must be synchronized since they experience different phase shifts with the observer transfer function. In general, a number of sample delays are calculated from the phase of the compensated FRF and the compensated signals are synchronized using delay buffers [46]. In this study, a Kalman Smoother approach is used per each axis to correct these phase shifts in a more systematic way which is described in Appendix B [83].

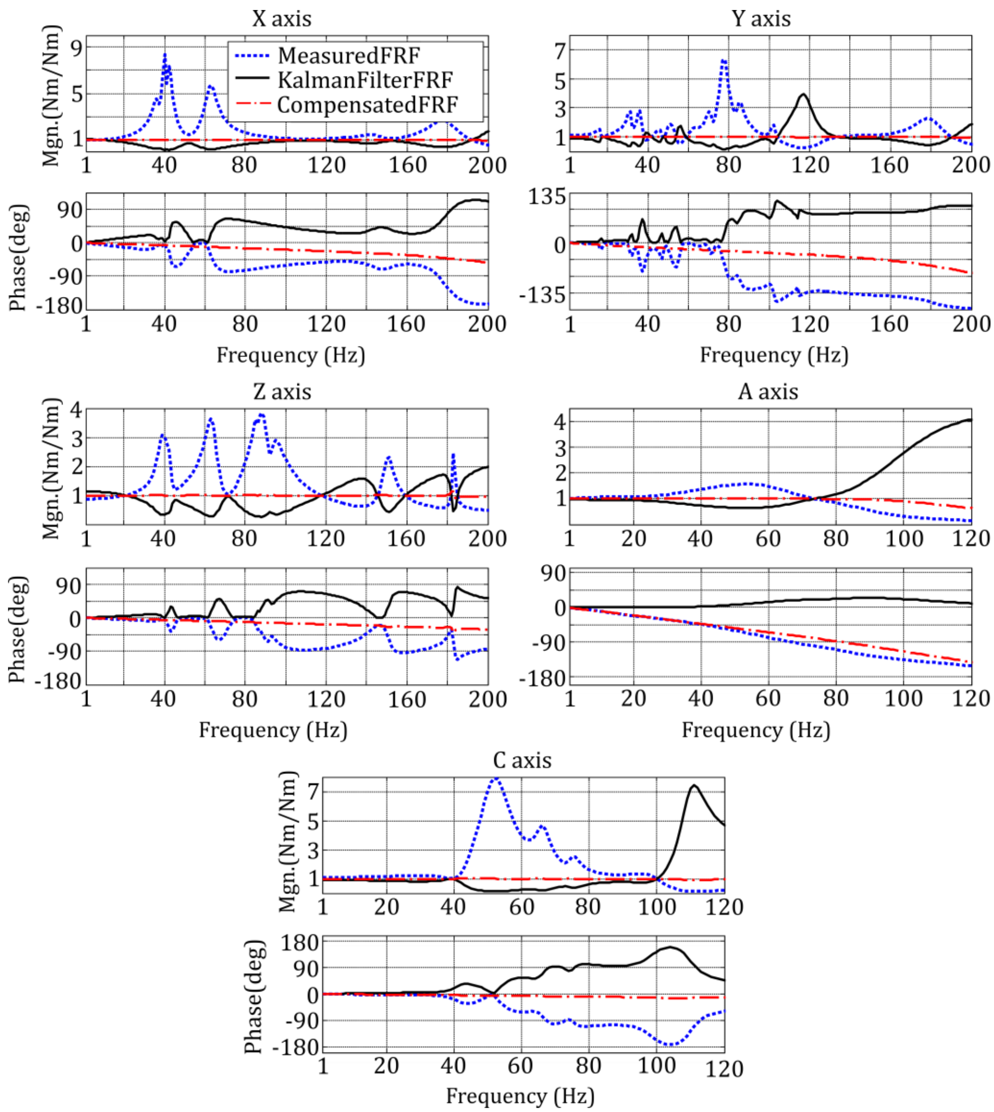

Figure 3.8: Measured and Kalman filter compensated drive disturbance FRFs

The identified Kalman filter gains (**K**) that minimizes the error covariance matrices are;

$$
\begin{aligned}
&\mathbf{K_x} = [0.0211 \quad 0.0233 \quad -0.0064 \quad -0.0085 \quad 0.0028 \quad 0.0016 \quad 4.1e-4 \quad \ldots \\
&2.9e-4 \quad -7.7e-4 \quad -3.9e-4 \quad 2.7e-4 \quad 1.1e-4 \quad 0.6076], \\
&\mathbf{K_y} = [-0.14 \quad 0.464 \quad 1.567 \quad -1.648 \quad -0.322 \quad 0.883 \quad -0.72 \quad \ldots \\
&-0.353 \quad 0.36 \quad 0.037 \quad 0.091 \quad 0.193 \quad -0.697 \quad 0.428 \quad \ldots \\
&0.898 \quad 0.195 \quad -0.507 \quad -0.084 \quad 0.283 \quad 0.015 \quad -0.041 \quad \ldots \\
&-8.8e-4 \quad 0.007 \quad -3.04e-5 \quad 0.9306], \\
&\mathbf{K_z} = [0.019 \quad 0.029 \quad -0.018 \quad 0.024 \quad 0.01 \quad 0037 \quad 0.014 \quad \ldots \\
&-0.019 \quad -0.031 \quad 0.01 \quad 0.039 \quad -0.02 \quad 0.01 \quad 8.9e-4 \quad \ldots \\
&0.002 \quad -4e-4 \quad 0.656], \\
&\mathbf{K_A} = [-0.001 \quad 0.006 \quad 0.016 \quad -0.055 \quad -0.044 \quad 0.096 \quad 0.069 \quad \ldots \\
&-0.066 \quad -0.067 \quad -0.024 \quad -0.002 \quad -1.66e-4 \quad -4 \quad -0.372], \\
&K_C = [0.01 \quad 0.015 \quad -0.006 \quad -0.007 \quad 0.003 \quad 0.003 \quad -0.001 \quad \ldots \\
&-9.68e-4 \quad 1.87e-4 \quad 1.08e-4 \quad 0.911]
\end{aligned}
\tag{3.31}
$$

The Kalman filter gain vector ($\mathbf{K}$) is taken as time invariant in the system once the covariance matrix converges to zero. As shown in Figure 3.8, the compensated system magnitude approaches unity and the bandwidth has been increased to 180 Hz for translational and to 120 Hz for the rotational drives. As a result, the measured cutting torque (τ_c) can be compensated accurately at tooth passing frequencies up to 180 Hz (i.e. 5400 rev/min for 2 fluted end mill) and the compensated torques ($\hat{\tau}_a$) on each drive are transferred to the tool tip as estimated actual cutting forces ($\hat{F}_a$) using the kinematic model of the five-axis machine. In summary, once the compensated torque values for each drive are obtained, they need to be transformed to the tool tip through the kinematic model of the machine tool that is described in the following section.

3.4 Kinematic Model of the Machine Tool for Force Transformation

The motion of the tool during five-axis operations depends on the movement of the three translational and two rotational drives. In order to transform the estimated cutting torque from the current drawn from each axis motor to the tool center position with respect to the machine table center (machine reference frame origin), the kinematics of the machine tool is modeled by applying the Denavit-Hartenberg (DH) method [84].

3.4.1 Kinematic Model of the Five-Axis Machine

The five-axis Quaser CNC machining center with a widely used tilting rotary table type kinematic configuration (see Figure 3.9) is used to demonstrate prediction of cutting forces from the feed drive motor current commands.

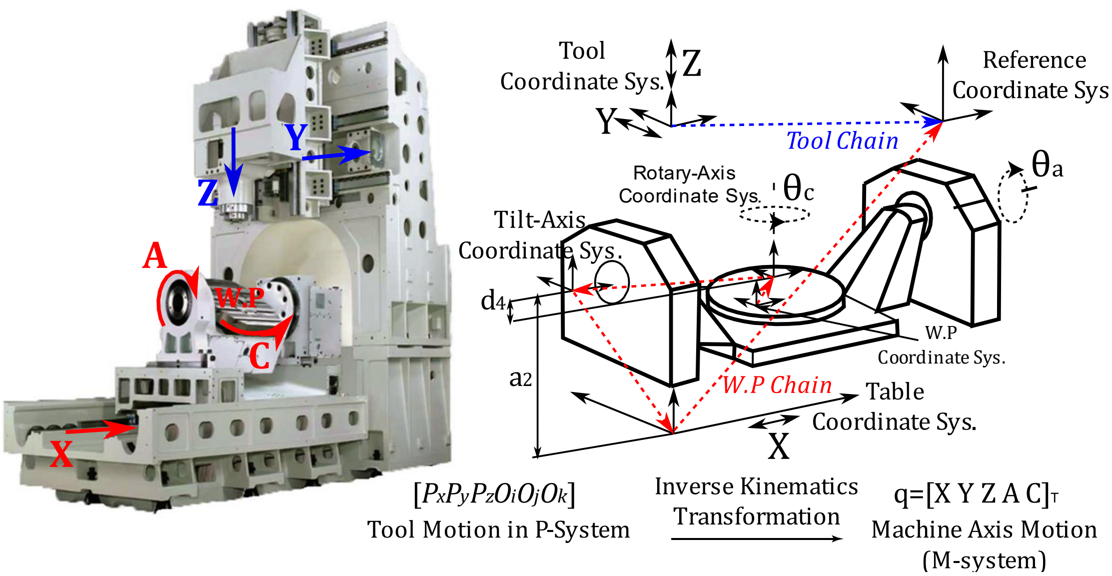

Figure 3.9: Kinematic configuration of the Quaser UX600 5-axis machining center with the Tool and Workpiece coordinate frames

The tool positions in workpiece coordinate system (*P-system*) is expressed as the position vector of the tool tip;

$$\mathbf{P_T}(t) = \begin{bmatrix} P_x & P_y & P_z \end{bmatrix}^T \tag{3.32}$$

and unit vector defining the tool orientation;

$$\mathbf{O_T} = \begin{bmatrix} O_i & O_j & O_k \end{bmatrix}^T \tag{3.33}$$

$\mathbf{P_T}(t)$ and $\mathbf{O_T}(t)$ in *P-system* are transformed into position commands of the drives of the machine tool in machine coordinate system (*M-system*) through the inverse kinematics solution of the machine tool as;

$$\mathbf{q}(t) = \begin{bmatrix} x(t) & y(t) & z(t) & \theta_A(t) & \theta_C(t) \end{bmatrix}^T \tag{3.34}$$

The angular positions of the drives from the tool orientation are expressed as;

$$\begin{aligned} \theta_A &= -\sin(O_k) \\ \theta_C &= \tan^{-1}(O_i, O_j) \end{aligned} \tag{3.35}$$

which means the tool orientation in the *P-system* can be calculated from;

$$\begin{bmatrix} O_i \\ O_j \\ O_k \end{bmatrix} = \begin{bmatrix} \cos\theta_A \sin\theta_C \\ \cos\theta_A \cos\theta_C \\ -\sin\theta_A \end{bmatrix} \tag{3.36}$$

The axis positions of the translational drives are evaluated from the tool tip position as;

$$\begin{bmatrix} x(t) \\ y(t) \\ z(t) \\ 1 \end{bmatrix} = \begin{bmatrix} \cos\theta_C & \sin\theta_C & 0 & 0 \\ -\cos\theta_A \sin\theta_C & -\cos\theta_A \cos\theta_C & \sin\theta_A & d_4 \sin\theta_A \\ \sin\theta_A \sin\theta_C & \sin\theta_A \cos\theta_C & \cos\theta_A & d_4 \cos\theta_A - a_2 \\ 0 & 0 & 0 & 1 \end{bmatrix} \begin{bmatrix} P_x(t) \\ P_y(t) \\ P_z(t) \\ 1 \end{bmatrix} \tag{3.37}$$

where d_4 and a_2 are linear offsets between the rotary drive coordinate frames (Figure 3.9). By taking the inverse of the homogenous DH transformation matrix in Eq. (3.37), the tool position in the *P-system* is expressed as a function of the axes positions (*M-system*) as;

$$\begin{bmatrix} P_x(t) \\ P_y(t) \\ P_z(t) \\ 1 \end{bmatrix} = \begin{bmatrix} -\cos\theta_C & -\cos\theta_A \sin\theta_C & \sin\theta_A \sin\theta_C & -a_2 \sin\theta_A \sin\theta_C \\ \sin\theta_C & -\cos\theta_A \cos\theta_C & \cos\theta_C \sin\theta_A & -a_2 \cos\theta_C \sin\theta_A \\ 0 & \sin\theta_A & \cos\theta_A & -a_2 \cos\theta_A - d_4 \\ 0 & 0 & 0 & 1 \end{bmatrix} \begin{bmatrix} x(t) \\ y(t) \\ z(t) \\ 1 \end{bmatrix} \tag{3.38}$$

The Jacobian matrix, which maps the differential change of the drive velocities to the differential change of the linear and angular velocities of the tool, can be calculated from Eq. (3.36) and (3.38) as;

$$\mathbf{J} = \begin{bmatrix} \frac{dP_x}{dx} & \frac{dP_x}{dy} & \frac{dP_x}{dz} & \frac{dP_x}{d\theta_A} & \frac{dP_x}{d\theta_C} \\ \frac{dP_y}{dx} & \frac{dP_y}{dy} & \frac{dP_y}{dz} & \frac{dP_y}{d\theta_A} & \frac{dP_y}{d\theta_C} \\ \frac{dP_z}{dx} & \frac{dP_z}{dy} & \frac{dP_z}{dz} & \frac{dP_z}{d\theta_A} & \frac{dP_z}{d\theta_C} \\ \frac{dO_i}{dx} & \frac{dO_i}{dy} & \frac{dO_i}{dz} & \frac{dO_i}{d\theta_A} & \frac{dO_i}{d\theta_C} \\ \frac{dO_j}{dx} & \frac{dO_j}{dy} & \frac{dO_j}{dz} & \frac{dO_j}{d\theta_A} & \frac{dO_j}{d\theta_C} \\ \frac{dO_k}{dx} & \frac{dO_k}{dy} & \frac{dO_k}{dz} & \frac{dO_k}{d\theta_A} & \frac{dO_k}{d\theta_C} \end{bmatrix}_{6x5} \tag{3.39}$$

3.4.2 Force Transformation Using the Jacobian Matrix

The Jacobian is used to define the relationship between forces at the tool and the torques at the drive motors. The force Jacobian is linked to the velocity Jacobian by the principal of virtual work, which denotes that the virtual work done in the tool space (external) and the virtual work done in the drive space (internal) should be equal at the static equilibrium. This means, given the infinitesimally small displacements at the tool ($\boldsymbol{\delta}_{\mathbf{T}}$) in the workpiece frame and the drive frames ($\boldsymbol{\delta}_{\mathbf{q}}$), equality of work done in both frames can be used as;

$$\mathbf{F}_{\mathbf{WP}}^{\mathbf{T}}\boldsymbol{\delta}_{\mathbf{T}} = \boldsymbol{\tau}_{\mathbf{Drives}}^{\mathbf{T}}\boldsymbol{\delta}_{\mathbf{q}} \tag{3.40}$$

where $\mathbf{F}_{\mathbf{WP}}$ contains the cutting forces and torques acting on the cutter in the workpiece frame and $\boldsymbol{\tau}_{\mathbf{Drives}}$ contains the drive forces and torques;

$$\mathbf{F_{WP}} = \begin{bmatrix} F_{wp-x} & F_{wp-y} & F_{wp-z} & \tau_{wp-i} & \tau_{wp-j} & \tau_{wp-k} \end{bmatrix}^T$$
$$\boldsymbol{\tau}_{\mathbf{Drives}} = \begin{bmatrix} \hat{F}_{X_a} & \hat{F}_{Y_a} & \hat{F}_{Z_a} & \hat{\tau}_{A_a} & \hat{\tau}_{C_a} \end{bmatrix}^T \tag{3.41}$$

By the definition of the Jacobian;

$$\boldsymbol{\delta}_{\mathbf{T}} = \mathbf{J}\boldsymbol{\delta}_{\mathbf{q}} \tag{3.42}$$

and substituting it into Eq. (3.40);

$$\mathbf{F_{WP}} = \mathbf{T_{WP\text{-}Tool}}\mathbf{F_{Tool}} \tag{3.43}$$

which should be true for all $\boldsymbol{\delta}_{\mathbf{q}}$ ($\mathbf{F_{WP}^T J} = \boldsymbol{\tau}_{\mathbf{Drives}}^{\mathbf{T}}$). Therefore;

$$\boldsymbol{\tau}_{\mathbf{Drives}} = \mathbf{J^T F_{WP}} \tag{3.44}$$

In order to map the cutting forces acted on the tool in the tool coordinate frame to the drive torques, the forces in the tool frame have to be transformed to the base coordinate frame in the kinematic chain (W.P frame in this study, see Figure 3.9) as;

$$\mathbf{F_{WP}} = \mathbf{T_{WP\text{-}Tool}}\mathbf{F_{Tool}} \tag{3.45}$$

where the transformation between the drive torques and the cutting forces acted on tool in the tool coordinate frame can be written by plugging Eq. (3.45) in (3.44) as;

$$\boldsymbol{\tau}_{\mathbf{Drives}} = \mathbf{J^T T_{WP\text{-}Tool} F_{Tool}} \tag{3.46}$$

The estimated cutting torque ($\hat{\tau}_a$) for the translational drives can be converted to the cutting force ($\hat{F}_a$) on the corresponding drive by using Eq. (3.11). The Jacobian matrix for the tilting rotary table type kinematic configuration used in this work is given as;

$$J = \begin{bmatrix} -\mathrm{c}\theta_C & -\mathrm{c}\theta_A \mathrm{s}\theta_C & \mathrm{s}\theta_A \mathrm{s}\theta_C & Y\mathrm{s}\theta_A \mathrm{s}\theta_C + (Z-a_2)\mathrm{c}\theta_A \mathrm{s}\theta_C & Xs\theta_C - Y\mathrm{c}\theta_A \mathrm{s}\theta_C + (Z-a_2)c\theta_C \mathrm{s}\theta_A \\ \mathrm{s}\theta_C & -\mathrm{c}\theta_A \mathrm{c}\theta_C & \mathrm{c}\theta_C \mathrm{s}\theta_A & Y\mathrm{c}\theta_C \mathrm{s}\theta_A + (Z-a_2)\mathrm{c}\theta_A \mathrm{c}\theta_C & Xc\theta_C + Y\mathrm{c}\theta_A \mathrm{s}\theta_C - (Z-a_2)s\theta_A \mathrm{s}\theta_C \\ 0 & \mathrm{s}\theta_A & \mathrm{c}\theta_A & Y\mathrm{c}\theta_A - Z\mathrm{s}\theta_A + a_2 \mathrm{s}\theta_A & 0 \\ 0 & 0 & 0 & -\mathrm{s}\theta_A \mathrm{s}\theta_C^{*} & \mathrm{c}\theta_A \mathrm{c}\theta_C^{*} \\ 0 & 0 & 0 & -\mathrm{c}\theta_C \mathrm{s}\theta_A^{*} & -\mathrm{c}\theta_A \mathrm{s}\theta_C^{*} \\ 0 & 0 & 0 & -\mathrm{c}\theta_A^{*} & 0^{*} \end{bmatrix}_{6x5} \tag{3.47}$$

where s and c stands for sine and cosine terms, respectively. The torque components at the tool tip are neglected since the primary objective is to find the cutting forces at the tool tip in X, Y, and Z directions. Hence, the torque components in the tool tip vector (τ_{t-i}) and the corresponding terms in the transpose Jacobian and transformation matrices (marked with *) are set to zero for the rest of the chapter. The rotation matrix from tool to workpiece frame is derived from the DH solution as;

$$T_{WP-Tool} = \begin{bmatrix} -c\theta_C & -c\theta_A s\theta_C & s\theta_A s\theta_C & 0 & 0 & 0 \\ s\theta_C & -c\theta_A c\theta_C & c\theta_C s\theta_A & 0 & 0 & 0 \\ 0 & s\theta_A & c\theta_A & 0 & 0 & 0 \\ 0 & 0 & 0 & -c\theta_C{}^* & -c\theta_A s\theta_C{}^* & s\theta_A s\theta_C{}^* \\ 0 & 0 & 0 & s\theta_C{}^* & -c\theta_A c\theta_C{}^* & c\theta_C s\theta_A{}^* \\ 0 & 0 & 0 & 0^* & s\theta_A{}^* & c\theta_A{}^* \end{bmatrix}_{6x6} \tag{3.48}$$

where calculating $\mathbf{J^T T_{WP\text{-}Tool}}$ term from Eq. (3.47) and (3.48), and substituting it in (3.46) results in;

$$\begin{bmatrix} \hat{F}_{X_a} \\ \hat{F}_{Y_a} \\ \hat{F}_{Z_a} \\ \hat{\tau}_{A_a} \\ \hat{\tau}_{C_a} \end{bmatrix}_{5x1} = \begin{bmatrix} 1 & 0 & 0 & 0 & 0 & 0 \\ 0 & 1 & 0 & 0 & 0 & 0 \\ 0 & 0 & 1 & 0 & 0 & 0 \\ 0 & a_2 - Z & Y & 0 & 0 & 0 \\ Yc\theta_A + (a_2 - Z)s\theta_A & -Xc\theta_A & Xs\theta_A & 0 & 0 & 0 \end{bmatrix}_{5x6} \begin{bmatrix} F_{t-x} \\ F_{t-y} \\ F_{t-z} \\ 0 \\ 0 \\ 0 \end{bmatrix}_{6x1} \tag{3.49}$$

From Eq. (3.49) the tool tip forces in the tool coordinate frame can be mapped to the drive torques as;

$$\begin{aligned} &\hat{F}_{X_a} = F_{t-x},\ \hat{F}_{Y_a} = F_{t-y},\ \hat{F}_{Z_a} = F_{t-z} \\ &\hat{\tau}_{A_a} = F_{t-y}(a_2 - z) + F_{t-z}y \\ &\hat{\tau}_{C_a} = F_{t-x}(yc\theta_A + (a_2 - z)s\theta_A) - F_{t-y}xc\theta_A + F_{t-z}s\theta_A \end{aligned} \tag{3.50}$$

Reorganizing Eq. (3.46) in the form of;

$$\mathbf{F}_{\mathbf{Tool}} = \left[\mathbf{J}^{\mathbf{T}} \mathbf{T}_{\mathbf{WP\text{-}Tool}} \right]^{+} \boldsymbol{\tau}_{\mathbf{Drives}} \tag{3.51}$$

where $[\ ]^{+}$ is the generalized matrix inverse and gives the tool tip (cutting) forces from the drive torque measurements. In summary, the flowchart of the prediction of cutting forces in five-axis milling using the feed drive current measurements can be seen in Figure 3.10.

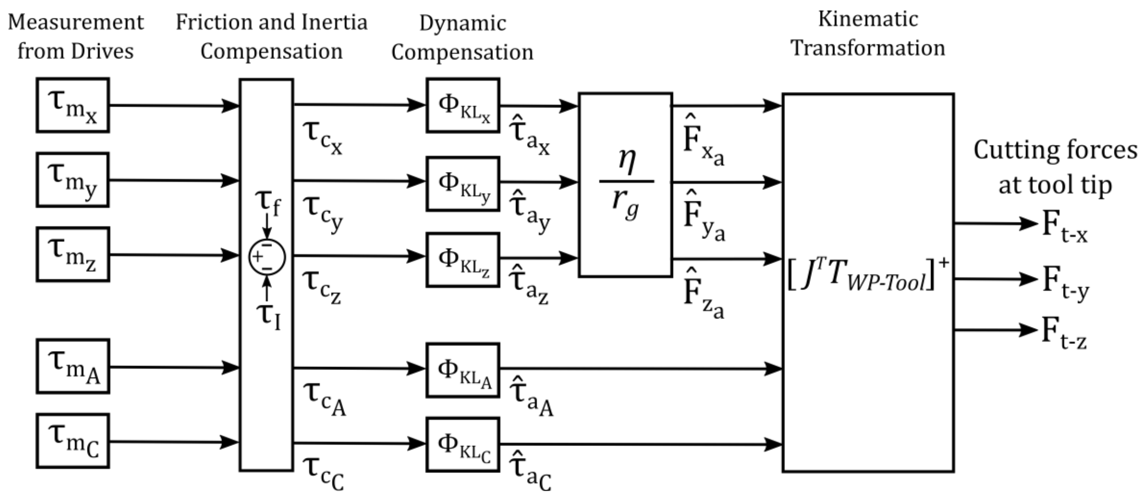

Figure 3.10: Flowchart of the overall procedure

3.5 Experimental Verification

The proposed force prediction method from the servo drives' current commands is experimentally validated on the Quaser UX-600 five-axis machining center. The algorithms are run on an external PC (Intel Core i7-3.40 GHz CPU, 8GB RAM), which communicates with the Heidenhain CNC via TNC Ethernet connection. A multithread real-time code is developed in C++ using the LSV-2 communication protocol that collects the tool center position, the tangential velocity with 333 Hz interpolator sampling frequency and commanded, noise-free digital motor currents, drive speeds, and spindle speed with 10 kHz sampling frequency. The workpiece material is Aluminum 7050 and tests are conducted with two different tools: a 20-mm diameter two-fluted end mill and a 16-mm diameter two-fluted ball end mill both with a regular pitch and 30^{0} helix angle. Two sets of experiments are conducted, where the first set consists of three-axis and the second set consists of five-axis milling operations. Spindle speeds are selected as 1000, 2000, 3000, 4000, 5000 and 5500 rev/min in order to cover the range of tooth passing frequencies, where the structural modes of the drives are located (see Figure 3.7). The reference cutting forces are measured with a stationary table dynamometer for three-axis and a rotary dynamometer for five-axis operations throughout the experiments. The measured and compensated torques/forces from the drives are compared to these reference forces for the verification of the methods.

Slot milling operations are performed with the 20 mm diameter end mill at 1000, 2000, 3000, 4000, 5000 and 5500 rev/min spindle speeds where the tooth passing frequencies (ω_t) are 33.3, 66.6, 100, 133.33, 166.67, 183.3 Hz, respectively. The axial depth of cut is selected as 4 mm and the feed rate is 0.2 mm/tooth, (see Figure 3.11, Figure 3.12 and Figure 3.13 for X, Y and Z directions, respectively).

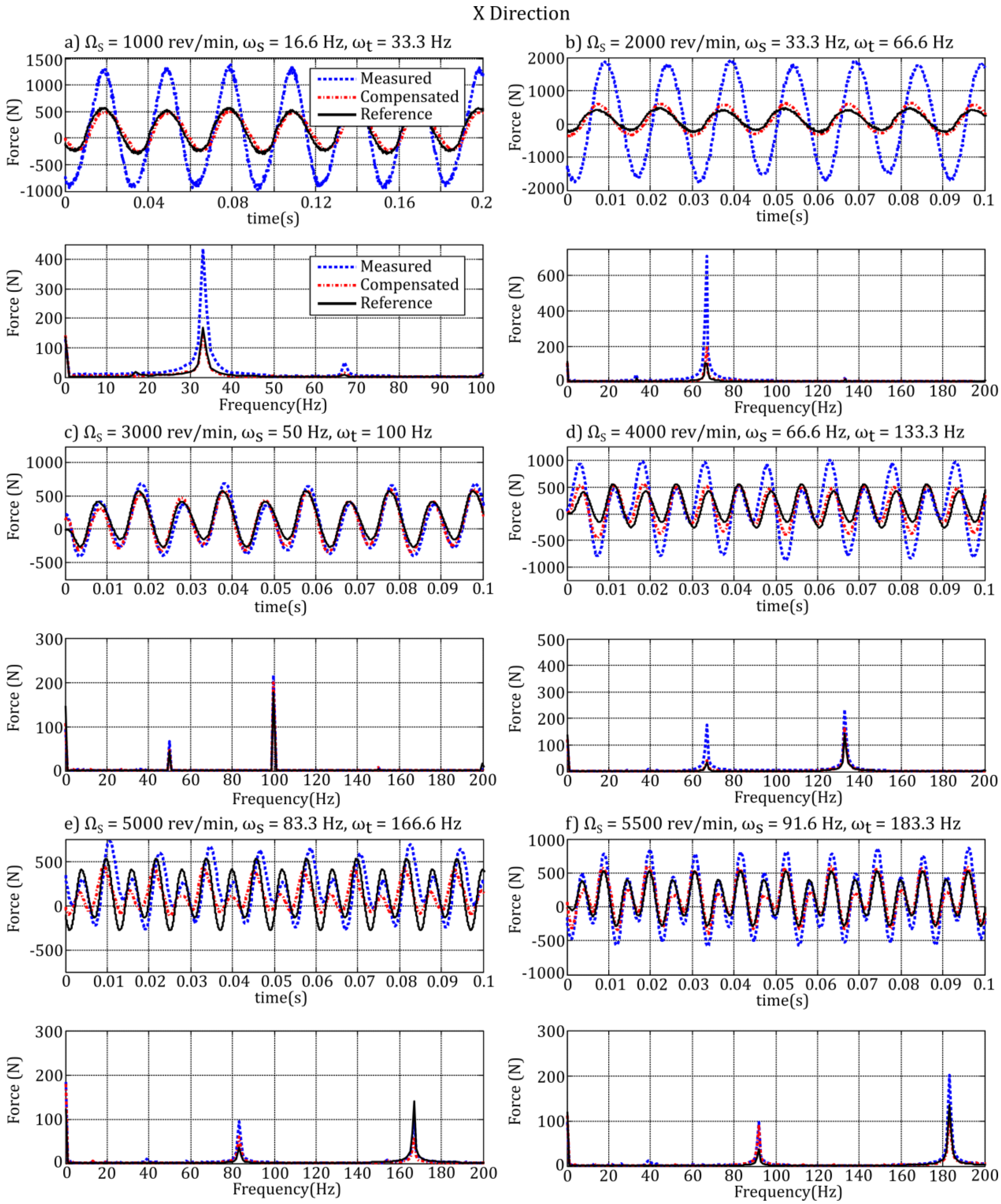

Figure 3.11: Comparison of measured and compensated forces from the feed drive current with reference forces measured by table dynamometer for three-axis milling with two-fluted end mill. Axial depth = 4 mm, Radial depth = 20 mm, feed = 0.2 mm/tooth, X Axis/Direction

In X direction (Figure 3.11), without Kalman filter compensation, the average errors between the reference forces measured with the dynamometer and estimated forces from drive motor current commands at the tooth passing frequency and its harmonics are 161%, 341%, 22%, 64%, 158% and 49% respectively at the spindle speeds of 1000, 2000, 3000, 4000, 5000 and 5500 rev/min. The errors are reduced to 18%, 6%, 4%, 12%, 32% and 17% with Kalman Filter compensation. The reason behind larger errors for 1000, 2000 and 5500 rev/min in the original measured drive signal is that the disturbance FRF of the X drive has modes with large magnitudes at the corresponding tooth passing frequency locations (see Figure 3.8), which are compensated by the designed Kalman Filter and the errors were reduced greatly as listed above.

For the Y direction (Figure 3.12), the behavior of the measured drive current is different due to the drive's individual disturbance FRF. In the Y direction, the errors between the reference and measured forces from the drive without compensation are 42%, 103%, 113%, 54%, 32% and 175% for 1000, 2000, 3000, 4000, 5000 and 5500 rev/min, respectively. After the Kalman filter compensation, they are reduced to 6%, 6%, 4%, 7%, 11% and 19%. As it can be seen from the results (Figure 3.12), the errors in the uncompensated drive measurement for 3000 and 5500 rev/min cases are particularly larger than the other spindle speeds. This can be explained in a similar fashion with the previous case, the corresponding tooth passing frequencies for these speeds are 100 and 183.3 Hz respectively, where the disturbance FRF of the Y drive has two distinct modes that distort the drive current measurements (see Figure 3.8). In addition, for the 5000 rev/min case where the spindle frequency hits a mode location in disturbance FRF exactly at 83.3 Hz (Figure 3.12-e), the measured drive current is around 4 times higher than the reference measurement which is corrected by the Kalman filter transfer function.

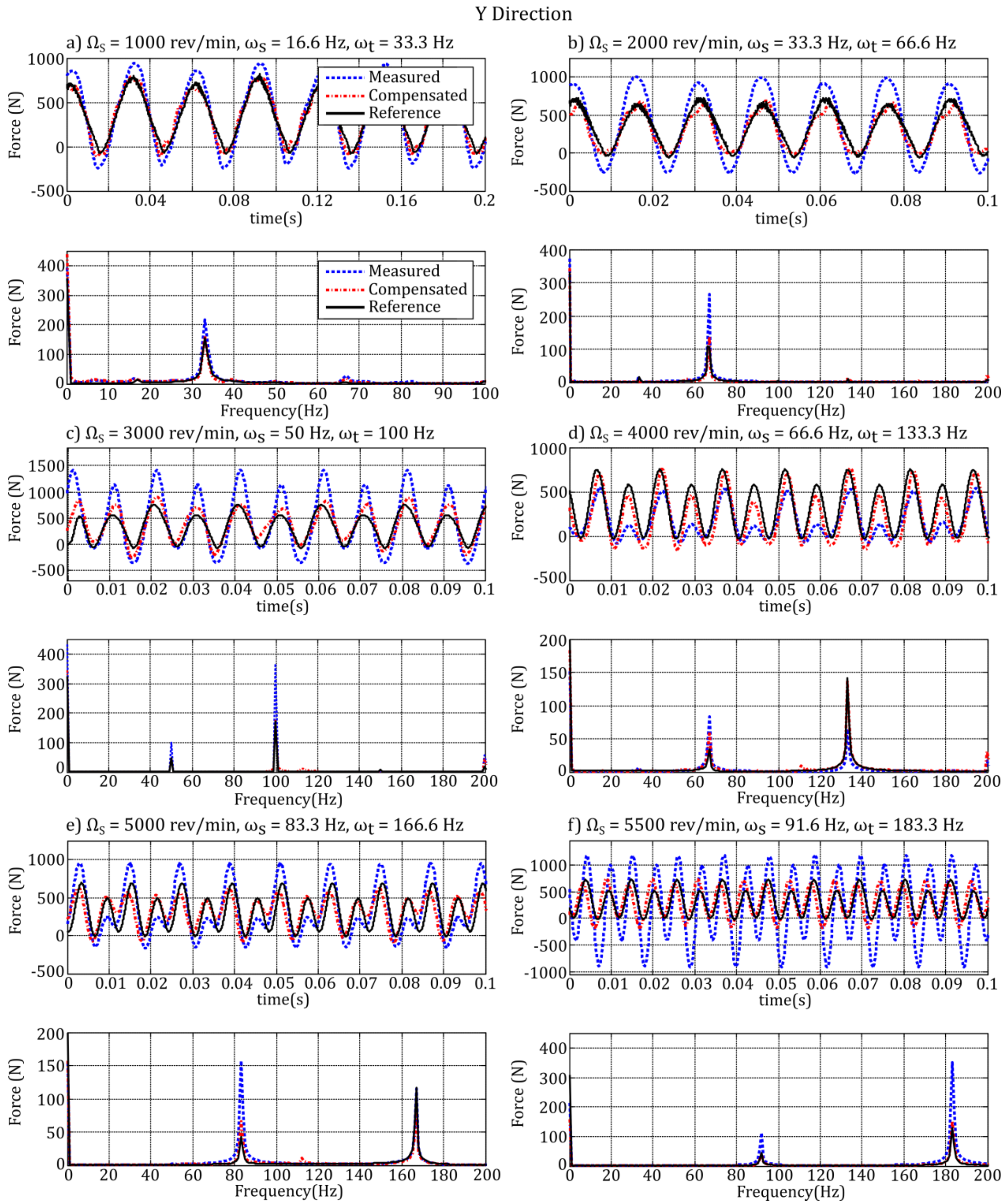

Figure 3.12: Comparison of measured and compensated forces from the feed drive current with reference forces measured by table dynamometer for three-axis milling with two-fluted end mill. Axial depth = 4 mm, Radial depth = 20 mm, feed = 0.2 mm/tooth, Y Axis/Direction

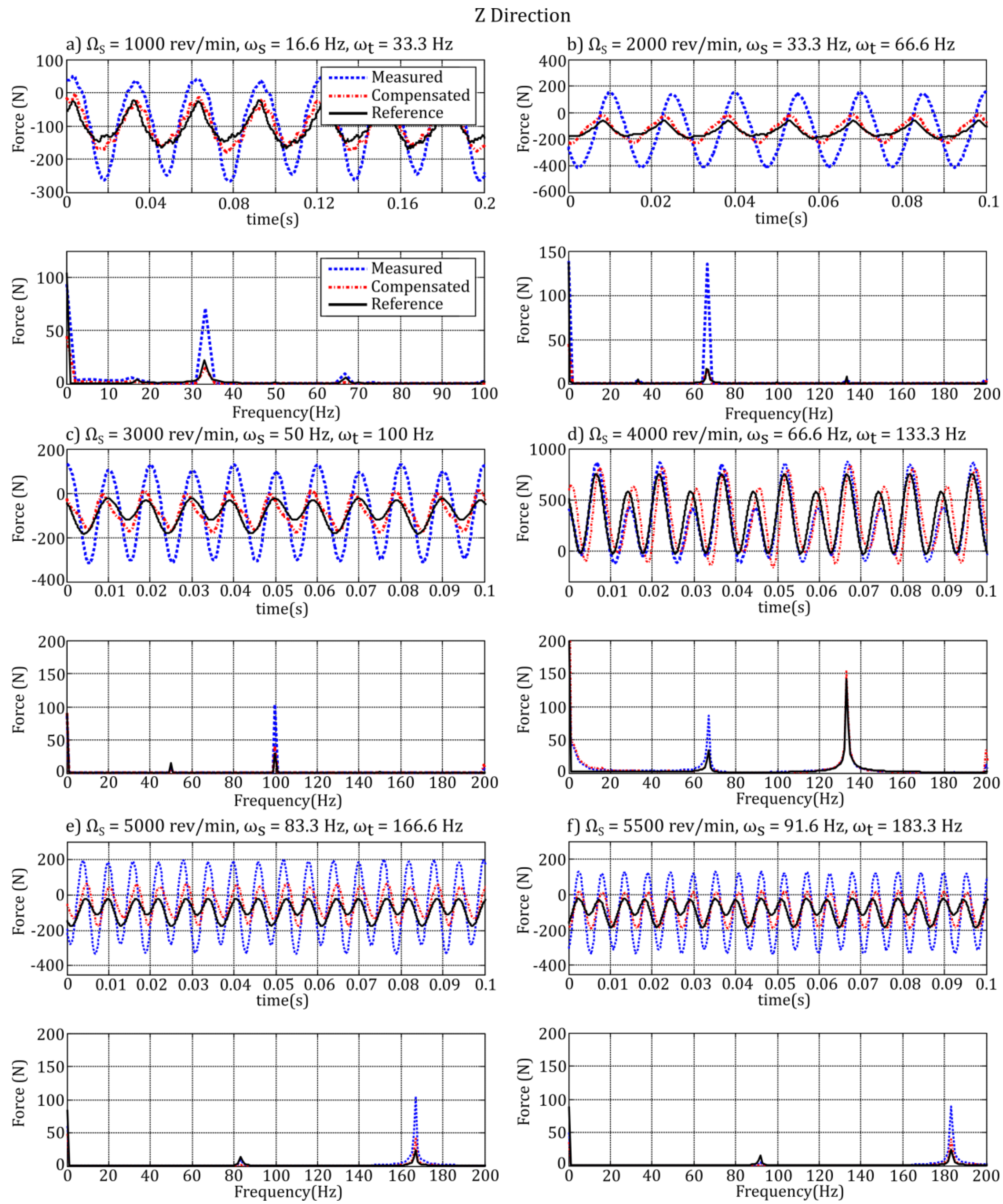

Figure 3.13: Comparison of measured and compensated forces from the feed drive current with reference forces measured by table dynamometer for three-axis milling with two-fluted end mill. Axial depth = 4 mm, Radial depth = 20 mm, feed = 0.2 mm/tooth, Z Axis/Direction

Finally, for the 3-axis verification, the Z direction results are given in Figure 3.13 where the initial errors between the directly identified forces from the drive measurements and the reference are 218%, 102%, 243%, 5%, 312% and 260% respectively for 1000, 2000, 3000, 4000, 5000 and 5500 rev/min spindle speeds. They were reduced to 23%, 10%, 26%, 4%, 70% and 60% after Kalman filter compensation. It should be noted that while the X and Y axes have distinct dominant modes, the Z axis modes are more coupled in the disturbance FRF, see Figure 3.7. As a result, these modes distort the transmitted force to the drives' motor current more aggressively compared to the X and Y drives. In addition, the forces in the Z direction tend to be lower than in the other directions in end milling operations since most cutter tools have low (< 30 degrees) helix angles. Low forces which are difficult to be identified from the drive current measurements and gravitational compensation in the Z direction performed by CNC to carry the slider/spindle body which changes the AC behavior of the Z drive current event at idle positions are the major reasons behind the lower accuracy in the Z direction.

A second set of experiments are conducted with a roughing operation for a turbine blade with freeform geometry by using the 16 mm diameter ball end mill. The spindle speed is selected as 1000 rev/min (ω_t = 33.3 Hz). The blade geometry, the extracted single blade, the roughing toolpath, and the workpiece after roughing operation with the experimental setup on the Quaser UX-600 are illustrated in Figure 3.14.

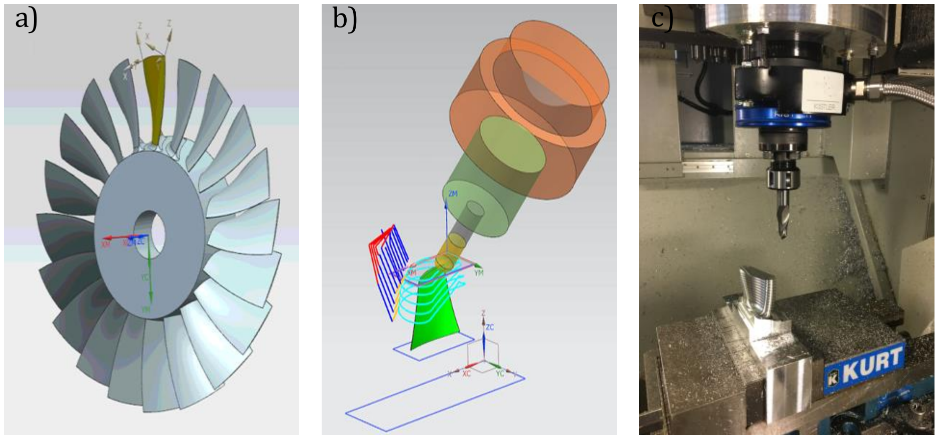

Figure 3.14: (a) Full turbine geometry, (b) Extracted single blade and toolpath in Siemens NX-9®, (c) Experimental setup on the Quaser UX-600 and workpiece after roughing operation

Comparison of the tool tip forces obtained from the feed drive current measurements through Kalman Filter compensation and kinematic transformation vs. the rotary dynamometer (reference) measurements are given in Figure 3.15, Figure 3.16 and Figure 3.17 for the X, Y and Z directions, respectively. The cutting forces estimated from the feed drive current measurements agree with reference measurements at the tooth passing frequency and its harmonics with mean errors of 21%, 16% and 27% for the X, Y and Z axes, respectively.

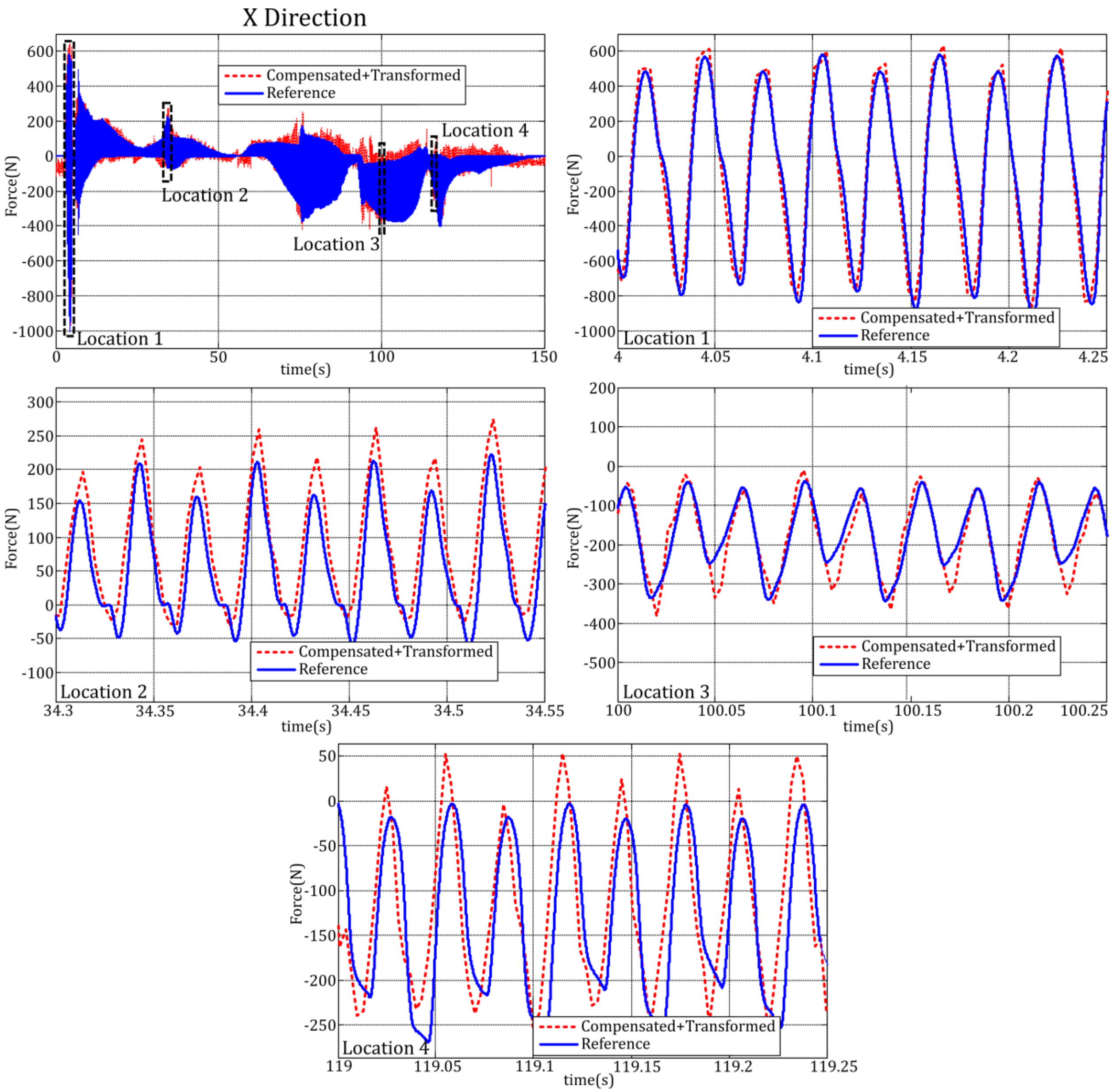

Figure 3.15: Comparison of compensated + transformed forces from the feed drive current measurements and the reference forces measured from the rotary dynamometer – X Direction

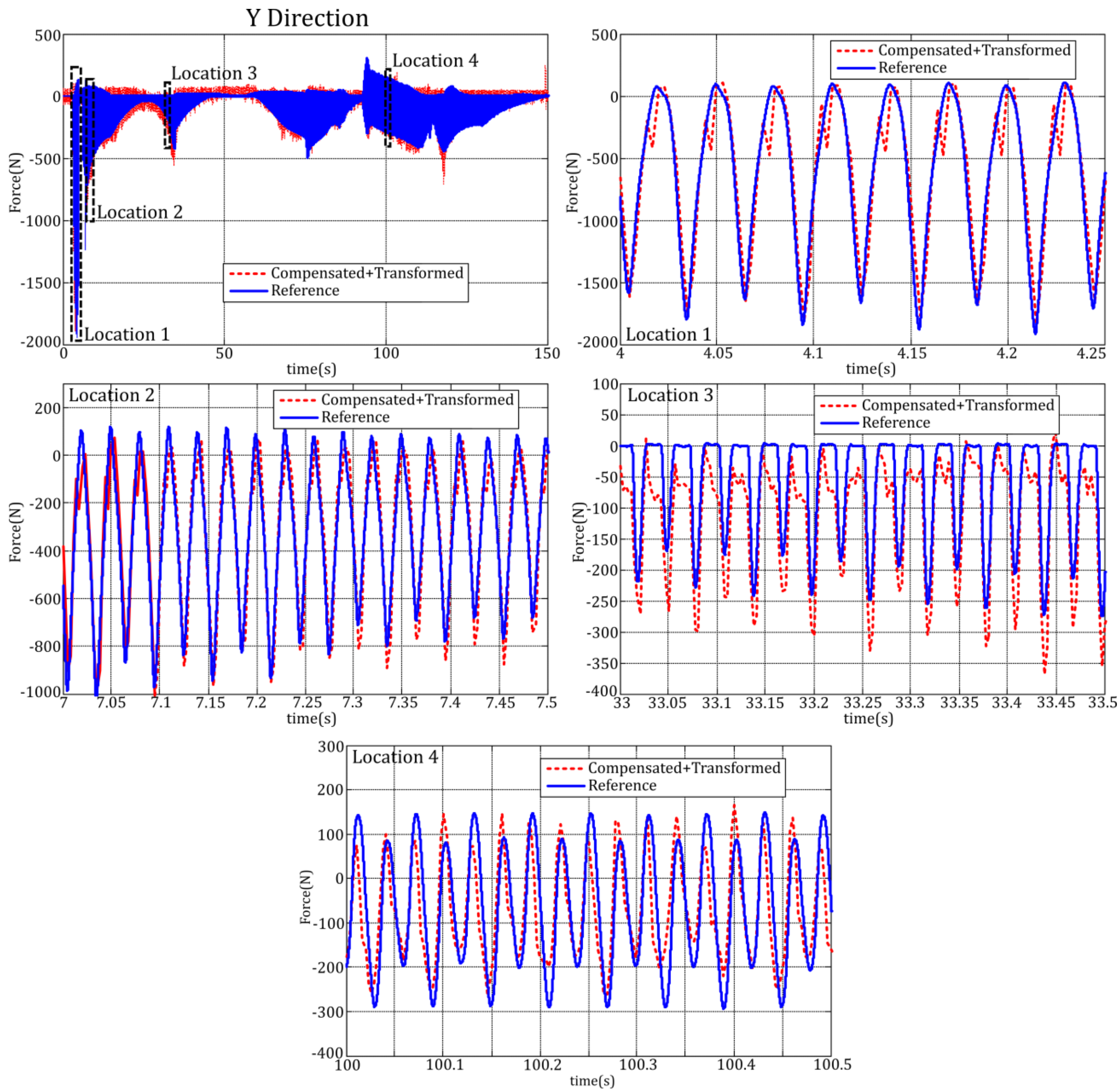

Figure 3.16: Comparison of compensated + transformed forces from the feed drive current measurements and the reference forces measured from the rotary dynamometer – Y Direction

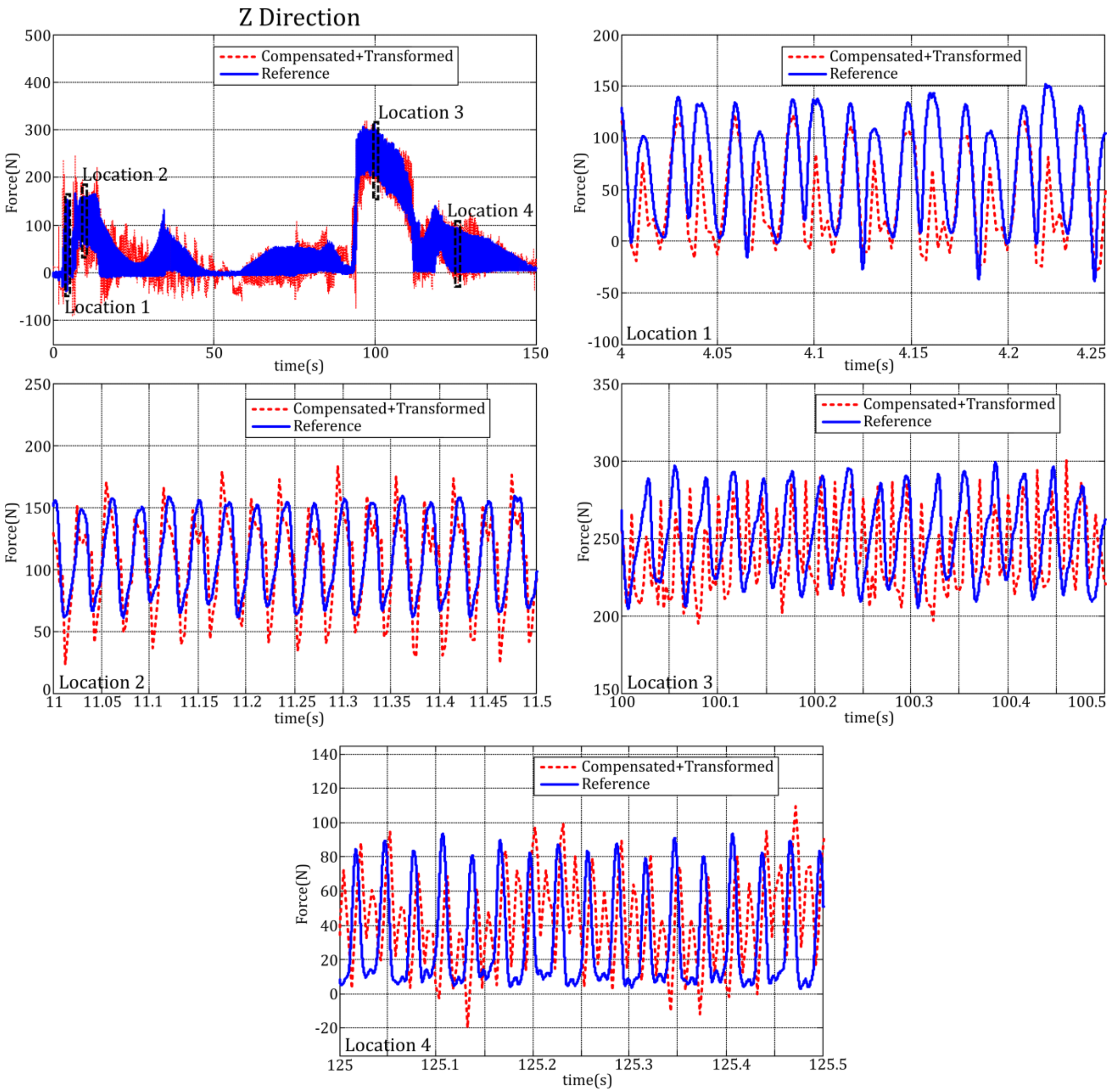

Figure 3.17: Comparison of compensated + transformed forces from the feed drive current measurements and the reference forces measured from the rotary dynamometer – Z Direction

Discrepancies between the cutting forces identified from the feed drive current commands and reference forces measured with the dynamometer can be attributed to errors in friction and inertia modeling, inaccuracies in experimentally identified drive disturbance FRFs and the position dependency of the structural modes (see Appendix C), especially for the rotary drives. Force prediction accuracy can be increased by investigating the position dependency of the drive disturbance FRFs and scheduling the corresponding Kalman Filter gains as a function of drive positions. Higher error in Z direction is due to the low cutting forces and varying AC trend of Z feed drive current even at idle positions as in the 3-axis milling case.

3.6 Summary

This chapter presents a methodology to predict cutting forces at the tool tip from feed drive motor current measurements without installing external sensors on the machine tool. The accuracy of the cutting force prediction depends on the modeling of friction, disturbance transfer function between the force at the tool and motor, kinematics of five-axis machines, and tuning of the Kalman Filter to compensate the effects of the structural modes in the disturbance transfer function. The bandwidth of the force monitoring can be extended up to the bandwidth of the current loop of the controller provided that the structural modes of the drive chain are well separated and modeled. The proposed method is targeted to be used for on-line process monitoring and control for machining of complex parts, both the methodology and the results are published in [1].

Chapter 4: Process State Predictions with Spindle Mounted Vibration Sensors Considering Speed and Load Dependent Dynamics

4.1 Overview

This chapter presents a sensory spindle system to predict tool tip vibrations and process forces by considering speed and load dependent spindle dynamics. Spindle is instrumented with externally installed vibration sensors (accelerometers) in X and Y directions and an offline map of structural dynamics of the system is identified under different preload and speed conditions. The offline map is accessed in-process to update the state observers accordingly and predict process states at the cutting interface between tool and workpiece with a sensor data fusion algorithm. Process state (i.e. tool tip vibration and cutting force) predictions are validated in milling tests with specially designed fixtures.

Although vibration sensors are installed on the spindle externally for research purposes, it is aimed to have a sensory spindle system with embedded vibration, force and thermocouple sensors in the future to utilize the system for production environment. The sensory spindle system is developed to be used as an alternative for the method presented in the previous chapter (Chapter 3) which uses CNC inherent data solely for process state predictions.

4.2 System Description and Identification of the Sensory Spindle

The sensory spindle system used in this study is illustrated in Figure 4.1 with the external sensor locations on GF AgieCharmilles – Mikron HPM 800U machine tool with a Step-Tec HPC170 CC spindle. The system is developed in collaboration with the Institute of Machine Tools and Manufacturing (IWF), ETH Zürich. Although several configurations with several accelerometers are used, final configuration in the cutting experiments is described here.

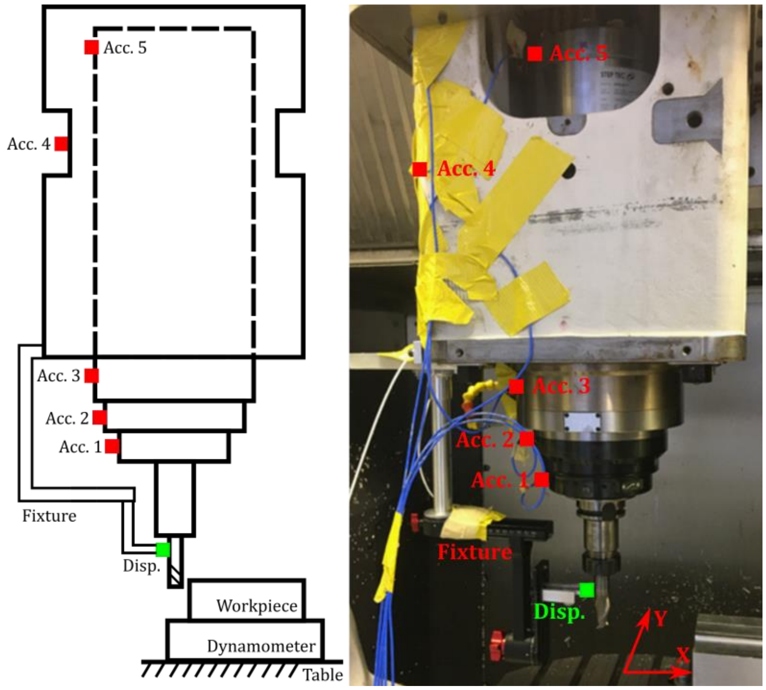

Figure 4.1: Overall layout of the sensory spindle with the installed accelerometers (Acc.) and a displacement sensor (Disp.) in X direction

There are five accelerometers in total where four of them are installed on the spindle (Acc. 1, 2, 3, 5) and one is installed on the slider of the machine tool (Acc. 4) (see Figure 4.1). Accelerometer measurements are numerically integrated twice to obtain the corresponding displacement signals. A non-contact eddy-current displacement sensor is mounted at the tool shank with two different fixtures shown in Figure 4.1 and Figure 4.2. A real-time signal analyzer (LDS Dactron Docus II) is used to collect all sensor data at 8192 Hz. An instrumented hammer is used to perform the FRF measurements where the impact is given at the tool tip when a dummy tool is used whereas it is given across the displacement sensor at the shank for a regular tool since hitting a rotating cutter at the tip where sharp edges are located is not possible. Based on the initial FRF measurements, it is decided to focus mainly on X direction due to its more responsive nature (see Figure 4.3 and Figure 4.6), and a single fixture (Figure 4.1) designed to use the non-contact displacement sensor to measure the tool vibration in-process. System identification and process state predictions are also validated experimentally for the Y direction but not presented here to avoid repetition.

4.2.1 Load Dependency of the Spindle Dynamics

First, load dependency of a dummy tool is investigated. Load is applied in Z direction by using magnets with a fixture designed and patented by IWF, ETH Zürich. The system is shown in Figure 4.2 where the magnet and the fixture are highlighted. With the designed fixture, magnet can be moved closer to or further from the tool to decrease or increase the applied load at the tool tip.

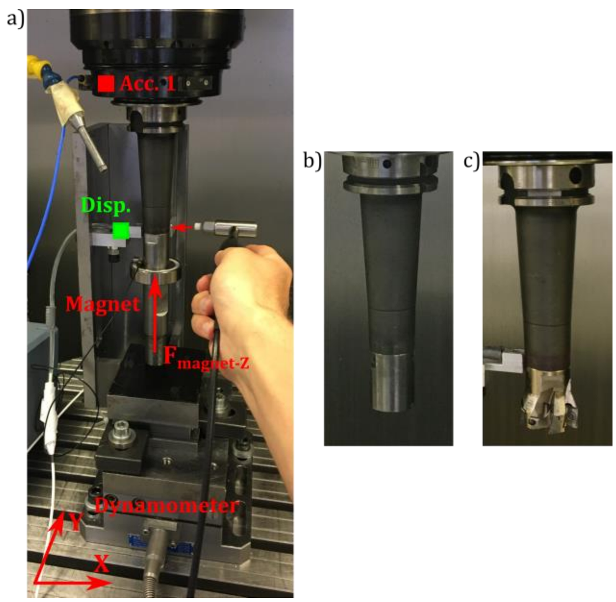

Figure 4.2: (a) Setup with the magnet to apply preload in Z direction at the tool tip, (b) dummy tip, (c) face mill

Load is applied only in Z direction since the effect of load in X and Y directions are found to be negligible compared to Z direction for this setup. A special dummy tool (Figure 4.2 – b) is used in the identification experiments but a face milling tool (Figure 4.2 – c) is used for the cutting experiments. The main reason being that the solid cylinder structure of the dummy tip with a planar surface at the bottom allows the magnet to apply higher forces than the face mill configuration.

Results for the dummy tool are presented to show the effect of the load in spindle-holder-tool pair dynamics in a wider range. Load applied at the tool tip by the magnet is calibrated with the dynamometer measurements located at the bottom of the system (Figure 4.2 – a). Five different load conditions are applied in Z direction at first as follows: 0, 100, 230, 330 and 430 N.

Tool tip FRFs in X direction under different load conditions are shown in Figure 4.3. The dominant mode is shifting from 980 Hz to 800 Hz as the load ($F_{magnet-Z}$) increases and the behavior between 600 and 1200 Hz is quite different between no load (0 N) and highest load (430 N) cases for the FRFs in X direction. Magnitudes at the dominant modes around 980 Hz and around 625Hz are also decreasing as load ($F_{magnet-Z}$) increases for the FRFs in Y direction (Figure 4.3).

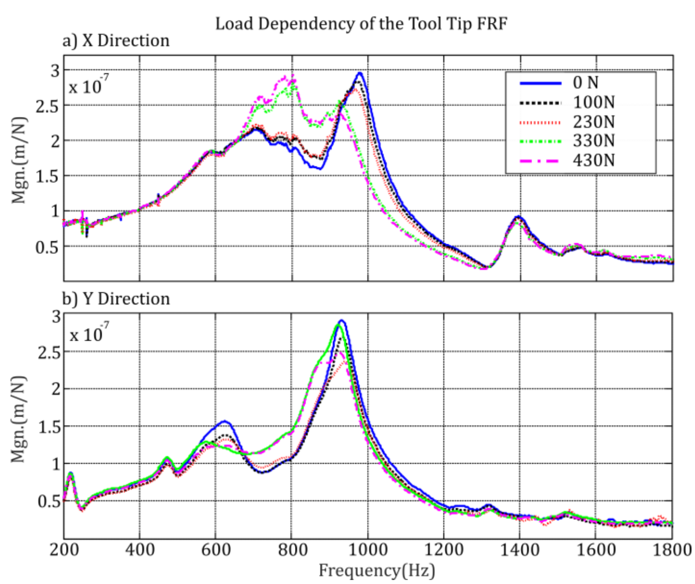

Figure 4.3: Load dependency of the tool tip FRF in X and Y directions

In addition, FRFs between the displacement sensor and the five accelerometers installed on the spindle for different load conditions are shown in Figure 4.4 and Figure 4.5 for the X direction where the Y direction also shows a very similar trend. In Figure 4.4, FRFs for the accelerometers located below the spindle assembly to the machine tool location are given which are closer to the tool tip. FRFs between the tool tip (d_{disp}) and the accelerometers (d_{acc_i} $(i = 1, \ldots, 5)$) are varying with load in a similar pattern. Hence, these effects should be considered in-process to predict the process states at the tool tip from accelerometer measurements.

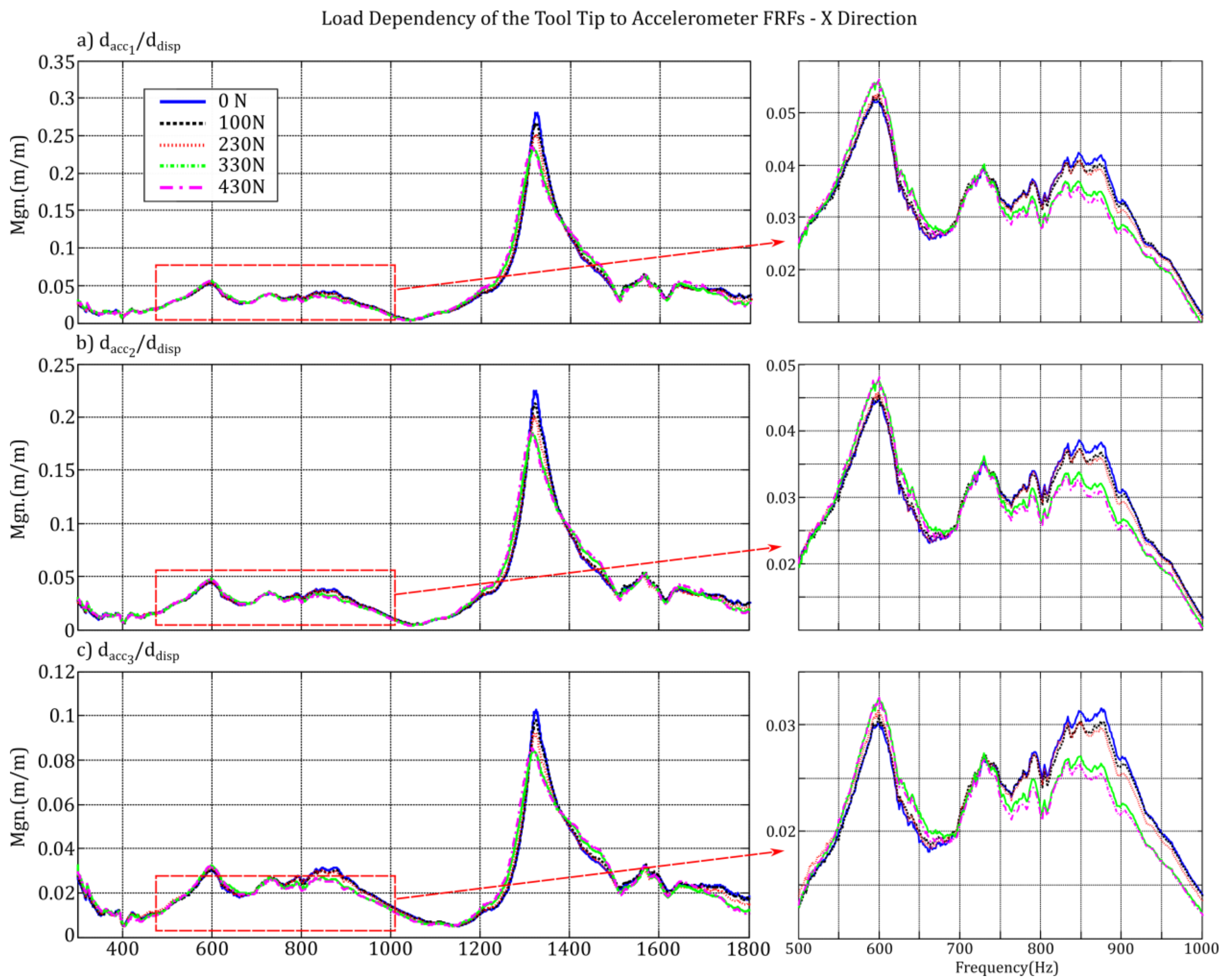

Figure 4.4: Load dependency of the tool tip to accelerometer FRFs below spindle assembly location in X direction

In Figure 4.5, FRFs for the accelerometer on the slider of the machine (Acc. 4) and at the top of the spindle itself (Acc. 5) are shown. It should be noted that these accelerometers are located above the spindle assembly location which is the main reason behind their different behavior than the accelerometers located below (Figure 4.4). Distinct behavior of the Acc. 4 FRF is due to its location on the machine tool rather than the spindle body itself (see Figure 4.1) which makes it a good candidate for spindle assembly health monitoring for future studies.

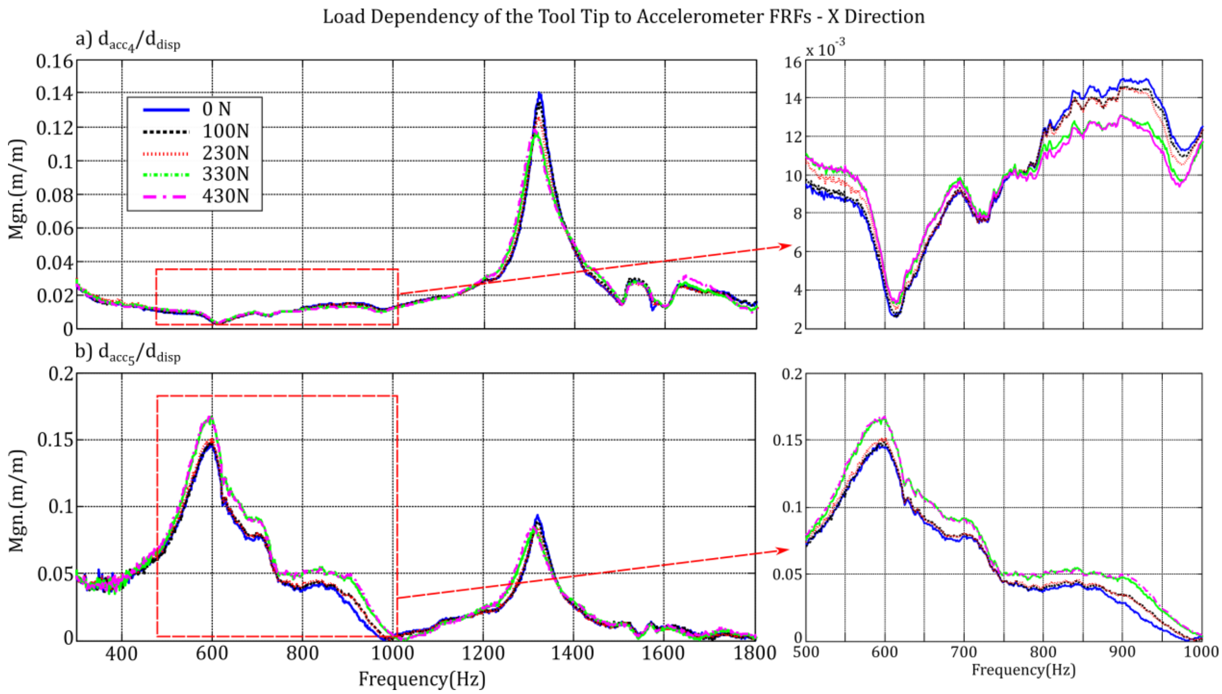

Figure 4.5: Load dependency of the tool tip to accelerometer FRFs above spindle assembly location in X direction

4.2.2 Speed Dependency of the Spindle Dynamics

Speed dependency of the spindle dynamics is investigated from 0 to 15000 rev/min with 1500 rev/min increments where impact is applied with an instrumented hammer across the displacement sensor as the tool is rotating. 50 impacts are applied for each speed to filter out the effect of rotating tool from the displacement sensor readings by subtracting the pure rotation parts from the tap test sections in frequency domain. Tool tip FRF variation with spindle speed is given in Figure 4.6.

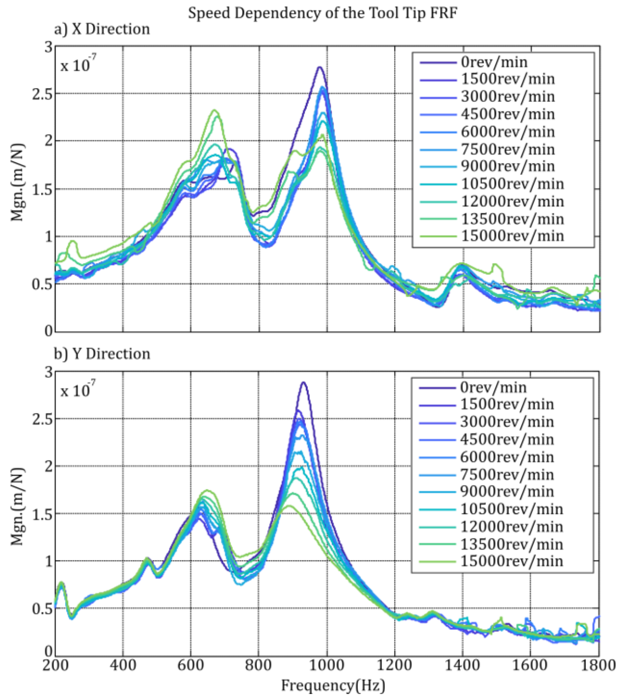

Figure 4.6: Speed dependency of the tool tip FRF in X and Y directions

Speed dependency of the dynamics at the tool tip are evident in the measurements (Figure 4.6) since magnitude at the dominant mode (980 Hz) decreased by 48% and 82% in X and Y directions, respectively. On the contrary, magnitude of the mode around 600 Hz increased by 45% and 25% for X and Y directions, respectively. This behavior can be attributed to variations in the centrifugal forces, gyroscopic moments acting on bearings, dynamic properties of the subassemblies (spindle, holder and tool) and the bearings themselves. Thus, tool point and tool point to accelerometer location FRFs measured at the idle state of the machining center will lead to incorrect process state predictions. As in the load dependency case, FRFs between the tool tip and the accelerometer locations (closest - Acc. 1 and furthest - Acc. 5 to the tool tip as an example) are shown in Figure 4.7 for the X direction. These FRFs are provided here since accelerometers installed on the non-rotating parts of the system will be used to predict the tool tip vibration and process forces which are exciting the system at the rotating parts (tool shank and tip).

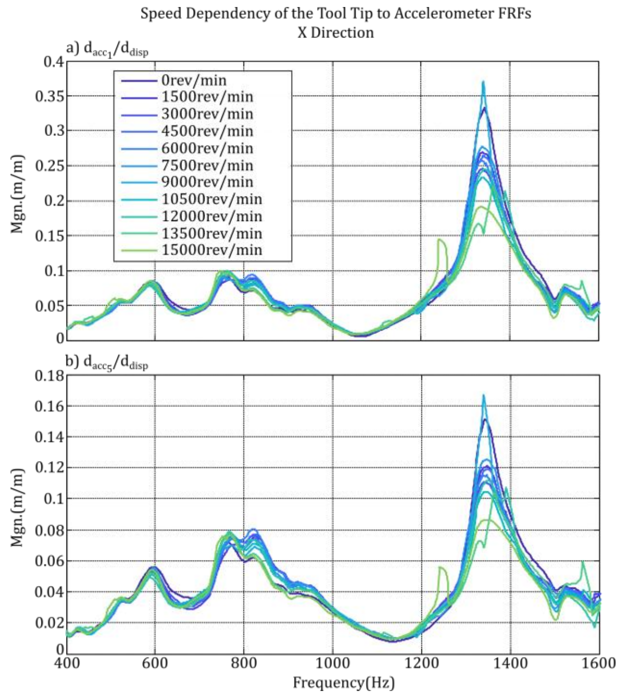

Figure 4.7: Speed dependency of the tool tip to accelerometer FRFs (d_{acc_1} and d_{acc_5}) in X direction

Similar to the load dependency case, dynamics of the tool tip and tool tip to accelerometer location FRFs are quite responsive to speed as well.

4.3 Load and Speed Dependent Dynamics Map of the Spindle

As shown in the previous two sections, dynamics of the spindle, holder and tool system vary with load and speed. In this study, a map of the spindle dynamics is created by varying the load from 0 to 450 N with around 50 N and speed from 0 to 15000 rev/min with 1500 rev/min increments. 110 FRFs are measured in X and Y direction (55 FRFs each) where 50 tap tests are performed for each condition to filter out the effect of spindle revolution on sensor measurements and take the average of them for a smooth, noise-free FRF. After the tap tests, a map for varying dynamics of the spindle with respect to load and speed is created which is accessed by the process state prediction algorithm, so it can self-adjust itself to in-process conditions. As an example, speed dependency of the tool tip FRF is shown in Figure 4.8 under different selected load conditions which gives the dynamics map of the structure in the X direction.

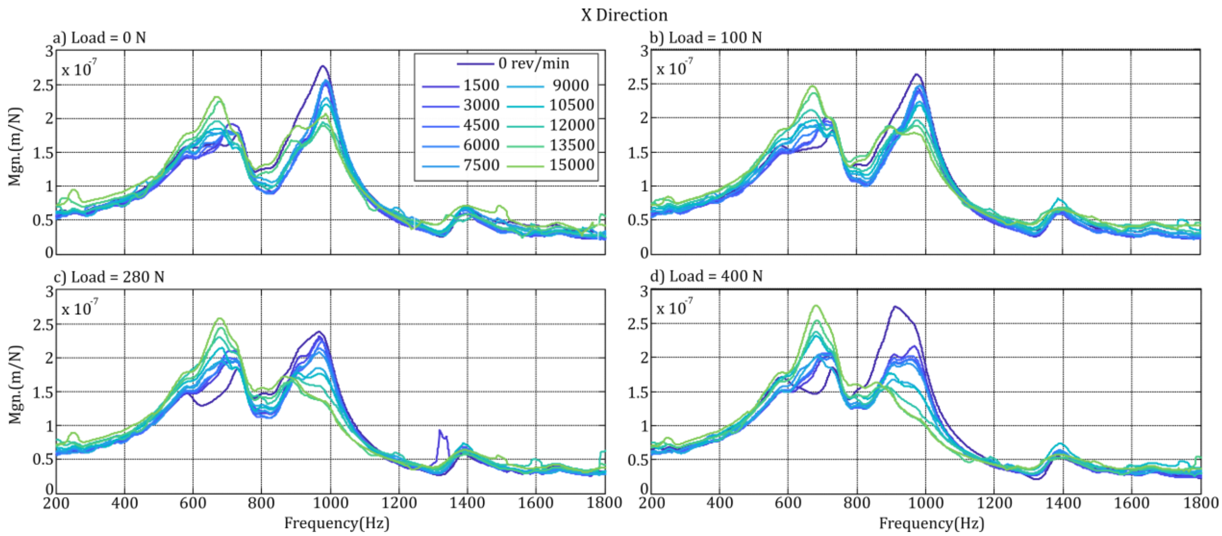

Figure 4.8: Load and speed dependent dynamics map of the X direction (tool tip FRF)

FRFs between the displacement sensor and the accelerometers are also measured under the same conditions to be used for process state predictions. For example, FRFs between the tool tip and the first accelerometer (Acc. 1 – see Figure 4.1) are given for 0 and 400 N load cases in Figure 4.9.

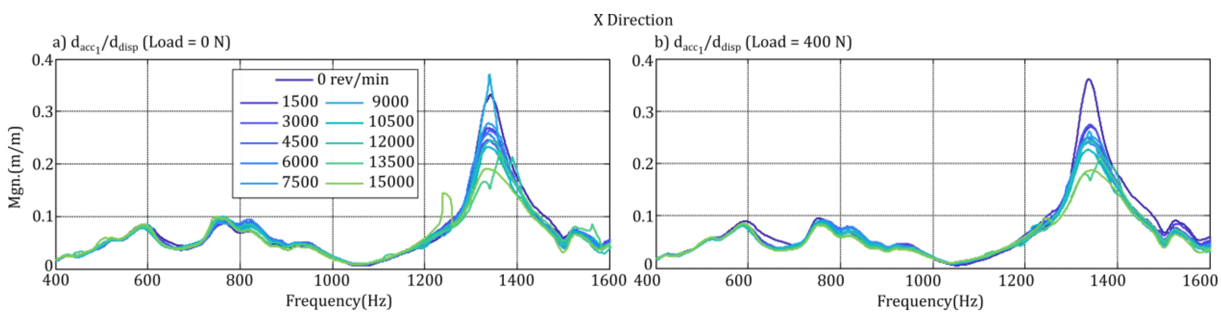

Figure 4.9: Map of the tool tip to accelerometer FRFs (d_{acc_1}) in X and Y directions

Results presented in Figure 4.9 show the necessity of considering the varying system dynamics in process state predictions at the tool tip. Measurements presented in this chapter so far belong to the dummy tool/face mill cutter where the corresponding FRFs of additional tools used in the verification experiments are provided as they are introduced in the following sections.

4.4 State Observer Design and Weighted Average Sensor Data Fusion

4.4.1 State Observer Design

To design state observers for the measured system dynamics, corresponding transfer functions must be known in s-domain, so they can be transformed to their corresponding state space representations. The common methodology to achieve this transformation is to perform manual curve-fitting techniques through selecting the “modes” in the measured FRF manually and obtain the transfer function in s-domain as done in Chapter 3. However; considering the excessive amount of FRFs measured in this portion of the research, an automated way of achieving this curve-fitting to obtain the transfer functions in s-domain is necessary.

Once the FRFs are measured through the modal tap tests, they are fed in to the MATLAB’s System Identification Toolbox® (Release 2016b or higher) [85] which utilizes a Vector Fitting method with Sanathanan-Koerner (SK) iterations and returns the corresponding modal parameters of the transfer function to be expressed in s-domain. Few examples for the curve fitting performance are provided in Figure 4.10 for both tool tip and tool tip to accelerometer location FRFs for the X direction.

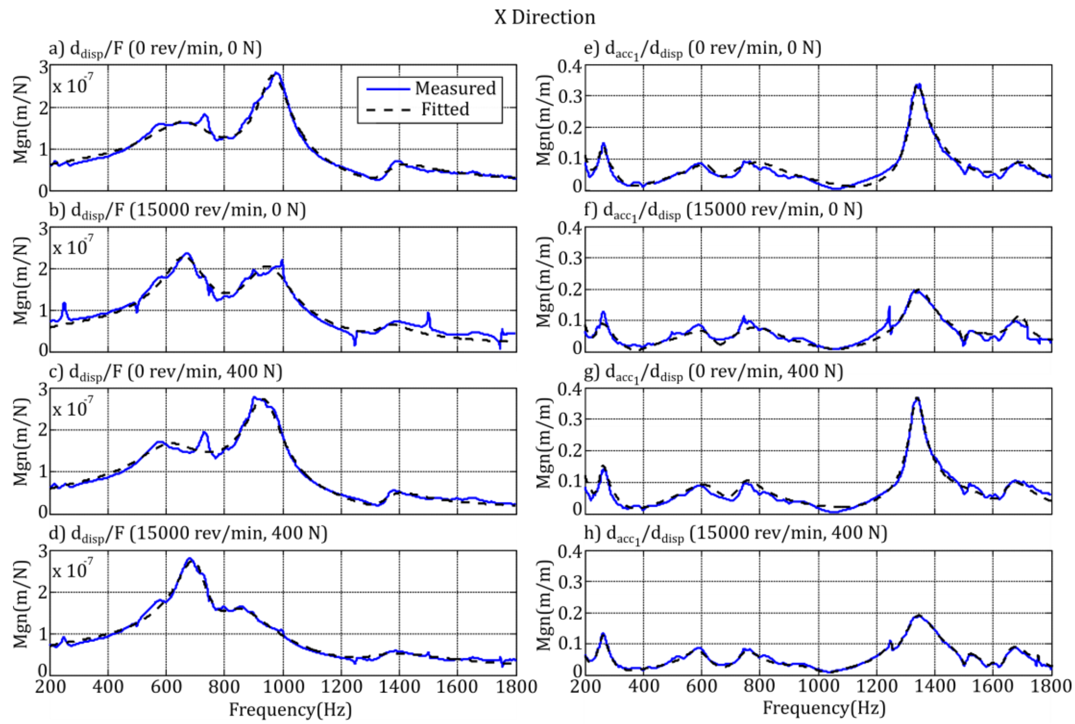

Figure 4.10: Examples for automated curve fitting to measured FRFs (in X Direction)

For a given FRF measurement, MATLAB's "modalfit" built-in function [85] provides the modal parameters after the curve fit as the natural frequencies (ω_{nk}), damping ratios (ζ_k) and the residues (a_k & β_k). As described in Chapter 3, transfer functions between the input and the outputs of the system can be written in the following from;

$$\Phi_{sys_{dm}}(s) = \frac{d_{acc_i}(s)}{d_{disp}(s)} = \sum_k \frac{\alpha_k + \beta_k s}{s^2 + 2\zeta_k \omega_{nk} s + \omega_{nk}^2}, \; \Phi_{sys_{Fm}}(s) = \frac{d_{acc_i}(s)}{F_1(s)} = \sum_k \frac{\alpha_k + \beta_k s}{s^2 + 2\zeta_k \omega_{nk} s + \omega_{nk}^2}$$

(4.1)

where vibrations (displacement) at the tool tip is d_{disp} and $d_{acc_i}(i=1,\ldots,5)$ at the accelerometer locations on the non-rotating parts of the spindle, $m(=1,\ldots,5)$ is the number of transfer functions between the displacement sensor and the accelerometers. Force (F_1) component has a fixed index since process forces excite the system closer to the measurement location at the tool tip.

Having the transfer functions ($\Phi_{sys_{dm}}$ or $\Phi_{sys_{Fm}}$), procedure of obtaining the expanded state space system, designing the Kalman Filter observer and identifying the corresponding noise covariance parameters in an automated way are performed in a similar way as presented in Chapter 3 and Chapter 5, respectively. Hence, they are not described in detail here again. Instead, construction of the input signal in the extended state space model with both DC and AC components is explained which is performed to achieve better state predictions considering the rich frequency content of the vibration sensors mounted on the spindle. Procedure is explained for the displacement transfer function ($d_{acc_i}(s)/d_{disp}(s)$) but it is identical for the force transfer function ($d_{acc_i}(s)/F_1(s)$). First, the following state space model is obtained from the curve-fitted transfer function as follows;

$$\begin{aligned} \dot{\mathbf{x}}_{\mathbf{disp}}(t) &= \mathbf{A}_{\mathbf{disp}}\mathbf{x}_{\mathbf{disp}} + \mathbf{B}_{\mathbf{disp}}\mathbf{u} \\ y_{disp}(t) &= \mathbf{C}_{\mathbf{disp}}\mathbf{x}_{\mathbf{disp}} \end{aligned} \tag{4.2}$$

Assumption of high sampling over the excitation frequency and treating the input signal as piecewise constant is not followed here as in Chapter 3 and the displacement signal (d_{disp}) is denoted by its AC and DC components in s domain as follows;

$$d_{disp}(s) = d_{disp\_DC}(s) + d_{disp\_AC}(s) = w_{disp\_DC} + w_{disp\_AC}(s)\frac{s}{s^2 + \Omega_{S-rs}^2} \tag{4.3}$$

where the derivative of the DC input is the dc process noise (w_{disp_DC}) and the AC input is represented as a cosine function with a periodic noise disturbance of (w_{disp_AC}) and base frequency of spindle revolution per second (Ω_{S-rs}). As given in Chapter 3, state space representation of the cosine function with the updated states is;

$$
\dot{\mathbf{x}}_{\mathbf{dispF}} = \underbrace{\begin{bmatrix} 0 & -\Omega_{S-rs}^2 \\ 1 & 0 \end{bmatrix}}_{\mathbf{A_{dispF}}} \underbrace{\begin{bmatrix} d_{disp\_AC} \\ \dot{d}_{disp\_AC} \end{bmatrix}}_{\mathbf{x_{dispF}}} + \underbrace{\begin{bmatrix} 1 \\ 0 \end{bmatrix}}_{\mathbf{B_{dispF}}} w_{disp\_AC}
$$

$$
d_{disp\_AC} = \underbrace{\begin{bmatrix} 1 & 0 \end{bmatrix}}_{\mathbf{C_{dispF}}} \underbrace{\begin{bmatrix} d_{disp\_AC} \\ \dot{d}_{disp\_AC} \end{bmatrix}}_{\mathbf{x_{dispF}}} \tag{4.4}
$$

Substituting Eq. (4.3) and (4.4) into Eq. (4.2) gives;

$$
\begin{aligned}
\dot{\mathbf{x}}_{\mathbf{disp}} &= \mathbf{A_{disp}} \mathbf{x_{disp}} + \mathbf{B_{disp}} (d_{disp\_DC} + \mathbf{C_{dispF}} \mathbf{x_{dispF}}) \\
y_{disp} &= \mathbf{C_{disp}} \mathbf{x_{disp}}
\end{aligned} \tag{4.5}
$$

Input of the system ($d_{disp} = d_{disp\_DC} + \mathbf{C_{dispF}} \mathbf{x_{dispF}}$) is considered as one of the states as;

$$
\begin{Bmatrix} \{\dot{\mathbf{x}}_{\mathbf{disp}}\} \\ \dot{\mathbf{d}}_{\mathbf{disp\_DC}} \\ \dot{\mathbf{x}}_{\mathbf{dispF}} \end{Bmatrix} = \underbrace{\begin{bmatrix} \mathbf{A_{disp}} & \mathbf{B_{disp}} & \mathbf{B_{disp}} \mathbf{C_{dispF}} \\ 0 & 0 & 0 \\ 0 & 0 & \mathbf{A_{dispF}} \end{bmatrix}}_{\mathbf{A_{exp\_disp}}} \underbrace{\begin{Bmatrix} \{\mathbf{x_{disp}}\} \\ \mathbf{d_{disp\_DC}} \\ \mathbf{x_{dispF}} \end{Bmatrix}}_{\mathbf{x_{exp\_disp}}} + \underbrace{\begin{bmatrix} 0 \\ \theta_{disp\_DC} \\ \theta_{disp\_AC} \end{bmatrix}}_{\mathbf{L_{disp}}} w_{disp}
$$

$$
\mathbf{y_{disp\_exp}} = \underbrace{\begin{bmatrix} \mathbf{C_{disp}} & 0 & 0 \end{bmatrix}}_{\mathbf{C_{exp\_disp}}} \begin{Bmatrix} \{\mathbf{x_{disp}}\} \\ \mathbf{d_{disp\_DC}} \\ \mathbf{x_{dispF}} \end{Bmatrix} + v_{disp} \tag{4.6}
$$

where the Kalman observer state space system is written with its gain vector of $\mathbf{K_{disp}}$;

$$
\begin{aligned}
\dot{\hat{\mathbf{x}}}_{\mathbf{exp\_disp}} &= \mathbf{A_{exp\_disp}} \hat{\mathbf{x}}_{\mathbf{exp\_disp}} + \mathbf{K_{disp}} (y_{disp\_\exp} - \mathbf{C_{exp\_disp}} \hat{\mathbf{x}}_{\mathbf{exp\_disp}}) \\
&= (\mathbf{A_{exp\_disp}} - \mathbf{K_{disp}} \mathbf{C_{exp\_disp}}) \hat{\mathbf{x}}_{\mathbf{exp\_disp}} + \mathbf{K_{disp}} y_{disp\_\exp} \\
\hat{y}_{disp\_\exp} &= \mathbf{C_{0\_disp}} \hat{\mathbf{x}}_{\mathbf{exp\_disp}} = \hat{d}_{disp} \leftarrow \mathbf{C_{0\_disp}} = \begin{bmatrix} 0 & 1 & \mathbf{C_{dispF}} \end{bmatrix}
\end{aligned} \tag{4.7}
$$

Derivation of Kalman Filter transfer function to estimate the actual displacement signal ($\hat{d}_{disp}$) through minimizing the error in state predictions is explained in Chapter 3 from Eq. (3.24) to (3.30). It should be noted that the contribution in this chapter does not lie within process or system modeling, but in investigating the in-process variation of spindle dynamics and showing that these variations should be considered to update the state observers to predict process states from spindle mounted vibration sensors accurately.

As an example, corresponding Kalman Filter FRFs of force to displacement ($\Phi_{sys_{Fm}}$) or displacement to displacement ($\Phi_{sys_{dm}}$) system transfer functions are provided in Figure 4.11 for the FRFs shown in Figure 4.10.

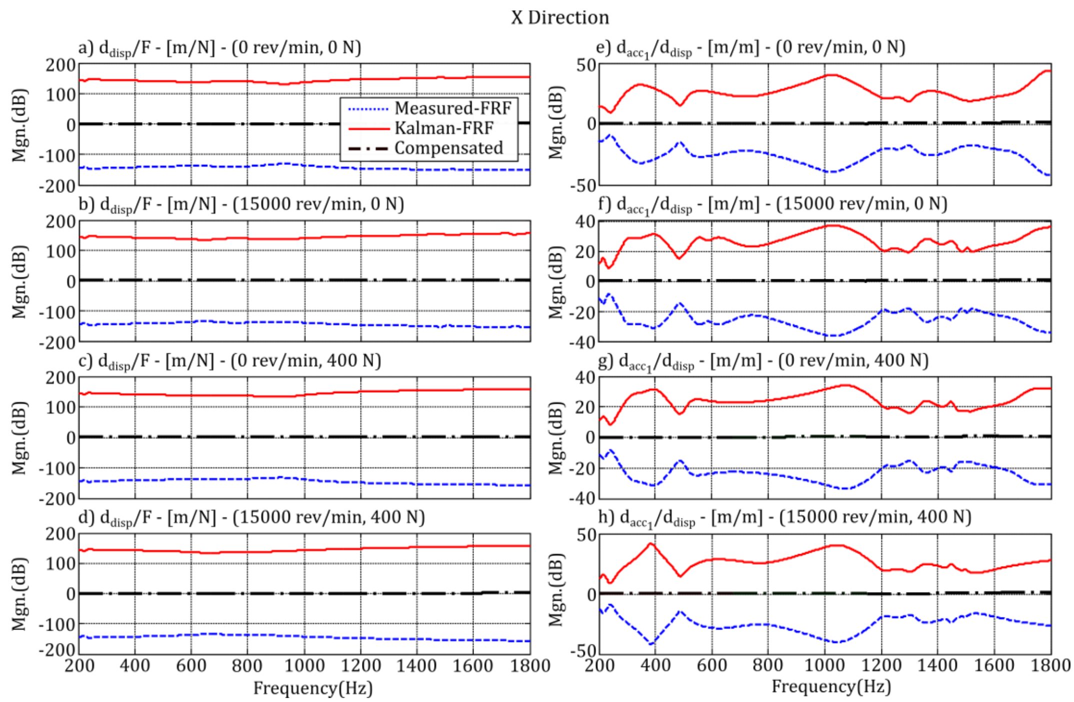

Figure 4.11: Measured (force to displacement - $\Phi_{sys_{F1}}$, displacement to displacement - $\Phi_{sys_{d1}}$), Kalman and Compensated FRFs for the cases presented in Figure 4.10

Considering both DC and AC components of the input signals (F_1 for force and d_{disp} for displacements FRFs) improves the compensation performance, which are also present at the experimental results where the rich frequency content of the process states are successfully captured.

4.4.2 Weighted Average Sensor Data Fusion

In this section, the weighted average sensor data fusion method used to predict process forces and vibrations at the tool tip from all five accelerometer signals is described. Although one accelerometer in each direction can be used to predict the process states in an acceptable level, data fusion provides enhanced accuracy and the advantage of eliminating sensor failure based down times in the production. Overall framework of the prediction procedure with data fusion is provided in Figure 4.12 with a flowchart where the supplementary visual on the experimental setup can be seen in Figure 4.13.

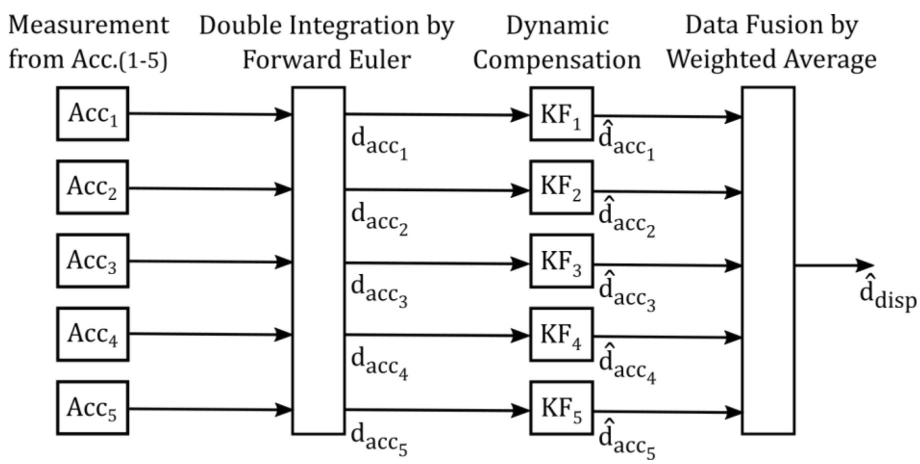

Figure 4.12: Flowchart of tool tip displacement prediction from accelerometers on spindle structure (force prediction follows the same procedure)

Acceleration measurements collected from the sensors are integrated twice by using the Forward Euler method to obtain the displacement (vibration) signals in discrete-time domain as follows;

$$d_{acc_i} = a_{acc_i} \frac{\Delta t^2}{z^2 - 2z + 1}, \; i = 1, \ldots, 5 \tag{4.8}$$

These displacements are fed into their individual Kalman Filter transfer functions to compensate the distortions in the signals coming from the load and speed dependent structural dynamics of the spindle system. Compensated displacements from each sensor are used to predict the displacement at the tool tip by utilizing a weighted average data fusion method.

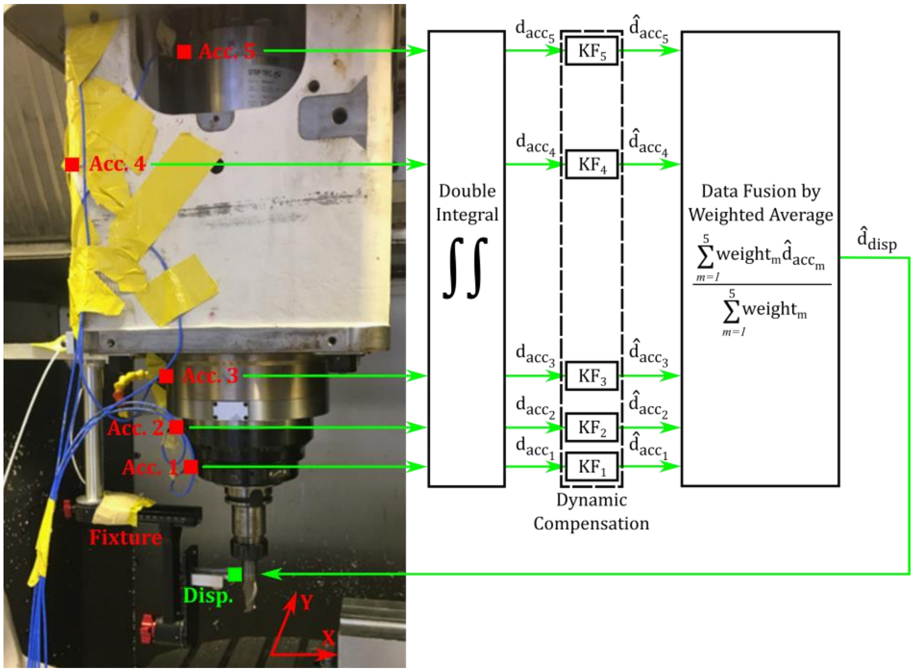

Figure 4.13: Framework of tool tip displacement prediction from accelerometer measurements

Weight assignment to individual sensors are done by considering the magnitude of the measured FRFs between the tool tip and accelerometers. First, magnitudes are normalized with respect to the highest value at every frequency along the spectrum. Then, weights are assigned to the accelerometers accordingly in a linear fashion which are used in the data fusion stage.

As an example, FRFs between the tool tip and accelerometer locations for the 20 mm diameter solid end mill cutter with 2 flutes (see Figure 4.13) are given in Figure 4.14 for 15000 rev/min with no load case. It is evident from these FRFs that each accelerometer has different magnitude of response along the frequency spectrum with respect to tool tip. Hence, it is proposed to assign weights to these sensors and prioritize them according to their magnitudes at a given frequency.

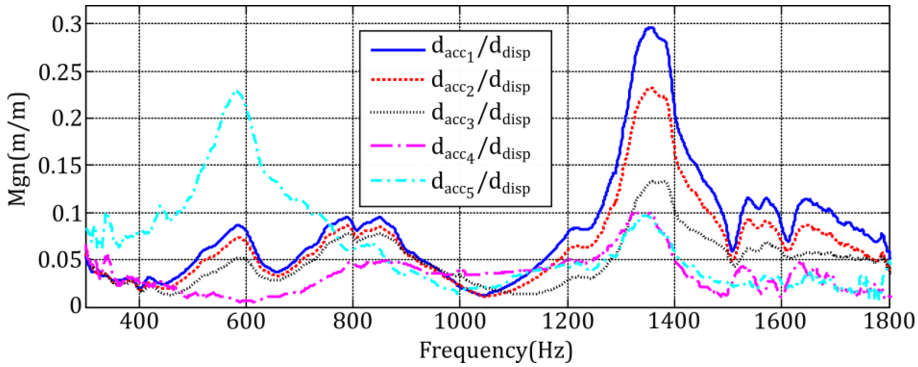

Figure 4.14: Tool tip to accelerometer location FRFs for 15000 rev/min without load case (20 mm diameter 2 fluted cutter shown in Figure 4.13)

First, weights (%) are assigned correspondingly to each accelerometer as follows;

$$weight_m(\omega) = \left[\frac{\left|\Phi_{sys_{dm}}(j\omega)\right|}{\sum_{i=1}^{5}\left|\Phi_{sys_{di}}(j\omega)\right|} \right], \; m = 0,...,5 \tag{4.9}$$

Calculated normalized weights in 0 to 1 range are given in Figure 4.15 for each sensor as a percentage. Naturally, summation of all weights at a certain frequency (ω) gives 1 (or 100% as a percentage);

$$\sum_{m=1}^{5} weight_m(\omega) = 1 \tag{4.10}$$

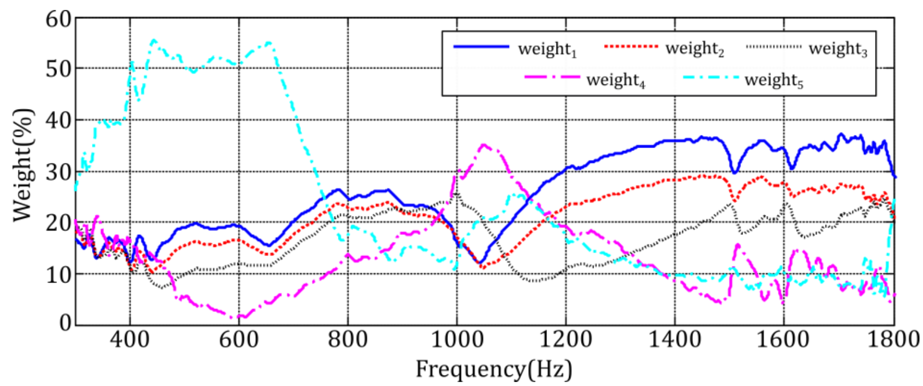

Figure 4.15: Assigned weights to the tool tip to accelerometer location FRFs given in Figure 4.14

In summary, curve fitted FRFs (given in Figure 4.14) are converted to discrete-time domain using bilinear (Tustin) approximation to calculate the weights along the frequency spectrum (Figure 4.15). These discrete-time transfer functions are then used to obtain the process state predictions from compensated sensor measurements where the displacement predictions are calculated as follows;

$$\hat{d}_{disp} = \frac{\sum_{m=1}^{5}\left[\frac{\left|\Phi_{sys_{dm}}(k)\right|}{\sum_{i=1}^{5}\left|\Phi_{sys_{di}}(k)\right|}\right]\hat{d}_{acc_m}}{\left[\frac{\left|\Phi_{sys_{dm}}(k)\right|}{\sum_{i=1}^{5}\left|\Phi_{sys_{di}}(k)\right|}\right]} \tag{4.11}$$

and the force predictions are calculated in a similar fashion with the corresponding discrete-time displacement to force transfer functions;

$$\hat{F}_{1} = \frac{\sum_{m=1}^{5}\left[\frac{\left|\Phi_{sys_{Fm}}(k)\right|}{\sum_{i=1}^{5}\left|\Phi_{sys_{Fi}}(k)\right|}\right]\hat{F}_{acc_m}}{\left[\frac{\left|\Phi_{sys_{Fm}}(k)\right|}{\sum_{i=1}^{5}\left|\Phi_{sys_{Fi}}(k)\right|}\right]} \tag{4.12}$$

This way, depending on the excitation frequency to the system (and its harmonics) coming from the cutting action at the tool-workpiece interface, the predictions are biased towards the signals coming from the sensors with higher weights at those specific frequencies. For example, if a milling operation with a 2-fluted end mill cutter is performed at 15000 rev/min, measurement of the accelerometer number 5 will be the most dominant signal at the tooth passing frequency (500

Hz) where accelerometer number 4 and 1 are the most dominant ones at the first and second harmonics of the tooth passing frequency, respectively (with the FRFs shown in Figure 4.14).

4.5 Experimental Verification

Presented methodology is verified through milling experiments where the workpiece material is Aluminum 7075 and tests are conducted with two different tools: a 40-mm diameter five-fluted face mill and a 20-mm diameter two-fluted end mill with a regular pitch angle. Spindle speeds are selected as 9000, 12000 and 15000 rev/min to cover a wide range of excitation frequency where the speed dependency of the system dynamics is evident. A fixture is designed by IWF in ETH Zürich to mount the displacement sensor to achieve in-process displacement measurement from the tool shank which has a dominant mode around 200 Hz (see Figure 4.16).

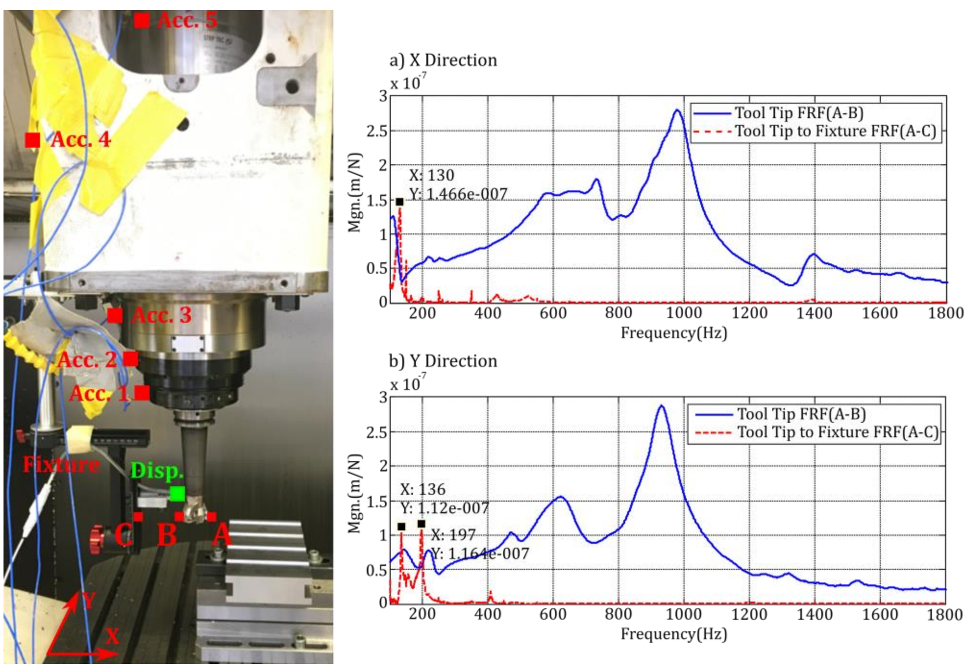

Figure 4.16: FRFs of tool tip and tool tip to fixture setup (A – location of hammer impact, B – Tool tip displacement measurement, C – Fixture displacement where the sensor is assembled)

As shown in Figure 4.16, after 250 Hz, FRF between the tool tip to fixture tip (location A to C, see Figure 4.16) is three orders of magnitude smaller than the tool tip FRF itself (location A to

B) in both X and Y directions. The fixture is kept at the presented form and the results are high pass filtered with a 250 Hz cutoff frequency to avoid this effect on the measurements.

In addition, dynamics of the dynamometer should also be considered for the high frequency content. Force to force FRFs in X and Y directions are measured with the workpiece installed on the dynamometer (see Figure 4.17) and the dynamically distorted force measurements are compensated through Kalman Filters.

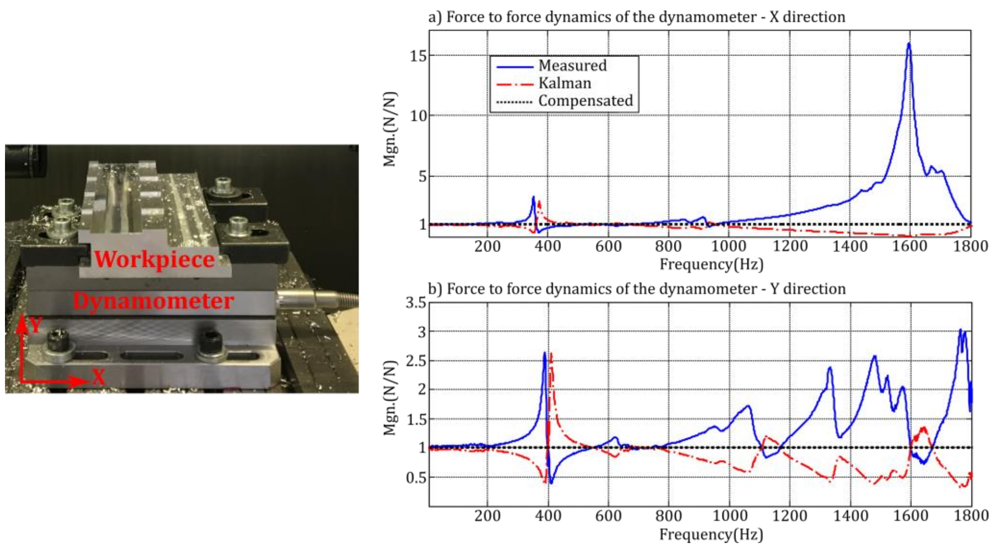

Figure 4.17: Measured force to force FRF of the dynamometer, designed Kalman Filter and resulting compensated FRFs in X and Y directions

4.5.1 Case 1: 40 mm diameter, 5-fluted Face Mill

First, 3 slot cutting experiments are performed with the 40 mm diameter, five-fluted face mill at 9000, 12000 and 15000 rev/min spindle speeds. Axial depth of cut is selected as 1.5 mm and the feed rate is 0.1 mm per tooth. To introduce rich frequency content to the measurements, impacts are given at the tool shank with an instrumented hammer during the cut for 9000 and 12000 rev/min speeds.

Tool vibration (at the shank where the displacement sensor is located) predictions from accelerometer measurements are compared with the displacement sensor measurements for three spindle speeds which are presented in Figure 4.18, Figure 4.19 and Figure 4.20 for 9000, 12000 and 15000 rev/min spindle speed cases, respectively.

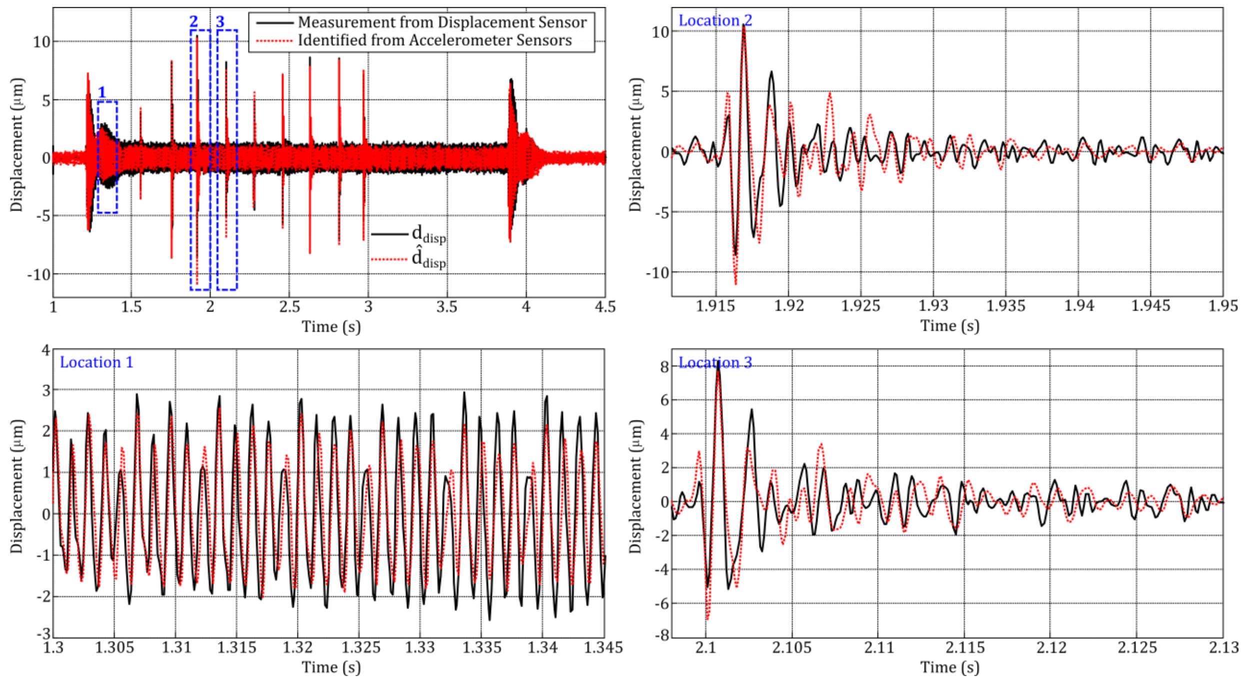

Figure 4.18: Tool vibration predictions - Ω_S = 9000 rev/min, slot milling, axial depth of cut = 1.5 mm, feed = 0.1 mm/tooth (d_{disp} - Measurement from displacement sensor, $\hat{d}_{disp}$ - Estimated displacement from accelerometers through sensor fusion)

For 9000 rev/min, tooth passing frequency corresponds to 750 Hz and the first harmonic is at 1500 Hz where both are located at speed and load dependent regions in the FRFs. Error between the displacement sensor measurements and predictions from accelerometers is below 15% along the cut including the transient regions at the beginning and the end of the cut. Displacements due to the impacts given to the tool shank during the cut are predicted with a high accuracy as well which shows that the system can monitor the frequency-rich transients.

The next speed is 12000 rev/min and the tooth passing frequency is 1000 Hz with its first harmonic located at 2000 Hz. Similar to the previous case, errors between the displacements measured with the displacement sensor and predicted from accelerometers are below 15%.

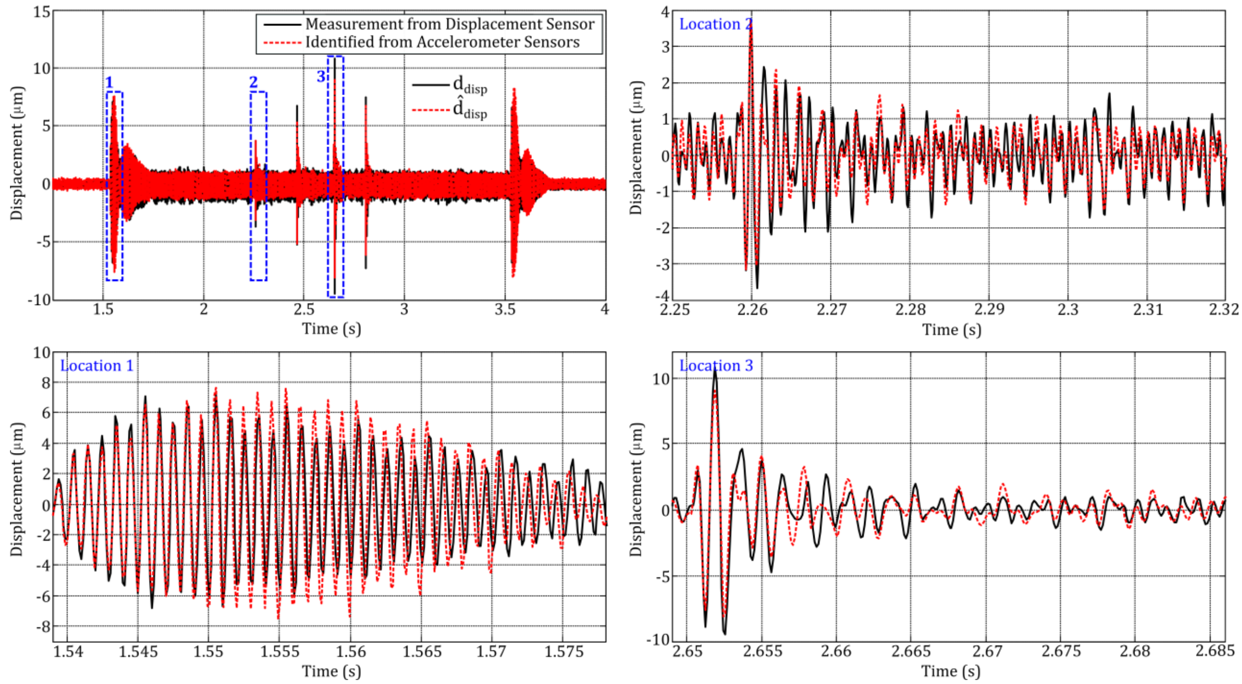

Figure 4.19: Tool vibration predictions - Ω_s = 12000 rev/min, slot milling, axial depth of cut = 1.5 mm, feed = 0.1 mm/tooth (d_{disp} - Measurement from displacement sensor, $\hat{d}_{disp}$ - Estimated displacement from accelerometers through sensor fusion)

For 15000 rev/min, predictions in both entry and exit transients as well as the steady state portion are in good agreement with the measurements where the error is below 20%. Higher errors compared to lower speeds is due to the high frequency content with the first harmonic of the tooth passing frequency being at 2500 Hz.

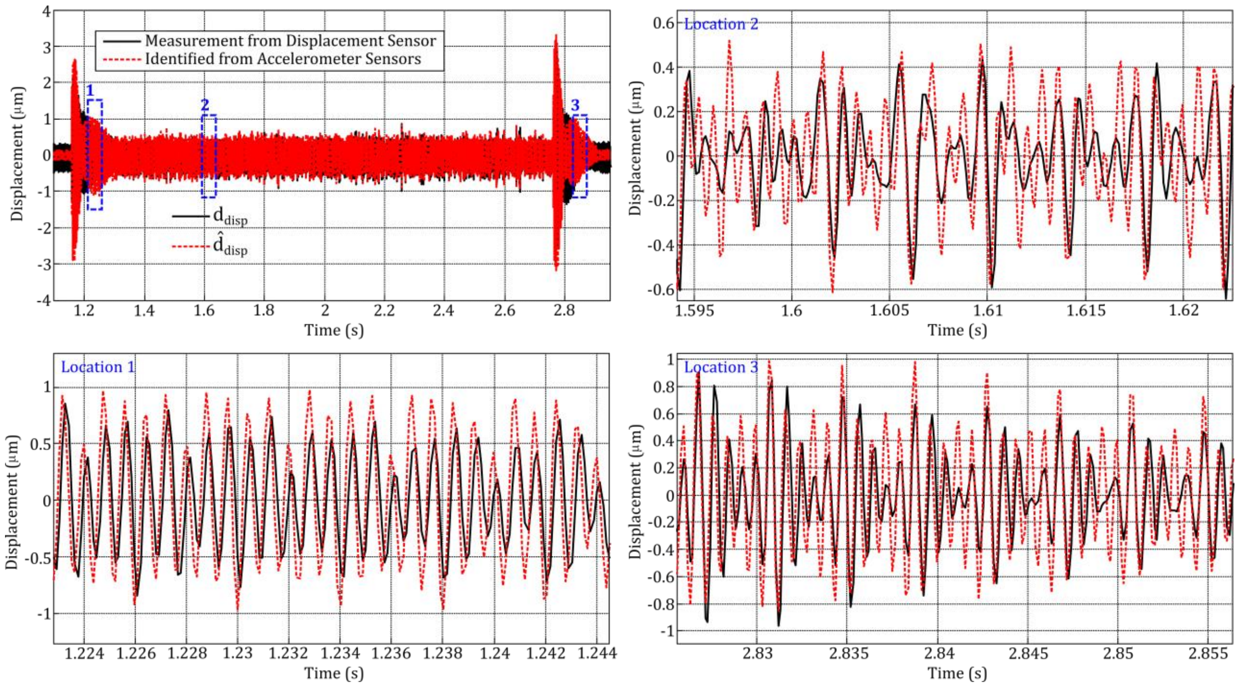

Figure 4.20: Tool vibration predictions - Ω_S = 15000 rev/min, slot milling, axial depth of cut = 1.5 mm, feed = 0.1 mm/tooth (d_{disp} - Measurement from displacement sensor, $\hat{d}_{disp}$ - Estimated displacement from accelerometers through sensor fusion)

In addition to the displacements, process forces are predicted as well which are given in Figure 4.21, Figure 4.22 and Figure 4.23 for 9000, 12000 and 15000 rev/min cases, respectively. For the force predictions, since the impact was given at the tool shank during the cut for 9000 and 12000 rev/min speed cases (no impact for 15000 rev/min), dynamometer measurements do not reflect the corresponding transients accurately (although they are dynamically compensated) due to the low contact stiffness between the tool and the workpiece during the operation. Hence, performance of force prediction is checked at steady cut portions, rather than the transients where the impacts are given at the tool shank.

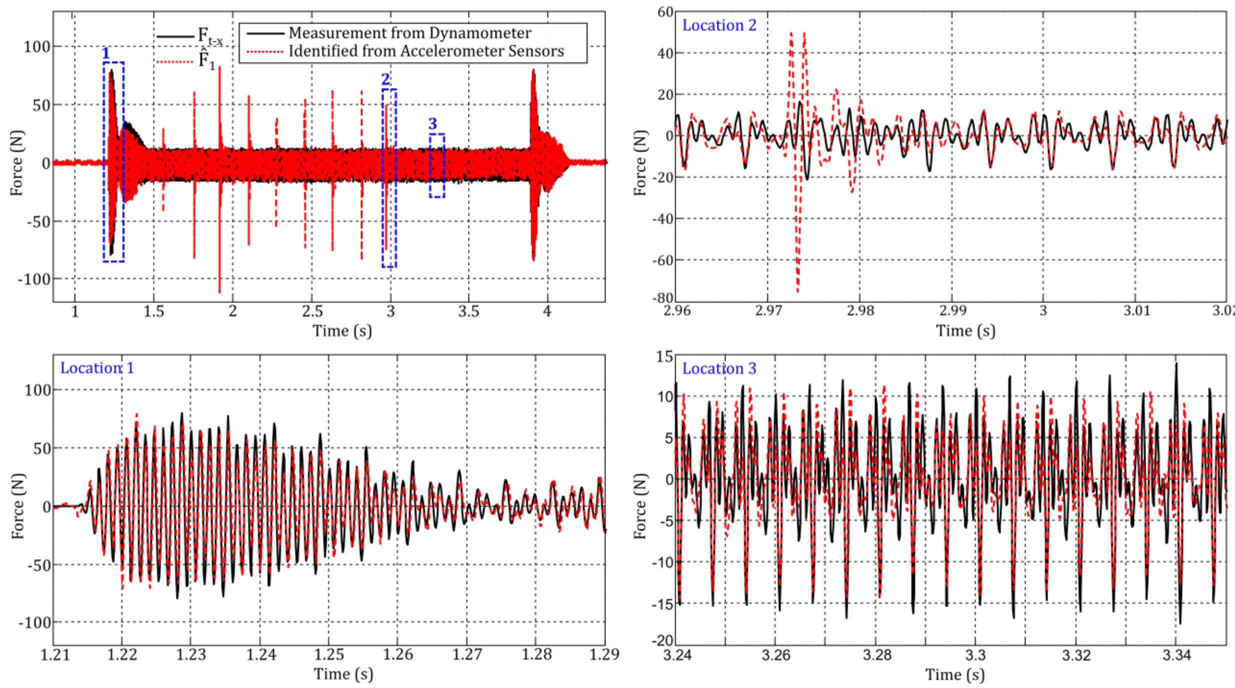

Figure 4.21: Process force predictions in normal direction - Ω_S = 9000 rev/min, slot milling, axial depth of cut = 1.5 mm, feed = 0.1 mm/tooth (F_{t-x} - Measurement from dynamometer in X direction of tool frame, $\hat{F}_1$ - Estimated force from accelerometers through sensor fusion)

Results for the 9000 rev/min speed (see Figure 4.21) show that force predictions from accelerometers and the measurements from the dynamometer agree in an acceptable level where the average error along the cut is below 20%. Entry to cut transients are predicted accurately and the low amplitude forces at the steady cut portion are captured.

Next, 12000 rev/min speed case shown in Figure 4.22 has a similar performance where the average error is below 25% at the entry-exit to cut transients and 18% at the steady cut portions.

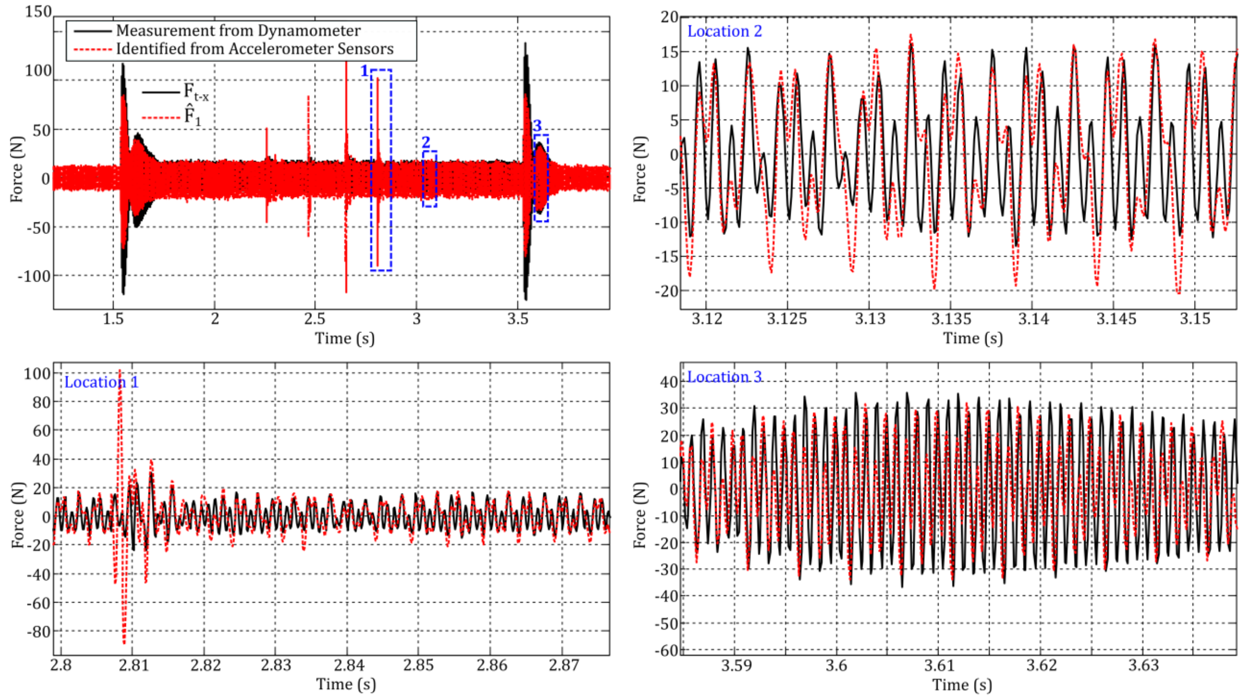

Figure 4.22: Process force predictions in normal direction - Ω_S = 12000 rev/min, slot milling, axial depth of cut = 1.5 mm, feed = 0.1 mm/tooth (F_{t-x} - Measurement from dynamometer in X direction of tool frame, $\hat{F}_1$ - Estimated force from accelerometers through sensor fusion)

For 15000 rev/min case, although average errors at the spindle (250 Hz) and the tooth passing (1250 Hz) frequencies are below 20%, error at the first harmonic of the tooth passing frequency (2500 Hz) reaches to 45-50%. This is the result of the frequency range (200-1800 Hz) used in the curve fitting with MATLAB's system identification toolbox [85] since the FRFs are measured until 2000 Hz. To overcome this issue and improve the predictions, identification experiments (FRF measurements) can be repeated with a higher impact force, or with a harder hammer tip (i.e. metal) so higher frequencies can be compensated with the proposed algorithm.

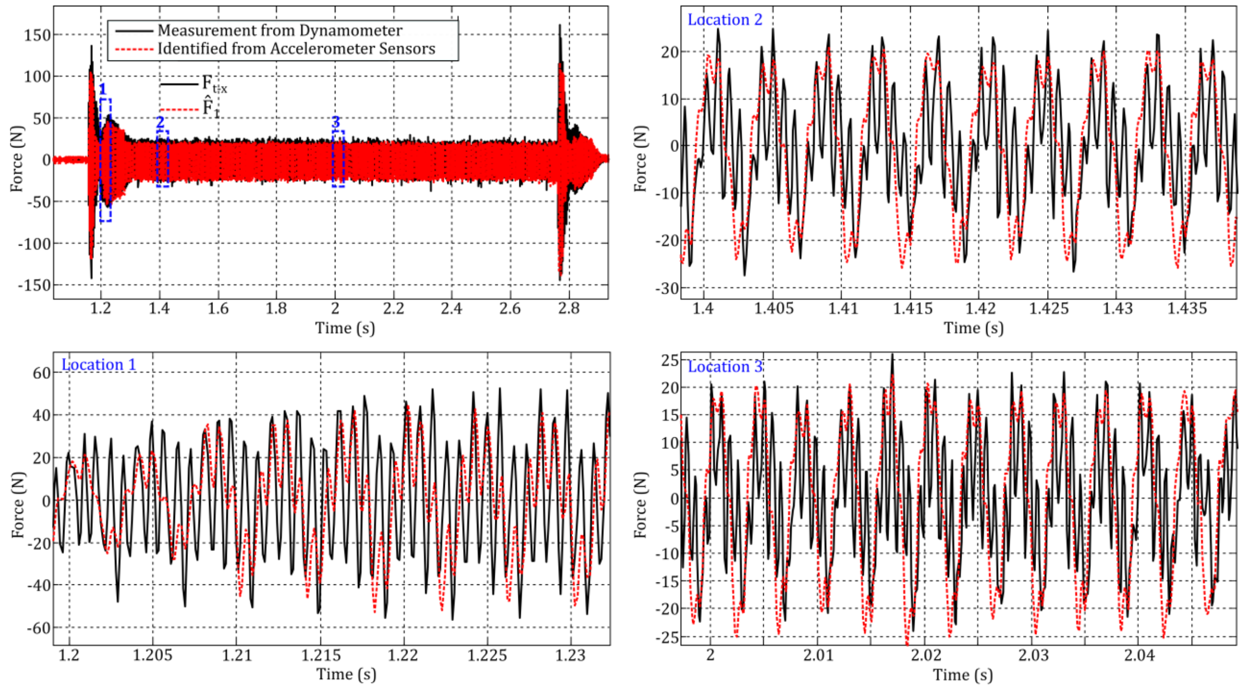

Figure 4.23: Process force predictions in normal direction - Ω_S = 15000 rev/min, slot milling, axial depth of cut = 1.5 mm, feed = 0.1 mm/tooth (F_{t-x} - Measurement from dynamometer in X direction of tool frame, $\hat{F}_1$ - Estimated force from accelerometers through sensor fusion)

4.5.2 Case 2: 20 mm diameter, 2-fluted End Mill

Next, quarter, half and full immersion cuts are performed at 9000, 12000 and 15000 rev/min spindle speeds, respectively, with a 20 mm diameter 2-fluted end mill. Axial depth of cut is selected as 5 mm and the feed rate is kept at 0.1 mm per tooth. Load in Z direction is detected below 35-40 N both from the dynamometer and Z drive current measurements (see Chapter 3), hence the corresponding system dynamics are used to update the state observers. To show the effectiveness of the proposed method in detail, individual vibration and force predictions from each accelerometer are shown with the global prediction after data fusion.

Results for the quarter immersion cut (5 mm width) at 9000 rev/min speed are shown in Figure 4.24.

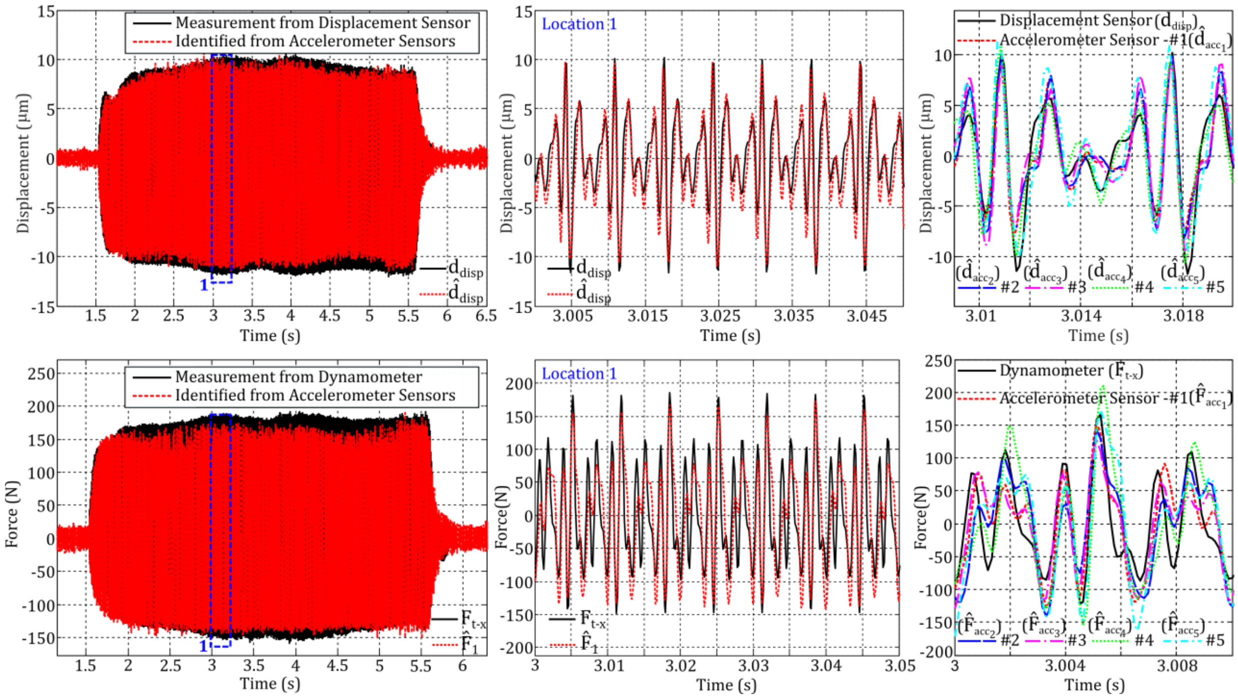

Figure 4.24: Tool vibration and process force predictions in normal direction - Ω_S = 9000 rev/min, quarter immersion milling, axial depth of cut = 5 mm, feed = 0.1 mm/tooth (d_{disp} - Measurement from displacement sensor, $\hat{d}_{disp}$ - Estimated displacement from accelerometers through sensor fusion, $\hat{d}_{acc_m}\ (m=1,\ldots,5)$ - Estimated displacements from individual accelerometers without sensor fusion, F_{t-x} - Measurement from dynamometer in X direction of tool frame, $\hat{F}_1$ - Estimated force from accelerometers through sensor fusion, $\hat{F}_{acc_m}\ (m=1,\ldots,5)$ - Estimated forces from individual accelerometers without sensor fusion)

Vibrations at the tool shank are predicted with a 15% error after data fusion. In addition, predictions from individual accelerometers can also be seen in Figure 4.24 which shows that if desired, any one of these sensors can be used individually to predict the states, but with a lower accuracy. Each sensor provides better predictions at the frequencies where they have higher magnitudes at their FRFs and correct each other with the weighted average method. For process forces, despite the intermittent nature of the quarter immersion cut, predictions have a good agreement with the dynamometer measurements. Predictions from individual sensors have 14%, 16%, 15%, 21% and 18% error between the dynamometer measurements from first to fifth accelerometer, respectively. After feeding them to the weighted average data fusion algorithm, maximum error is reduced to 8%.

A half immersion experiment is performed with 12000 rev/min speed (see Figure 4.25) and vibration predictions have 9% error in the steady cut region. For the force predictions, the error is around 20% at the entry region and 17% at the exit, steady cut portion has less than a 6% error since the multiple sensors are correcting each other with the data fusion.

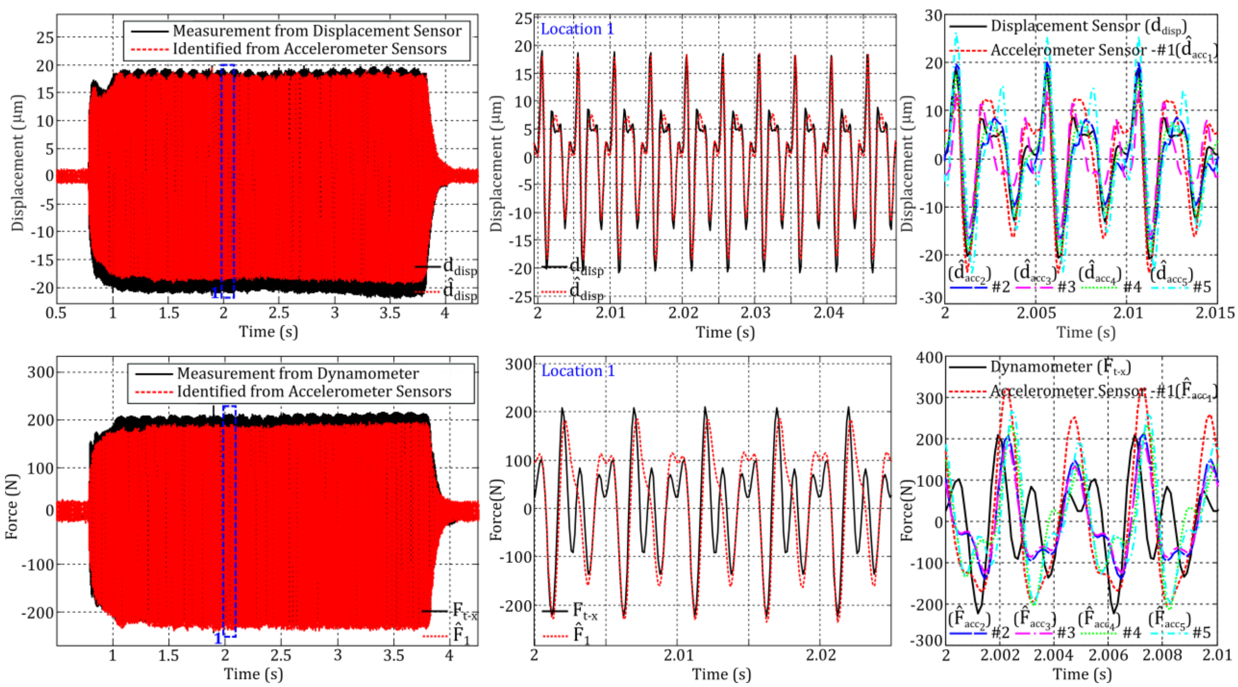

Figure 4.25: Tool vibration and process force predictions in normal direction - Ω_S = 12000 rev/min, half immersion milling, axial depth of cut = 5 mm, feed = 0.1 mm/tooth (d_{disp} - Measurement from displacement sensor, $\hat{d}_{disp}$ - Estimated displacement from accelerometers through sensor fusion, $\hat{d}_{acc_m}$ $(m = 1,...,5)$ - Estimated displacements from individual accelerometers without sensor fusion, F_{t-x} - Measurement from dynamometer in X direction of tool frame, $\hat{F}_1$ - Estimated force from accelerometers through sensor fusion, $\hat{F}_{acc_m}$ $(m = 1,...,5)$ - Estimated forces from individual accelerometers without sensor fusion)

Finally, a slot cutting experiment is performed at 15000 rev/min speed (see Figure 4.26). Tool vibration predictions suffer at the beginning and end of the cut whereas the prediction error is below 5% in the steady cut region. Force predictions have less than 9% error in entry and exit regions, and it drops to 4% during a steady cut.

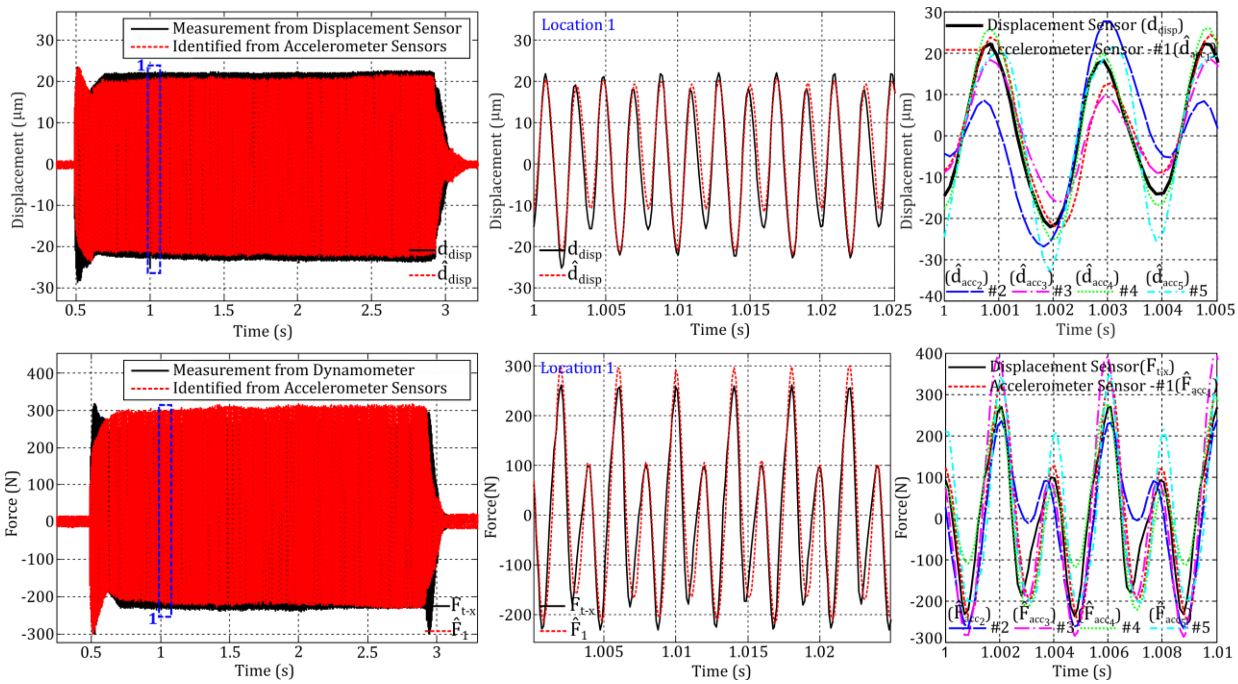

Figure 4.26: Tool vibration and process force predictions in normal direction - Ω_S = 15000 rev/min, full immersion milling, axial depth of cut = 5 mm, feed = 0.1 mm/tooth (d_{disp} - Measurement from displacement sensor, $\hat{d}_{disp}$ - Estimated displacement from accelerometers through sensor fusion, $\hat{d}_{acc_m}(m=1,...,5)$ - Estimated displacements from individual accelerometers without sensor fusion, F_{t-x} - Measurement from dynamometer in X direction of tool frame, $\hat{F}_1$ - Estimated force from accelerometers through sensor fusion, $\hat{F}_{acc_m}(m=1,...,5)$ - Estimated forces from individual accelerometers without sensor fusion)

The difference between two teeth in terms of chip load (hence force) in all speed cases is due to the runout at the tool tip which is measured as 35-40 micron. The same behavior is not seen in the vibration measurements and predictions since they are located at the tool shank, instead of the tool tip where cutter flutes are interacting with the workpiece mounted on the dynamometer.

4.6 Summary

This chapter presents a tool vibration and cutting force prediction method with spindle mounted vibration sensors. Speed and load dependent system dynamics are identified through modal tap tests with specially designed fixtures which are then used to update the state observers according to in-process conditions. In addition, multiple sensors installed strategically on spindle structure are used with a data fusion algorithm where prioritizing sensors with a higher magnitude of response along the frequency spectrum improves prediction accuracy. Using multiple sensors also improves robustness with reinforced process state predictions and reduces the risk of downtimes due to sensor failures. The algorithm is experimentally verified in milling tests.

Chapter 5: On-line Chatter Detection in Milling using Spindle and Feed Drive Motor Current Measurements

5.1 Overview

This chapter presents an on-line chatter detection method in milling using drive motor current commands supplied by the CNC system. The methodology is described by using the spindle drive motor current command although it has been applied to the feed drives as well which is demonstrated in the results section. The transfer function of spindle velocity controller is constructed by reading the control law parameters and measuring the Frequency Response Function (FRF) of the system automatically using an external computer communicating with the CNC in real time. By subtracting the rigid body based FRF from the measured FRF of the velocity controller that includes the flexibilities, the structural modes of the spindle drive are identified. The closed loop transfer function between the cutting torque at the tool and corresponding noise free digital current commanded by the CNC is formed. The effects of structural dynamic modes of the spindle are compensated via a proposed observer. The bandwidth of the compensated FRF of the current command over cutting torque disturbance has been increased to 2.5 kHz with 10 kHz communication speed limit of the CNC with external PC. After removing the forced vibration components, the frequency and presence of chatter are detected from the Fourier Spectrum of the current commands supplied by CNC in real time. The proposed system is experimentally validated in milling tests.

5.2 Spindle Drive System Identification

As in the feed drive system described in Chapter 3, the cutting forces at the tool tip are transmitted to the spindle motor as disturbance torque through the drive structure and servo amplifier. The total torque delivered to the spindle motor (τ_{mS}) is spent to overcome friction, inertial and cutting loads as given in Eq. (3.1);

$$\tau_{mS} = K_{tS} I_{actS} = J_{eS} \frac{d\Omega_S}{dt} + \tau_{fS} + \tau_{cS} \tag{5.1}$$

where Ω_S is the angular velocity of the spindle shaft, J_{eS} is the equivalent inertia of the spindle structure, τ_{cS} is the cutting and τ_{fS} is the friction torque which is identified using the Coulomb Friction model for the spindle drive since it often operates with a constant velocity during cutting operation;

$$\tau_{fS} = \tau_{coulomb-S} + B_e \Omega_S \tag{5.2}$$

The Coulomb friction ($\tau_{coulomb-S}$) and viscous friction coefficient (B_e) are identified by conducting series of tests at steady state speeds while measuring the current, and the inertia (J_{eS}) is estimated from the step response of the velocity changes as described in [1] and [55]. The identified mechanical transfer function parameters of the spindle drive are given in Table 5.1.

Table 5.1: Induction motor parameters of the spindle drive (1st Speed Range = 0-3300 rev/min, 2nd Speed Range = 3300-24000 rev/min). Identified mechanical parameters: $J_{eS} = 0.0316[\text{kg.m}^2]$, $B_{eS} = 0.009[\text{Nm/(rad/s)}]$, $K_{tS} = 1.343[\text{Nm/A}]$ for the 1st and $K_{tS} = 1.571[\text{Nm/A}]$ for the 2nd Speed Ranges. (# of poles (P) = 2)

	1st Speed Range (0-3300 rev/min)	Wye-Delta Starter	2nd Speed Range (3300-24000 rev/min)
R_S (Stator Resistance)	0.156		0.156
R_r (Rotor Resistance)	0.135		0.135
X_S (Stator Leakage Reactance)	0.0042	$\leftarrow$ *YD Winding Switch* $\rightarrow$	0.00024
X_r (Rotor Leakage Reactance)	0.0041		0.00024
X_m (Motor Magnetizing Reactance)	0.0213		0.0127
Nominal Frequency (Hz)	100		100

The friction and inertial loads are separated from the motor torque measurements to predict the cutting torque for the spindle drive. However; the cutting forces are distorted by the structural dynamics of the spindle (or feed) drive system as they are transmitted to the motor's current amplifier as a disturbance torque. The motor torque is proportional to the actual current (I_{actS}) supplied to the motor where K_{tS} is the torque constant. While the actual (I_{act}) and nominal command current (I_{nom}) can be assumed to be the same for permanent magnet DC servo motors used in feed drives within the current loop bandwidth which leads to a speed independent constant value for K_t, the actual current is both speed and disturbance load dependent for induction motors used on spindle drives. Hence, the transfer function between the actual and commanded nominal current needs to be derived as a function of winding and speed for induction motors in order to estimate the disturbance torque. The spindle drive's transfer function is modeled to predict the chatter from motor current as follows.

The five-axis Quaser UX-600 machining center is equipped with Weiss 176039 – V7 type spindle with an induction motor which has been used to validate the proposed chatter detection algorithm. The machine is controlled by Heidenhain iTNC 530 CNC. The velocity control block diagram of the spindle drive is given in Figure 5.1-a where both velocity (G_Ω) and current (G_I) controllers have a Proportional Integral (PI) structure whose gains are directly obtained from the CNC as;

$$G_\Omega = \frac{20s + 600}{s};\ G_I = \frac{3.1s + 1010}{s} \tag{5.3}$$

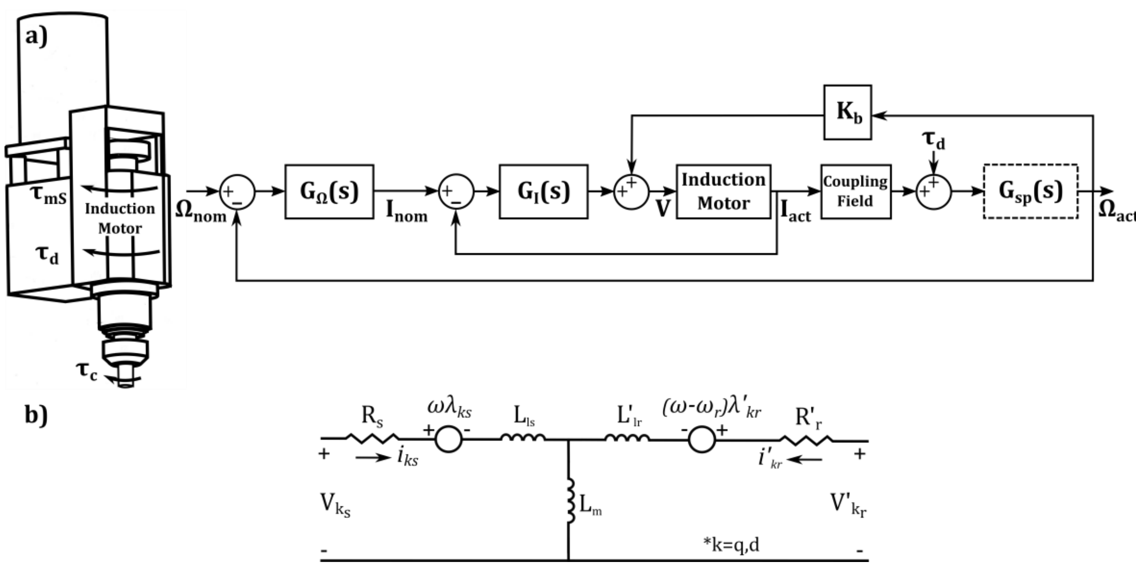

Figure 5.1: a) Block diagram of the spindle control loop (G_Ω = Velocity Controller, Ω_{nom} = Nominal Velocity, Ω_{act} = Actual Velocity, G_I = Current Controller, I_{nom} = Nominal Current, I_{act} = Actual Current, K_b = Back emf constant = 0.12 V/rad/s. G_{sp} = Spindle Drive), b) Induction motor equivalent circuit (3 phase symmetrical, $k = q, d, 0$), Slip = difference between synchronous and operating speed: $S = (n_s - n_r)/n_s$ where n_s is stator electrical and n_r is rotor mechanical speed, ($X = \omega L$ [86])

The closed loop transfer function of the current loop is derived from the winding parameters of the induction motor of the spindle. The equivalent circuit of the induction motor is given in Figure 5.1-b with the winding parameters specified by the manufacturer as listed in Table 5.1.

The derivation of voltage equations in arbitrary reference frame for a 3-phase symmetrical induction motor are given in [86] and summarized as follows;

$$
\begin{aligned}
&V_{qs} = R_s i_{qs} + \frac{\omega_a}{\omega_b}\psi_{ds} + \frac{1}{\omega_b}\frac{d\psi_{qs}}{dt} = R_s i_{qs} + \frac{\omega_a}{\omega_b}\left[X_{ss} i_{ds} + X_M i^{'}_{dr}\right] \\
&+\frac{1}{\omega_b}\frac{d}{dt}\left[X_{ss} i_{qs} + X_M i^{'}_{qr}\right] \\
&V_{ds} = R_s i_{ds} - \frac{\omega_a}{\omega_b}\psi_{qs} + \frac{1}{\omega_b}\frac{d\psi_{ds}}{dt} = R_s i_{ds} - \frac{\omega_a}{\omega_b}\left[X_{ss} i_{qs} + X_M i^{'}_{qr}\right] \\
&+\frac{1}{\omega_b}\frac{d}{dt}\left[X_{ss} i_{ds} + X_M i^{'}_{dr}\right] \\
&V_{0s} = R_s i_{0s} + \frac{1}{\omega_b}\frac{d\psi_{0s}}{dt} = R_s i_{0s} + \frac{1}{\omega_b}\frac{d}{dt} X_s i_{0s} \\
&V^{'}_{qr} = R^{'}_r i^{'}_{qr} + (\frac{\omega_a-\omega_r}{\omega_b})\psi^{'}_{dr} + \frac{1}{\omega_b}\frac{d\psi^{'}_{qr}}{dt} = R^{'}_r i^{'}_{qr} + (\frac{\omega_a-\omega_r}{\omega_b})\left[X^{'}_{rr} i^{'}_{dr} + X_M i_{ds}\right] \\
&+\frac{1}{\omega_b}\frac{d}{dt}\left[X^{'}_{rr} i^{'}_{qr} + X_M i_{qs}\right] \\
&V^{'}_{dr} = R^{'}_r i^{'}_{dr} - (\frac{\omega_a-\omega_r}{\omega_b})\psi^{'}_{qr} + \frac{1}{\omega_b}\frac{d\psi^{'}_{dr}}{dt} = R^{'}_r i^{'}_{dr} - (\frac{\omega_a-\omega_r}{\omega_b})\left[X^{'}_{rr} i^{'}_{qr} + X_M i_{qs}\right] \\
&+\frac{1}{\omega_b}\frac{d}{dt}\left[X^{'}_{rr} i^{'}_{dr} + X_M i_{ds}\right] \\
&V^{'}_{0r} = R^{'}_r i^{'}_{0r} + \frac{1}{\omega_b}\frac{d\psi^{'}_{0r}}{dt} = R^{'}_r i^{'}_{0r} + \frac{1}{\omega_b}\frac{d}{dt} X^{'}_r i^{'}_{0r}
\end{aligned}
\tag{5.4}
$$

where $X_{ss} = X_s + X_M$ and $X^{'}_{rr} = X^{'}_r + X_M$. The angular velocity of the arbitrary reference frame and base electrical frame are ω_a and ω_b, respectively, and ψ terms are the flux linkages per second as a function of 3-phase current terms ($i_{(q,d,s)}$) [86]. $i^{'}_{(q,d,0)r}$, $V^{'}_{(q,d,0)r}$, $\psi^{'}_{(q,d,0)r}$ terms are the rotor variables referred to the stator windings by the turn ratios of the rotor N_r and stator N_s components as;

$$i'_{(q,d,0)r} = {N_r}/{N_s}\, i_{(q,d,0)r}\ ; V'_{(q,d,0)r} = {N_r}/{N_s}\, V_{(q,d,0)r}\ ; \psi'_{(q,d,0)r} = {N_r}/{N_s}\, \psi_{(q,d,0)r} \tag{5.5}$$

Electromagnetic torque generated by the induction motor is derived from the energy stored in the coupling field in machine frame [86] which can be expressed in term of d-q phase currents as;

$$T_e = (\frac{3P}{4})(\frac{X_M}{\omega_b})(i_{qs}i'_{dr} - i_{ds}i'_{qr}) \tag{5.6}$$

As shown in Eq. (5.6), unlike in permanent magnet dc servo motor, the torque is not proportional to current for induction motors but it is a function of both the speed and the amount of field load [86]. However; when the induction motor is driven using field-oriented control (as in iTNC 530), the flux linkage and torque components of current are aligned along the orthogonal d (direct) and q (quadrature) axes, respectively [86]. This orthogonal alignment enables dynamic torque response given that the flux linkage is not affected when the torque is controlled by q-axis current. Hence, the induction motor behaves similar to a DC motor for certain speed and load ranges provided that the parameters are calibrated for each range from the energy stored in the coupling field in machine frame as detailed in [55], [87], [88]. In this study, once the commanded current, hence the voltage input to the induction motor is known, d and q-axis components of the current are simulated, and the generated torque is calculated from the q-axis current component [86], [89]. It is observed that the relation between the q-axis current and the generated torque shows consistent characteristics within the first and second speed ranges which agrees with Heidenhain CNC's tabulated steady state induction motor torque parameters given in Table 5.1.

Due to highly non-linear nature of the induction motor system [86], and the couplings between the q and d frames, the analytical derivation of its transfer function is not a trivial task without considerable assumptions [89]. Therefore, a time domain model of the induction motor has been constructed by implementing the governing motor Equations (5.4), (5.5) and (5.6) in MATLAB/Simulink® environment. The harmonic response of the motor current is simulated by inputting a sinusoidal voltage ($V(t)=\sin\omega t$) with a unit amplitude and obtaining the amplitude (I_a) and phase (ϕ) of the current as $I(t)=I_a\sin(\omega t-\phi)$ using the motor winding parameters given in Table 5.1. The frequency response function is obtained up to 2500 Hz which is the limit of the CNC's velocity loop Nyquist sampling frequency, and the following transfer functions are identified from the curve fitting simulations based on the induction motor model for two speed ranges as follows;

$$\begin{aligned}
\left.\frac{I_{act}(s)}{V(s)}\right._1 &= \frac{1}{1.658e-7s^2+0.002008s+0.7521};\ \text{Speed range 1} \\
&\in \text{(1-3300) [rev/min]} \\
\left.\frac{I_{act}(s)}{V(s)}\right._2 &= \frac{1}{5.968e-8s^2+0.0003651s+0.2106};\ \text{Speed range 2} \\
&\in \text{(3300-24000) [rev/min]}
\end{aligned} \tag{5.7}$$

Since the current and velocity controller parameters are obtained from the CNC directly (Eq. (5.3)), having the induction motor's model enables us to calculate the open and closed current loop transfer functions from simulations. The aim of having this model and calculating the current loop transfer functions is to leave the spindle drive's transfer function ($G_{sp}(s)$) as the only unknown in the system (Figure 5.1-a), and identify it ($G_{sp}(s)$) from the open velocity loop (Eq. (5.9)) FRF measurement (Figure 5.3-a) as described in this section. After this is achieved, the transfer function between the disturbance torque (τ_d) and the commanded current (I_{nom}) (Eq. (5.12)) can be calculated which is then used for compensating the dynamical distortions in the commanded current signal with the proposed observer for robust chatter detection.

For the CNC systems where the system identification toolbox allows; the induction motor's transfer function can also be identified from open or close loop current FRF measurements to avoid modeling the induction motor. However; some induction motors have multiple speed ranges and it is not always possible to measure the current loop FRF for each speed range depending on the CNC installed on the machine tool. Therefore, once the induction motor is modeled, after identifying the spindle drive's transfer function $G_{sp}(s)$; open/closed loop current FRF, hence the open/closed loop velocity and finally the disturbance FRF for each speed range can be obtained to be used for chatter detection as described in the following sections. The procedure is described step by step as follows;

First, by combining the transfer functions of the controller Eq. (5.3) and the motor circuit Eq. (5.7), the closed loop transfer function of the current controller for two speed ranges ($G_{m-1,2}(s)$) are evaluated as follows;

$$
\begin{aligned}
G_{m-1}(s) &= \frac{I_{act}(s)}{I_{nom}(s)_1} = \frac{0.0093s^2 + 3.185s + 50.5}{4.973e-10\,s^4 + 6.033e-6\ s^3 + 0.01166s^2 + 3.38s + 50.5} \\
G_{m-2}(s) &= \frac{I_{act}(s)}{I_{nom}(s)_2} = \frac{0.0093s^2 + 3.185s + 50.5}{1.79e-10\,s^4 + 1.098e-6\ s^3 + 0.00995s^2 + 3.353s + 50.5}
\end{aligned}
\tag{5.8}
$$

The FRF of the closed current loop is simulated and compared with the experimental measurements collected from Heidenhain CNC (TNCOpt®) system identification tool box through sine sweep tests for both speed ranges, see Figure 5.2. The test was conducted at zero speed for range 1, and at 4000 (rev/min) for the second speed range.

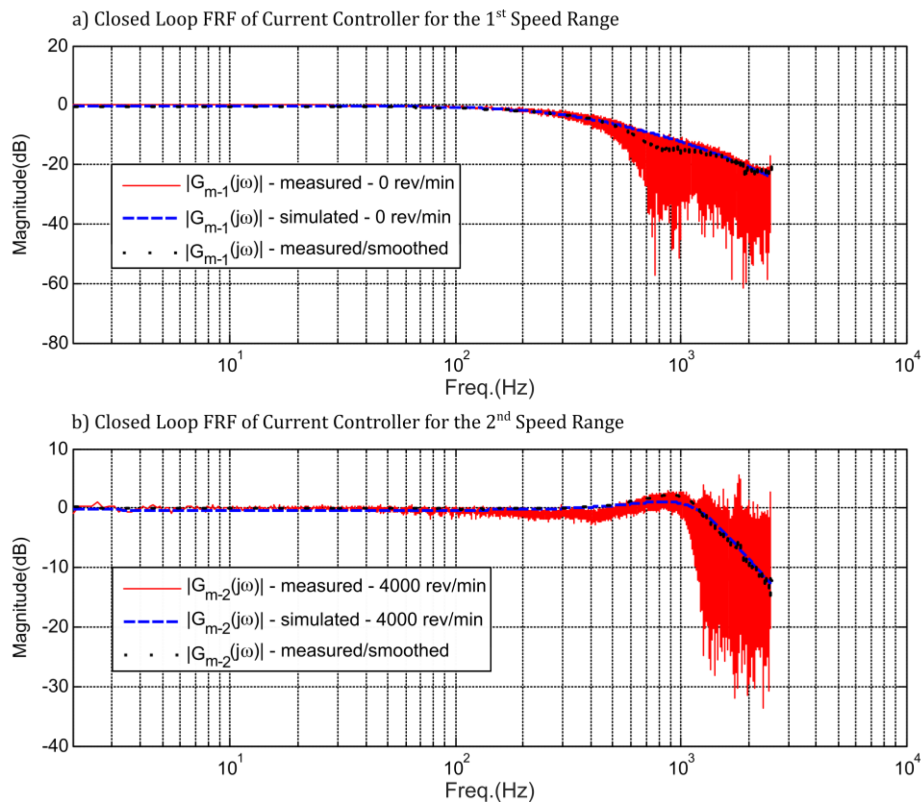

Figure 5.2: a) Simulated and Measured FRF of Closed Loop Current Controller for the 1st Speed Range (Bandwidth – Measured=385 Hz, Simulated=360 Hz), b) for the 2nd Speed Range (Bandwidth – Measured=1190 Hz, Simulated=1240 Hz)

The open loop transfer function (Figure 5.1-a) of the spindle's velocity controller ($G_{o\Omega}(s)$) is constructed from Equations (5.1), (5.3) and (5.8) as;

$$G_{o\Omega}(s) = \frac{\Omega_{act}(s)}{\Omega_{nom}(s)} = G_{\Omega}(s).G_m(s).K_t.G_{sp}(s) \tag{5.9}$$

where the spindle's mechanical transfer function is assumed to be rigid body from Eq. (5.1), i.e. $G_{sp}(s) = 1/(J_e\, s + B_e)$ initially. The FRF of the simulated and measured open velocity loop controller are given for the first speed range in Figure 5.3-a. The second speed range exhibits a similar behavior (see Appendix D).

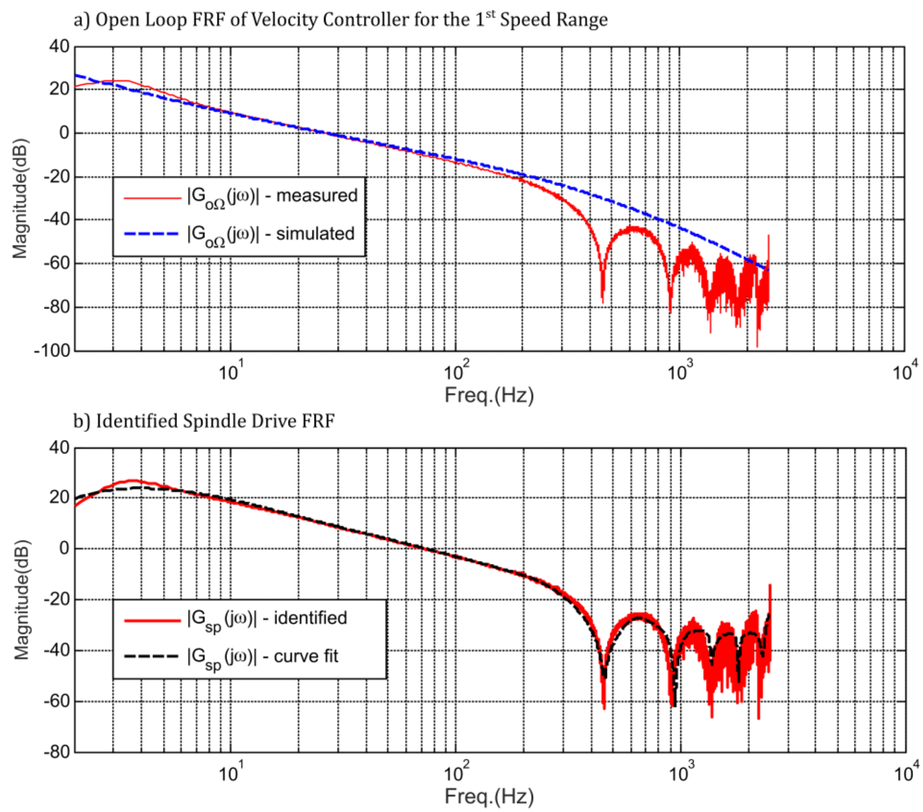

Figure 5.3: a) Simulated and measured FRF of open loop velocity controller for the 1st Speed Range, b) Identified and curve fitted spindle drive FRF

Discrepancy between the initial simulation and the measured FRF (Figure 5.3-a) after about 300 Hz is due to the structural dynamic modes of the spindle assembly. The simulated FRF of the open loop velocity controller given in Eq. (5.9) is subtracted from the measured one to isolate the contributions of the structural modes. The remaining FRF is identified by a modal curve fitting technique (using CutPro® Modal Analysis [81]), which leads to the following transfer function as in Chapter 3;

$$G_{sp}(s) = \frac{\Omega_{act}(s)}{\tau_m(s)} = \sum_k \frac{\alpha_k + \beta_k s}{s^2 + 2\zeta_k \omega_{nk} s + \omega_{nk}^2} \tag{5.10}$$

where α_k & $\beta_k, \varsigma_k, \omega_{nk}$ are the residues, damping and natural frequency of mode k, respectively (see Appendix E). Since every transfer function in the block diagram is known accurately at this point, the FRF of the closed velocity loop controller ($G_{c\Omega}(s)$) is calculated and compared with the measurement as a validation (Figure 5.4);

$$G_{c\Omega}(s) = \frac{\Omega_{act}(s)}{\Omega_{nom}(s)} = \frac{G_{\Omega}(s).G_m(s).K_t.G_{sp}(s)}{1+G_{\Omega}(s).G_m(s).K_t.G_{sp}(s)} \tag{5.11}$$

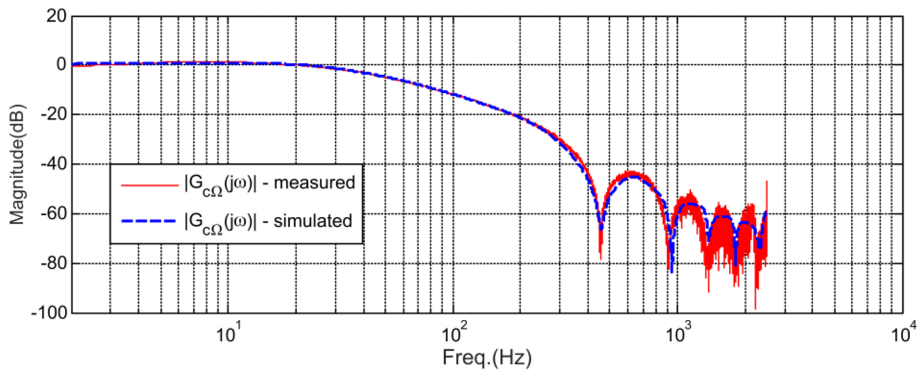

Figure 5.4: Simulated and measured FRF of closed loop velocity controller for the 1st speed range (bandwidth – measured = 38 Hz, simulated = 34 Hz)

The transfer functions between the disturbance torque (τ_d) and the nominal current (I_{nom}) as well as the actual velocity measured from encoder (Ω_{act}) are evaluated as;

$$G_{d\tau}(s) = \frac{I_{nom}(s)}{\tau_d(s)} = \frac{G_{sp}(s).G_{\Omega}(s)}{1+G_{\Omega}(s).G_m(s).K_t.G_{sp}(s)} \tag{5.12}$$

$$G_{d\Omega}(s) = \frac{\Omega_{act}(s)}{\tau_d(s)} = \frac{G_{sp}(s)}{1+G_{\Omega}(s).G_m(s).K_t.G_{sp}(s)} \tag{5.13}$$

and simulated as shown in Figure 5.5. The current command (I_{nom}) or the actual velocity measurement (Ω_{act}) can be both used to detect the presence of chatter.

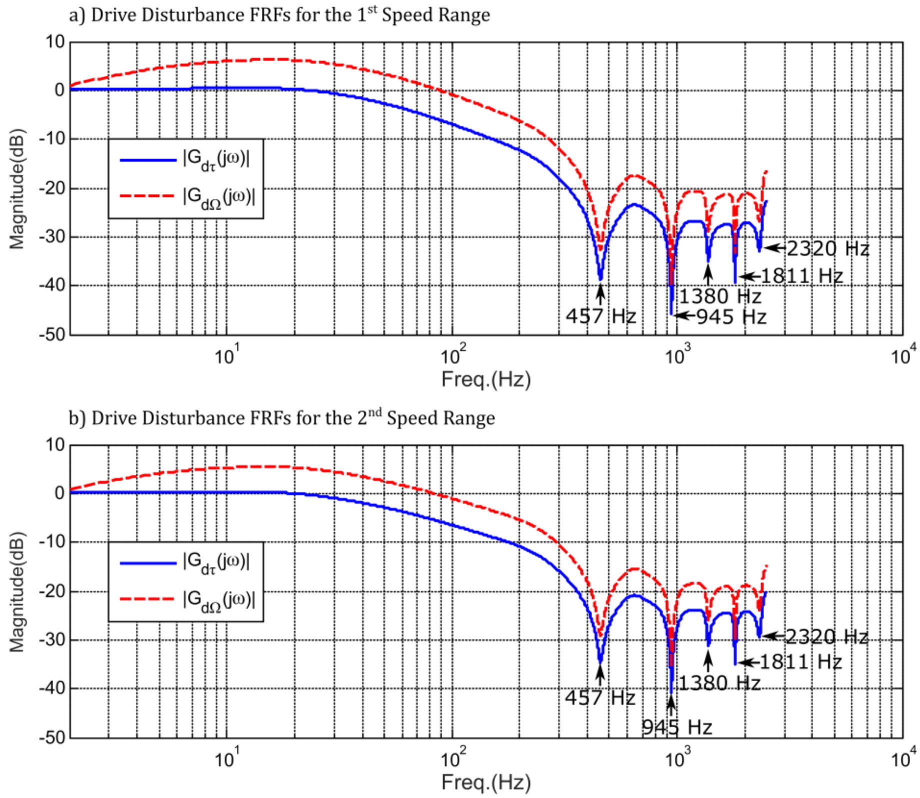

Figure 5.5: a) Nominal current (I_{nom}) / Disturbance torque (τ_d) - ($G_{d\tau}(s) = I_{nom}(s)/\tau_d(s)$) and Actual velocity (Ω_{act}) / Disturbance torque (τ_d) – ($G_{d\Omega}(s) = \Omega_{act}(s)/\tau_d(s)$) FRFs for the 1st and b) for the 2nd Speed Range

For verification purposes, the disturbance transfer function identified with the sine-sweep measurements (Eq. (5.12)) is validated through modal tap tests by applying torque from the tool tip with an instrumented hammer (τ_d - disturbance input) and measuring the commanded current (I_{nom}) from the spindle drive which is shown in Figure 5.6.

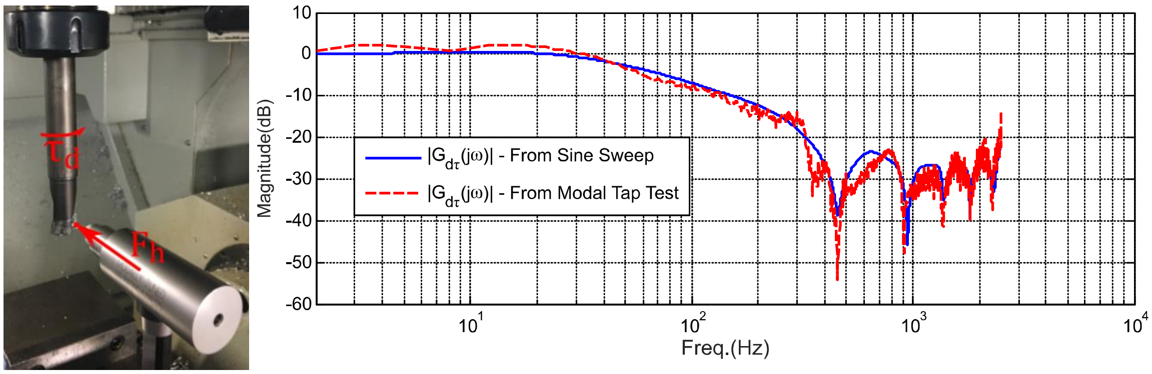

Figure 5.6: Verification of the simulated disturbance TF ($G_{d\tau}(s) = I_{nom}(s)/\tau_d(s)$) through Modal Tap Test

Modal tap test is performed within the 1st speed range (0 rev/min) since it is practically not possible to apply a torque input to the system with the instrumented hammed when the spindle is rotating. Impact is applied tangent to the periphery of the tool, and input torque is calculated by multiplying the impact force with the tool radius.

In addition, although this chapter solely focuses on the speed dependency of the drive disturbance transfer function due to induction motor dynamics (Y-D winding switch at 3300 rev/min due to wye(Y)-delta(D) starter mechanism), it should also be noted that the structural dynamics of the spindle system may change as a function of speed, load and thermal expansion as reported in [30] (see Chapter 4 in this thesis). Postel et al. [31] also recently presented a method to update the spindle's structural dynamics by detecting the changes in the natural frequency by monitoring vibrations during machining.

5.3 Dynamic compensation of Spindle Drive Current Measurements

The cutting forces are transmitted to the spindle drive motor as disturbance torque through the drive's structural chain and servo amplifier as shown in Figure 5.1-a. As described earlier in Chapter 3, in milling, the cutting forces are periodic at tooth passing frequency, which is equal to spindle speed times number of teeth on the cutter. Therefore, the bandwidth of the disturbance transfer function between the cutting force and drive motor current (or actual velocity signal) must be high enough to capture the frequency content of the milling forces and the chatter vibrations from the motor current. A state observer has been designed to reduce the influence of the amplifier and structural dynamic modes which distort the measurements containing frequencies above the bandwidth of the current amplifier which is about 380Hz in this study.

The state space representation of Eq. (5.12), the transfer function between the nominal current (I_{nom}) and disturbance torque (τ_d) can be expressed as;

$$\begin{aligned} \dot{\mathbf{x}}_{\mathbf{s}}(t) &= \mathbf{A}_{\mathbf{s}}\mathbf{x}_{\mathbf{s}}(t) + \mathbf{B}_{\mathbf{s}}u_s(t) = \mathbf{A}_{\mathbf{s}}\mathbf{x}_{\mathbf{s}}(t) + \mathbf{B}_{\mathbf{s}}\tau_d(t) \\ y_s(t) &= I_{nom}(t) = \mathbf{C}_{\mathbf{s}}\mathbf{x}(t) + \mathbf{D}_{\mathbf{s}}u_s(t) \end{aligned} \tag{5.14}$$

where $\mathbf{x}_S\mathbf{(t)}$ and $y_S(t)$ are state and output vectors for the spindle drive disturbance transfer function, respectively. The state space model in continuous domain consists of the state $\mathbf{A}_S$, the input $\mathbf{B}_S$, the output $\mathbf{C}_S$ and the input transmission $\mathbf{D}_S$ matrices. System is then rewritten in a canonical form by changing the coordinates of the system matrices through a transformation matrix $\mathbf{T}_c$ (i.e. $\mathbf{x}_S \rightarrow \mathbf{T}_c\mathbf{x}_S$) were the disturbance torque (τ_d) to the system is modeled as another state as follows;

$$\mathbf{x}_{\mathbf{exp_s}} = \begin{Bmatrix} \{\mathbf{x}_{\mathbf{s}}\} \\ \tau_d \end{Bmatrix} \tag{5.15}$$

and the expanded state space equation becomes;

$$\begin{aligned} \dot{\mathbf{x}}_{\mathbf{exp_s}}(t) &= \underbrace{\begin{bmatrix} \mathbf{A}_{\mathbf{sn}} & \mathbf{B}_{\mathbf{sn}} \\ 0 & 0 \end{bmatrix}}_{\mathbf{A}_{\mathbf{exps}}} \underbrace{\begin{Bmatrix} \{\mathbf{x}_{\mathbf{s}}\} \\ \tau_d \end{Bmatrix}}_{\mathbf{x}_{\mathbf{exps}}} + \underbrace{\begin{bmatrix} 0 \\ 1 \end{bmatrix}}_{\mathbf{\Gamma}_{\mathbf{s}}} w_s\ (t) \\ I_{nom} &= \underbrace{[\mathbf{C}_{\mathbf{sn}} \quad 0]}_{\mathbf{C}_{\mathbf{exps}}} \underbrace{\begin{Bmatrix} \{\mathbf{x}_{\mathbf{s}}\} \\ \tau_d \end{Bmatrix}}_{\mathbf{x}_{\mathbf{exps}}} + v_s(t) \end{aligned} \tag{5.16}$$

where the disturbance torque is a state of the system and the current command depends on the system dynamics and the noise characteristics as in Eq. (3.23) (Chapter 3). For the purpose of chatter detection from spindle drive current command measurements, a discrete state observer is designed in the following Luenberger form [90];

$$\begin{aligned} \hat{\mathbf{x}}_{\mathbf{exps}}(k+1) &= \mathbf{A}_{\mathbf{ds}}\hat{\mathbf{x}}_{\mathbf{exps}}(k) + \mathbf{L}_{\mathbf{ds}}(y_{\exp s}(k) - \hat{y}_{\exp s}(k)) \\ \hat{y}_{\exp s}(k) &= \hat{\tau}_d(k) = \mathbf{C}_{\mathbf{exps}}\hat{\mathbf{x}}_{\mathbf{exps}}(k) \end{aligned} \tag{5.17}$$

where $\hat{\mathbf{x}}_{\mathbf{exps}}(k)$ and $\hat{y}_{\exp s}(k)$ are the estimated state and output vectors, $\mathbf{L}_{\mathbf{ds}}$ is the discretized Luenberger observer gain. The observer error is expressed as;

$$\begin{aligned} \mathbf{e}_{\mathbf{s}}(k) &= \hat{\mathbf{x}}_{\mathbf{exps}}(k) - \mathbf{x}_{\mathbf{exps}}(k) \\ \mathbf{e}_{\mathbf{s}}(k+1) &= (\mathbf{A}_{\mathbf{ds}} - \mathbf{L}_{\mathbf{ds}}\mathbf{C}_{\mathbf{ds}})\mathbf{e}_{\mathbf{s}}(k) \end{aligned} \tag{5.18}$$

where $\mathbf{A}_{\mathbf{ds}}$ and $\mathbf{C}_{\mathbf{ds}}$ are the state and output matrices of the discrete observer, respectively. The estimation error converges to zero when eigenvalues of ($\mathbf{A}_{\mathbf{ds}} - \mathbf{L}_{\mathbf{ds}}\mathbf{C}_{\mathbf{ds}}$) lies within the unit circle [91].

An LQE (Linear Quadratic Estimator) algorithm is used to place the observer poles to achieve the desired performance by minimizing the state estimation error covariance matrix defined as;

$$\mathbf{P}_{\mathbf{s}} = E\left[\mathbf{e}_{\mathbf{s}} \quad \mathbf{e}_{\mathbf{s}}^{\mathbf{T}}\right] \tag{5.19}$$

where the differential equation for the covariance matrix $\mathbf{P}_{\mathbf{s}}$ is solved by the Ricatti Equation [82] and has to converge to zero for the optimal observer performance as in Eq. (3.28);

$$\begin{aligned} \dot{\mathbf{P}}_{\mathbf{s}}(\mathbf{t}\,|\,\mathbf{t}) = 0 = {} & \mathbf{A}_{\mathbf{exps}}(t)\mathbf{P}_{\mathbf{s}}(t\,|\,t) + \mathbf{P}_{\mathbf{s}}(t\,|\,t)\mathbf{A}_{\mathbf{exps}}^{\mathbf{T}}(t) \\ & + \mathbf{\Gamma}_{\mathbf{s}}(t)\mathbf{Q}_{\mathbf{s}}(t)\mathbf{\Gamma}_{\mathbf{s}}^{\mathbf{T}}(t) - \mathbf{P}_{\mathbf{s}}(t\,|\,t)\mathbf{C}_{\mathbf{exps}}^{\mathbf{T}}(t)\mathbf{R}_{\mathbf{spindle}}^{\mathbf{-1}}\mathbf{C}_{\mathbf{exps}}(t)\mathbf{P}_{\mathbf{s}}(t\,|\,t) \end{aligned} \tag{5.20}$$

where $\mathbf{R}_{\mathbf{spindle}}$ is the noise covariance matrix which is determined as the RMS of the spindle drive current command measurement and the observer gain vector is evaluated as;

$$\mathbf{L_{ds}} = \mathbf{P_s}\ \mathbf{C^T_{exps}}\ \mathbf{R^{-1}_{spindle}} \tag{5.21}$$

where the difference between the procedure shown in Chapter 3 lies in the identification of system ($\mathbf{Q_S}$) noise covariance matrix which is numerically calculated using the Nelder-Mead method [85] to achieve a desired bandwidth with minimum error for the compensated monitoring system with following constraints:

- Minimum root-mean-square error (e_{RMS}) between the compensated FRF and unit gain (0 dB)
- Minimum signal to noise ratio ($Power_{signal} / Power_{noise} > 10dB$)
- Maximum bandwidth achievable by ensuring the numerical stability of Linear Quadratic Estimator (LQE) without violating the remaining constraints ($-3dB < e_{RMS} < +3dB$)

The measurement noise covariance ($\mathbf{R_{spindle}}$) identified from the current and encoder signals, the system noise covariance matrix ($\mathbf{Q_S}$) calculated by Nelder-Mead searching algorithm [85], and the evaluated Luenberger observer gain vectors ($\mathbf{L_{ds}}$) for spindle drive disturbance transfer function are listed in Table 5.2.

Table 5.2: Measurement and system noise covariances with Luenberger observer gain vectors for 1st and 2nd Speed Ranges

	1st Speed Range	2nd Speed Range
$\mathbf{R_{spindle}}$	$[0.378]$	$[0.3711]$
$\mathbf{Q_S}$	$\left[diag\left\{20.10^3\right\}_{21x21}\right]$	$\left[diag\left\{18.10^3\right\}_{21x21}\right]$
$\mathbf{L_{ds}}$	$[-0.02, 0.19, 0.47, -1.96, -2.02, 5.1, 4.01,$ $-3.81, 2.15, -8.16, -1.88, 3.7, -0.26, 1.09,$ $1.97, -0.42, -0.94, -0.17, 0.11, 0.03, 7.29]$	$[-0.022, 0.176, 0.42, -1.75, -1.81, 4.33, 0.35,$ $-0.28, -0.68, -0.27, 0.73, 0.81, 0.24, -0.31,$ $-0.19, -0.01, 0.02, 0.005, -0.001, 0.02, 7.13]$

The signal to noise ratio constraint of the Nelder-Mead algorithm [85] can be tuned to accommodate the compensations and handle the disturbances, hence inaccuracies in the system identification phase. The overall structure of the system between the disturbance torque input (τ_d) and measured current output (I_{nom}) signals as well as the state observer which is used to obtain the estimated disturbance torque ($\hat{\tau}_d$) from the measured current output is given in Figure 5.7.

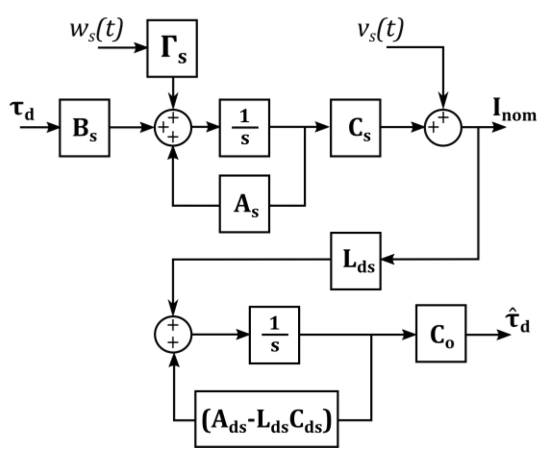

Figure 5.7: Schematic of the system and the state observer

The transfer function of the Luenberger state observer can be written as follows;

$$G_{L\tau} = \frac{\hat{\tau}_d}{I_{nom}} = C_s\left[sI - (A_{ds} - L_{ds}C_{ds})^{-1}\right]L_{ds} \tag{5.22}$$

where the transfer function of the compensated system (Figure 5.8) becomes the product of the uncompensated system given in Eq. (5.12) and the observer transfer function Eq. (5.22) as follows;

$$G_{c\tau}(s) = \frac{\hat{\tau}_d(s)}{\tau_d(s)} = \frac{I_{nom}(s)}{\tau_d(s)} \cdot \frac{\hat{\tau}_d(s)}{I_{nom}(s)} \tag{5.23}$$

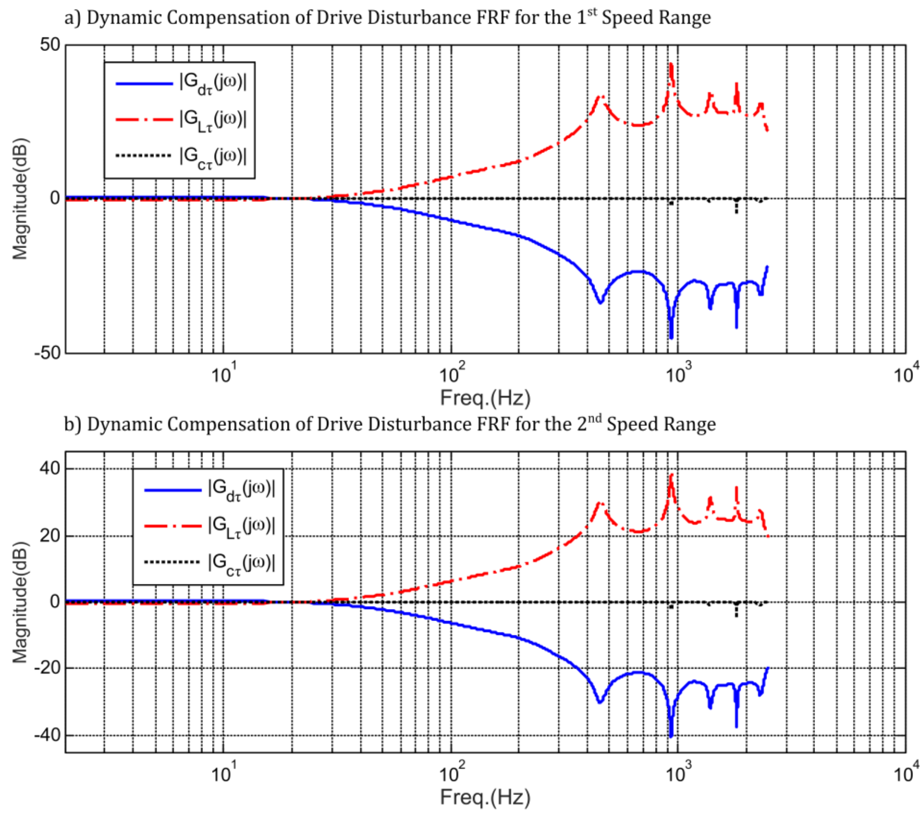

Figure 5.8: Dynamic compensation of spindle drive disturbance TF ($G_{d\tau}(s)$ - Eq. (5.12)): a) 1st Speed Range, b) 2nd Speed Range

As shown in Figure 5.8, the compensated FRF magnitude (Eq. (5.23)) approaches to unity and the bandwidth has been increased up to 2500 Hz which is the limit of the CNC's velocity loop Nyquist sampling frequency. Sampling time of the velocity control loop is 0.2 ms for the Heidenhain iTNC 530 used in this study, given that the sampling and the communication times can be lower for different CNCs, bandwidth of the proposed chatter detection system can be increased further.

Once the compensated current signals are obtained, they need to be evaluated on-line in order to decide whether the cutting operation is stable or not as described in the following section.

5.4 Detection of Chatter Frequency

If a regular pitch milling cutter with N number of teeth is used at Ω_{S-rs} (rev/sec) spindle speed, chatter free stable milling process will exhibit periodic forces and forced vibrations at tooth passing frequency ($\omega_t[Hz] = N\Omega_{S-rs}$) when there is no run-out. If the cutter has a variable pitch or run-out, the stable milling process becomes periodic at spindle frequency (Ω_{S-rs}). In order to generalize the detection algorithm for any milling tool, it is assumed that the chatter free milling process exhibits forced vibrations at the spindle's rotational frequency (Ω_{S-rs}) and its harmonics (l) which covers the tooth passing frequency (Figure 5.9).

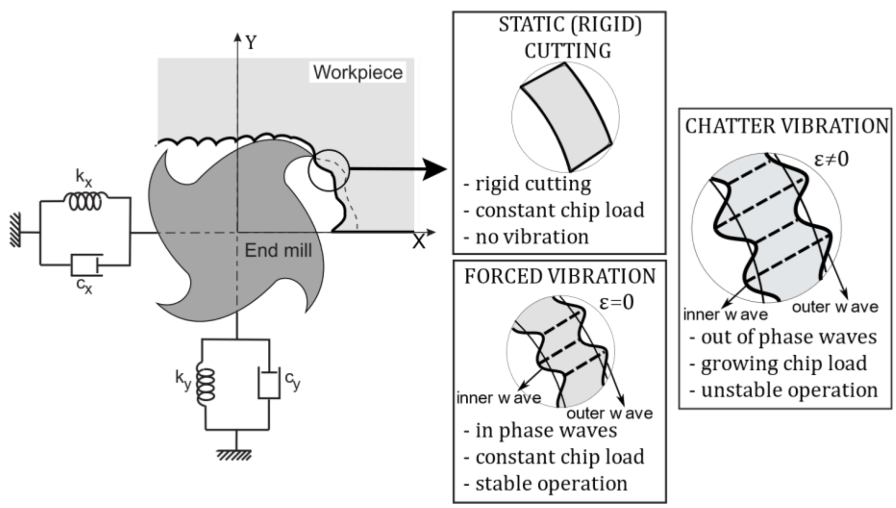

Figure 5.9: Flexibilities in the milling operation and cutting with rigid, forced and chatter vibration cases [51]

The frequency (ω_d) spectrum of the stable process will be dominated by the harmonics of spindle speed;

$$\omega_d = l\Omega_{S-rs} \ ; \ l \in \{1, 2, ...\} \tag{5.24}$$

Most commonly observed type of chatter vibrations are referred as Hopf Bifurcation in the literature [51], [52], [53]; when the process chatters at frequency ω_c, the frequency spectrum of forces and vibrations will have both periodic forced vibrations at spindle speed (Ω_{S-rs}) and its harmonics ($l\Omega_{S-rs}$), as well as the chatter frequency ω_c and at $\omega_c \pm l\Omega_{S-rs}$. The frequency spectrum of the unstable process will exhibit the following pattern;

$$\omega_d \in [l\Omega_{S-rs},\ (\omega_c \pm l\Omega_{S-rs})] \quad ; \quad l \in (1,2,..) \tag{5.25}$$

If the forced vibrations ($l\Omega_{S-rs}$) are removed from the frequency spectrum of the measured signals, the remaining spectra will be dominated by chatter only at frequencies ($\omega_c \pm l\Omega_{S-rs}$). The forced excitation is removed from the observer compensated disturbance torque measurement ($\hat{\tau}_d$) using the following comb filter in discrete time intervals (k);

$$G_{cb}(z) = \frac{\Delta\hat{\tau}_d(k)}{\hat{\tau}_d(k)} = \frac{\beta\left[1 - z^{-d}\right]}{1 - \alpha z^{-d}} \tag{5.26}$$

which is implemented in on-line monitoring as follows;

$$\Delta\hat{\tau}_d(k) = \alpha_{comb} \cdot \Delta\hat{\tau}_d(k-d) + \beta_{comb}\left[\hat{\tau}_d(k) - \hat{\tau}_d(k-d)\right] \tag{5.27}$$

where α_{comb} and β_{comb} are the bandwidth coefficients of the comb filter, and d is the integer number of samples collected in one spindle period. The filter coefficients are designed as follows;

$$\gamma = \frac{\sqrt{1 - |G_{cb}|^2}}{|G_{cb}|} \tan\frac{d\omega_{bw}}{4} \ ; \ \alpha_{comb} = \frac{2}{1+\gamma} - 1 ; \ \beta_{comb} = \frac{1}{1+\gamma} \tag{5.28}$$

where ω_{bw} is the desired normalized bandwidth with a quality factor of Q_{comb};

$$\omega_{bw} = \frac{2\pi.\left(\Omega_{S-rs} / \omega_{sampling}\right)}{Q_{comb}} \tag{5.29}$$

Q_{comb} is set to 10 and the gain of the filter is selected as $|G_{cb}| = 0.708 = -3dB$ at the sampling frequency ($\omega_{sampling}$) of 5000 Hz. These parameters must be selected in a way that the magnitude of the comb filter at the spindle frequency and its harmonics converges to zero not to distort the neighboring frequencies and miss critical information related to chatter. A sample comb filter designed to remove the spindle frequency and its harmonics from the frequency spectrum of the measured signal can be seen in Figure 5.10.

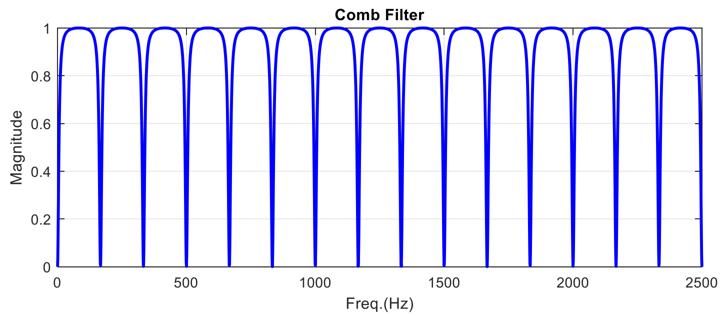

Figure 5.10: Comb filter designed to remove a spindle frequency of 166.67 Hz (10000 rev/min) and its harmonics

First, the estimated disturbance torque ($\hat{\tau}_d(n)$) is passed through the comb filter transfer function at each sampling interval n , as described in Eq. (5.26), followed by applying the Discrete Fourier transform (DFT) with a moving window as;

$$X(k\omega_r) = \frac{1}{N_{samples}} \sum_{n=0}^{N_{samples}-1} \Delta\hat{\tau}_d(n).e^{-jk\frac{2\pi}{N_{samples}}n} \quad ; \quad k = 0,1,2,..,\frac{N_{samples}}{2} \tag{5.30}$$

where $X(k\omega_r)$ is the discrete-time Fourier transform at frequency $k\omega_r$ with a frequency resolution of ω_r (rad/s) . The number of samples ($N_{samples}$) is selected as 4096 for the computational speed which corresponds to a frequency resolution of $\omega_r = 1.22$ Hz and the frequency content of the estimated and comb filtered disturbance torque is checked at every 0.1 second to monitor the occurrence of chatter vibrations. If the magnitude of the highest peak in the comb filtered DFT is higher than a certain predefined percentage (is set to 150% in this work) of the magnitude of the tooth passing frequency (ω_t) in the unfiltered signal then the cut is determined to have chatter, otherwise, it is stable.

5.5 Experimental Verification

5.5.1 Chatter Detection Experiments

The proposed chatter detection method from drive current measurements is experimentally validated on the same Quaser UX-600 CNC machining center where algorithms run on an external PC (Intel® Core™ i7-3.40 GHz CPU, 8 GB RAM). External PC can communicate with the Heidenhein iTNC 530 CNC via TNC Ethernet connection and the multi-threaded on-line code in C++ collects noise free digital spindle drive motor current command data at 5 or 10 kHz sampling frequency using the LSV-2 communication protocol.

The Aluminum 7050 workpiece material is milled at full immersion with regular pitch tools with different diameters and flute numbers (see Table 5.3).

Table 5.3: Tool, Tool Holder and Insert Specifications for the Cutters used in experiments

Tool #	Tool Diameter (mm)	Tool Stick Out Length (mm)	Tool Specification	Tool Holder	Holder Extension	Insert Type
1	50 5 teeth	NA	Sandvik CoroMill® R390-050Q22-11M	Sandvik® C4 – 391.05-22 025	Sandvik C5 – 391.02-40 085	R390 11T308E - NL
2	25 4 teeth	60	Sandvik CoroMill® R390-025A25-11L	Sandvik® C4 – 392.41014-63 40	NA	R390 11T308E - NL
3	20 4 teeth	80	Sandvik CoroMill® R390-020A20L-11L	Seco® E9304 5875 40120	NA	R390 11T308E - NL
4	10 2 teeth	60	Sandvik CoroMill® R216.32-10025-AK32A H10F	Sandvik® Hydro Grip 392.410CGA-63 20 088B	NA	NA

Tool tip FRF measurements in feed and normal directions as well as their corresponding stability diagrams are given in Figure 5.11 and Figure 5.12, respectively. If the spindle speed and axial depth of cut pair is selected above the stability curves shown in Figure 5.12, process will be unstable (chatter) whereas if it is under the stability curve, process will be stable (chatter free) [53].

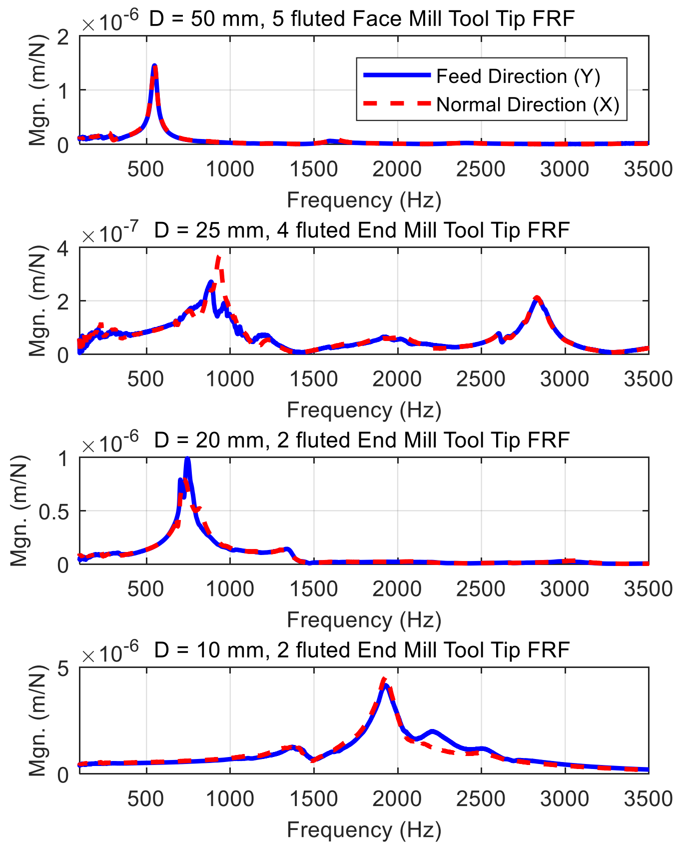

Figure 5.11: Tool tip FRFs of tools used for verification experiments

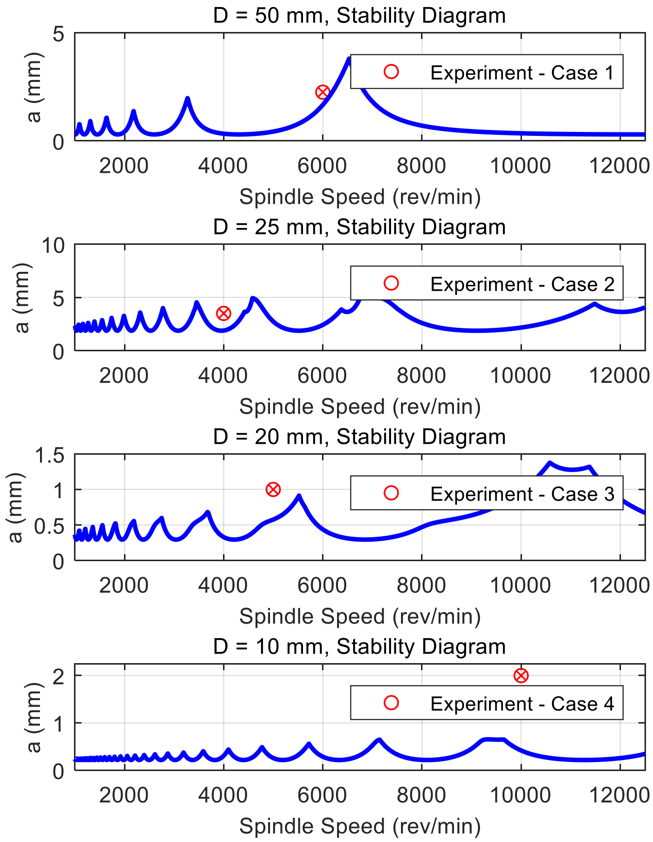

Figure 5.12: Corresponding stability diagrams for full radial immersion cases

The identified modal parameters of the tools are given in Table 5.4.

Table 5.4: Modal parameters in X (normal) and Y (feed) directions

			X Direction (Normal)			Y Direction (Feed)		
Tool #	Tool Diameter (mm)	#	ω_n(Hz)	ζ(%)	k(N/m)	ω_n(Hz)	ζ(%)	k(N/m)
1	50 5 teeth	1	282	5.3	5.9e7	300	1.1	6.6e7
		2	546	2.8	1.2e7	546	2.5	1.3e7
		3	1621	1.5	2.8e8	1607	2.9	2.9e8
2	25 4 teeth	1	871	4.2	1.7e8	821	4.5	6.9e7
		2	932	4.4	2.9e7	928	4.1	4.5e7
		3	1196	3.6	3.1e8	1169	4.3	1.6e8
		4	2003	9	1e8	1983	6.8	1.4e8
		5	2805	2.2	1.3e8	2812	1.9	1.4e8
3	20 4 teeth	1	717	3.5	1.3e7	734	3.6	2.5e6
		2	817	4.8	1.5e7	1026	0.3	3.3e7
		3	1364	1.8	2.9e7	1355	1.8	2.8e7
4	10 2 teeth	1	1413	2	2.1e7	1446	1.5	3.8e7
		2	1915	4.5	3e6	1924	3	5e6
		3	2400	5.9	1.9e7	2219	4.5	6.1e6
		4	2550	0.03	4.3e10	2540	3	3.6e7

Sound measurements collected with a cardioid SHURE® PG81 microphone are used as a reference to compare the results against CNC supplied current commands. Surface profiles generated at the cutting tests are measured with Mitutoyo® Surftest SV-500 to further validate the stable/unstable classification which are presented at the end of this chapter.

The presence of chatter is decided by monitoring the magnitude ratio of spectrums ($|\omega_c|/|\omega_t|$) at the chatter frequency (ω_c) and the tooth passing frequency (ω_t). In the following figures for experimental results, signals labeled with "DFT" stands for the Discrete Fourier Transformation of the corresponding signal mentioned in the figure title, and "Comb+DFT" stands for the comb filtered (Eq. (5.26)) DFT signal to show the frequency content after removing the spindle, tooth passing frequency and their harmonics. The variation of the magnitude ratio ($|\omega_c|/|\omega_t|$) before and after the dynamic compensation is listed in the tables to illustrate the outcome of the presented method.

First experiment is performed with a 5 fluted 50 mm diameter face mill where the spindle speed and axial depth of cut are selected as 6000 rev/min and 2.25 mm, respectively. The process is above the stability limit hence it chattered (see Figure 5.12 for the stability diagram and Figure 5.13 for the current and sound measurements).

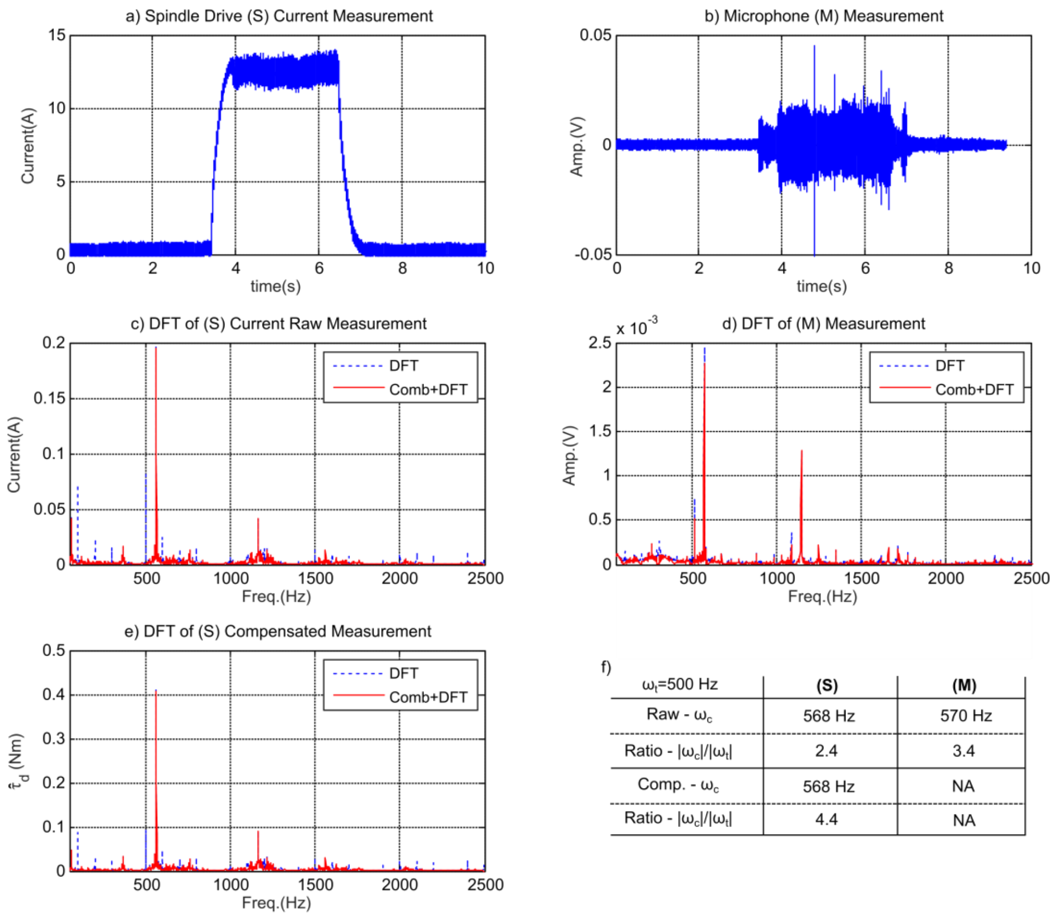

ω_t=500 Hz	(S)	(M)
Raw - ω_c	568 Hz	570 Hz
Ratio - $\lvert\omega_c\rvert/\lvert\omega_t\rvert$	2.4	3.4
Comp. - ω_c	568 Hz	NA
Ratio - $\lvert\omega_c\rvert/\lvert\omega_t\rvert$	4.4	NA

Figure 5.13: Chatter test with a 50 mm diameter 5 Fluted Face Mill (Tool #1) at spindle speed $\Omega_S = 6000$[rev/min] ,tooth passing frequency (ω_t) = 500 Hz, axial depth of cut = 2.25 mm, full immersion cut with feed rate of 0.1 mm/rev/tooth. Workpiece material Al7050; **a)** Spindle Drive Motor Current Command, **b)** Microphone Measurement, DFT and Comb Filtered DFT of; **c)** Spindle Current Raw Measurement, **d)** Microphone Measurement, **e)** Spindle Current Compensated Measurement (first 4096 samples of the cut), **f)** Identified chatter frequencies and $|\omega_c|/|\omega_t|$ ratio for raw and compensated Spindle Current command measurements compared with the Microphone

The chatter occurred at 570 Hz which is evident from both spindle motor current and microphone measurements as shown in Figure 5.13. However, the reduced magnitude of the current signals at higher frequencies can lead to false chatter detection as mentioned in [61]. The distortion of FRFs of the motor current by the structural dynamics of the spindle drive reduces the bandwidth of the sensing system unless they are compensated as proposed in this thesis. The chatter detection with the proposed compensation strategy is validated by conducting a cutting test with a 25 mm diameter 4 fluted end mill having a dominant mode around 930 Hz (see Figure 5.11). A full immersion milling test is conducted at 4000 rev/min spindle speed with 3.5 mm axial depth of cut, which corresponds to an unstable cutting condition (see Figure 5.14).

For this case, although the chatter frequency identified from drive measurements match with the microphone signal, the magnitude at the chatter frequency (935 Hz) is lower than magnitude at the tooth passing frequency (266.67 Hz) and its harmonics when the structural disturbance is not compensated from the current signals (Figure 5.14 – c&f). As a result, the chatter detection where the criteria is; $|\omega_c|/|\omega_t| > 1.5$ fails. This phenomenon does not exist on microphone signal which has a wide bandwidth ($\sim$ 18 kHz) and not distorted by the machine structure/servo drives (Figure 5.14 b&d). On the other hand, as described earlier in this chapter, the cutting torque is transmitted to the motor through the chain of spindle structure, current amplifier, motor winding and velocity/current servo loops. The disturbance FRF ($G_{d\tau}(j\omega)$) in between the nominal current (I_{nom}) and the disturbance torque (τ_d) is shown in Figure 5.5, where the current sensor system attenuates the transmitted torque to the current loop greatly at frequencies 457 Hz (-32 dB=0.025) , 945 Hz (-39 dB=0.0112), 1380 Hz (-31 dB=0.028), 1811 Hz (-35 dB=0.018) and 2320 Hz (-29 dB=0.035). As a result, the raw current command signals are highly distorted and give incorrect chatter detection by attenuating the signals at chatter frequency and amplifying them at the neighboring frequencies where the structure has natural modes, see Figure 5.11 and Table 5.4.

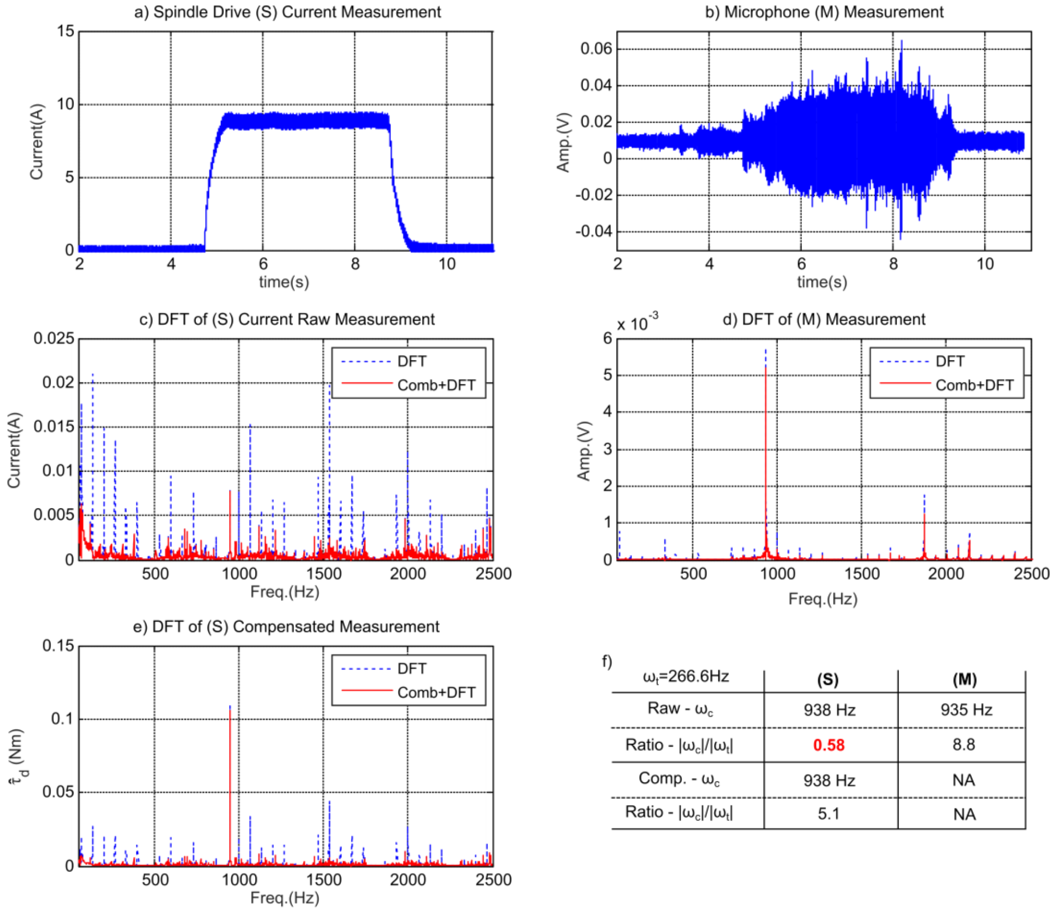

Figure 5.14: Chatter test with a 25 mm diameter 4 Fluted End Mill (Tool #2) at spindle speed $\Omega_S = 4000$[rev/min] ,tooth passing frequency (ω_t) = 266.67 Hz, axial depth of cut = 3.5 mm, full immersion cut with feed rate of 0.1 mm/rev/tooth. Workpiece material Al7050; **a)** Spindle Drive Motor Current Command, **b)** Microphone Measurement, DFT and Comb Filtered DFT of; **c)** Spindle Current Raw Measurement, **d)** Microphone Measurement, **e)** Spindle Current Compensated Measurement (first 4096 samples of the cut), **f)** Identified chatter frequencies and $|\omega_c|/|\omega_t|$ ratio for raw and compensated Spindle Current command measurements compared with the Microphone

However, when the structural, motor/servo dynamics are compensated and the forced vibrations are removed by comb filtering the spindle and tooth passing frequency harmonics, the amplitude at the chatter frequency (938 Hz) is corrected which becomes high as in the microphone measurement (Figure 5.14 – e&f).

Next, a 20 mm 2 fluted end mill is used where the chatter detection fails unless the current signals are compensated. Chatter occurs at 771 Hz, and the amplitude at the chatter frequency is less than the amplitude of forced vibrations at tooth passing frequency of 166.67 Hz when the current signals are not compensated, see Figure 5.15 – c&f. When the signals are compensated, the magnitude ratio of chatter over the tooth passing frequency becomes 6 (Figure 5.15 – e&f), hence the chatter is detected successfully.

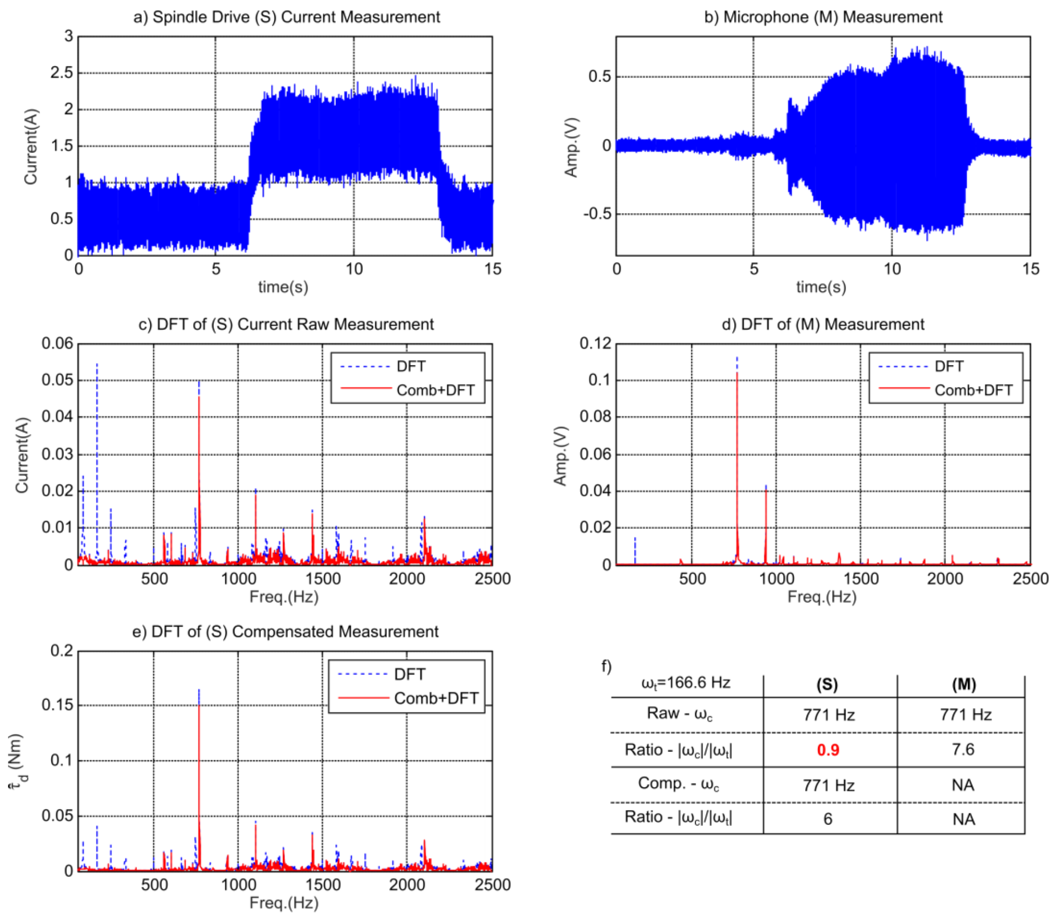

Figure 5.15: Chatter test with a 20 mm diameter 2 Fluted End Mill (Tool #3) at spindle speed $\Omega_S = 5000$[rev/min], tooth passing frequency (ω_t) = 166.67 Hz, axial depth of cut = 1 mm, full immersion cut with feed rate of 0.1 mm/rev/tooth. Workpiece material Al7050; **a)** Spindle Drive Motor Current Command, **b)** Microphone Measurement, DFT and Comb Filtered DFT of; **c)** Spindle Current Raw Measurement, **d)** Microphone

Measurement, **e)** Spindle Current Compensated Measurement (first 4096 samples of the cut), **f)** Identified chatter frequencies and $|\omega_c|/|\omega_t|$ ratio for raw and compensated Spindle Current command measurements compared with the Microphone

In the 3 cases presented so far, although the uncompensated spindle drive measurements failed to give a reliable magnitude ratio of ($|\omega_c|/|\omega_t|$), identified chatter frequencies are in an agreement with the microphone measurements since the frequency range of these experiments are still below 1-1.5 kHz. In order to show a case with higher frequency content, a 10 mm 2 fluted end mill is used where the dominant mode of the tool lies around 1920 Hz (Figure 5.11). For this case, raw current measurement from the spindle drive fails to give both the correct chatter frequency and the magnitude ratio due to the decaying magnitude behavior of the corresponding disturbance transfer function given in Eq. (5.22). The dynamic distortions on the raw spindle drive measurement are clearly evident in the results presented in Figure 5.16.

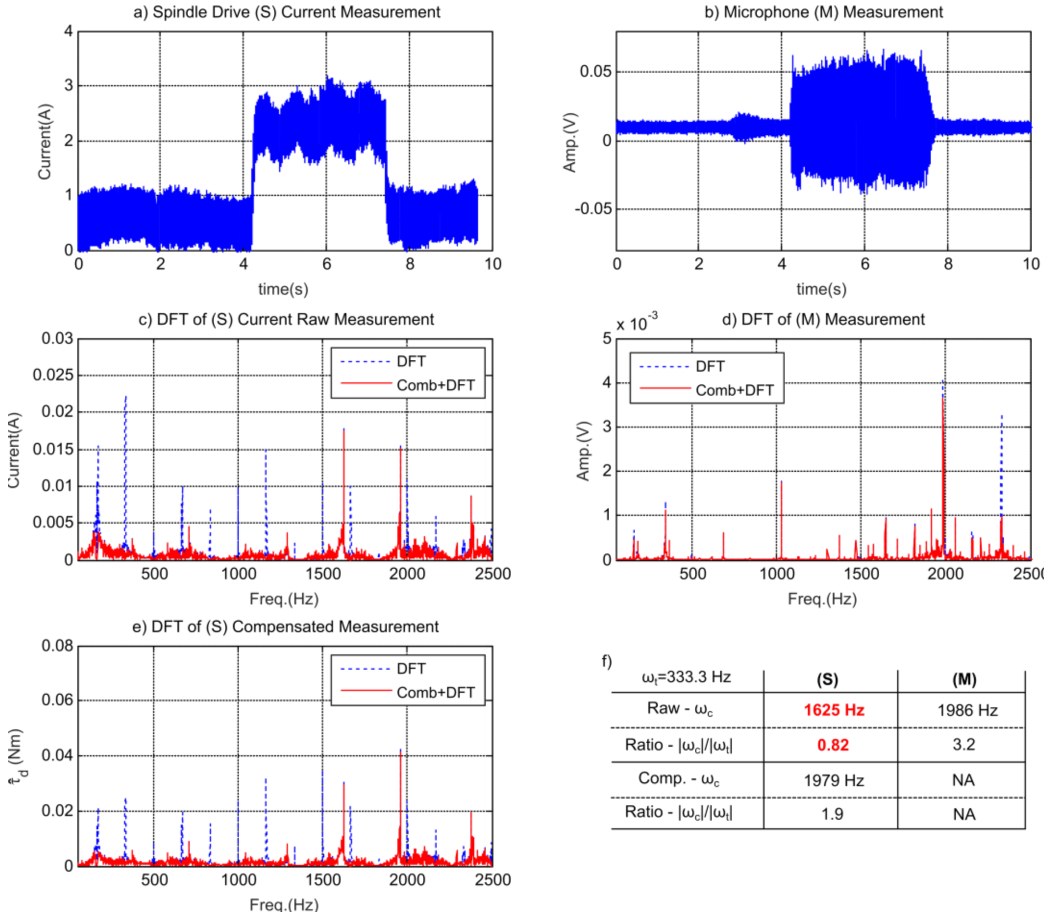

f)

ω_t=333.3 Hz	(S)	(M)
Raw - ω_c	1625 Hz	1986 Hz
Ratio - $\lvert\omega_c\rvert/\lvert\omega_t\rvert$	0.82	3.2
Comp. - ω_c	1979 Hz	NA
Ratio - $\lvert\omega_c\rvert/\lvert\omega_t\rvert$	1.9	NA

Figure 5.16: Chatter test with a 10 mm diameter 2 Fluted End Mill (Tool #4) at spindle speed $\Omega_S = 10000$[rev/min], tooth passing frequency (ω_t) = 333.33 Hz, axial depth of cut = 2 mm, full immersion cut with feed rate of 0.1 mm/rev/tooth. Workpiece material Al7050; **a)** Spindle Drive Motor Current Command, **b)** Microphone Measurement, DFT and Comb Filtered DFT of; **c)** Spindle Current Raw Measurement, **d)** Microphone Measurement, **e)** Spindle Current Compensated Measurement (first 4096 samples of the cut), **f)** Identified chatter frequencies and $|\omega_c|/|\omega_t|$ ratio for raw and compensated Spindle Current command measurements compared with the Microphone

The chatter frequency is identified incorrectly as 1625 Hz with an incorrect ratio of ($|\omega_c|/|\omega_t|$), see Figure 5.16 – c&f. However; after the compensation with the state observer, the peak in the comb filtered DFT occurs at the correct chatter frequency (1979 Hz, Figure 5.16 – e&f), which also agrees with the microphone measurement.

Although the methodology is presented by modeling the spindle drive current command in this chapter, the proposed chatter detection is applied to the feed drive by identifying the disturbance transfer function Eq. (5.12) as described in Chapter 3 and [1]. The bandwidth of the disturbance transfer function identified in Chapter 3 for the feed drive (Y axis) is increased from 200 Hz to 2.5 kHz for chatter detection purpose by using the Luenberger state observer. The chatter detection from feed drive current command is tested with the 2 fluted – 10 mm diameter end mill (see Figure 5.17). The raw current measurement from feed drive led to incorrect chatter frequency of 2292 Hz (Figure 5.17 – c&f), whereas the chatter frequency is correctly identified as 1979 Hz after the compensation with the proposed state observer (Figure 5.17 – e&f).

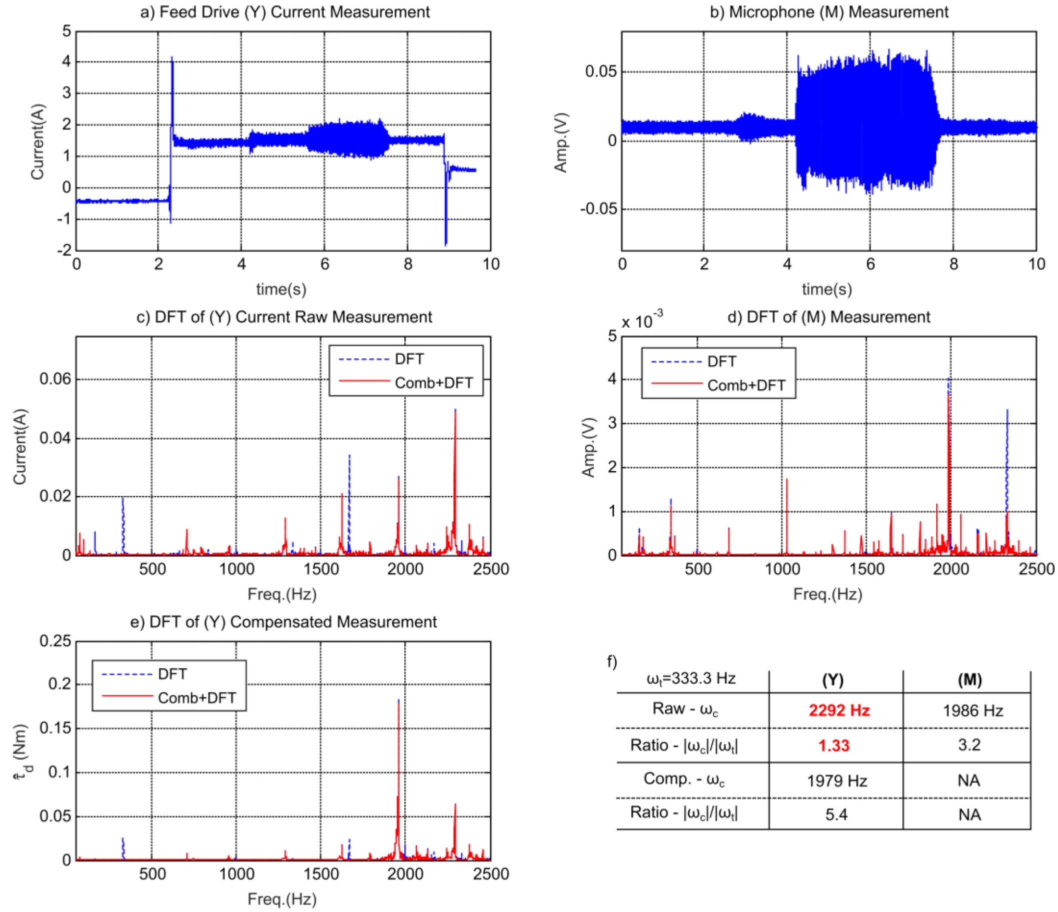

ω_t=333.3 Hz	(Y)	(M)
Raw - ω_c	2292 Hz	1986 Hz
Ratio - $\lvert\omega_c\rvert/\lvert\omega_t\rvert$	1.33	3.2
Comp. - ω_c	1979 Hz	NA
Ratio - $\lvert\omega_c\rvert/\lvert\omega_t\rvert$	5.4	NA

Figure 5.17: Chatter test with a 10 mm diameter, 2 Fluted End Mill (Tool #4) at spindle speed $\Omega_S = 10000$[rev/min], tooth passing frequency (ω_t) = 333.33 Hz, axial depth of cut = 2 mm, full immersion cut with feed rate of 0.1 mm/rev/tooth. Workpiece material Al7050; **a)** Feed Drive (Y axis) Motor Current Command, **b)** Microphone Measurement, <u>DFT and Comb Filtered DFT of;</u> **c)** Feed Drive Current Raw Measurement, **d)** Microphone Measurement, **e)** Feed Drive Current Compensated Measurement (first 4096 samples of the cut), **f)** Identified chatter frequencies and $|\omega_c|/|\omega_t|$ ratio for raw and compensated Feed Drive Current command measurements compared with the Microphone

For each case/tool with chatter vibrations presented so far, a stable cut is performed with a lower axial depth of cut to show the distinction between the unstable and stable cases and the corresponding measurements are given in Figure 5.18. It can be seen from the compensated measurements that the stable cutting conditions do not violate the chatter threshold set in this study

($|\omega_c|/|\omega_t| > 1.5$). Therefore, it can be concluded that the proposed methodology is able to distinguish stable cuts from unstable cases which prevents false alarms during the operation.

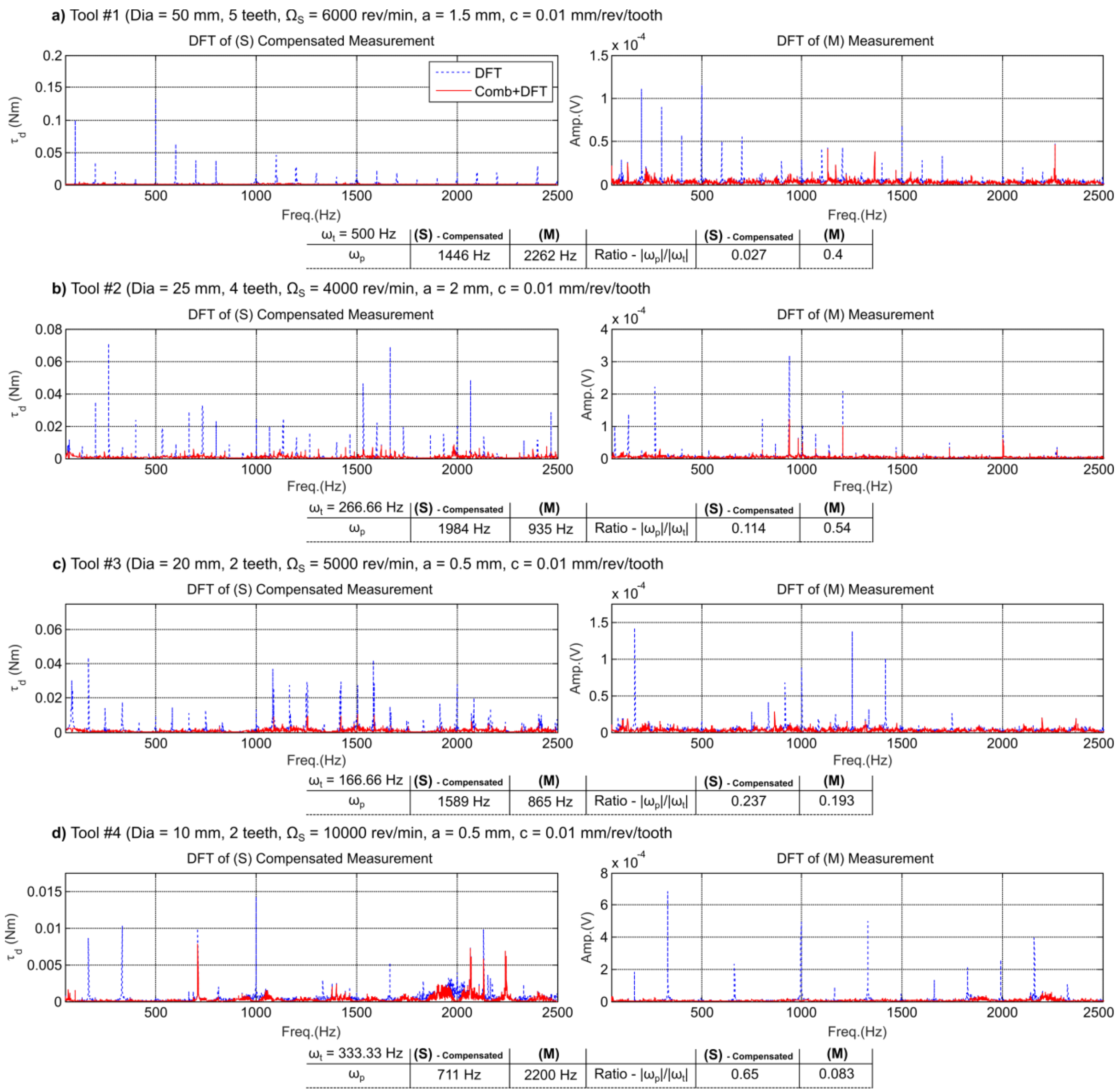

Figure 5.18: Stable cutting operations with the listed cutting conditions for a) Tool #1, b) Tool #2, c) Tool #3, d) Tool #4 (ω_p is the frequency with the highest magnitude in the comb filtered signal)

In addition, instead of relying solely on microphone signal for verification, surface profiles of stable and unstable cutting operations are measured as well which are given in Figure 5.19.

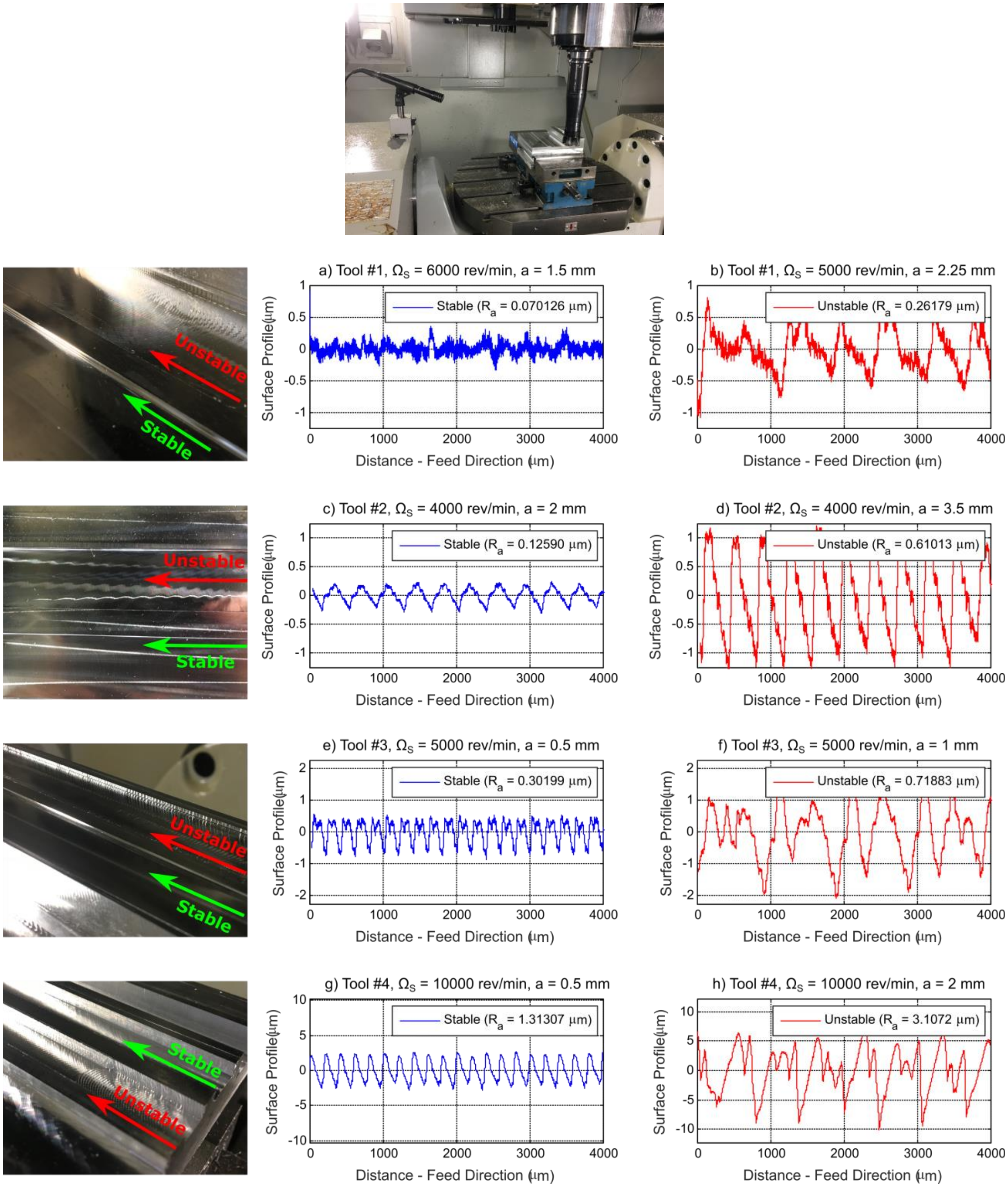

Figure 5.19: Experiment setup with surface profiles of stable and unstable cutting experiments presented throughout this chapter

The methodology presented in this study can be used as a foundation for other chatter detection algorithms or indicators (as in [58], [59], [61]) since the estimated disturbance torque from the drive current measurements contain sufficient and reliable information regarding the cutting process without interfering with the work envelope.

5.5.2 Resultant Force Prediction Experiments

Disturbance transfer function of the spindle drive can also be used to predict the tangential cutting force at the tool tip from the spindle drive current measurements in time domain for other process monitoring tasks. Relation between the estimated disturbance spindle torque ($\hat{\tau}_d$) and the tangential cutting force at the tool tip ($\hat{F}_t$) is as follows;

$$\hat{F}_t = \frac{\hat{\tau}_d}{r_{tool}} \tag{5.31}$$

where r_{tool} is the tool radius. Estimated disturbance spindle torque ($\hat{\tau}_d$) is identified at every sampling time as described in Section 5.3, which means tangential cutting force at the tool tip ($\hat{F}_t$) is also identified in-process. However; in most of the process monitoring and control applications, resultant forces in X-Y plane is used in order to incorporate forces both in tangential and radial directions in the analysis [5], [53].

Knowing the process geometry and physics of end milling operations [53], resultant force in X-Y plane can be estimated from the tangential force signal in an acceptable level for regular end mill tools. First, cutting forces in feed and tangential direction can be written as follows;

$$\begin{aligned} F_t &= K_{tc} ac \sin(\phi) + K_{te} a \\ F_r &= K_{rc} ac \sin(\phi) + K_{re} a \end{aligned} \tag{5.32}$$

where a is the axial depth of cut, c is the feed rate and ϕ is the instantaneous angle of immersion. K_{tc} and K_{rc} are the cutting force coefficients contributed by the shearing action in tangential and radial directions, respectively where K_{te} and K_{re} are the edge constants. These cutting coefficients are assumed to be constant for a tool-work material pair and they are usually evaluated either mechanistically from experiments or by using the orthogonal to oblique transformations as described in [92]. The resultant force in X-Y plane ($F_{\text{resultant}}$) can be written as follows;

$$F_{\text{resultant}} = \sqrt{F_x^2 + F_y^2} = \sqrt{F_t^2 + F_r^2} \tag{5.33}$$

For the scope of this study, edge forces are neglected for simplicity and K_{rc}, radial cutting force coefficient is assumed to be 50% of the tangential component, K_{tc} [53]. With these assumptions, resultant force given in Eq. (5.33) can be rewritten as;

$$\begin{aligned} F_{\text{resultant}} &= \sqrt{F_t^2 + F_r^2} = \sqrt{(K_{tc}ac\sin(\phi))^2 + (0.5K_{tc}ac\sin(\phi))^2} \\ &\cong 1.11F_t \end{aligned} \tag{5.34}$$

which means the resultant force in X-Y plane can be approximated from the tangential force component identified from the spindle drive current measurements as given in Eq. (5.31).

This method brings simplicity compared to using feed drive current measurements to identify the resultant force at the tool tip since it does not require extensive system identification experiments. As described in Chapter 3, forces at the tool tip can be predicted from feed drive measurements given that the friction and structural dynamics of each individual axes are modeled, and kinematics of the machine tool is solved accurately. The approach presented here which gives the resultant forces from spindle drive current measurement is less accurate because of certain assumptions made as listed above, however, it is very practical since the dynamics of the spindle drive are identified through automated sine sweeps and friction behavior is not crucial given that the spindle is rotating at a constant speed along the toolpath.

For verification of this method, first, the same 3-axis milling experiments presented in Chapter 3 are used where the work material is Aluminum 7050 and tool is a 20-mm diameter two-fluted end mill. Axial depth of cut is selected as 4 mm and it is a slot cutting operation with 0.2 mm/tooth feed rate. Spindle speeds are selected as 1000, 2000, 3000, 4000, 5000 and 5500 rev/min where the limiting factor was the 180-200 Hz bandwidth of the compensated feed drive dynamics. As it can be seen from the results presented in Figure 5.20, resultant forces identified from the compensated spindle drive current measurements match with the reference table dynamometer measurements with an acceptable accuracy where the mean error at the spindle and tooth passing frequencies are below 35% for all the cases. Specifically, mean errors were 15%, 18%, 32%, 19%, 27% and 24% respectively at the spindle speeds of 1000, 2000, 3000, 4000, 5000 and 5500 rev/min. Reference forces identified from raw spindle current measurements have a reducing magnitude behavior as the spindle speed, hence the tooth passing frequency which is the excitation frequency to the drive increases. This observation agrees with the measured disturbance FRF of the spindle drive as shown in Figure 5.5. Designed Luenberger observer is correcting this decaying magnitude behavior at every time step with its corresponding transfer function.

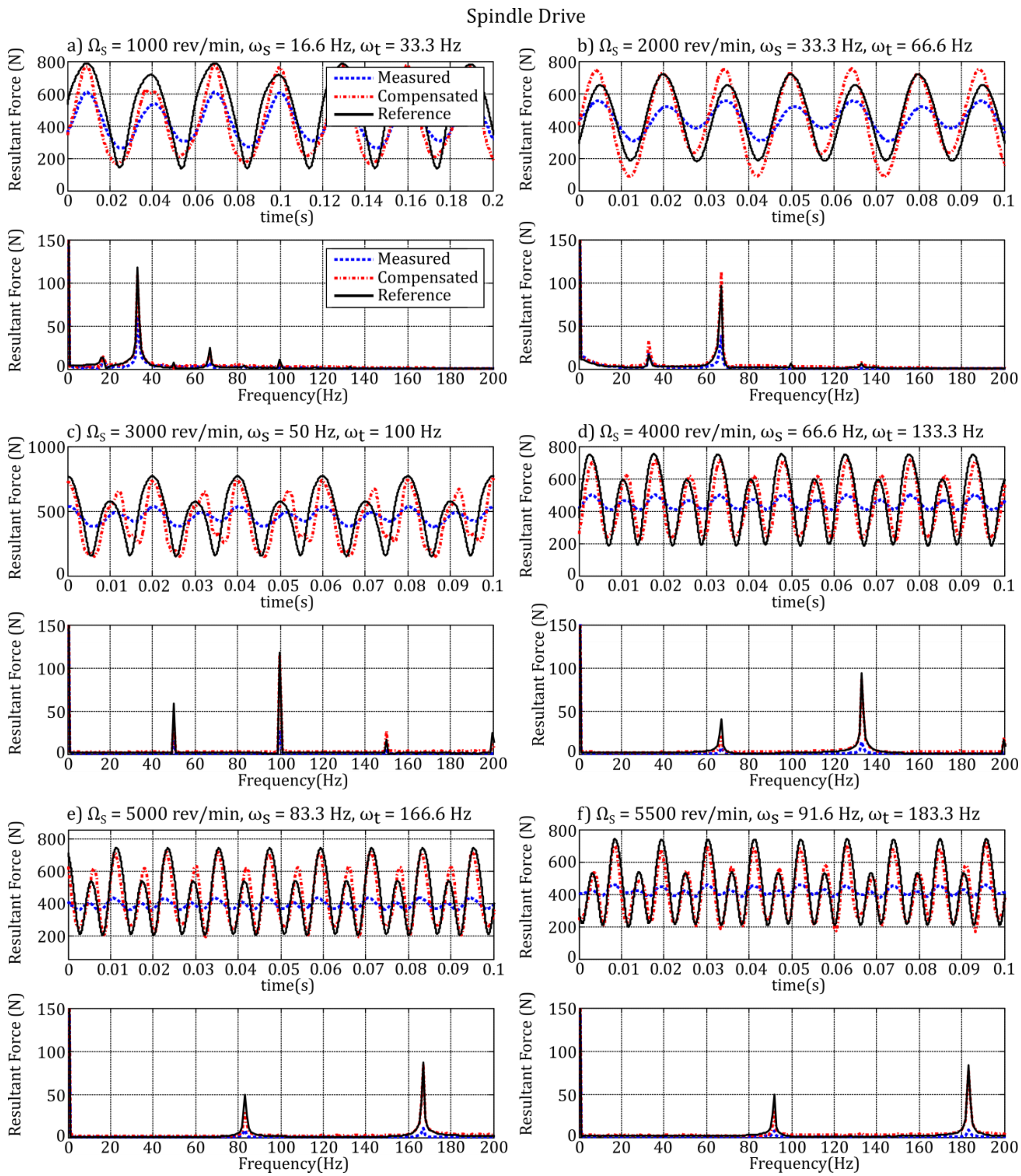

Figure 5.20: Comparison of measured and compensated resultant forces from the spindle drive current with reference forces measured by table dynamometer for three-axis milling with two-fluted end mill. Axial depth = 4 mm, Radial depth = 20 mm, feed = 0.2 mm/tooth, Spindle Drive

Second, since the spindle drive offers higher bandwidth as described in this chapter ($\approx$ 2500 Hz), cutting experiments with higher spindle speeds are performed at 12000, 15000 and 18000 rev/min with a 20 mm diameter four-fluted end mill in order to scan a wider range of excitation frequencies to the system from 200 to 1200 Hz. However; for these cases, reference measurements from dynamometer must also be dynamically compensated since the bandwidth of the table dynamometer is around 750-800 Hz. Force to force transfer functions of the dynamometer are measured in X and Y directions and corresponding Kalman Filters are designed to compensate these dynamical distortions as shown in Figure 5.21.

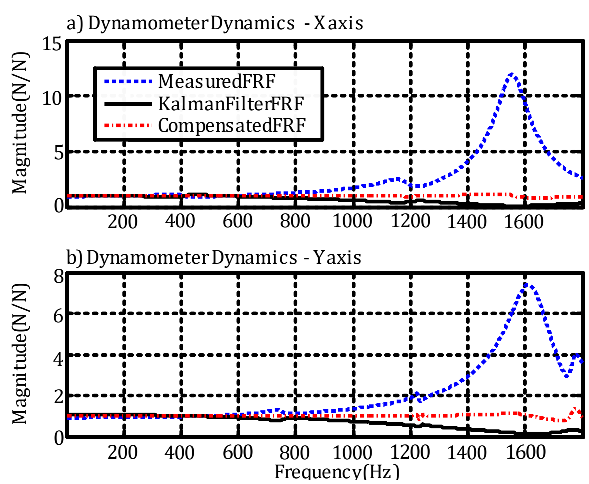

Figure 5.21: Measured force to force FRF of the dynamometer, designed Kalman Filter and Compensated FRFs

Results of the high spindle speed experiments are shown in Figure 5.22 where the reference measurements from dynamometer are also compensated and labeled as "Reference*'. The frequency spectrum of the measurements shows the wide range of excitation to the spindle drive which are all compensated by the proposed observer and the average error between the compensated drive and compensated dynamometer measurements are 35%, 40% and 32% respectively at the spindle speeds of 12000, 15000 and 18000 rev/min. Although errors are higher than previous cases, it should be noted that the resultant force is obtained from compensated spindle drive current with certain assumptions as listed in this section and even reference forces measured by dynamometer are dynamically compensated since its bandwidth is violated in both directions.

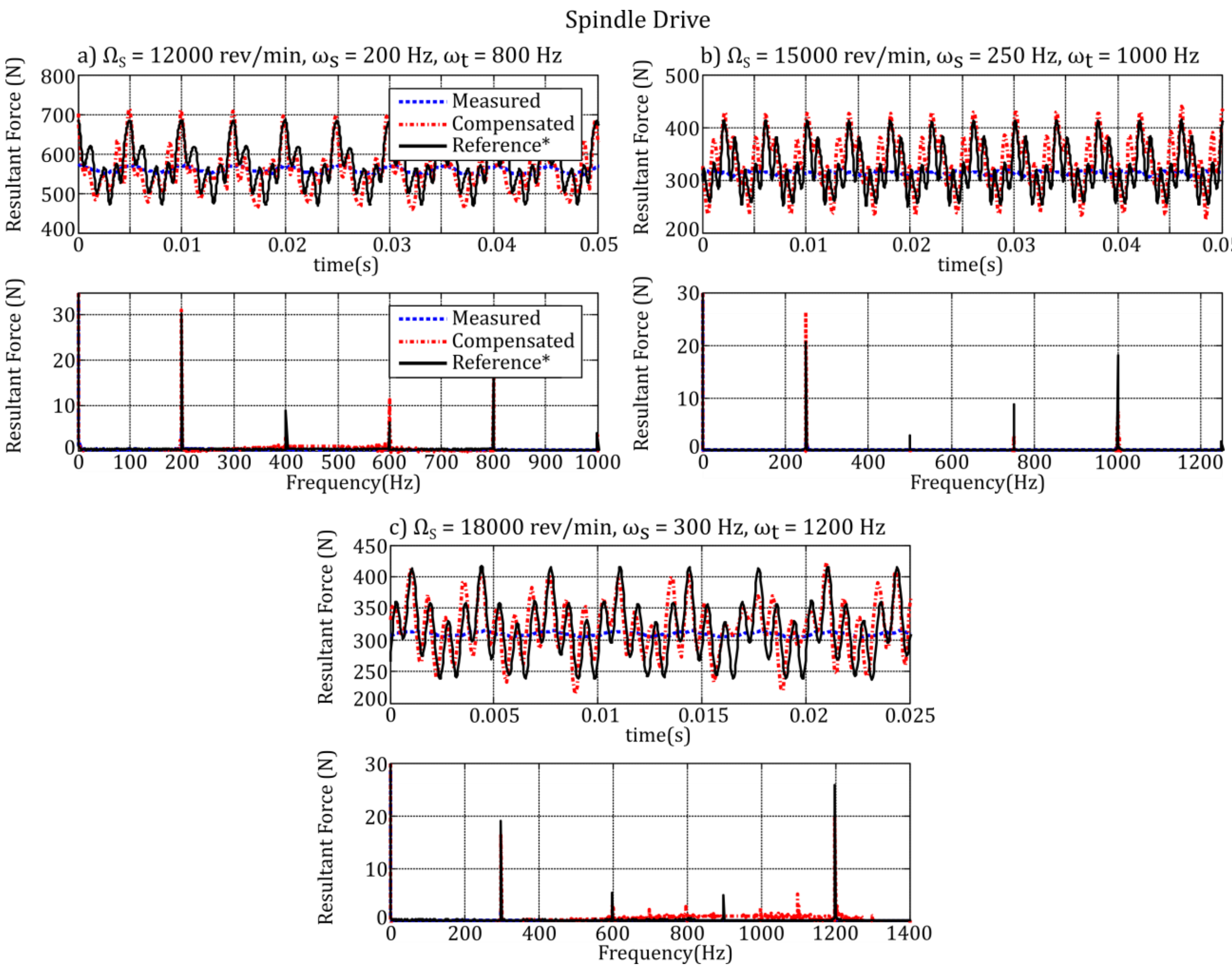

Figure 5.22: Comparison of measured and compensated resultant forces from the spindle drive current with compensated reference forces measured by table dynamometer for three-axis milling with four-fluted end mill. Axial depth = 4 mm, Radial depth = 20 mm, feed = 0.2 mm/tooth, Spindle Drive

5.6 Summary

This chapter presents a method for chatter detection from the drive motor current that is readily available within the CNC system. It is shown that the bandwidth of the spindle drive's torque disturbance transfer function can be significantly increased by compensating the effects of structural dynamic modes which distort the transmitted cutting torque from tool tip to spindle drive servo. The proposed methodology does not require an experience based or case dependent frequency region selection for seeking the chatter frequency since it considers the true dynamics of the drive for the entire frequency range without any need to install external sensors on the machine. The application of the method is shown only using the most practical sensory data, the spindle motor current command supplied by the CNC. However, the approach is also applied to spindle speed and feed drive motor current commands successfully using the same approach, but not shown here in detail to avoid repetition of the modeling process. The proposed method is targeted to be used for on-line chatter detection to achieve unattended machining systems and the methodology as well as the results have been published in [4]. Finally, it is also shown that the compensated torque value can be used to practically estimate the resultant cutting force at the tool tip which can be used for on-line monitoring and control tasks.

Chapter 6: Integration of Virtual and On-line Machining Process Control and Monitoring

6.1 Overview

This chapter presents a virtually assisted on-line milling process monitoring and control system. A part machining process is simulated to predict the cutting forces, torque, power, chip load and other process states along the toolpath. The simulated machining states are accessed by an on-line monitoring system which detects the tool failure, adaptively adjusts the feed and detects chatter by predicting the forces from the feed and spindle drive motor current supplied by CNC. The tool breakage is detected from the average spindle torque, and the load on the cutting tool is maintained at the desired level by adaptively controlling the feed rate where the integration of virtual simulation with on-line measurements avoids false tool failure detection and transient overloads of the tools during adaptive control. The chatter is detected and avoided with the method presented in Chapter 5, and the locations of chatter events are mapped to tool path contained in virtual model. The robustness of algorithms is ensured by sending the part geometry changes and average force patterns from the stored, virtual part machining system. The uncertainties in the virtual model, such as cutting force coefficients, are calibrated from the on-line measurements at the beginning of the milling operation from a steady cut region. The system has been implemented on a CNC machining centre for use in production.

6.2 Integration of Virtual Model and On-line Application

The predicted cutting forces from feed and spindle drive motors (Chapter 3 and 5, respectively) are used for tool breakage detection and adaptive force control. The machine is Quaser UX-600 CNC machining centre and the on-line algorithms are run on an external PC (Intel® Core™ i7-

3.40 GHz CPU, 8 GB RAM) which communicates with the Heidenhein CNC via Ethernet connection. A multi-threaded on-line code is developed in C++ using the LSV-2 communication protocol which collects commanded, noise free digital motor currents, drive speeds, tool centre point position, spindle speed, and tangential velocity between 330 Hz and 10 kHz sampling frequency. External PC can vary the spindle and feed speeds at 10 Hz interval which is sufficient for the targeted tool condition and process monitoring/control tasks outlined in this chapter. Overall structure of the integrated virtual and on-line system given in the introduction section of this thesis is revisited here in Figure 6.1.

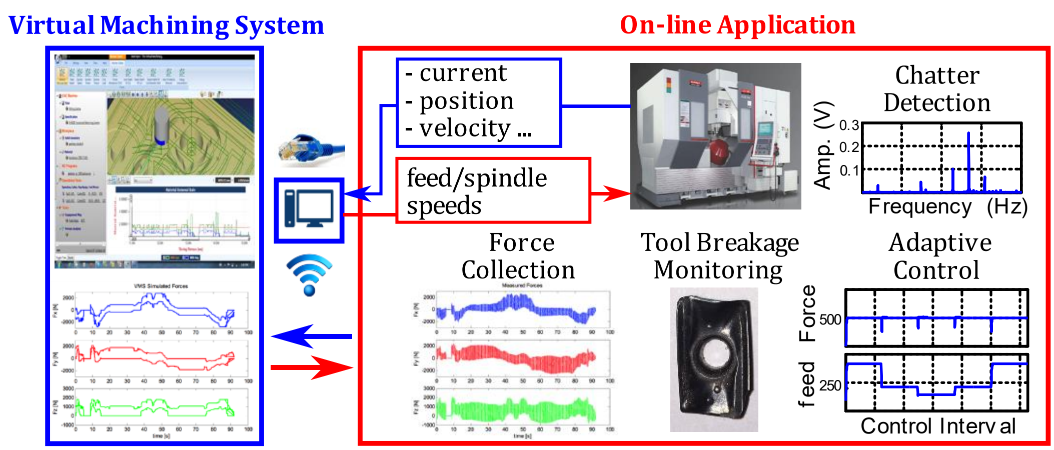

Figure 6.1: Parallel execution of virtual and on-line system with information exchange on external PC [5]

First, prior to cutting operation, part machining process is simulated using MACHpro® Virtual Machining System [93] to calculate cutter-workpiece engagement (CWE), cutting forces, torque, power and machining states along the toolpath. These machining states are stored in a file and accessed by on-line machining process monitoring and control system as a virtual feedback to avoid false tool failure detection and to prevent transient force peaks during adaptive control where the uncertainties in the virtual model are updated for improved simulation accuracy.

The proposed virtual model integrated on-line process monitoring and control system is demonstrated on an Aluminum 7050 part (see Figure 6.2) throughout this chapter where the details of the virtual process model as well as the monitoring and control algorithms are described in detail with examples from a part machining case. Facing, profiling and two slot milling operations are performed with a two fluted 20 mm diameter end mill with a regular pitch and 30 degrees helix angle. Spindle speed is selected as 1000 rev/min throughout the operations. Sample part is designed in a way that the cutter workpiece engagement (CWE) profile has sharp changes along the toolpath for each operation (Figure 6.2) where the purpose is to show that the virtual model feedback to on-line algorithms eliminates the false alarms and transient overloads of the tool for entire part machining.

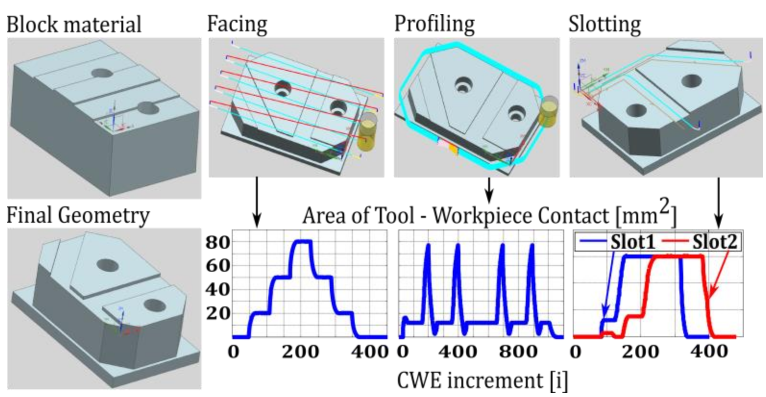

Figure 6.2: A test part with various milling operations and corresponding area of tool-workpiece contact

6.2.1 Generating Virtual Model States and the Feedback File

In order to simulate the process states and generate the virtual feedback file which assists the on-line algorithms, in-house developed MACHpro® Virtual Machining System [93] is used in this study. In this section, MACHpro® Virtual Machining System and the structure of the virtual feedback file are explained.

The main window of MACHpro® with the corresponding verification part's (Figure 6.2) project is given in Figure 6.3 and the explanations for bullet-points can be found in Table 6.1. First, the solid block geometry, work material and the toolpath files are provided to software where it automatically extracts the tools used in the toolpath file and their geometries to the project. Later, the toolpath sampling distance is given where the software calculates the engagement map between the tool and workpiece at the corresponding discrete tool center positions. In this study, it was set to 0.4 millimeters (mm) in order to have a high simulation resolution which means the software calculates the engagement maps and process states every 0.4 mm along the toolpath.

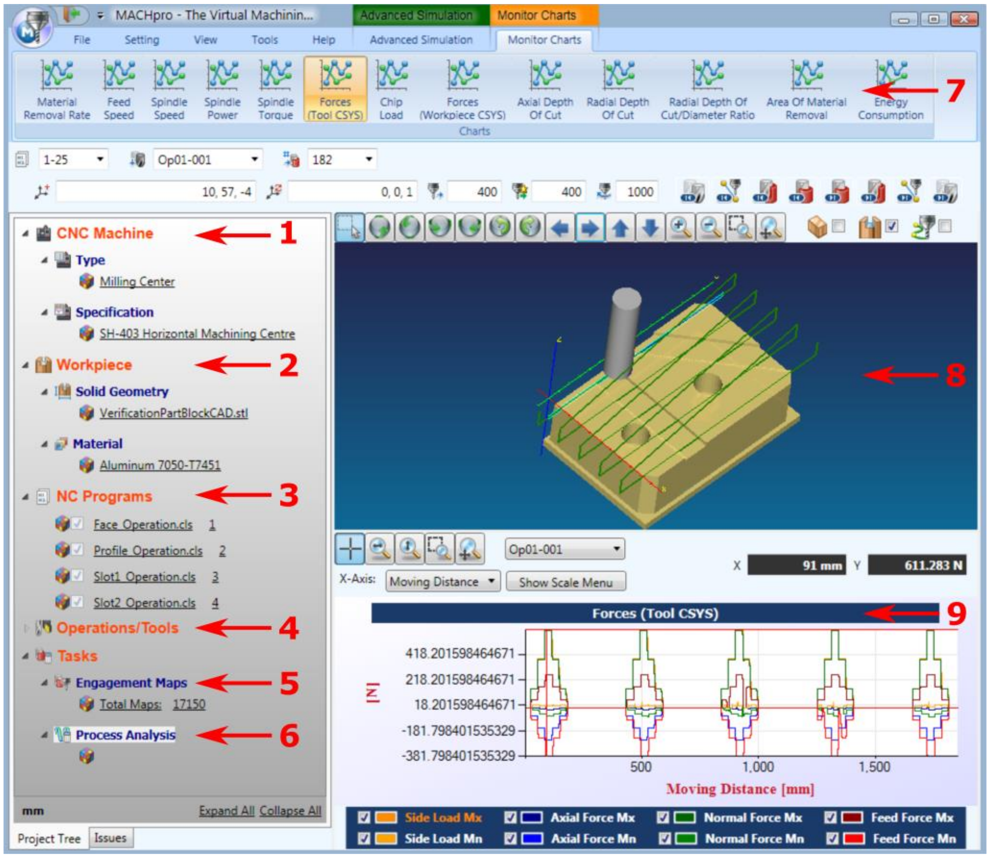

Figure 6.3: A screenshot from MACHpro® Virtual Machining System [93] with the corresponding verification part's (shown in Figure 6.2) project

Table 6.1: Explanations for the bullet-points shown in Figure 6.3 about MACHpro® Virtual Machining System

Point #	Module Name	Explanation
1	CNC Machine	Type of the CNC machine should be specified
2	Workpiece	CAD model of the initial block is uploaded as an ".stl" file and the work material is selected from the material database
3	NC Programs	NC Programs are uploaded for each operation which have tool geometry, tool path and process parameter information
4	Operations/Tools	Tools are extracted from NC programs with their geometries automatically
5	Engagement Maps	Engagement maps between the cutter and work material are calculated with the engagement map sampling distance
6	Process Analysis	Process states (force, torque, power etc.) are selected to be simulated by the software along the tool path
7	Process States	Simulated process states are listed to be selected for the Graph Monitor
8	Part and Toolpath Visual	Visual of the final part with the corresponding operation's toolpath
9	Graph Monitor	A window to see the selected process state along the toolpath, can be plotted as a function of time or the toolpath distance

As can be seen in Figure 6.3, MACHpro® simulates the process forces, torque, power etc. for a given simulation step distance. In addition, the software is also capable of optimizing the machining operation by scheduling the feed rate along the toolpath by respecting to the process and machine tool constraints. However; since it is not within the scope of this thesis, only the simulation aspect of the software is used and shown here.

Once the part machining is simulated by considering the process physics, cutter workpiece engagement as well as the process states along the toolpath are exported as an ".xml" file which is then post-processed by a MATLAB script in order to organize and synchronize the tool tip position, engagements and the process states which forms the virtual feedback file to the on-line monitoring and control functions as shown in Figure 6.4 where the details of each column in the file are explained in Table 6.2.

	1	2	3	4	5	6	7	8	9
	A	B	C	D	E	F	G	H	I
1	Pos. X (mm)	Pos. Y (mm)	Pos. Z (mm)	f_c (mm/min)	Binary Cut Index	Gain of CWE	K_{tc} (N/mm^2)	$F_{resultant}$ (N)	NC Line #
53	10	-13.2	-4	400	0	0	0	0	22
54	10	-12.8	-4	400	0	0	0	0	22
55	10	-12.4	-4	400	0	0	0	0	22
56	10	-12	-4	400	0	0	0	0	22
57	10	-11.6	-4	400	0	0	0	0	22
58	10	-11.2	-4	400	0	0	0	0	22
59	10	-10.8	-4	400	0	0	0	0	22
60	10	-10.4	-4	400	0	0	0	0	22
61	10	-10	-4	400	1	0.976	758	148	24
62	10	-9.6	-4	400	1	0.976	758	148	24
63	10	-9.2	-4	400	1	0.976	758	148	24
64	10	-8.8	-4	400	1	0.976	758	148	24
65	10	-8.4	-4	400	1	0.976	758	148	24
66	10	-8	-4	400	1	0.976	758	148	24
67	10	-7.6	-4	400	1	0.976	758	148	24
68	10	-7.2	-4	400	1	0.976	758	148	24
69	10	-6.8	-4	400	1	0.976	758	148	24
70	10	-6.4	-4	400	1	0.976	758	148	24
71	10	-6	-4	400	1	0.976	758	148	24
72	10	-5.6	-4	400	1	0.976	758	148	24

•
•
•

	A	B	C	D	E	F	G	H	I
1	Pos. X (mm)	Pos. Y (mm)	Pos. Z (mm)	f_c (mm/min)	Binary Cut Index	Gain of CWE	K_{tc} (N/mm^2)	$F_{resultant}$ (N)	NC Line #
128	10	16.8	-4	400	1	0.976	758	148	24
129	10	17.2	-4	400	1	0.976	758	148	24
130	10	17.6	-4	400	1	0.976	758	148	24
131	10	18	-4	400	1	0.976	758	148	24
132	10	18.4	-4	400	1	0.976	758	148	24
133	10	18.8	-4	400	1	0.976	758	148	24
134	10	19.2	-4	400	1	0.976	758	148	24
135	10	19.6	-4	400	1	0.976	758	148	24
136	10	20	-4	400	1	2.498	758	378.7	24
137	10	20.4	-4	400	1	2.498	758	378.7	24
138	10	20.8	-4	400	1	2.498	758	378.8	24
139	10	21.2	-4	400	1	2.498	758	378.7	24
140	10	21.6	-4	400	1	2.498	758	378.8	24
141	10	22	-4	400	1	2.498	758	378.8	24
142	10	22.4	-4	400	1	2.498	758	378.8	24
143	10	22.8	-4	400	1	2.498	758	378.8	24
144	10	23.2	-4	400	1	2.498	758	378.8	24
145	10	23.6	-4	400	1	2.498	758	378.8	24
146	10	24	-4	400	1	2.498	758	378.8	24
147	10	24.4	-4	400	1	2.498	758	378.8	24

Figure 6.4: Virtual feedback file generated from the CWE and process state outputs of MACHpro® Virtual Machining System

Table 6.2: Explanations for the bullet-points shown in Figure 6.4 about virtual feedback file

Point #	Column Title	Explanation
1	Pos. X	Position of tool tip in X axis (mm)
2	Pos. Y	Position of tool tip in Y axis (mm)
3	Pos. Z	Position of tool tip in Z axis (mm)
4	f_c (mm/min)	Tangential (commanded) feed rate at the tool tip (mm/min)
5	Binary Cut Index	A binary index for determining when the tool is in or out of cut, the index is 0 when tool is out and 1 when it is in cut
6	Gain of CWE	Gain of cutter-workpiece engagement (mm)
7	K_{tc}	Tangential cutting coefficient (N/mm^2)
8	$F_{\text{resultant}}$	Resultant force in X-Y plane (N)
9	NC Line #	Corresponding line # in the NC file running on the machine

Virtual feedback file shown in Figure 6.4 is an input to the on-line C++ code where the monitoring and control functions are running on the External PC.

6.2.2 Reading and Writing Data from/to CNC using External PC

On-line measurements from the CNC are obtained through LSV-2 C style library, designed to communicate with Heidenhain TNC. It supports both serial (RS-232 and RS-422) interfaces and ethernet connection for data transfer to external computers or other devices. Although only simple file servers can be implemented via the serial interfaces when using the ME or FE protocol, the LSV-2 protocol makes it possible to realize complex tasks with a bidirectional structure based on DIN 66019. LSV-2 protocol provides access to the integral oscilloscope of the iTNC530 which is available on the machine panel from External PC where the functions in the library hide the low-level telegram-based communication mechanism and enables user to create functionalities easily. In addition, Heidenhain DNC, a C style library, is used to write data to send commands to CNC in-process, such as changing feed or spindle overrides to monitor and control the process in an on-line manner. Structure of the read (LSV-2) and write (DNC) libraries are explained in this section with their specific purposes.

The following block diagram (Figure 6.5) shows the overall structure of the software components and their interaction with the iTNC 530 CNC;

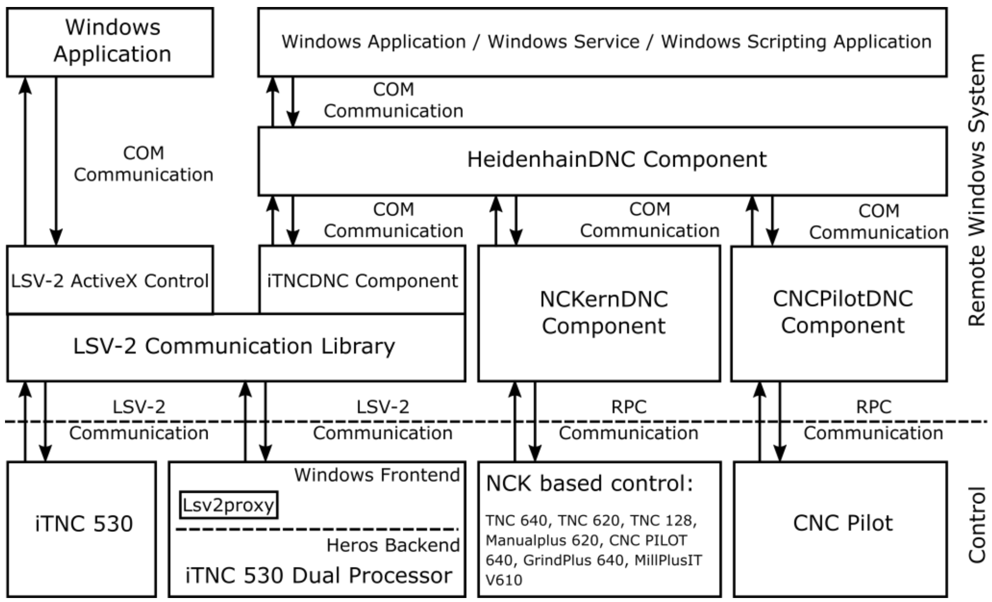

Figure 6.5: Communication structure between iTNC 530 and Windows Application on External PC [94]

Heidenhain iTNC530 CNC installed on Quaser UX-600 machine has 3 milliseconds position interpolation sampling time which corresponds to 333 Hz read frequency of the tool tip nominal position from external PC. It is important to note that the CNC provides some of the channels (tool tip position, drive velocities, tangential feed rate etc.) with the position interpolator frequency (333 Hz) and the rest (nominal or actual current, linear or rotary drive encoder pulses, axes positions in machine reference coordinates) with the current loop frequency (10 kHz).

Once the data is read from the CNC and processed by the monitoring and control algorithms, two values are changed on the CNC from the External PC in-process: feed and spindle speed overrides. For this task, DNC library of the Heidenhain iTNC 530 is used which gives access to the PLC addresses, hence, feed and spindle override values. The software and communication structure are shown in Figure 6.6.

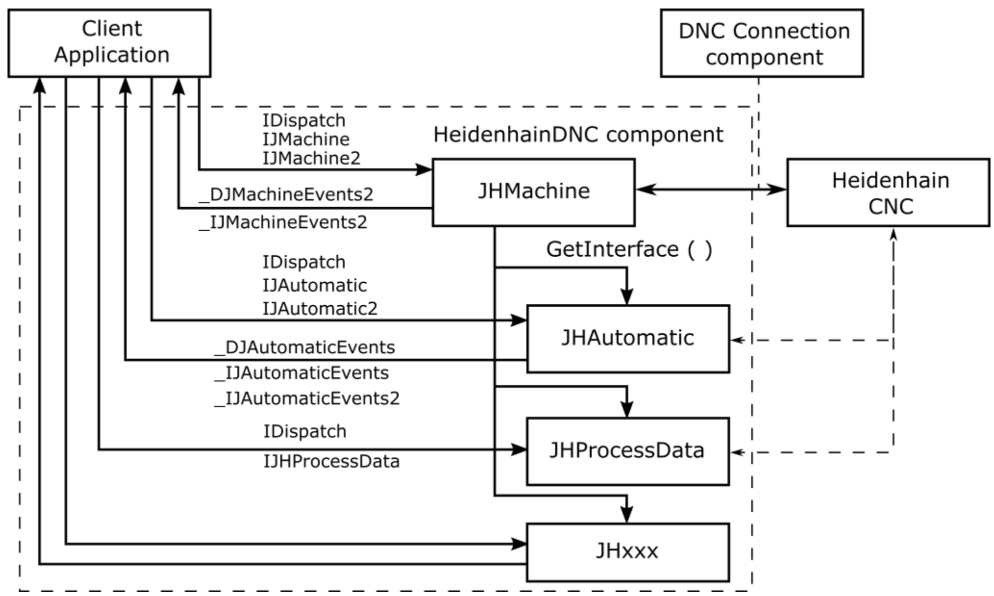

Figure 6.6: Communication structure between the PLC and Windows Application on External PC [94]

Special DNC libraries of Heidenhain iTNC530; JHMachine, JHAutomatic and JHProcessData gives access to the PLC addresses from the External PC where any action can be taken as on the machine panel. NC start/stop, coolant on/off, emergency stop, feed-spindle override change and similar operations can be performed from the external PC during machining. In addition, parameters on machine’s kinematic table, control parameters or any other machine setup related parameter can be changed through DNC library when the machine is not operating for safety and part integrity reasons.

In summary, LSV-2 library (Figure 6.5) is used to read data from CNC with high sampling frequency (330 Hz to 10 kHz) where DNC library (Figure 6.6) is used to change PLC addresses such as feed and spindle overrides (10 to 15 Hz) from External PC.

6.2.3 Synchronization of the Virtual Feedback File and the On-line Operation

Once the virtual feedback file is uploaded and available on the External PC, the next step is to establish the synchronization with operation on the machine, so the virtual model and the on-line monitoring and control functions can work in parallel by exchanging information.

In this study, the synchronization between the virtual feedback file and the on-line operation is achieved through tool tip position tracing. First three columns of the virtual feedback file are the X, Y and Z positions of the tool tip, moving along toolpath with the engagement map sampling distance (see Figure 6.4) where the nominal (commanded) X, Y, Z positions of the tool tip are measured from the CNC by using the LSV2 library. Once a tool tip position is measured from the CNC, it is searched in the virtual feedback file until the corresponding interval is found. The tolerance for this position tracing is set to 20 microns per axis which means the measured nominal position value is searched in the virtual feedback file with ± 10 microns tolerance for each direction. The position search itself is also designed for fast, on-line application where it starts searching the corresponding position in the virtual feedback file from the previous iteration.

The described position tracing, hence virtual feedback file synchronization is running in parallel with the monitoring and control functions in a multi-thread structure where a circular buffer is used to exchange information between threads as well as sending commands to CNC in an organized way without missing data. CWin Thread Class of C++ is used for this purpose where the threads are started by AfxBeginThread for both LSV-2 and DNC connections. Multi-thread structure with the circular buffering can be seen in Figure 6.7 where the position synchronization is prioritized since it is essential that the connection between the virtual model and the on-line functions is not interrupted throughout the toolpath.

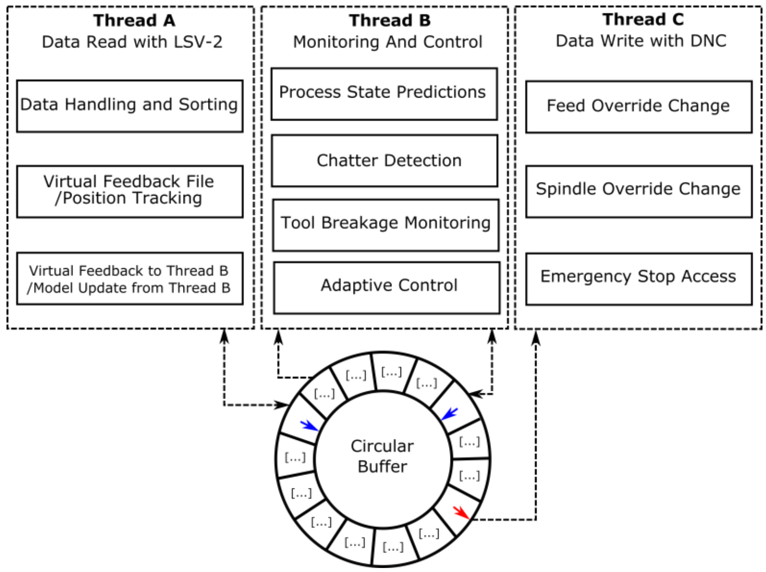

Figure 6.7: Multi-thread structure of the on-line C++ code running on External PC

This multi-thread structure is essential to run both LSV-2 and DNC functions in-parallel since DNC actions interrupt LSV-2 connection to the integral oscilloscope of iTNC530 at every execution. Re-establishing the connection of LSV-2 to CNC after every override command using DNC is not acceptable since all the monitoring and control functions would sleep during this log-in time which is approximately around 25-30 milliseconds. Multi-thread code prevents this issue since LSV-2 thread keeps reading data without interruption as DNC library is varying the feed and spindle overrides from its individual thread. This way, both LSV-2 and DNC libraries are connected to CNC throughout the toolpath where the main thread is working on the virtual feedback file, on-line application synchronization and providing critical feedback to monitoring and control functions.

It should be noted that the engagement map sampling distance in the virtual model determines the resolution of the virtual feedback. For example, if the engagement map sampling distance is selected too high, poor resolution in the virtual feedback can cause problems in the on-line operations such as late threshold updates for tool breakage monitoring or late look-ahead action for preventing the transient overloads of the tool during adaptive control. This distance is selected as 0.4 mm in this study by considering the demonstration part's features, it can also be adaptively calculated depending on the part geometry and the toolpath with certain algorithms in the future.

6.3 Tool Breakage Monitoring with Virtual Feedback

Tool breakage in milling is detected with the algorithm given in [53] but with the feedback from the virtual machining system. The average cutting torque per tooth period ($\tau_{sa}(m)$) is evaluated from the spindle motor current by compensating the distortions in the signal caused by the structural dynamics as described in Chapter 5;

$$\tau_{sa}(m) = \sum_{i=1}^{I} \frac{\hat{\tau}_d(i)}{I} \tag{6.1}$$

where $\hat{\tau}_d$ is the compensated spindle torque measurement (see Chapter 5.3), I is the number of compensated torque samples collected at tooth period (m). The average spindle torque per tooth period must remain constant if there is no change in the CWE geometry, and the cutter is free of tooth breakage and run-out. In such conditions, all teeth on the milling cutter produce equal average cutting torque, hence the first differences of the average cutting forces should be zero [53];

$$\Delta\tau_{sa}(m) = \tau_{sa}(m) - \tau_{sa}(m-1) = (1 - z^{-1})\tau_{sa}(m) \tag{6.2}$$

The average cutting torque profile will reflect the changes in the chip load and be nonzero if the CWE is varying, tooth is damaged or run-out exists. If the tool runs into a transient geometry along the geometrically complex toolpaths, the torque profile will follow the geometric trend. A first-order adaptive time series filter is used to remove the slow varying DC trend caused by varying CWE as given in [53];

$$\varepsilon_1(m) = \left(1 - \hat{\phi}_1 z^{-1}\right)\left[\tau_{sa}(m) - \tau_{sa}(m-1)\right] = \left(1 - \hat{\phi}_1 z^{-1}\right)\Delta\tau_{sa}(m) \tag{6.3}$$

where $\hat{\phi}_1$ is estimated from measurements $\Delta\tau_{sa}(m)$ using a standard recursive least squares (RLS) algorithm at each period which is described in [53] and [46] thoroughly. In addition, the effect of tool runout can also produce high-amplitude residuals which can be removed by comparing the tooth's performance by itself one revolution before as follows;

$$\varepsilon_2 = (1-\hat{\phi}_2 z^{-1})[\tau_{sa}(m) - \tau_{sa}(m-N)] = (1-\hat{\phi}_2 z^{-1})\Delta^N \tau_{sa}(m) \tag{6.4}$$

where N is the number of flutes on the tool and $\hat{\phi}_2$ is estimated in a similar fashion as $\hat{\phi}_1$. In previous studies ([28, 53]), these two adaptive time series filters are run recursively in parallel at every tooth period and the maximum residuals of both filters are measured at the beginning of the cut (for few spindle revolutions) to be compared with the rest of the operation. It is assumed that the tool is not broken within this period and the breakage thresholds are selected by scaling the maximum residuals measured at the beginning of the cut by pre-determined factors (α_1 and α_2) as follows;

$$\begin{aligned} LIMIT_1 &= \alpha_1 \max\left(\varepsilon_1(k=1),\ldots,\varepsilon_1(k=\#Sr)\right) \\ LIMIT_2 &= \alpha_2 \max\left(\varepsilon_2(k=1),\ldots,\varepsilon_2(k=\#Sr)\right) \end{aligned} \tag{6.5}$$

where k is the spindle period and ($\#Sr$) is the number of spindle revolutions that the initial residues are calibrated at the beginning of the cut.

Threshold factors (α_1 and α_2) are usually intuitively selected between 2 and 3 in the literature ([28, 53]) as constant values throughout the toolpath which works for single axis, unidirectional cutting operations with constant cutter-workpiece engagement (CWE) conditions in laboratory environment for verification purposes. However; if the algorithm is run on a real part machining environment, it is very challenging to determine the threshold values in an adaptive manner along the multi-axis toolpath with changing CWE conditions. Therefore, it is proposed to use the feedback from the virtual machining model which runs in parallel with the online operation and adaptively change the tool breakage threshold values as a function of process geometry and chip load. This way, tool breakage algorithm is not blind to varying CWE conditions and capable of eliminating false breakage alarms caused by transient changes along the toolpath. In addition, the virtual feedback minimizes the need for the second residue given in Eq. (6.4) since adaptive threshold is capable of handling the runout on the tool given that the initial calibration is done accurately. Threshold value is re-written as follows;

$$LIMIT_1 = \sigma_{TB}\tau_{sa-simulated} \tag{6.6}$$

where σ_{TB} is a percentage value which means the tool breakage threshold is adaptively changed as a function of the simulated average torque per tooth period. Now breakage threshold is a function of process geometry, kinematics, material properties and true chip load along the toolpath since the virtual model considers the listed items to calculate process states (average torque value for this part). The threshold value (σ_{TB}) is selected as 40% in this study during the experiments, however it can also be an adaptive value given that the system is planned to be run in production where these parameters must be updated for consecutive operations.

In order to show the effectiveness of the presented method by comparing it with the existing methods, a face milling operation shown in Figure 6.2 is experimented.

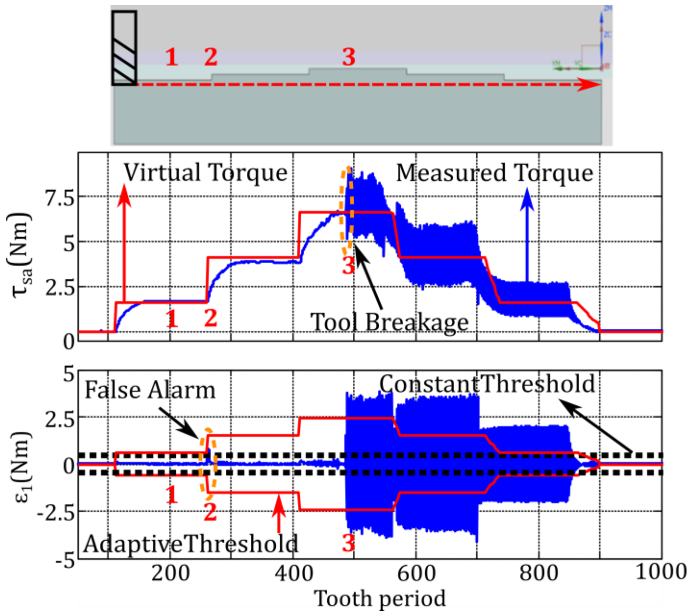

Figure 6.8: Robust detection of tool breakage around tooth period 500 with the feedback from virtual machining system

As illustrated in Figure 6.8, tool is traveling along the toolpath which has varying engagement (i.e. axial depth of cut) conditions and on-line measured torque values are mapped on calculated ones with the virtual model. Residue (ε_1) is plotted with both constant (identified as described above in this section and also in [53]), and adaptive thresholds (calculated as given in Eq. (6.6) with 40%). At location #1 in Figure 6.8, tool is in cut with steady conditions, hence the residue value is almost zero as expected since both flutes of the tool are under almost the same chip load which creates very close torque values. Since engagement conditions do not vary rapidly, both constant and adaptive threshold methods work without a false alarm at location #1.

At location #2, axial depth of cut is suddenly increasing in a step manner which creates an unbalance between the two flutes in terms of axial depth, hence torque values. For the instant that the tool is merging into the new region at location #2, one of the flutes is experiencing the new, higher axial depth for a spindle revolution where the previous flute's signal is still at the lower depth, which creates an imbalance between the two torque values reflected on the residues. This peak in the residue value purely caused by the transient geometry change along the toolpath is considered as “tool breakage” event if the constant threshold check method is used since this value was calibrated at the beginning of the cut in the lower depth region. However; since the adaptive threshold is a function of CWE geometry with the virtual feedback, the proposed method is able to neglect this false breakage alarm and it does not stop the operation unnecessarily.

In summary, the constant threshold method cannot distinguish the tool failure from the step changes in CWE geometry and gives false alarm at tooth periods 262-270. However; the proposed integrated system calibrates the cutting force coefficients from the CWE information and measured tangential force at the beginning of the cut and predicts the average torque accurately as the CWE geometry changes. The residual threshold is adaptively adjusted and alerts the tool condition monitoring system whenever both the measured and residual torque violate the limits. The virtual machine assisted algorithm does not give false alarm at step change (tooth periods 262-270) but detects the true tool failure event imposed around tooth period 500 (location 3# in Figure 6.8).

At location #3, operation is paused and one of the inserts of the cutter is changed with a damaged one to impose the breakage event to the experiments in a controlled way. For the sake of illustration purposes, algorithm is not allowed to set the feed override to 0% and stop the operation when the breakage is detected, and constant violation of the threshold after location #3 can be seen in the residue plot (Figure 6.8). The algorithm is able to stop the operation at tool breakage event by using the feed override PLC address through the DNC library in 150-200 milliseconds which corresponds to 3-4 spindle revolutions with 1000 rev/min. The same operation is repeated and the region where the tool breakage is detected (location #3) and “set feed override to 0%” command sent to the CNC is shown in Figure 6.9.

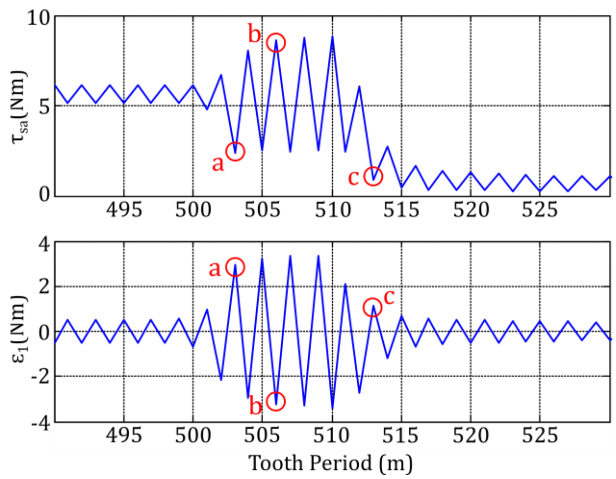

Figure 6.9: Tool breakage event around tooth period 500 where the operation is automatically stopped (Location #3 in Figure 6.8)

In Figure 6.9, peak (a) is the first violation of the adaptive threshold where the next 3 tooth periods are checked until peak (b) to make sure of the breakage event. At peak (b) location, feed override is set to 0%, which is referred as "feed halt" in the literature, command is sent to the CNC and it takes 6 tooth periods since the machine stops its motion after that moment as shown at peak (c). After feed halt, since tool motion is stopped in the middle of the cut, one of the flutes keep touching the workpiece due to the runout on the tool, that is why both average torque per flute and corresponding residue values are not converging to zero but to a very small number (< 0.25 Nm). For this experiment, one spindle revolution takes 60 milliseconds with 1000 rev/min, 6 tooth periods from peak (b) to (c) correspond to 3 spindle revolutions, hence operation is stopped within 180 milliseconds once the tool breakage alarm is triggered.

The algorithm is now more reliable and can be used in production since the thresholds are adaptive as a function of process geometry, physics and can be set as a % of the predicted values by considering only the disturbances caused by the tool run out.

6.4 Adaptive Control of Milling Forces with Virtual Feedback

In addition to chatter detection and tool breakage monitoring modules, adaptive control is used to keep the peak forces ($F_p(k)$) at the desired reference level ($F_r(k)$) by manipulating the feed rate in-process at spindle periods (k). The main objective is to prevent tool shank breakage and constrain the bending deflections of the tool by keeping the resultant forces at a desired level throughout the operation. The resultant peak force in X-Y plane at each spindle period is estimated from the feed drive motor current commands as described in Chapter 3.

Block diagram of the adaptive control system with the virtual model feedback is shown in Figure 6.10.

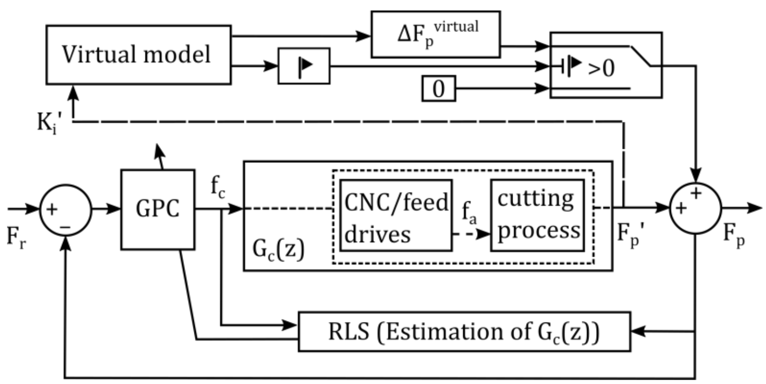

Figure 6.10: Block diagram of the adaptive control system with the virtual model feedback

As illustrated in the block diagram (Figure 6.10), the input to the adaptive control system is the reference level of the maximum cutting force (F_r) which can be directly correlated to maximum static deflections left on finished surface to keep them within the tolerance of the workpiece. The actual cutting forces are monitored from feed drive current command measurements with the method presented in Chapter 3. The peak force (F_p) at each spindle period (k) is evaluated from the actual cutting forces, sent back as a feedback which is subtracted from the reference force level (F_r) and passed to the control law in order to calculate the feed command

(f_c) sent to the CNC. The feed command (f_c) is sent as a voltage command to the feed drive motors which move the table at an actual feed velocity (f_a). Since most of the machine tool cascade drive control dynamics are tuned to be overdamped with no overshoot, they can be assumed to have first-order dynamics. The cutting process itself also feels the change in the chip load and the depth of cut at least after one tooth period which means the cutting process can also be approximated as a first-order system with a time constant equal to one or more tooth periods (less than a spindle period). The combined CNC, machine tool feed drive and cutting process transfer function ($G_c(z)$) has time-varying parameters because CWE geometry varies along the toolpath. The commanded feed rate (input) and the peak force values (output) are sent to an on-line recursive least squares (RLS) algorithm which estimates the parameters of the combined transfer function ($G_c(z)$) at every adaptive control interval. The estimated parameters are used to update the control law in an adaptive manner since they are adjusted according to the changes in the cutting process.

Although the combined feed drive and cutting process transfer function ($G_c(z)$) can be approximated to have second-order dynamics, the order is increased by one to account for the non-linear relationship between the feed rate (i.e. chip load) and the cutting forces. Therefore, the discrete time transfer function ($G_c(z)$) between the peak cutting force ($F_p(k)$) and commanded feed rate ($f_c(k)$) is expressed as;

$$G_c(z) = \frac{F_p(k)}{f_c(k)} = \frac{z^{-1}B(z^{-1})}{A(z^{-1})} = \frac{z^{-1}(b_0 + b_1 z^{-1} + b_2 z^{-2})}{1 + a_1 z^{-1} + a_2 z^{-2}} \tag{6.7}$$

where the parameters of polynomials B and A vary with time, depending on the CWE changes along the toolpath. Corresponding parameters (b_0, b_1, b_2, a_1, a_2) are estimated recursively through an RLS algorithm at each spindle (control) interval (k) from measured peak force (F_p) and commanded feed (f_c) vectors. The details of the on-line recursive parameter identification algorithm (RLS) is given in Appendix F ([53], [46]). Once the machining process transfer function ($G_c(z)$) is identified, control law should be updated to calculate the next commanded feed rate which is described next.

In this thesis, adaptive generalized predictive control (GPC) method described in [53] is used since it is robust to future transient CWE changes and cutting forces, as well as the varying time delay between the feed command generated by the controller and its actual execution by the CNC. The GPC method is devised for an ARIMAX forecast model where the details can be found in [53]. It uses a prediction approach where the controller predicts the changes in the controlled variable that will occur in the future using the present and past process knowledge and control.

The predictions are done at discrete samples of j and the GPC output (f_c) is calculated to minimize the error between the reference (F_r) and measured peak (F_p) forces, within the minimum and maximum horizon, N_1 and N_2, respectively. The ARIMAX model is an extended version of the ARIMA (autoregressive integrated moving average) method which is also referred as the vector ARIMA or the dynamic regression model. The model assumes that the future values of a variable vector linearly depend on its past values, as well as on the values of the past (stochastic) transients. The plant transfer function can be written in the following ARIMAX form;

$$F_p(k) = \frac{B(z^{-1})}{A(z^{-1})} f_c(k-1) + \frac{\zeta_{AR}(k)}{(1-z^{-1})A(z^{-1})} \tag{6.8}$$

where $\zeta_{AR}(k)$ is assumed to be an uncorrelated random noise sequence and a j step ahead peak force prediction is obtained by expressing the noise term by its partial fraction expansion as follows [53];

$$\frac{z^j \zeta_{AR}(k)}{(1-z^{-1})A(z^{-1})} = z^j E_j \zeta(k) + \frac{F_j(k)}{(1-z^{-1})A(z^{-1})} \zeta_{AR}(k) \tag{6.9}$$

which leads to the Diophantine equation as follows [53];

$$\begin{aligned} &1 = E_j(z^{-1})A(z^{-1})(1-z^{-1}) + z^{-j}F_j(z^{-1}) \\ &\deg(E_j(z^{-1})) = j-1, \ \deg(F_j(z^{-1})) = \deg(A(z^{-1})) = 2 \end{aligned} \tag{6.10}$$

where E_j and F_j are calculated for a given $A(z^{-1})$ and prediction interval j. The j step ahead prediction of peak cutting force (F_p) at control interval (k) is given as [53];

$$\hat{F}_p(k+j) = G_j(z^{-1})\Delta f_c(k+j-1) + F_j F_p(k) \tag{6.11}$$

where $\Delta = (1-z^{-1})$ and $G_j(z^{-1}) = E_j B(z^{-1})$. The GPC algorithm takes predicted output values within the prediction output horizon when calculating the commanded feed rate. Minimum and maximum prediction output horizons are selected as $N_1 = 1$ and $N_2 = 4$, respectively as in [53]. GPC considers that future control inputs ($f_c(k+j)$) do not change beyond the control horizon NU which is set to be 1 ($\Delta f_c(k+1) = \Delta f_c(k+2) = \Delta f_c(k+3) = 0$). With these, Eq. (6.11) becomes;

$$\left\{\hat{F}_p\right\} = \left\{G_I\right\}\Delta f_c(k) + \left\{f\right\} \tag{6.12}$$

where the derivations of vector $\{f\}$ which contains present and past measured peak forces ($F_p(k-i), i = 0,1,2$) and past feed commands ($f_c(k-i),\ i = 1,2$) and recursively calculated polynomials G_j and F_j are given in Appendix G. GPC determines the commanded feed rate value by minimizing the expected value of a quadratic cost function containing future predicted errors ($F_r - F_p$) within the output horizon as follows [53];

$$J(f_c, k) = E\sum_{j=N_1}^{N_2}\left[\hat{F}_p(k+j) - F_r(k+j)\right]^2 + \lambda\left[\Delta f_c(k)\right]^2 \tag{6.13}$$

where λ is the weighting factor on the control input increment ($f_c(k) - f_c(k-1)$) defined between 0 and 1 and selected as 0.25 in this study to soften the impact of sudden CWE changes along the toolpath on the adaptive algorithm. The minimization of the quadratic cost function through ($\partial J / \partial f_c = 0$) leads to the input feed command at control (spindle) interval k as follows;

$$f_c(k) = f_c(k-1) + \frac{1}{\{G_I\}^T\{G_I\} + \lambda}\{G_I\}^T\left(\{F_r\} - \{f\}\right) \tag{6.14}$$

The polynomials in the GPC algorithm are recursively calculated at each control (spindle) interval where the details of the computations can be found in Appendix G.

GPC algorithm described in this section is adopted from [53] but with the added virtual model feedback as shown in the block diagram given in Figure 6.10. Adaptive control system described so far has not been adopted by industry due to large transient force peaks, overloads of the tool which either breaks the tool or damages the part due to excessive deflections when the CWE geometry suddenly increases. When the tool enters into a cavity or the depth of cut is low, the corresponding peak force becomes low; hence the adaptive controller increases the feed rate to increase the force towards the reference value. When the tool exits the cavity or the depth of cut suddenly increases, the servo cannot reduce the feed quickly, the resulting high feed rate creates a large cutting load spike that breaks the tool, damages the part or might violate the tolerances of the workpiece due to the corresponding deflection peak at the tool tip. Hence, the intensive adaptive control research in the past has not been successfully used in practice.

This problem is solved by introducing the virtual model feedback which considers the CWE geometry conditions and simulated forces from the virtual machining system to the adaptive control algorithm ahead of sudden geometry changes in a look-ahead manner. Since the virtual feedback file and the on-line operation is running in synchronization, a look-ahead algorithm is used to prevent the transient overloads of the tool, collisions and increasing trend of feed rate at the exit locations which causes excessive amount of burrs. As the operation is running on the machine with virtual feedback file tracing, half second long look-ahead of a toolpath distance is checked in the virtual feedback file for every control interval; if the CWE area and the chip load are a certain percentage (15% in this study) higher than the current one, the flag value shown in the block diagram (Figure 6.10) is set to 1, and 0 otherwise. When the flag value is 1, the incoming force predicted by the virtual machining system is fed into the controller as a disturbance force prior the actual CWE change in the real operation. As a result, the adaptive controller slows down the feed rate before tool goes in to the higher CWE area or chip load region and prevents force overloads and collision spikes; hence the adaptive controller becomes robust and practical to be used in production, especially for roughing operations. In addition, the flag value is set to 2 when the tool is in the cavities, the controller is halted, and the feed rate is kept at a safe level to prevent excessive feed rates which may lead to collisions or exit burrs as the tool is leaving the workpiece.

In order to compare the conventional and virtual model assisted GPC, face milling operation of the demo part (Figure 6.2) with sharp transient CWE changes is used here as an example. Results of no adaptive control, conventional adaptive control and adaptive control with virtual model feedback cases are illustrated in Figure 6.11.

Reference force is selected as 325 N because feed override limits of the Heidenhain CNC is in between 20-150%. Programmed feed rate in NC program is 400 mm/min and the force profile follows the step increase and decrease CWE profile of the part along the toolpath which is labeled as (NoAC) in Figure 6.11. When the adaptive control is activated with 325 N reference force, controller is able to keep the actual resultant cutting forces at the desired level with 5% error which is allowed in the algorithm to prevent oscillatory feed profile.

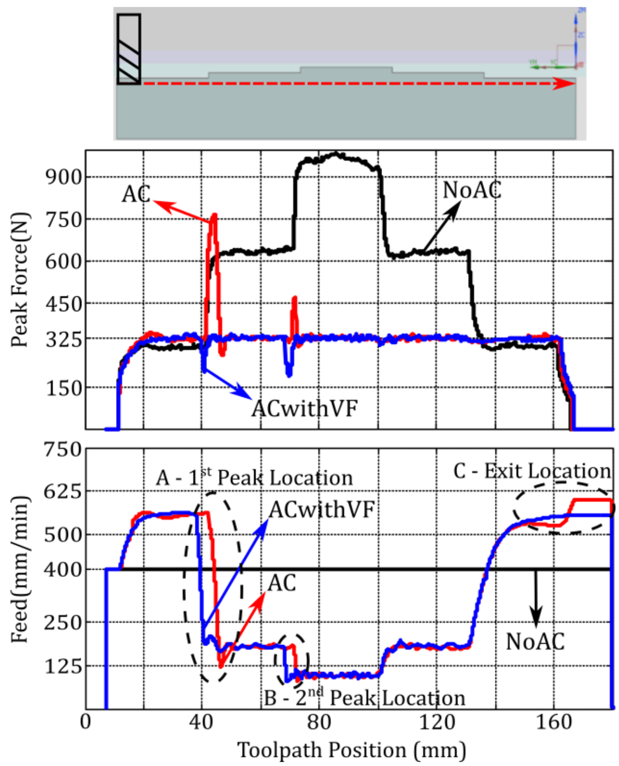

Figure 6.11: Virtual model assisted GPC, adaptive control (AC) with force identified from feed drive current command measurements, no AC (NoAC), conventional AC (AC) and AC with virtual machining model feedback (ACwithVF) for the face milling operation of the demo part shown in Figure 6.2

This type of conventional adaptive controller produces force overshoots at locations A and B (Figure 6.11) where CWE area suddenly increases because it is blind to current and future process geometry. Forces increase to almost 800 N at location A, which increases the error and the controller slows down the feed rate to take the force value back to the reference level. However; these kinds of large transient overloads of cutter tools are not desirable as mentioned earlier.

Similarly, at location B, tool is going into another deeper region suddenly and force overshoot can be seen in conventional adaptive control case.

When the virtual model feedback is activated, half a second long look-ahead of tool path distance in virtual feedback file warns the controller before location A and B by setting the flag value to 1 (Figure 6.10), injecting the incoming force overshoot to the controller as a disturbance, enables controller to reduce the feed rate prior to the depth increase, hence prevent transient overloads of the tool and force overshoots (see ACwithVF in Figure 6.11).

In addition, in the exit region (location C in Figure 6.11), the conventional adaptive controller is blind to the process geometry and it increases the feed rate to take the forces back to reference level as the tool is leaving the workpiece. Naturally, cutting force will approach and converge to zero when tool is at the exit region, as the controller increases the feed rate in this region, tool leaves the workpiece by accelerating, which leaves exit burrs on the finished workpiece (see Figure 6.12).

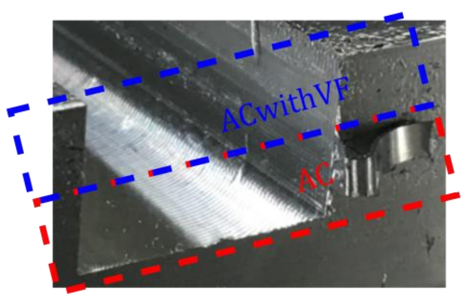

Figure 6.12: Burr formation with (AC) and (AC with VF) at the exit region (location C in Figure 6.11)

However; with the virtual model assisted adaptive controller, the flag value is set to 2 when the tool is in the exit region (location C), controller is halted, and the feed rate is kept at a constant level which enables tool to exit the workpiece smoothly and prevent exit burrs which requires manual cleaning or polishing on the produced part.

6.5 Experimental Verification

In this chapter, profile and two slot milling operations are demonstrated experimentally on a part shown in Figure 6.2. The results for the face milling are given in Sections 6.3 and 6.4, hence, they are not shown here. Rest of the results for the profile and two slot milling operations are summarized as follows. First, tool breakage monitoring results for individual operations are given in Figure 6.13. The virtual model and on-line measured average torque per tooth period values are in an agreement since cutting force coefficients in the virtual model are calibrated at the beginning of the cut (first 10 spindle revolutions).

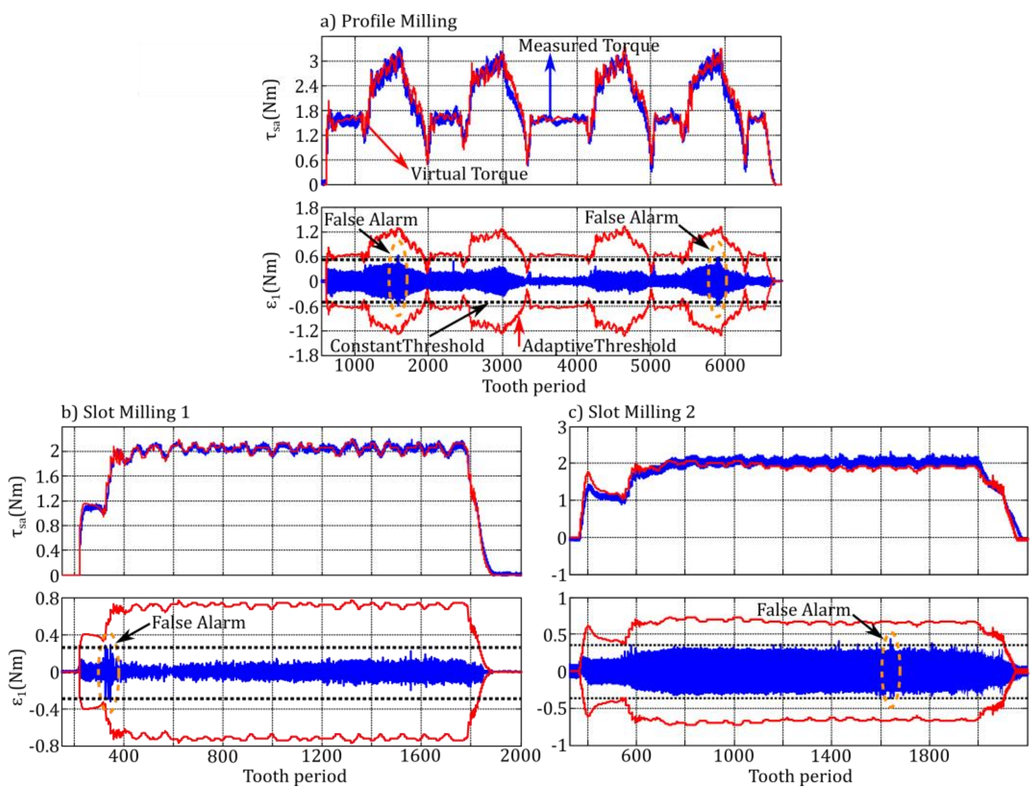

Figure 6.13: Tool breakage monitoring results for the demo part shown in Figure 6.2

For comparison of the previous, constant threshold-based method and the adaptive threshold with the virtual model feedback, false alarm locations with the constant threshold check are highlighted in Figure 6.13. These false alarms are neglected by the virtual model assisted tool breakage monitoring algorithm since the virtual model feedback adaptively changes the threshold value as a function of process geometry and physics.

Next, adaptive control results are given in Figure 6.14 where constant feed rate with no adaptive control (NoAC), conventional adaptive control (AC) and virtual model assisted adaptive control (ACwithVF) cases can be compared with each other for every operation.

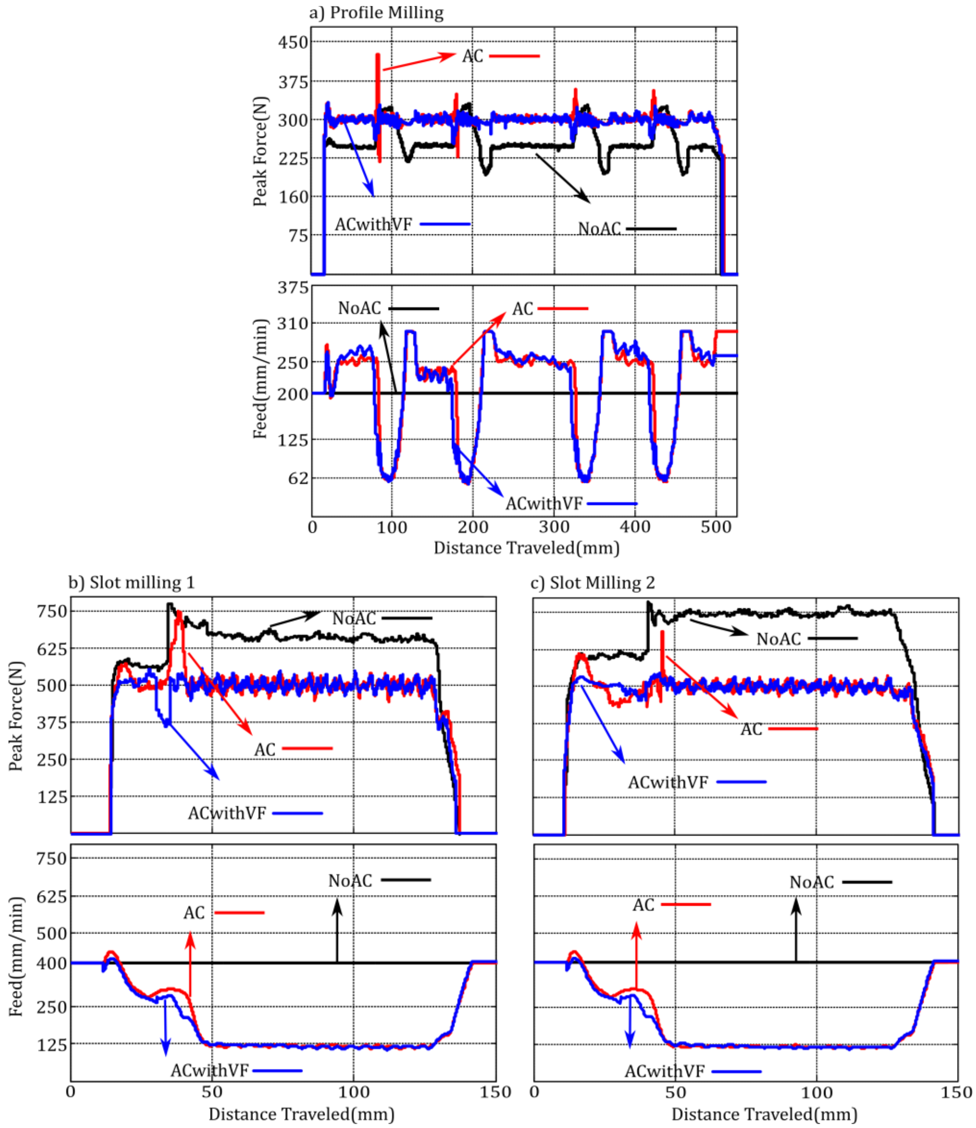

Figure 6.14: Virtual model assisted GPC, adaptive control (AC) with force identified from feed drive current command measurements, no AC (NoAC), conventional AC (AC) and AC with virtual machining model feedback (ACwithVF) for the demo part shown in Figure 6.2

It is evident that the virtual model assisted adaptive control benefits from the virtual feedback which warns the GPC algorithm prior to the sharp CWE increase, enables it to reduce the feed rate and prevents the transient overloads of the tool. As shown in Figure 6.14, peak force profile with the virtual model assisted adaptive controller is overshoot free where the forces are at the desired reference levels for each operation. The final machined part is shown in Figure 6.15.

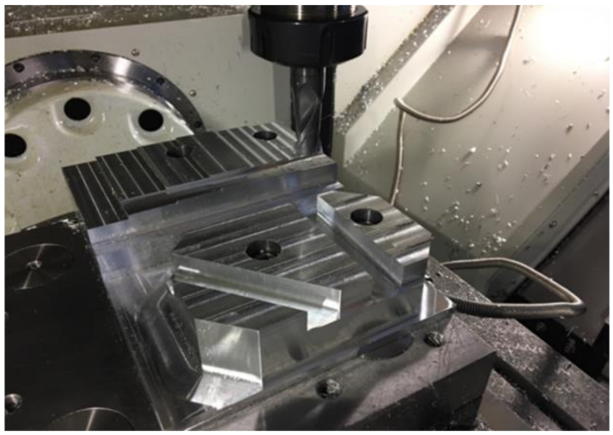

Figure 6.15: Final machined part on Quaser UX-600 machining center

Finally, it should be noted that the priority in the integrated system is given to the chatter detection/avoidance since the stability of the cutting process is the most important aspect and the tool breakage monitoring, as well as the adaptive control algorithms are designed for stable, chatter-free operations. Given that the process is stable, tool breakage monitoring has the next priority. Only when the operation is chatter-free, and tool is determined to be healthy, adaptive control is applied to increase the productivity further. The flowchart of the procedure is given in Figure 6.16 to show the structure clearly.

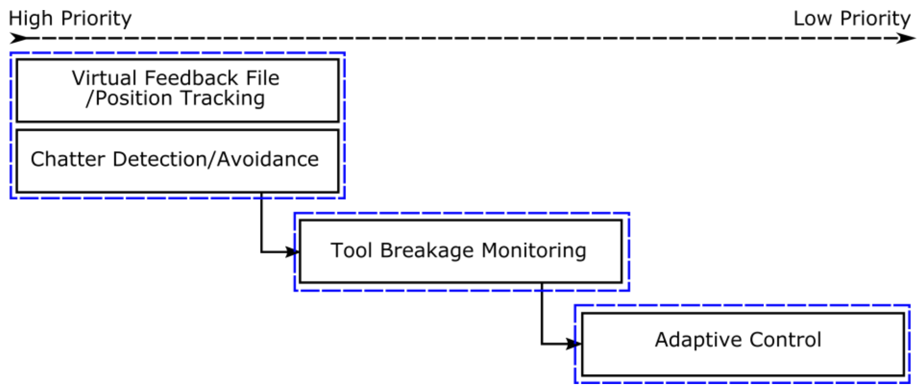

Figure 6.16: Priority levels of the integrated virtual and on-line monitoring and control system

6.6 Summary

This chapter presents a novel virtual machining integrated on-line process monitoring and control system. The use of CNC inherent force sensing eliminates the need to mount costly and impractical sensors on the machine. The proposed system in this chapter brings such critical information from the Virtual Machining system and enables the on-line monitoring and control algorithms to detect the tool failure and control the process more robustly. The application of the new approach has been proven on a demo part. The proposed method is aimed to let the machine tool to self-adjust itself to varying conditions in production by making robust decisions with the virtual machining feedback. The methodology as well as the results have been published in [5].

Chapter 7: Conclusion

7.1 Conclusion

In this thesis, a virtual model integrated on-line machining process monitoring and control system is introduced as a novel step toward achieving a digital twin for machining systems. Process states (i.e. cutting forces) are predicted from feed drive current commands by modeling the friction, inertia and compensating the effect of structural dynamics on the measurements. The friction model can capture the non-linear effects and transients where motion direction changes. After separating the friction and inertial loads from the current commands, which are due to the rigid body motion of the system, remaining disturbance torque coming from the cutting operation at the tool-workpiece interface is obtained. The distortion of the measured disturbance torque by the structural dynamics of the feed drive chain as it is transferred from the tool-workpiece interface to the servo is compensated by Kalman Filters designed individually for each drive. The bandwidth of the disturbance transfer functions of the feed drives are increased from 15-20 Hz to 180-200 Hz which covers a wide range of spindle and tooth passing frequencies used for difficult to cut materials. These compensated cutting forces (for translational drives) and torques (for rotational drives) are then mapped to the tool tip using the kinematic model of the multi-axis machine tool. The study shows that it is possible to achieve an external sensorless monitoring system by using the feed drive motor current commands readily available in CNC systems.

In addition, in-process varying dynamics of the tool, holder and spindle assembly are investigated by multiple vibration sensors installed on the spindle body and corresponding Kalman filters are updated accordingly. Process states are predicted from each vibration sensor to obtain more robust predictions with the data fusion method and the system can be used as an alternative to the force monitoring method based on CNC inherent data. It is also aimed to embed these vibration sensors inside the spindle for production environment as a future work.

The chatter vibrations are also detected from CNC drive current measurements without installing external sensors. Prior to state observer design, transfer function of the spindle drive is automatically identified with frequency sine-sweep tests using external PC – CNC connection. Knowing the transfer functions of the current and velocity controllers, transfer function between the disturbance torque coming from the tool tip and nominal (commanded) current supplied by the velocity controller is calculated and a Luenberger observer is used to compensate for the dynamical distortions in the measured nominal current signals. Proposed methodology does not require case dependent observers or filter tuning since the true dynamics of the system are considered where the presented results show that correct chatter frequency is identified regardless of the excitation frequency or the tool tip dynamics. The application of the method is shown mainly using the spindle motor current command. The proposed method is also able to predict the tangential component of the cutting force from the spindle drive current measurements which is then used to estimate the resultant force in X-Y plane. This method provides a practical and industry friendly way of estimating the resultant forces with an acceptable accuracy without going through extensive modeling of each translational and rotary feed drive on the machine tool. These practically estimated resultant forces can also be used for process monitoring and control applications.

Following the process state prediction and chatter vibration detection by using CNC drive measurements, a novel virtual process model integrated on-line process monitoring and control system is developed. First, the cutting process is simulated using in-house developed MACHpro® Virtual Machining System and the corresponding process states along the toolpath are stored in a virtual feedback file on an External PC. These simulated process states are accessed by the on-line monitoring and control system during the operation where the virtual model feedback prevents false tool breakage alarms, large transient overloads of the tool and collisions during adaptive control. The uncertainties in the virtual model, such as cutting force coefficients, are calibrated from on-line measurements for improved accuracy in the virtual model for future simulations. In order to read data from CNC, to run the process state and chatter vibration detection algorithms, and to trace the virtual model feedback file and change the feed and spindle speed overrides simultaneously, a multi-threaded on-line C++ code is developed by synchronizing the data flow in between threads using a circular buffer structure. The proposed system is demonstrated in machining a sample on a 5-axis CNC machining center. The prevention of false alarms, force overshoots and collisions are illustrated by disabling and enabling the virtual model feedback in consecutive passes.

In summary, this thesis presents an integrated virtual process model and on-line process monitoring system. The system predicts process states using CNC inherent data without installing external sensors within the work envelope. The proposed framework is aimed to let the machine tool run unattended by self-adjusting itself to varying in-process conditions with the aid of the virtual process model.

7.2 Future Research Directions

The methods presented in this thesis serve as a proof of concept for a digital machining twin to achieve an intelligent, self-adjusting and unattended machining systems utilizing CNC inherent data. The following future research can be carried out to improve the proposed system:

- Friction of feed drive system is represented using LuGre model which can be improved by considering the strengthening or aging at zero relative sliding velocity, which is a widely observed phenomenon where the static friction increases logarithmically with stationary contact time.
- Identification of drive disturbance FRFs is achieved through modal tap tests in this study. Alternatively, transfer function between the disturbance torque and nominal current can be calculated using frequency sine-sweeps, and the structural dynamics between the cutting region and the servo location can be added using receptance coupling or a similar tool to achieve automated system identification.
- Drive disturbance FRFs are identified in the cutting region of the sample part. As shown in Appendix B, these FRFs are position dependent and can also be coupled depending on the machine tool configuration. Following identification of these position dependent FRFs, gains of the state observers (Kalman Filters in this study) can be scheduled according to tool tip position in machine coordinate frame for improved force prediction accuracy.
- The induction motor of the spindle is modeled in time-domain using Simulink tool of MATLAB due to its highly non-linear, speed and load dependent behavior. For faster system identification, it can be modeled analytically by using practical assumptions.
- Identified disturbance transfer function of the spindle drive relies on high torsional stiffness of the tool, holder and spindle structure. The model can be extended to cover tools with

torsional modes located lower than the bandwidth of the compensated disturbance transfer function (< 2500 Hz).

- The process monitoring system can be extended to cover tool wear and machine tool health (i.e. spindle or feed drive) monitoring. Both the virtual machining process and machine tool models can be calibrated based on on-line measurements simultaneously. In return, virtual tools can provide useful information to the on-line algorithms in regards to preventative maintenance of spindle and feed drives to reduce downtimes and deciding when to change the tool due to wear prior to tool breakage or poor surface finishes.
- Integrated virtual process model assisted on-line monitoring and control system can be implemented within CNC itself to prevent additional delays coming from the communication and execution between External PC and CNC.
- Tool breakage percentage threshold value between the virtual process model and the on-line application can be selected by learning from the previous available data.
- Vibration sensors installed on the spindle body can be embedded inside which will make the system more practical to use in production environment. Having reliable vibration, force and thermocouple sensors strategically placed close to the bearings and assembly locations inside the spindle will provide more insight about the process states and spindle structure’s health.

References

[1] D. Aslan and Y. Altintas, "Prediction of cutting forces in five-axis milling using feed drive current measurements," *IEEE/ASME Transactions on Mechatronics,* vol. 23, pp. 833-844, 2018.

[2] J. Yang, D. Aslan, and Y. Altintas, "Identification of workpiece location on rotary tables to minimize tracking errors in five-axis machining," *International Journal of Machine Tools and Manufacture,* vol. 125, pp. 89-98, 2018.

[3] J. Yang, D. Aslan, and Y. Altintas, "A feedrate scheduling algorithm to constrain tool tip position and tool orientation errors of five-axis CNC machining under cutting load disturbances," *CIRP Journal of Manufacturing Science and Technology,* vol. 23, pp. 78-90, 2018.

[4] D. Aslan and Y. Altintas, "On-line chatter detection in milling using drive motor current commands extracted from CNC," *International Journal of Machine Tools and Manufacture,* vol. 132, pp. 64-80, 2018.

[5] Y. Altintas and D. Aslan, "Integration of virtual and on-line machining process control and monitoring," *CIRP Annals-Manufacturing Technology,* vol. 66, pp. 349-352, 2017.

[6] R. Teti, K. Jemielniak, G. O'Donnell, and D. Dornfeld, "Advanced monitoring of machining operations," *CIRP Annals-Manufacturing Technology,* vol. 59, pp. 717-739, 2010.

[7] F. Klocke, S. Kratz, and D. Veselovac, "Position-oriented process monitoring in freeform milling," *CIRP Journal of Manufacturing Science and Technology,* vol. 1, pp. 103-107, 2008/01/01/ 2008.

[8] G. Totis, O. Adams, M. Sortino, D. Veselovac, and F. Klocke, "Development of an innovative plate dynamometer for advanced milling and drilling applications," *Measurement,* vol. 49, pp. 164-181, 2014.

[9] H. C. Mohring, K. M. Litwinski, and O. Gummer, "Process monitoring with sensory machine tool components," *CIRP Annals-Manufacturing Technology,* vol. 59, pp. 383-386, 2010.

[10] Z. Y. Xie, Y. Lu, and J. G. Li, "Development and testing of an integrated smart tool holder for four-component cutting force measurement," *Mechanical Systems and Signal Processing,* vol. 93, pp. 225-240, 2017.

[11] A. Sampath and S. Vajpayee, "Tool health monitoring using acoustic emission," *International Journal of Production Research,* vol. 25, pp. 703-719, 1987.

[12] D. Choi, W. T. Kwon, and C. N. Chu, "Real-time monitoring of tool fracture in turning using sensor fusion," *The International Journal of Advanced Manufacturing Technology,* vol. 15, pp. 305-310, 1999.

[13] T. Moriwaki and K. Okushima, "Detection for cutting tool fracture by acoustic emission measurement," *CIRP Annals-Manufacturing Technology,* vol. 29, pp. 35-40, 1980.

[14] D. Yan, T. I. El-Wardany, and M. A. Elbestawi, "A multi-sensor strategy for tool failure detection in milling," *International Journal of Machine Tools and Manufacture,* vol. 35, pp. 383-398, 1995.

[15] J. Tlusty and G. C. Andrews, "A critical review of sensors for unmanned machining," *CIRP Annals-Manufacturing Technology,* vol. 32, pp. 563-572, 1983.

[16] J. Jeppsson, "Aerospace manufacturing: Making HSM work," *Manufacturing Engineering,* vol. 124, pp. 72-82, 2000.
[17] J. L. Stein and J. F. Tu, "A state-space model for monitoring thermally induced preload in anti-friction spindle bearings of high-speed machine tools," *ASME Journal of Dynamic Systems, Measurement, and Control,* vol. 116, pp. 372-386, 1994.
[18] A. A. D. Sarhan, A. Matsubara, M. Sugihara, H. Saraie, S. Ibaraki, and Y. Kakino, "Monitoring method of cutting force by using additional spindle sensors," *JSME International Journal Series C Mechanical Systems, Machine Elements and Manufacturing,* vol. 49, pp. 307-315, 2006.
[19] M. C. Kang, J. S. Kim, and J. H. Kim, "A monitoring technique using a multi-sensor in high speed machining," *Journal of Materials Processing Technology,* vol. 113, pp. 331-336, 2001.
[20] S. S. Park and Y. Altintas, "Dynamic compensation of spindle integrated force sensors with Kalman Filter," *ASME Journal of Dynamic Systems Measurement and Control,* vol. 126, pp. 443-452, 2004.
[21] G. Byrne and G. E. O'Donnell, "An integrated force sensor solution for process monitoring of drilling operations," *CIRP Annals-Manufacturing Technology,* vol. 56, pp. 89-92, 2007.
[22] A. Albrecht, S. S. Park, Y. Altintas, and G. Pritschow, "High frequency bandwidth cutting force measurement in milling using capacitance displacement sensors," *International Journal of Machine Tools and Manufacture,* vol. 45, pp. 993-1008, 2005.
[23] D. A. Smith, S. Smith, and J. Tlusty, "High performance milling torque sensor," *ASME Journal of Manufacturing Science and Engineering,* vol. 120, pp. 504-514, 1998.
[24] J. F. G. Oliveira, F. Ferraz Júnior, R. T. Coelho, and E. J. Silva, "Architecture for machining process and production monitoring based in open computer numerical control," *Proceedings of the Institution of Mechanical Engineers, Part B: Journal of Engineering Manufacture,* vol. 222, pp. 1605-1612, 2008.
[25] K. Matsushima, P. Bertok, T. J. M. Sata, and C. f. B. Manufacturing, "In-process detection of tool breakage by monitoring the spindle motor current of a machine tool," pp. 145-153, 1982.
[26] N. Constantinides and S. Bennett, "An investigation of methods for the on-line estimation of tool wear," *International Journal of Machine Tools and Manufacture,* vol. 27, pp. 225-237, 1987.
[27] M. A. Mannan and S. Broms, "Investigation into temperature dependence of motor current measurements applied to monitoring and adaptive control," *CIRP Annals-Manufacturing Technology,* vol. 41, pp. 451-454, 1992.
[28] Y. Altintas, "Prediction of Cutting Forces and Tool Breakage in Milling from Feed Drive Current Measurements," *ASME Journal of Engineering for Industry,* vol. 114, pp. 386-392, 1992.
[29] H. Shinno, H. Hashizume, and H. Yoshioka, "Sensor-less monitoring of cutting force during ultraprecision machining," *CIRP Annals-Manufacturing Technology,* vol. 52, pp. 303-306, 2003.
[30] O. Özşahin, E. Budak, and H. N. Özgüven, "In-process tool point FRF identification under operational conditions using inverse stability solution," *International Journal of Machine Tools and Manufacture,* vol. 89, pp. 64-73, 2015.

[31] M. Postel, O. Özsahin, and Y. Altintas, "High speed tooltip FRF predictions of arbitrary tool-holder combinations based on operational spindle identification," *International Journal of Machine Tools and Manufacture,* vol. 129, pp. 48-60, 2018.
[32] A. Ertürk, H. N. Özgüven, and E. Budak, "Effect analysis of bearing and interface dynamics on tool point FRF for chatter stability in machine tools by using a new analytical model for spindle–tool assemblies," *International Journal of Machine Tools and Manufacture,* vol. 47, pp. 23-32, 2007.
[33] C.-W. Lin, Y.-K. Lin, and C.-H. Chu, "Dynamic models and design of spindle-bearing systems of machine tools: A review," *International Journal of Precision Engineering and Manufacturing,* vol. 14, pp. 513-521, 2013.
[34] H. Cao, B. Li, and Z. He, "Chatter stability of milling with speed-varying dynamics of spindles," *International Journal of Machine Tools and Manufacture,* vol. 52, pp. 50-58, 2012.
[35] M. Rantatalo, J.-O. Aidanpää, B. Göransson, and P. Norman, "Milling machine spindle analysis using FEM and non-contact spindle excitation and response measurement," *International Journal of Machine Tools and Manufacture,* vol. 47, pp. 1034-1045, 2007.
[36] C. H. Cheng, T. L. Schmitz, and G. Scott Duncan, "Rotating tool point frequency response prediction using RCSA," *Machining Science and Technology,* vol. 11, pp. 433-446, 2007.
[37] B. A. Mascardelli, S. S. Park, and T. Freiheit, "Substructure coupling of micro-end mills," pp. 145-150, 2006.
[38] A. Matsubara, S. Tsujimoto, and D. Kono, "Evaluation of dynamic stiffness of machine tool spindle by non-contact excitation tests," *CIRP Annals-Manufacturing Technology,* vol. 64, pp. 365-368, 2015.
[39] I. Zaghbani and V. Songmene, "Estimation of machine-tool dynamic parameters during machining operation through operational modal analysis," *International Journal of Machine Tools and Manufacture,* vol. 49, pp. 947-957, 2009.
[40] N. Suzuki, Y. Kurata, T. Kato, R. Hino, and E. Shamoto, "Identification of transfer function by inverse analysis of self-excited chatter vibration in milling operations," *Precision Engineering,* vol. 36, pp. 568-575, 2012.
[41] M. Eynian, "Vibration frequencies in stable and unstable milling," *International Journal of Machine Tools and Manufacture,* vol. 90, pp. 44-49, 2015.
[42] U. V. Kumar and T. L. Schmitz, "Spindle dynamics identification for receptance coupling substructure analysis," *Precision Engineering,* vol. 36, pp. 435-443, 2012.
[43] N. Grossi, L. Sallese, F. Montevecchi, A. Scippa, and G. Campatelli, "Speed-varying machine tool dynamics identification through chatter detection and receptance coupling," *Procedia CIRP,* vol. 55, pp. 77-82, 2016.
[44] B. Denkena, D. Dahlmann, and H. Boujnah, "Tool deflection control by a sensory spindle slide for milling machine tools," *Procedia CIRP,* vol. 62, pp. 329-334, 2017.
[45] B. Denkena, K. M. Litwinski, and H. Boujnah, "Detection of tool deflection in milling by a sensory axis slide for machine tools," *Mechatronics,* vol. 34, pp. 95-99, 2016.
[46] S. S. Park, "High frequency bandwidth cutting force measurements in milling using the spindle integrated force sensor system," Ph.D. dissertation, University of British Columbia, Vancouver, Canada,, 2003.
[47] S. A. Tobias, *Machine-Tool Vibration*. London: Blackie, 1965.

[48] F. Koenigsberger and J. Tlusty, *Machine Tool Structures. vol. 1*. Oxford: Pergamon Press, 1970.

[49] I. Minis and R. Yanushevsky, "A new theoretical approach for the prediction of machine tool chatter in milling," *Journal of Engineering for Industry,* vol. 115, pp. 1-8, 1993.

[50] Y. Altintaş and E. Budak, "Analytical prediction of stability lobes in milling," *CIRP Annals-Manufacturing Technology,* vol. 44, pp. 357-362, 1995.

[51] S. D. Merdol and Y. Altintas, "Multi frequency solution of chatter stability for low immersion milling," *Journal of Manufacturing Science and Engineering,* vol. 126, pp. 459-466, 2004.

[52] T. Insperger, G. Stépán, P. V. Bayly, and B. P. Mann, "Multiple chatter frequencies in milling processes," *Journal of Sound and Vibration,* vol. 262, pp. 333-345, 2003.

[53] Y. Altintas, *Manufacturing Automation : Metal Cutting Mechanics, Machine Tool Vibrations, and CNC Design*, 2nd ed. Cambridge ; New York: Cambridge University Press, 2012.

[54] Y. Altintas and P. K. Chan, "In-process detection and suppression of chatter in milling," *International Journal of Machine Tools and Manufacture,* vol. 32, pp. 329-347, 1992.

[55] G. S. Sekhon, "Monitoring and control of machining operations," M.A.S.c. thesis, University of British Columbia, Vancouver, Canada,, 2013.

[56] T. L. Schmitz, K. Medicus, and B. Dutterer, "Exploring once-per-revolution audio signal variance as a chatter indicator," *Machining Science and Technology,* vol. 6, pp. 215-233, 2002.

[57] M. Mitsuishi, S. Warisawa, and R. Hanayama, "Development of an intelligent high-speed machining center," *CIRP Annals-Manufacturing Technology,* vol. 50, pp. 275-280, 2001.

[58] Y. Fu, Y. Zhang, H. Zhou, D. Li, H. Liu, H. Qiao*, et al.*, "Timely online chatter detection in end milling process," *Mechanical Systems and Signal Processing,* vol. 75, pp. 668-688, 2016.

[59] E. Kuljanic, M. Sortino, and G. Totis, "Multisensor approaches for chatter detection in milling," *Journal of Sound and Vibration,* vol. 312, pp. 672-693, 2008.

[60] L. Sallese, N. Grossi, J. Tsahalis, A. Scippa, and G. Campatelli, "Intelligent fixtures for active chatter control in milling," *Procedia CIRP,* vol. 55, pp. 176-181, 2016.

[61] E. Soliman and F. Ismail, "Chatter detection by monitoring spindle drive current," *The International Journal of Advanced Manufacturing Technology,* vol. 13, pp. 27-34, 1997.

[62] Y. Kakinuma, Y. Sudo, and T. Aoyama, "Detection of chatter vibration in end milling applying disturbance observer," *CIRP Annals-Manufacturing Technology,* vol. 60, pp. 109-112, 2011.

[63] T. Yoneoka, Y. Kakinuma, K. Ohnishi, and T. Aoyama, "Disturbance observer–based in-process detection and suppression of chatter vibration," *Procedia CIRP,* vol. 1, pp. 44-49, 2012.

[64] T. Shimoda, H. Fujimoto, N. Kumagai, and Y. Terada, "External sensorless adaptive chatter avoidance in NC machining by applying disturbance observer using high resolution linear encoder," in *Proceedings of the 2017 IEEE International Conference on Advanced Intelligent Mechatronics (AIM)*, 2017, pp. 879-884.

[65] M.-S. Lan and Y. Naerheim, "In-process detection of tool breakage in milling," *Journal of Engineering for Industry,* vol. 108, pp. 191-197, 1986.

[66] Y. Altintas, "In-process detection of tool breakages using time series monitoring of cutting forces," *International Journal of Machine Tools and Manufacture,* vol. 28, pp. 157-172, 1988.

[67] J. Tlusty and M. A. A. Elbestawi, "Analysis of transients in an adaptive control servomechanism for milling with constant force," *Journal of Engineering for Industry,* vol. 99, pp. 766-772, 1977.

[68] L. K. L. Saunders, "Process dynamics models for the control of end milling," in *Proceedings of the 2000 American Control Conference.*, 2000, pp. 2563-2567, vol.4.

[69] Y. Liu, T. Cheng, and L. Zuo, "Adaptive control constraint of machining processes," *The International Journal of Advanced Manufacturing Technology,* vol. 17, pp. 720-726, 2001.

[70] R. Neugebauer, B. Denkena, and K. Wegener, "Mechatronic systems for machine tools," *CIRP Annals-Manufacturing Technology,* vol. 56, pp. 657-686, 2007.

[71] L. N. L. d. Lacalle, A. Lamikiz, J. A. Sanchez, and I. F. d. Bustos, "Simultaneous measurement of forces and machine tool position for diagnostic of machining tests," *IEEE Transactions on Instrumentation and Measurement,* vol. 54, pp. 2329-2335, 2005.

[72] M. Nouri, B. K. Fussell, B. L. Ziniti, and E. Linder, "Real-time tool wear monitoring in milling using a cutting condition independent method," *International Journal of Machine Tools and Manufacture,* vol. 89, pp. 1-13, 2015.

[73] H. C. Möhring, K. M. Litwinski, and O. Gümmer, "Process monitoring with sensory machine tool components," *CIRP Annals-Manufacturing Technology,* vol. 59, pp. 383-386, 2010.

[74] R. Koike, K. Ohnishi, and T. Aoyama, "A sensorless approach for tool fracture detection in milling by integrating multi-axial servo information," *CIRP Annals-Manufacturing Technology,* vol. 65, pp. 385-388, 2016.

[75] A. Verl, U. Heisel, M. Walther, and D. Maier, "Sensorless automated condition monitoring for the control of the predictive maintenance of machine tools," *CIRP Annals-Manufacturing Technology,* vol. 58, pp. 375-378, 2009.

[76] F. J. A. M. van Houten and F. Kimura, "The virtual maintenance system: A computer-based support tool for robust design, product monitoring, fault diagnosis and maintenance planning," *CIRP Annals-Manufacturing Technology,* vol. 49, pp. 91-94, 2000.

[77] M. Hayashi, H. Yoshioka, and H. Shinno, "An adaptive control of ultraprecision machining with an in-process micro-sensor," *Journal of Advanced Mechanical Design, Systems, and Manufacturing,* vol. 2, pp. 322-331, 2008.

[78] A. Yuen, "Trajectory generation, control, and geometric error compensation for a 9-axis micromachining center," Ph.D. dissertation, University of British Columbia, Vancouver, Canada,, 2018.

[79] K. Johanastrom and C. Canudas-de-Wit, "Revisiting the LuGre friction model," *IEEE Control Systems Magazine,* vol. 28, pp. 101-114, 2008.

[80] P. I. Ro, W. Shim, and S. Jeong, "Robust friction compensation for submicrometer positioning and tracking for a ball-screw-driven slide system," *Precision Engineering,* vol. 24, pp. 160-173, 2000.

[81] CUTPRO^{TM} Advanced Machining Simulation System, Manufacturing Automation Laboratory, The University of British Columbia, Canada, 2000.

[82] R. G. Brown and P. Y. C. Hwang, *Introduction to Random Signals and Applied Kalman Filtering : with MATLAB Exercises and Solutions,* 3rd ed. ed.: New York: Wiley, 1997.

[83] J. Hartikainen, A. Solin, and S. Särkkä, *Optimal Filtering with Kalman Filters and Smoothers–A Manual for Matlab Toolbox EKF/UKF*, 2011.

[84] J. Denavit and R. S. Hartenberg, "A kinematic notation for lower-pair mechanisms based on matrices," *ASME Journal of Applied Mechanics,* vol. 22, pp. 215-221, 1955.

[85] T. Mathworks, "MATLAB® and Optimization Toolbox Release," *Natick, Massachusetts, United States.*, 2017.

[86] P. Krause, O. Wasynczuk, S. D. Sudhoff, and S. Pekarek, *Analysis of Electric Machinery and Drive Systems* vol. 75: John Wiley & Sons, 2013.

[87] Y. T. Oh, W. T. Kwon, and C. N. Chu, "Drilling torque control using spindle motor current and its effect on tool wear," *The International Journal of Advanced Manufacturing Technology*, vol. 24, pp. 327-334, 2004.

[88] W. Tae Kwon and I. Jun Hong, "Estimation of the cutting torque without a speed sensor during CNC turning," *Journal of Mechanical Science and Technology,* vol. 19, p. 2205, 2005.

[89] T. M. Wolbank and P. E. Macheiner, "Modulation of transient reactances of induction machines caused by different types of eccentricity," in *Proceedings of the 2007 IEEE International Symposium on Diagnostics for Electric Machines, Power Electronics and Drives*, 2007, pp. 89-94.

[90] D. G. Luenberger, *Introduction to Dynamic Systems: Theory, Models, and Applications,* vol. 1: Wiley New York, 1979.

[91] A. Laub and M. Wette, "Algorithms and software for pole assignment and observers," California Univ., Santa Barbara (USA). Dept. of Electrical and Computer Engineering, 1984.

[92] E. Budak, Y. Altintaş, and E. J. A. Armarego, "Prediction of milling force coefficients from orthogonal cutting data," *Journal of Manufacturing Science and Engineering,* vol. 118, pp. 216-224, 1996.

[93] MACHpro™ Advanced Virtual Machining System, Manufacturing Automation Laboratory, The University of British Columbia, Canada, 2011.

[94] Heidenhain, "Technical Manual Catalogue - iTNC 530 HSCI," 2013.

Appendices

Appendix A Normalized Equivalent State-Space Matrices of the Rotary and Translational Feed Drives

A Axis;

$$\mathbf{A_A} = \begin{bmatrix} \{A_{A1}\}_{1x12} \\ diag\{A_{A2}\}_{11x11}, [0]_{11\times1} \end{bmatrix}$$

$$\{A_{A1}\} = [-1374 \quad -891.7 \quad -408.2 \quad -482.7 \quad -300 \quad -383.1 \quad -309.2 \quad \ldots$$
$$-229.1 \quad -220.2 \quad -174.7 \quad -146.4]$$

$$\{A_{A2}\} = \begin{bmatrix} 4096 & 2048 & 1024 & 1024 & 512 & 512 & 512 & 256 & 256 & 128 & 128 \end{bmatrix}^T$$

$$\mathbf{B_A} = \begin{bmatrix} 16 & 0 & 0 & 0 & 0 & 0 & 0 & 0 & 0 & 0 & 0 & 0 \end{bmatrix}^T$$

$$\mathbf{C_A} = [1.288 \quad -0.01161 \quad 0.3942 \quad -0.1527 \quad 0.4932 \quad -0.5031 \quad 1.077 \quad \ldots$$
$$-0.7235 \quad 0.4528 \quad -2.704 \quad -4.568 \quad -4.44]$$

$$\mathbf{D_A} = \begin{bmatrix} -0.00522 \end{bmatrix}$$

C Axis;

$$\mathbf{A_C} == \begin{bmatrix} \{A_{C1}\}_{1x10} \\ diag\{A_{C2}\}_{9x9}, [0]_{9\times1} \end{bmatrix}$$

$$\{A_{C1}\} = [-254.2 \quad -487.9 \quad -191.6 \quad -680.5 \quad -203.1 \quad -436.4 \quad -89.57 \quad \ldots$$
$$-256.7 \quad -55.19 \quad -220.6]$$

$$\{A_{C2}\} = \begin{bmatrix} 2048 & 512 & 512 & 512 & 512 & 512 & 256 & 256 & 128 \end{bmatrix}^T$$

$$\mathbf{B_C} = \begin{bmatrix} 32 & 0 & 0 & 0 & 0 & 0 & 0 & 0 & 0 & 0 \end{bmatrix}^T$$

$$\mathbf{C_C} = [5.219 \quad 2.102 \quad 5.303 \quad 6.649 \quad 6.765 \quad 6.569 \quad 3.299 \quad \ldots$$
$$5.133 \quad 2.01 \quad 4.942]$$

$$\mathbf{D_C} = \begin{bmatrix} 0.3761 \end{bmatrix}$$

X Axis;

$$\mathbf{A_x} == \begin{bmatrix} \{A_{x1}\}_{1x12} \\ diag\left\{A_{x2}\right\}_{11x11}, [0]_{11\times1} \end{bmatrix}$$

$$\{A_{x1}\} = [-273.6 \quad -1202 \quad -220.4 \quad -852.1 \quad -95.78 \quad -399.5 \quad -57.62 \quad ...$$
$$-316.9 \quad -55.73 \quad -224.3 \quad -37.45 \quad -233.8]$$

$$\{A_{x2}\} = \begin{bmatrix} 2048 & 1024 & 1024 & 1024 & 512 & 512 & 256 & 256 & 256 & 128 & 128 \end{bmatrix}^T$$

$$\mathbf{B_x} = \begin{bmatrix} 64 & 0 & 0 & 0 & 0 & 0 & 0 & 0 & 0 & 0 & 0 & 0 \end{bmatrix}^T$$

$$\mathbf{C_x} = \begin{bmatrix} 64 & 0 & 0 & 0 & 0 & 0 & 0 & 0 & 0 & 0 & 0 & 0 \end{bmatrix}$$

$$\mathbf{D_x} = \begin{bmatrix} 0.317 \end{bmatrix}$$

Y Axis;

$$\mathbf{A_y} == \begin{bmatrix} \{A_{y1}\}_{1x24} \\ diag\left\{A_{y2}\right\}_{23x23}, [0]_{23\times1} \end{bmatrix}$$

$$\{A_{y1}\} = [-475.1 \quad -884.7 \quad -84.94 \quad -152.2 \quad -48.24 \quad -224 \quad -117.5 \quad ...$$
$$-397.1 \quad -171.7 \quad -449 \quad -158.6 \quad -332.4 \quad -94.29 \quad -161.8 \quad -71.67 \quad ...$$
$$-204.5 \quad -67.63 \quad -161.6 \quad -37.16 \quad -148.7 \quad -41.73 \quad -138.1 \quad -17.18 \quad -89.21]$$

$$\{A_{y2}\} = [4096 \quad 4096 \quad 2048 \quad 1024 \quad 512 \quad 512 \quad 512 \quad 512 \quad 512 \quad 512 \quad 512 \quad 512...$$
$$...512 \quad 256 \quad 256 \quad 256 \quad 256 \quad 256 \quad 128 \quad 128 \quad 128 \quad 128 \quad 64]^T$$

$$\mathbf{B_y} = \begin{bmatrix} 64 & 0 & 0 & 0 & 0 & 0 & 0 & 0 & 0 & 0 & 0 & 0 & 0 & 0 & 0 & 0 & 0 & 0 & 0 & 0 & 0 & 0 & 0 & 0 \end{bmatrix}^T$$

$$\mathbf{C_y} = [1.914 \quad 0.3712 \quad 0.5438 \quad 0.2173 \quad 0.4085 \quad 0.6071 \quad 1.213 \quad 1.639 \quad ...$$
$$2.066 \quad 2.513 \quad 2.155 \quad 2.352 \quad 1.416 \quad 1.381 \quad 1.172 \quad 2.036 \quad ...$$
$$1.192 \quad 1.832 \quad 0.6987 \quad 1.882 \quad 0.827 \quad 1.917 \quad 0.3491 \quad 1.328]$$

$$\mathbf{D_y} = \begin{bmatrix} 0.147 \end{bmatrix}$$

Z Axis;

$$\mathbf{A_z} == \begin{bmatrix} \{A_{z1}\}_{1x16} \\ diag\left\{A_{z2}\right\}_{15x15}, [0]_{15\times1} \end{bmatrix}$$

$$\{A_{z1}\} = [-245 \quad -850.1 \quad -91 \quad -535.3 \quad -99.12 \quad -333.5 \quad -102.7 \quad -454.2 \quad ...$$
$$-111.1 \quad -347 \quad -62.96 \quad -288.5 \quad -68.93 \quad -236.6 \quad -28.12 \quad -147.7]$$

$$\{A_{z2}\} = [4096 \quad 2048 \quad 1024 \quad 1024 \quad 1024 \quad 512 \quad 512 \quad 512 \quad ...$$
$$512 \quad 512 \quad 256 \quad 256 \quad 256 \quad 256 \quad 128]^T$$

$$\mathbf{B_z} = \begin{bmatrix} 64 & 0 & 0 & 0 & 0 & 0 & 0 & 0 & 0 & 0 & 0 & 0 & 0 & 0 & 0 & 0 \end{bmatrix}^T$$

$$\mathbf{C_z} = [6.682 \quad 1.031 \quad 2.565 \quad 1.439 \quad 2.887 \quad 1.45 \quad 3.074 \quad 2.739 \quad ...$$
$$3.393 \quad 2.638 \quad 1.948 \quad 2.568 \quad 2.145 \quad 2.295 \quad 0.8807 \quad 1.46]$$

$$\mathbf{D_z} = \begin{bmatrix} 0.2422 \end{bmatrix}$$

Appendix B Kalman Smoother

Kalman smoother is applied to compensated forces in each axis to fix the phase shift introduced by the disturbance transfer function further. It is crucial to correct the phase shifts of compensated signals as much as possible before mapping them to the tool tip with the kinematics solution.

Smoothing corresponds to consideration of additional measurements from the past and future states and acts similar to forward-backward filtering. Since targeted process monitoring and control algorithms run in tooth passing or spindle rotation periods, delay buffers are designed (with 6 milliseconds duration) with 60 nominal current data points ($\cong$ 0.1 millisecond sampling time) to apply the Kalman Smoother with past and future available data points. Given that the estimated states are $\hat{x}_{\exp}$ (see Eq. (3.26)), Kalman smoother works as follows;

$$\hat{\mathbf{x}}_{\mathbf{exp,s_k}} = \hat{\mathbf{x}}_{\mathbf{exp}} + \mathbf{K}_{\mathbf{s,k}}(\hat{\mathbf{x}}_{\mathbf{exp,s_{k+1}}} - \mathbf{A}_{\mathbf{exp}}\hat{\mathbf{x}}_{\mathbf{exp}}) \tag{B.1}$$

where Kalman smoother gain is calculated as;

$$\mathbf{K}_{\mathbf{s,k}} = \frac{\mathbf{P}_{\mathbf{k}}\mathbf{A}_{\mathbf{exp_k}}{}^{\mathbf{T}}}{\mathbf{A}_{\mathbf{exp_k}}\mathbf{P}_{\mathbf{k}}\mathbf{A}_{\mathbf{exp_k}}{}^{\mathbf{T}} + \mathbf{Q}_{\mathbf{k}}} \tag{B.2}$$

and the smoother error covariance matrix (used as a smoothing performance criteria [83]) is updated as;

$$\mathbf{P}_{\mathbf{s,k}} = \mathbf{P}_{\mathbf{k}} + \mathbf{K}_{\mathbf{s,k}}(\mathbf{P}_{\mathbf{s,k+1}} - \mathbf{P}_{\mathbf{k+1}})\mathbf{K}_{\mathbf{s,k}}{}^{\mathbf{T}} \tag{B.3}$$

Compensated measurements are iteratively smoothed, and the synchronized estimations follow the on-line measurements with a delay of 6 milliseconds. Buffer size can be adjusted in order to reduce the delay further by sacrificing from the smoothing performance. Further details of the buffering and Kalman smoother algorithm can be found in [52] and [83], respectively.

Appendix C Position Dependency of the Drive Disturbance FRFs

Translational Drives;

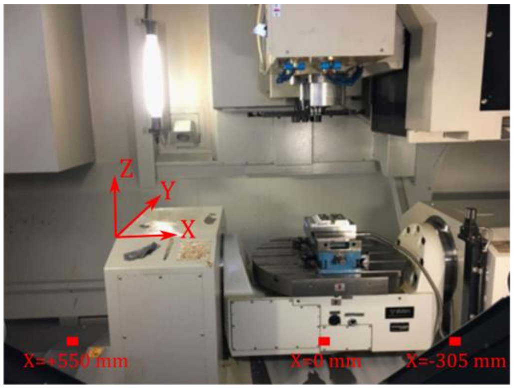

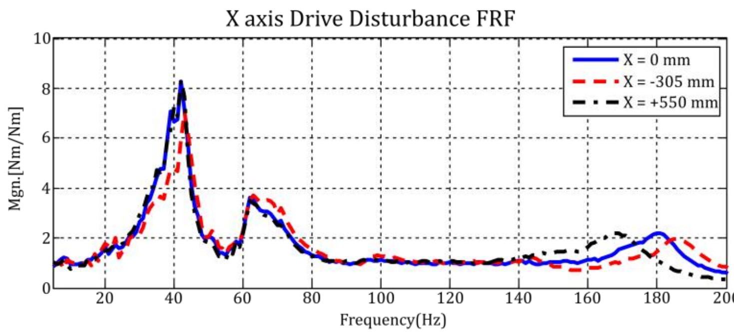

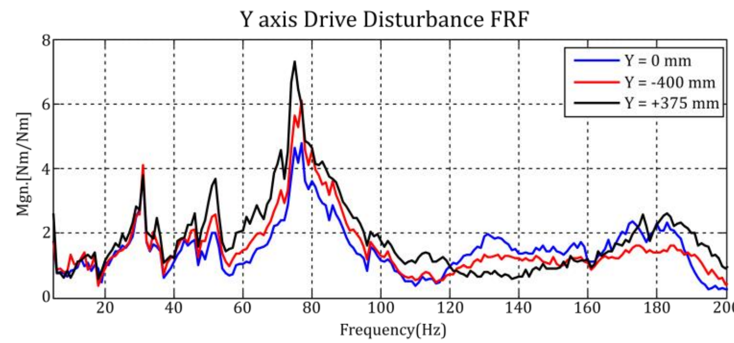

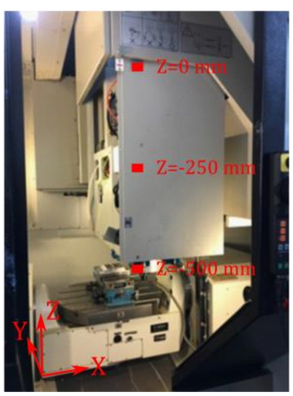

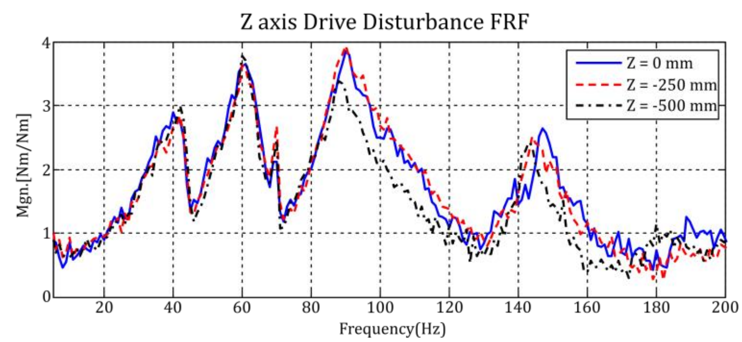

Rotary Drives;

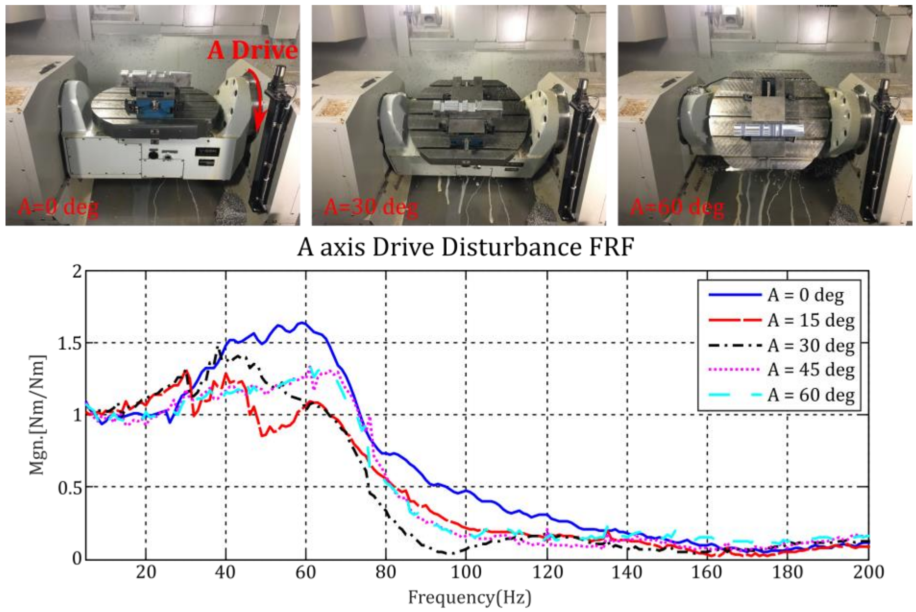

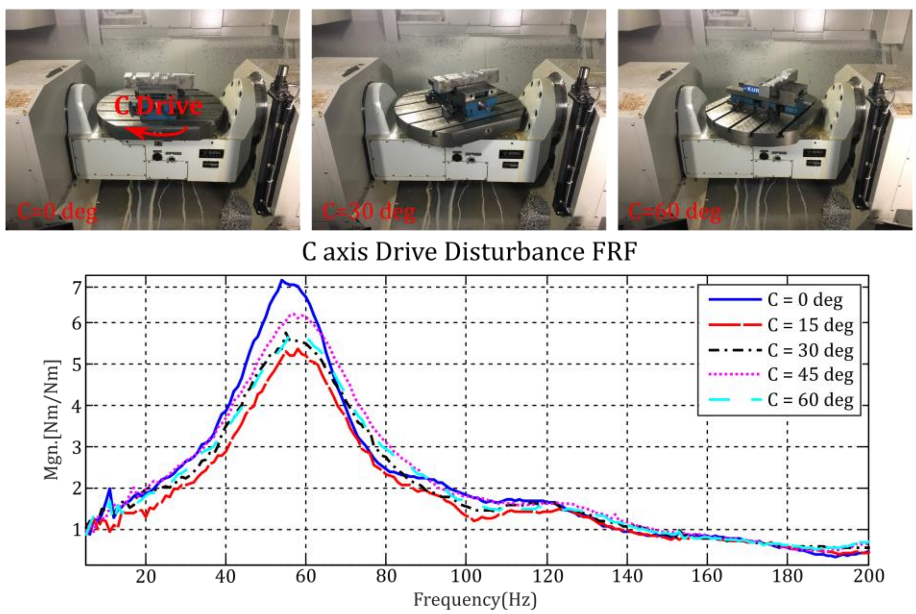

Appendix D FRF of the Velocity Loop - Simulated and Measured with Sine Sweep Tests

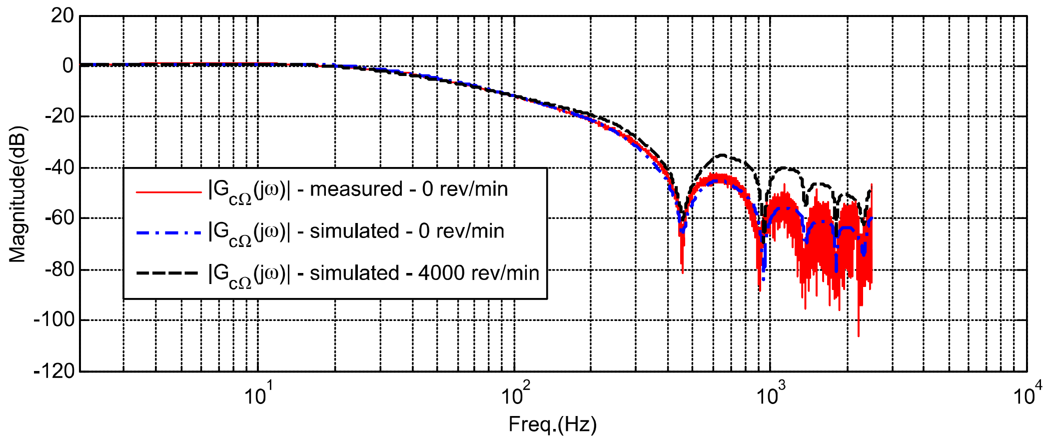

As illustrated above, the second speed range (4000 rev/min) exhibits a similar behavior with the first speed range (0 rev/min). Velocity closed loop FRF for the second speed range could not be measured due to the limitations in the Heidenhain CNC (TNCOpt®) system identification tool box.

Appendix E Identified Transfer Function Modal Parameters of the Spindle Drive

		1st Speed Range (0-3300 rev/min)				2nd Speed Range (3300-24000 rev/min)			
	Mode	ω_{nk} (Hz)	ζ_k (%)	α_k	β_k	ω_{nk} (Hz)	ζ_k (%)	α_k	β_k
Spindle Drive; $\frac{\Omega_{act}(s)}{\tau_m(s)}$	1	21.9	83	8.6e1	-9.1e-1	21.4	77	8.5e1	-1.7e1
	2	66.8	94	-9.1e1	-2.9e2	232.7	60	- 9.1e1	7.7e1
	3	258.8	50	1.8e1	6.4e1	445.9	35	4.4	-5.5
	4	457.9	50	-8.9	-1e1	666.5	20	- 3.6e1	4.9
	5	640	15	-1.7	4.4	843.8	25	2.7e1	-3.8e1
	6	875	12	-4.9e-1	-1.8	1157.7	15	1.7e1	1.1e1
	7	1050	12	6.1e-1	1	1355.6	5.4	-2.3	3.9e-1
	8	1350	4	-3.5e-1	-9.9e-1	1659.8	10.9	8.3	2
	9	1800	3	-2.5e-1	1.3e-2	1766.2	8	-6.2	2.2
	10	2417	5	-4.3e-1	5.4e-1	2415.7	4.7	-1	2.3

Appendix F Recursive Parameter Estimation Algorithm

Recursive least squares algorithm used to find the transfer function parameters of the combined feed drive and cutting process transfer function (G_c) given in Eq. (6.7) – Chapter 6 is summarized in this section [46]. First, the estimated parameter vector (coefficients of the transfer function - G_c) is written as;

$$\hat{\theta}(t) = \begin{bmatrix} \hat{a}_1 & \hat{a}_2 & \hat{b}_0 & \hat{b}_1 & \hat{b}_2 \end{bmatrix}^T \tag{F.1}$$

and the regression (observation) vector consists of previous input (commanded feed rate - f_c) and output (peak force at each spindle period (k) - F_p) samples is constructed as;

$$\phi(t) = \begin{bmatrix} -F_p(k-1) & -F_p(k-2) & f_c(k-1) & f_c(k-2) & f_c(k-3) \end{bmatrix}^T \tag{F.2}$$

The estimated parameter vector is updated at every time step as follows;

$$\hat{\theta}(t) = \hat{\theta}(t-1) + a(t)k(t)(F_p(t) - \phi^T(t)\hat{\theta}(t-1)) \tag{F.3}$$

where $k(t)$ is the estimation gain;

$$k(t) = P(t-1)\phi(t)(1 + \phi^T(t)P(t-1)\phi(t))^{-1} \tag{F.4}$$

Covariance matrix $P(t)$ is calculated as;

$$P(t) = c_1 \frac{\bar{P}(t)}{tr(\bar{P}(t))} + c_2 I \tag{F.5}$$

and auxiliary covariance matrix $\bar{P}(t)$ is;

$$\begin{aligned} &\bar{P}(t) = \bar{P}(t-1) - a(t)k(t)\phi^T(t)P(t-1) \\ &a(t) = \begin{cases} 1 \ \ if \ \ \left| F_p(t) - \phi^T(t)\hat{\theta}(t-1) \right| > 2\delta, \\ \qquad 0 \ \ otherwise, \end{cases} \end{aligned} \tag{F.6}$$

c_1 and c_2 are greater than zero and δ is an estimate of the magnitude tolerable fluctuation of the output of the process or noise. When the adaptive control algorithm runs in a steady cut region where the process conditions do not change for a long period, the covariance matrix usually becomes too small or large which leads to numerical instability. Therefore, trace of the covariance matrix ($tr(P(k))$) should be monitored and the covariance matrix should be reset to its initial value when it becomes too small or large along the toolpath [53].

Appendix G Generalized Predictive Control (GPC) Algorithm

The recursive algorithm of GPC is summarized in this section [53]. The Diophantine equation becomes as follows when $j=1$;

$$1=\Delta A(z^{-1})E_1(z^{-1})+z^{-1}F_1(z^{-1}) \tag{G.1}$$

which yields $e_{10}=1,\ f_{10}=-(a_1-1),\ f_{11}=-(a_2-a_1),$ and $f_{12}=a_2$ where vector $\{f\}$ is;

$$\{f\}=\begin{Bmatrix} g_{11} & g_{12} & f_{10} & f_{11} & f_{12} \\ g_{22} & g_{23} & f_{20} & f_{21} & f_{22} \\ g_{33} & g_{34} & f_{30} & f_{31} & f_{32} \\ g_{44} & g_{45} & f_{40} & f_{41} & f_{42} \end{Bmatrix} \begin{Bmatrix} \Delta f_c(k-1) \\ \Delta f_c(k-2) \\ F_p(k) \\ F_p(k-1) \\ F_p(k-2) \end{Bmatrix} \tag{G.2}$$

For $j>1$, Diophantine equations at j and $j+1$ becomes;

$$\Delta A\left[E_{j+1}-E_j\right]+z^{-j}\left[z^{-1}F_{j+1}-F_j\right]=0 \tag{G.3}$$

which leads to;

$$\begin{gathered} e_{10}=e_{20}=e_{30}=e_{40}=e_0=1 \\ e_{21}=e_{31}=e_{41}=e_1 \\ e_{32}=e_{42}=e_2 \\ e_{43}=e_3 \end{gathered} \tag{G.4}$$

and

$$\begin{aligned} e_{j-1} &= f_{j-1,0} \\ f_{j,i} &= f_{j-1,i+1-e_{j-1}(a_{i+1}-a_i)},\ i=0,1,2 \end{aligned} \tag{G.5}$$

The polynomial G_j is then calculated as follows;

$$G_j=E_jB=E_j(b_0+b_1z^{-1}+b_2z^{-2}) \tag{G.6}$$

These equations are recursively solved at each prediction step ($G_j = E_j B = E_j (b_0 + b_1 z^{-1} + b_2 z^{-2})$) and the individual parameters are given as;

$E_j (j = 1,2,3,4)$;

$$\begin{aligned} E_1 &= e_0 \\ E_2 &= e_0 + e_1 z^{-1} \\ E_3 &= e_0 + e_1 z^{-1} + e_2 z^{-2} \\ E_4 &= e_0 + e_1 z^{-1} + e_2 z^{-2} + e_3 z^{-3} \end{aligned} \tag{G.7}$$

$F_j (j = 1,2,3,4)$;

$$\begin{aligned} F_1 &= f_{10} + f_{11} z^{-1} + f_{12} z^{-2} \\ F_2 &= f_{20} + f_{21} z^{-1} + f_{22} z^{-2} \\ F_3 &= f_{30} + f_{31} z^{-1} + f_{32} z^{-2} \\ F_4 &= f_{40} + f_{41} z^{-1} + f_{42} z^{-2} \end{aligned} \tag{G.8}$$

$G_j (j = 1,2,3,4)$. ;

$$\begin{aligned} G_1 &= g_{10} + g_{11} z^{-1} + g_{12} z^{-2} \\ G_2 &= g_{20} + g_{21} z^{-1} + g_{22} z^{-2} + g_{23} z^{-3} \\ G_3 &= g_{30} + g_{31} z^{-1} + g_{32} z^{-2} + g_{33} z^{-3} + g_{34} z^{-4} \\ G_4 &= g_{40} + g_{41} z^{-1} + g_{42} z^{-2} + g_{43} z^{-3} + g_{44} z^{-4} + g_{45} z^{-5} \end{aligned}$$

The contents of the prediction, reference and gain vectors are as follows;

$$\left\{\hat{F}_p\right\} = \left\{\begin{pmatrix} \hat{F}_p(k+1) \\ \hat{F}_p(k+2) \\ \hat{F}_p(k+3) \\ \hat{F}_p(k+4) \end{pmatrix}\right\}, \ \left\{F_r\right\} = \left\{\begin{pmatrix} F_r(k+1) \\ F_r(k+2) \\ F_r(k+3) \\ F_r(k+4) \end{pmatrix}\right\}, \ \left\{G_I\right\} = \left\{\begin{pmatrix} g_0 \\ g_1 \\ g_2 \\ g_3 \end{pmatrix}\right\} \tag{G.9}$$

where recursively calculated polynomials E_j, F_j and G_j are [53];

$$
\begin{aligned}
&For\ j=1;\\
&e_0=1,\ f_{10}=-(a_1-1),\ f_{11}=-(a_2-a_1),\ f_{12}=a_2,\\
&g_0=g_{10},g_{11}=b_1,g_{12}=b_2\\
&For\,j=2;\\
&e_1=f_{10},\ f_{20}=f_{11}-e_1(a_1-1),\ f_{21}=f_{12}-e_1(a_2-a_1),\\
&f_{22}=e_1a_2,g_{20}=b_0,g_1=g_{21}=b_1+e_1b_0,g_{22}=b_2+e_1b_1,g_{23}=e_1b_2\\
&For\ j=3;\\
&e_2=f_{20},\ f_{30}=f_{21}-e_2-(a_1-1),\ f_{31}=f_{22}-e_2(a_2-a_1),\ f_{32}=e_2a_2,\\
&g_{30}=g_0,g_{31}=g_1,g_2=g_{32}=b_2+e_1b_1+e_2b_0,g_{33}=e_1b_2+e_2b_1,g_{34}=e_2b_2\\
&For\ j=4;\\
&e_3=f_{30}.\ f_{40}=f_{31}-e_3(a_1-1),\ f_{41}=f_{32}-e_3(a_2-a_1),\ f_{42}=e_3a_2,g_{40}=g_0,\\
&g_{41}=g_2,g_3=g_{43}=e_1b_2+e_2b_1+e_3b_0,g_{44}=e_2b_2+e_3b_1,g_{45}=e_3b_2
\end{aligned}
\tag{G.10}
$$